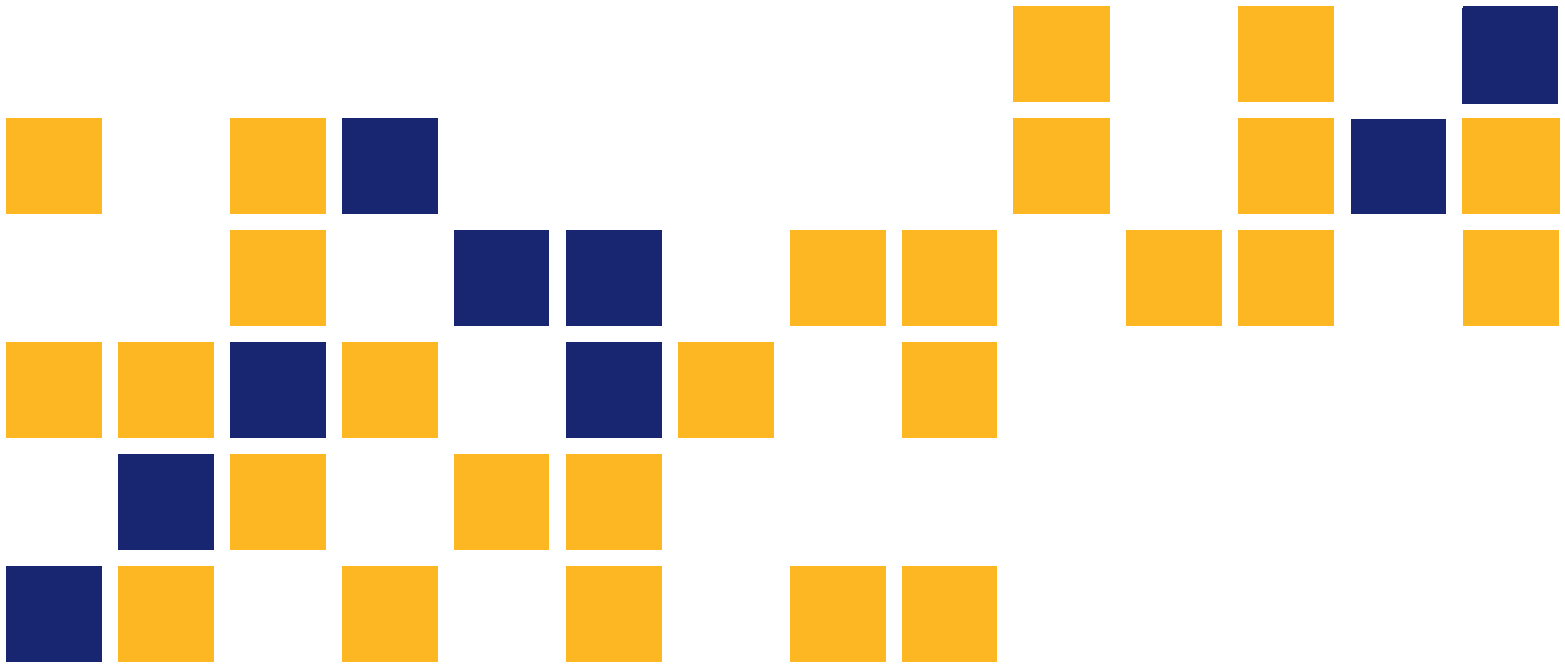# Enhancement of Welded Steel Bridge Girders Susceptible to Distortion-Induced Fatigue

Caroline Bennett, Ph.D., P.E.
Adolfo Matamoros, Ph.D.
Ron Barrett-Gonzalez, Ph.D.
Stan Rolfe, Ph.D., P.E.

The University of Kansas Center for Research, Inc.

AD ASTRA PER ASPERA

Kansas
Department of Transportation

Appendix A: Table of Contents

Appendix A: List of Tables

Appendix A: List of Figures

Appendix A: Development of the Angles-with-Plate Repair

Appendix A is organized around the development and testing of the angles-with-plate repair technique, which was developed such that it could be applied under traffic and without removal of a concrete bridge deck.

Appendices A.1 and A.2 are focused on the development of the angles-with-plate repair technique performed using a girder segment test set-up; Appendix A.1 presents the physical tests, and A.2 presents the corresponding finite element results.

Appendices A.3 and A.4 are focused on the testing of the angles-with-plate retrofit technique in a three-girder test bridge set-up. A.3 presents the physical tests, and A.4 presents a parametric analysis performed using computational simulations.

Appendix A.1: Repairing Distortion-Induced Fatigue Cracks in Steel Bridge Girders using Angles-with-Plate Retrofit Technique, Part I: Physical Simulations

Fatih Alemdar[1]

Daniel Nagati [2]

Adolfo B. Matamoros[3]

Caroline R. Bennett[4]

Stanley T. Rolfe[5]

A.1.1 Abstract

Physical simulations of 914 mm (36 in.) deep girder-cross frame subassemblies subjected to cyclic loading were carried out to study the effects of distortion-induced fatigue and to evaluate the effectiveness of a new retrofit measure. The new repair method consists of adding steel angles connecting the girder web to the cross frame transverse connection plate (CP), and a steel plate on the opposite side of the girder web. Parameters of the experimental study included the retrofit configuration and length of the fatigue cracks. Test results showed that the new angles-with-plate retrofit measure was effective in preventing fatigue crack reinitiation for both horseshoe-shaped cracks around the CP-to-web weld and cracks along the flange-to-web weld. When the retrofit measure was implemented, specimens were able to exceed the number of cycles equivalent to infinite fatigue life for AASHTO Fatigue Category A details without any measureable fatigue crack growth, regardless of crack configuration.

A test trial was also carried out to measure fatigue crack reinitiation life of the web gap region with undersized crack-arrest holes. Experimental results showed that, for the stress range imposed at the web gap region of the specimens and the crack-arrest hole diameter evaluated,

---

[1] Fatih Alemdar, PhD, Assistant Professor, Yildiz Technical University, Istanbul, Turkey

[2] Daniel Nagati, MS, Assistant Civil/Structural Engineer, Black and Veatch Corporation, 11401 Lamar Ave, Overland Park, KS 66211

[3] Adolfo B. Matamoros, PhD, Professor, University of Kansas, 1530 W. 15th St., Lawrence KS, 66045

[4] Caroline R. Bennett, PhD, P.E., Associate Professor, University of Kansas, 1530 W. 15th St., Lawrence KS, 66045

[5] Stanley T. Rolfe, P.E., PhD, A.P. Learned Distinguished Professor, University of Kansas, 1530 W. 15th St., Lawrence KS, 66045

fatigue cracks reinitiated at 40,000 cycles, which was below the limit for AASHTO Fatigue Category E' details.

A.1.2 Introduction and Background

In a national survey carried out by Linderberg and Schultz (2007), Department of Transportation (DOT) engineers from various states reported 11 different types of commonly-observed fatigue cracks in steel bridges. One of the most frequently reported areas exhibiting fatigue damage were transverse connection plate (CP) web gaps in positive and negative moment regions of girders. This type of cracking is caused by out-of-plane distortion of the web gap, induced by secondary actions generated when adjacent girders experience different vertical deflections (Keating 1994).

There are several existing repair methods for distortion-induced fatigue damage (Keating and Fisher 1987; Fisher et al. 1990; Cousins and Stallings 1998). In general, existing repair methods are aimed at reducing stress demands in the web gap region by either increasing flexibility of the girder web in the out-of-plane direction or restraining lateral motion of the web, which is often accomplished by constraining the transverse connection plate (CP) to the girder flange.

Providing direct connectivity between a transverse connection plate and girder flange has been shown to be highly effective (Fisher et al. 1990), but in some instances can be challenging to implement. For example, bolting a connecting angle to the girder flange requires partial removal of the concrete deck if the repair is being implemented in a top web gap. A different approach, simpler to fabricate on-site, was investigated in this study. The proposed retrofit measure, designated angles-with-plate repair, was developed to reduce the stress demands at critical locations within the web gap region. The angles and plate components provide an alternate load path that reduces the fraction of the force transferred through the welds and redistributes the out-of-plane force over a larger area of the girder web.

A comprehensive computational study, described in Appendix A.2, was carried out to provide basic guidelines for configuration of the angles-with-plate retrofit measure. A discussion of the calculated stress field and behavior of the web gap region of the subassemblies for various crack configurations is also presented in Appendix A.2. The main goal of this paper was to

present results of an experimental program performed to validate the findings of the computational study. A third phase of the study, which consists of field evaluation of the angle-with-plate repair method in an existing bridge and experimental evaluation using a reduced-scale model of a full bridge system, is currently underway (Richardson, 2012).

A.1.3 Objective and Scope

The main objective of this research was to verify experimentally the effectiveness of a new repair method for distortion-induced fatigue. The significance of this new repair method is that it is simpler to implement and more cost-effective than existing retrofit measures. Performance of the method was investigated experimentally using 914 mm (36 in.) deep girder-cross frame subassemblies subjected to cyclic loading.

A secondary goal of the research was to evaluate the performance of undersized crack-arrest holes as a stop-gap repair measure for distortion-induced fatigue. This method of repair was investigated because it is commonly used in steel bridges.

A.1.4 Experimental Program

The top flange of a girder in a bridge system is restrained from lateral motion by the bridge deck, while the bottom flange is free or nearly free to move in the out-of-plane direction. These boundary conditions are very difficult to replicate in a sub-component test due to the difficulties associated with simulating the flexural stiffness of the slab and the stiffness of the remaining segment of the girder at the edges of the component. The subassemblies evaluated in this study were placed upside-down (se Figure A.1 to A.3) with respect to the orientation of a bridge girder, meaning that the unrestrained flange was at the top of the subassembly while the restrained flange was attached to the reaction floor. One of the effects of attaching the specimen to the reaction floor in this manner was that bending stresses due to dead and live gravity loads that occur in bridge girders were eliminated from the subassemblies, leaving only out-of-plane demands imposed by the cross frame. Consequently, the stress field imposed on the specimens is a better representation of behavior expected near gravity-load inflection points of bridges, or in regions of bridge girders where live load-induced bending stresses are small compared with the magnitude of stresses induced by out-of-plane forces.

9

The web gap region of the girder subassembly was cyclically loaded under a constant force range while the initiation and propagation of fatigue cracks was monitored. Given the characteristics of the stress field at the web gap region, experimental results provided insight about crack propagation behavior under the combined effects of fracture modes 1 and 3 (opening and shear modes). The experimental program also allowed for direct comparisons between the two mitigation methods studied.

While the boundary conditions of the subassemblies constitute a limitation of the study, a large number of computer simulations were carried out to verify that the stress field in the web gap region of the subassemblies was similar to that calculated in the web gap region of girders in bridge systems. A study comprising more than 1,000 large-scale simulations of bridge systems described in Appendix D.1 and D.2 of this report showed that the computed stress fields at the web gap of the subassemblies was similar to that calculated in the girders of bridge systems, and that the critical points for fatigue-crack initiation were the same. A second computational study carried out by Richardson (2012) showed that the effect of the angles-with-plate retrofit measure on the web gap region of an existing bridge structure was similar to the effect observed in the simulations of the subassemblies.

A.1.5 Specimen Dimensions

The girder subassemblies were built-up welded I-shape sections with a depth of 918 mm (36-$^1/_8$ in.). The thickness of the web was 10 mm ($^3/_8$ in.) and the web height was 876 mm (34-$^1/_2$ in.). The top and bottom flanges each had a width of 279 mm (11 in.), and thicknesses were 25 mm (1 in.) and 16 mm ($^5/_8$ in.), respectively. The transverse connection plate at the centerline of the girder was attached to the web with a 5 mm ($^3/_{16}$ in.) fillet weld. The CP had a thickness of 10 mm ($^3/_8$ in.), a width of 127 mm (5 in.), and a height of 873 mm (34$^3/_8$ in.). In the bottom web gap, the CP had a clipped end of 32 mm (1$^1/_4$ in.) and a 3 mm ($^1/_8$ in.) gap between the CP and bottom flange. At the top of the girder, the CP was fabricated as milled-to-bear against the inside face of the top flange, without any welded connection. It is common for aging bridges across the national inventory to have the CP connected to the compression flange and not the tension flange. Although less common, there are a significant number of bridges without positive attachment between either flange and the CP. The type of detail used in this study was adopted

after consultation with the Kansas Department of Transportation (KDOT) because it was suggested that this was the most common detailing practice use in aging bridges in the state of Kansas.

At both ends of the girder, transverse stiffeners were welded to the web and both flanges on both sides of the web. The stiffener dimensions at the girder ends were 10x876x127 mm ($^3/_8$ x 34-½ x 5 in.). The girder subassembly was attached to the laboratory floor with C5x9 channels (Figures A.1 and A.2) connected to the girder through fully-tightened 19 mm ($^3/_4$ in.) diameter A325 bolts spaced at 305 mm (1 ft) (Figure A.2). A cross frame, consisting of three L76x76x10 mm (L3x3x$^3/_8$ in.) angles with an X- configuration and a horizontal member (Figure A.3), connected the specimen to the actuator (Figure A.1 and A.3). The cross frame was connected to a WT section used to stabilize the free end of the cross frame and to prevent warping and bending of the frame while loading the specimen.

Figure A.1: Experimental setup
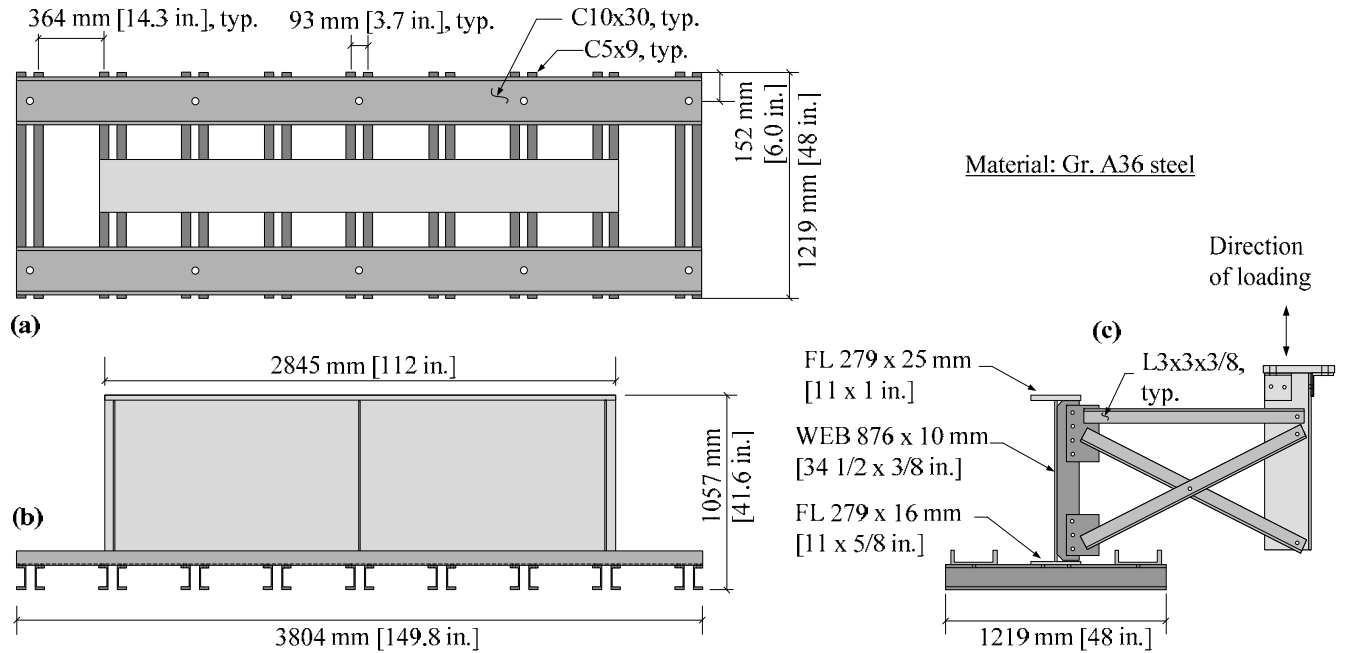
Figure A.2: Girder specimen
(a) Plan view (cross-frame not shown for clarity); (b) elevation view; (c) Girder cross-section at mid-length of girder

Elevation   *Cross-Section*
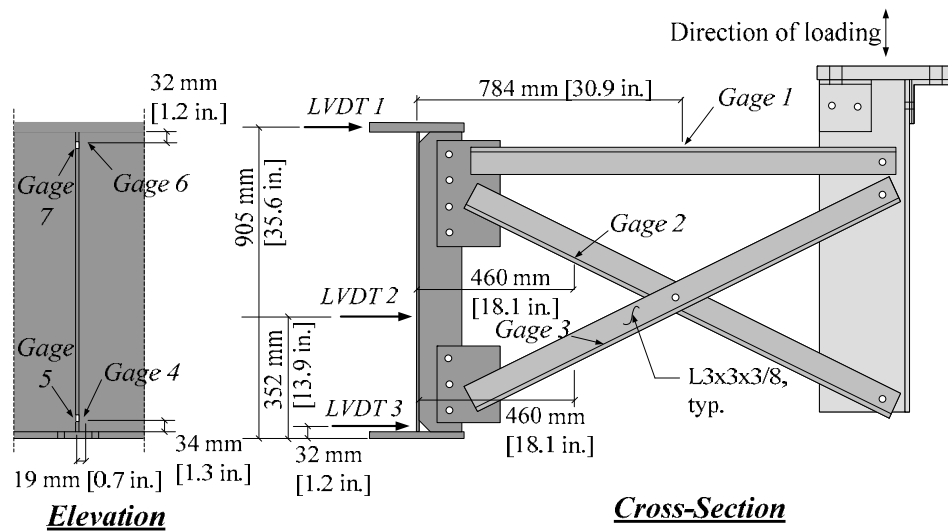
Figure A.3: Instrumentation on 2.8 m (9.3 ft) girder specimens

A.1.6 Material Properties

All the plates used to fabricate the built-up section were Gr. A36 steel. After the test was concluded, tensile coupons were cut from the web and flanges of Specimen 2. The web coupons (1 through 3) had a 230 mm (9 in.) test length while the flange coupons (4 through 9) had a 57 mm ($2^1/_4$ in.) test length in accordance with ASTM E8/E8M (2009). Coupons had different size because the thickness of the web was considerably lower than the thickness of the flanges. Coupons extracted from the web were sheet-type, while coupons from the flange were plate-type. Flange coupons were cut parallel to the direction of rolling, and the web coupons were cut perpendicular to the direction of rolling. Measured material properties are presented in Table A.1. The variation in percent elongation observed in the material tests is attributable to the difference in tensile coupon dimensions.

Table A.1: Tensile Coupon Test Results

Coupon #	Description	F_y, MPa (ksi)	F_u, MPa (ksi)	E, GPa (ksi)	% Elongation
1	Web	372 (54)	524 (76)	192 (27900)	19
2	Web	352 (51)	531 (77)	216 (31400)	20
3	Web	379 (55)	531 (77)	205 (29800)	22
	Average:	**365 (53)**	**531 (77)**	**205 (29700)**	**20**
4	Thinner FL	331 (48)	490 (71)	172 (25000)	38
5	Thinner FL	331 (48)	483 (70)	196 (28500)	37
6	Thinner FL	345 (50)	490 (71)	210 (30400)	39
	Average:	**338 (49)**	**490 (71)**	**193 (28000)**	**38**
7	Thicker FL	317 (46)	483 (70)	218 (31600)	39
8	Thicker FL	310 (45)	483 (70)	222 (32200)	39
9	Thicker FL	324 (47)	483 (70)	216 (31400)	37
	Average:	**317 (46)**	**483 (70)**	**218 (31700)**	**38**

A.1.7 Instrumentation

Specimens were instrumented with linear variable differential transformers (LVDTs) and strain gages at locations shown in Figure A.3. The LVDTs were attached to an instrumentation column which was tied to the reaction floor. Reference readings were taken at zero load and subtracted from the measured displacements under load. Two strain gages were located on the fascia side of the web, behind the transverse connection plate, at the top and bottom of the web (gages 5 and 7). Another two gages were located on the right side of the transverse connection plate (gages 4 and 6, Figure A.3), on the interior face of the girder. The loading protocol was

defined based on the stress range recorded at strain gage 4, located 17 mm (0.65 in.) to the right of the CP. This location was selected because computer simulations showed that the stress field was nearly constant in this region, and the stress was considered to be representative of the bending stress induced by the out-of-plane motion in the web gap. Figure A.4 shows that for monotonically-applied load there was very good correlation between strain gage readings and simulation results, with strain gage readings being slightly higher than the computed results. For reference, the measured stress range under the applied cyclic load recorded by gage 4 was 196 MPa (29 ksi).

LVDTs were used to measure the out-of-plane deflections at three different locations on the centerline of the girder (Figure A.3). The first LVDT was placed at the top flange, the second at mid-depth of the web, and the third directly behind the bottom of the CP, on the fascia side of the web. A comparison between measured and computed deflections at the centerline of the girder for an applied load of 17 kN (3.8 kips) is presented in Figure A.5. The difference between the measured and calculated deflections in Figure A.5 is attributed to the difficulty of simulating all the sources of flexibility that take place in a physical test. For example, small rigid body displacements and rotations caused by slip between the laboratory floor and the reaction system introduce deformations in the physical specimen that are very difficult to simulate accurately in an FE model. Because computer models neglect such sources of flexibility, it was expected that deflection measurements from the physical simulations would be greater than the deflections computed using FE models. Figure A.5 shows that, as expected, computed deflections for the nominal force range were lower in magnitude than those measured. To provide a comparison of the goodness of fit between computed and measured deflected shapes, the computed deflected shape was scaled so that the deflection at the top of the girder would be the same as the measured deflection. The scaled deflected shape is shown as a dotted line in Figure A.5. It is apparent from Figure A.5 that the slope of the scaled deflected shape matched the measured deflected shape very closely, and that the main difference between the two lines stemmed from the level of restraint of the flange against out-of-plane rotation in the physical model.
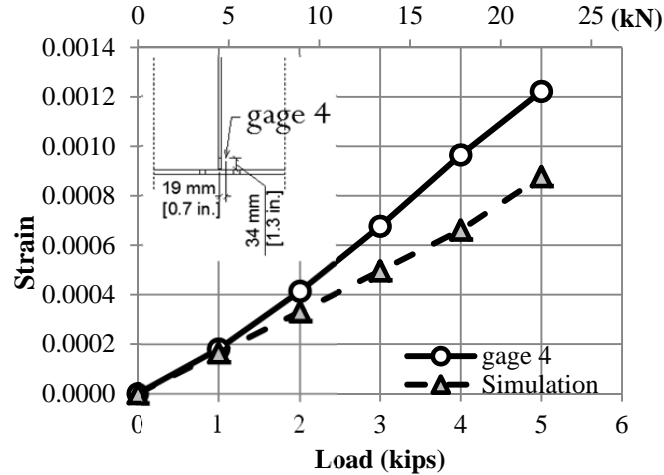
Figure A.4: Comparison between strain gage readings and simulation results for monotonically-applied load
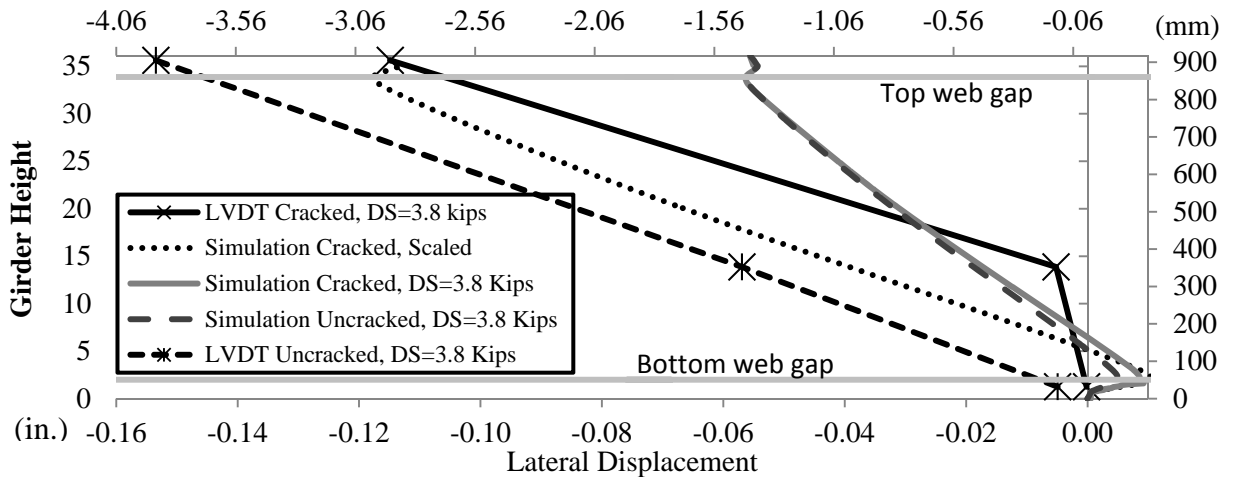
Figure A.5: Comparison between LVDT Readings and computed deformations

A.1.8 Test Procedure

Specimens were subjected to cyclic loading causing out-of-plane distortion of the web gap. The maximum load applied was 20 kN (4.6 kip) and the minimum was 3.6 kN (0.8 kip). These load values induced a stress range of 197 MPa (29 ksi) at the top of the web gap region. The tests were performed using two different actuators, with the frequency of loading limited by the capacity of the servovalve of the hydraulic actuator that was employed. Loading rates for the two actuators were 0.5 and 2 Hz. Crack growth was monitored periodically. Test trials were stopped when crack length exceeded a predefined threshold or when the number of cycles exceeded the infinite fatigue life limit in the AASHTO (2013) S-N fatigue design curve (Figure

15

A.6). Because the measured stress range was 197 MPa (29 ksi), infinite fatigue life was defined in this study as the number of cycles in the S-N curve of the AASHTO LRFD Bridge Design Specification (AASHTO 2013) corresponding to a Category A detail (approximately 1.2 million cycles at a stress range of 197 MPa, 29 ksi).
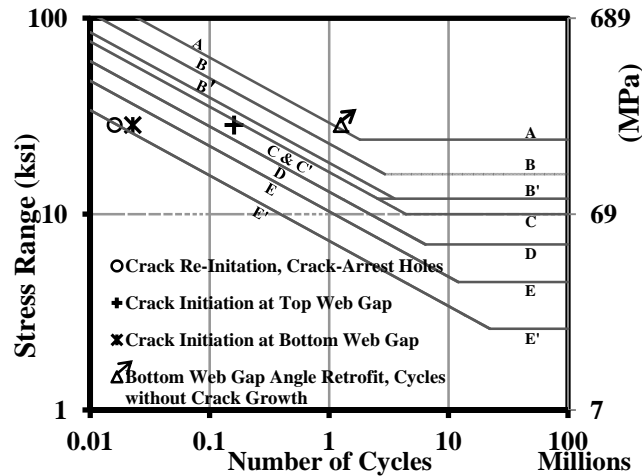
Figure A.6: Experimental results for Specimen 2 trials

The experimental program is summarized in Table A.2. Three specimens were evaluated with a total of 14 different test trials. Specimen 1 was fabricated to have a pre-existing horizontal crack with a length of 38 mm ($1^{1}/_{2}$ in.), positioned 17 mm (0.65 in) from the top of the bottom flange, and was used primarily to calibrate the results of the finite element model. Specimen 2 was used to evaluate the performance of the two mitigation measures, angles-with-plate and crack-arrest holes, for a given crack configuration in the web gap. During testing of Specimen 2, a crack was observed in the top web gap, so tests were performed with the angles-and-plate retrofit measure in both the top and bottom web gaps. Specimen 3 was used to evaluate the effectiveness of the angles-and-plate retrofit measure for various fatigue crack lengths. During all trials, specimens were inspected periodically to measure crack growth.

16

Table A.2: Experimental Program

Specimen	Test Trial	Configuration
1	1	Pre-Cracked, Unretrofitted
2	1	Un-cracked, Unretrofitted
2	2	203 mm (8 in.) Horizontal Crack Bottom Web Gap, Angles with Plate Retrofit Bottom Web Gap
2	3	203 mm (8 in.) Horizontal Crack Bottom Web Gap, 84 mm (3.3 in.) Horizontal Crack Top Web Gap, Angles with Plate Retrofit Bottom and Top Web Gap
2	4	216 mm (8.5 in.) Horizontal Crack Bottom Web Gap, 84 mm (3.3 in.) Horizontal Crack Top Web Gap, Crack-Stop Hole Retrofit
2	5	216 mm (8.5 in.) Horizontal Crack Bottom Web Gap, 84 mm (3.3 in.) Horizontal Crack Top Web Gap, Angles with Plate Retrofit Bottom and Top Web Gap
3	1	UnCracked, Unretrofitted
3	2	51 mm (2 in.) Horizontal Crack, Angles with Plate Retrofit Bottom Web Gap
3	3	51 mm (2 in.) Horizontal Crack, Unretrofitted
3	4	102 mm (4 in.) Horizontal Crack, Angles with Plate Retrofit Bottom Web Gap
3	5	102 mm (4 in.) Horizontal Crack, Unretrofitted
3	6	152 mm (6 in.) Horizontal Crack, Angles with Plate Retrofit Bottom Web Gap
3	7	152 mm (6 in.) Horizontal Crack, Unretrofitted
3	8	203 mm (8 in.) Horizontal Crack, Angles with Plate Retrofit Bottom Web Gap

A.1.9 Configuration of Retrofit Measures

As indicated, two different mitigation measures were evaluated experimentally. The first was the angles-with-plate retrofit, and the second consisted of drilling undersized crack-arrest holes at the tips of the fatigue cracks, a retrofit measure that is widely employed in steel bridges.

A.1.9.1   Angles with Plate Retrofit Measure

Retrofit element dimensions evaluated experimentally were chosen based on results of the computer simulations described in Appendix A.2 of this report and on availability of structural steel shapes. Angle and plate sizes were L152x152x19 (L6x6x$^3/_4$) and 457x457x19 (18x8x$^3/_4$), respectively (Figure A.7). Angles were connected to the web and transverse connection plate with two fully-tensioned bolts on each leg (Figures A.7 and A.8). A 10 mm ($^3/_8$ in.) thick shim plate was placed between the CP and the angle to eliminate the need for any chamfering or grinding of the edge of the angles. The angles and back plate were removed every 250,000 cycles to allow for inspection of the web gap region and measurement of crack growth.
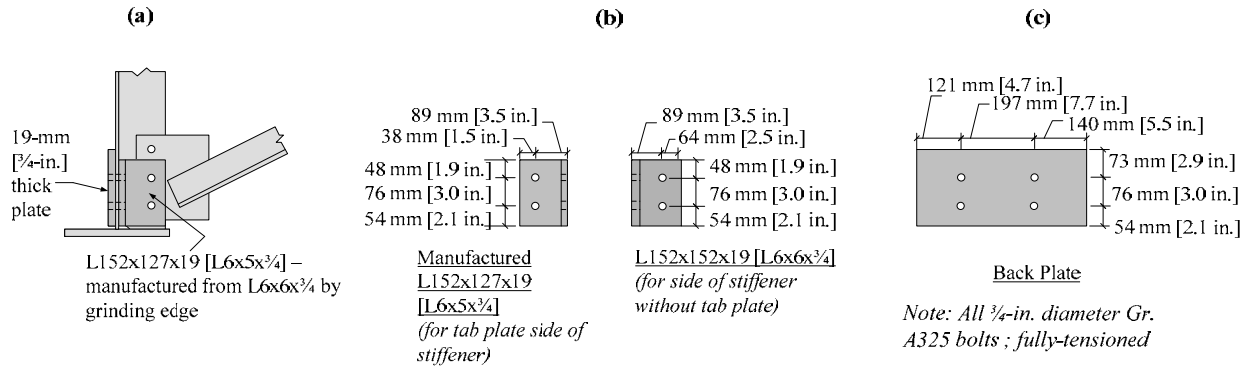
Figure A.7: Dimensions of angles and plate evaluated experimentally
(a) Side view, (b) Angle dimensions, (c) Plate dimension

Figure A.8: Angles-with-plate retrofit
(a) Back plate on fascia side of girder, (b) Angles connecting the CP and web

A.1.9.2　　　Crack Arrest Holes

Equations proposed by Rolfe and Barsom (1977) and by Fisher et al. (1980 and 1990) state that the minimum radius of a crack-arrest hole needed to prevent crack reinitiation is given by

$$\rho = \left(\frac{\Delta K_{total}}{C\sqrt{\sigma_y}} \right)^2 = \left(\frac{\Delta\sigma\sqrt{\pi a}}{C\sqrt{\sigma_y}} \right)^2 \qquad\qquad \textbf{Equation A.1}$$

where ρ is the hole radius, $\Delta\sigma$ is the stress range, a is the half-length of the crack, σ_y is the yield stress of the steel, and C is a constant. The constant C was defined as 26.3 for stress in units of MPa and crack length in mm (10 for ksi and in.) by Rolfe and Barson (1977), and 10.5 for stress in units of MPa and crack length in mm (4 for ksi and in.) by Fisher et al. (1990). While Rolfe and Barson (1977) calibrated the equation using tension specimens, Fisher et al. (1990) performed their calibration using steel girders. The equation developed by Fisher et al. (1990) has an upper limit of 103 MPa (15 ksi) for the stress range induced by out-of-plane bending, well below the 200 MPa (29 ksi) nominal stress applied to the girders that are reported on in this paper. The minimum diameter calculated using Equation A.1 for a stress range of 200 MPa (29 ksi) and a crack length of 51 mm (2 in.) is 25 mm (1 in.) according to the Rolfe and Barsom (1977) criterion, and 153 mm (6 in.) according to the criterion proposed by Fisher et al. (1990).

Equation A.1 is difficult to implement for several reasons. The stress field in the area surrounding the connection is very complex, which makes it difficult to define a stress range caused by out-of-plane forces. Furthermore, lack of understanding of how the constant C was calibrated can lead to improper use of the equation resulting in crack-arrest holes that excessively weaken the web gap region without being effective in preventing crack reinitiation. While it is recognized in this particular case that stress demands are outside the limit that Equation A.1 was developed for, if the constant proposed by Fisher et al. (1990) were adopted, drilling holes at both ends of the crack would require removing 305 mm (12 in.) of steel (corresponding to two crack-arrest holes each with a diameter of approximately 152 mm, or 6 in., at each of the two tips of the crack), which is significantly larger than the 51 mm (2 in.) length of the crack. As

illustrated by these calculations, crack-arrest hole diameters calculated with Equation A.1 are often very large and would result in excessive weakening of the web gap region, or may be impossible to drill because there is insufficient space. Because the goal of this study was to evaluate the performance of the mitigation method in the manner in which it is often implemented, a review of bridge inspection records was undertaken followed by a discussion with maintenance engineers from KDOT. Based on the information gathered through this process, a commonly-used crack-arrest hole diameter of 21 mm ($^{13}/_{16}$ in.) was selected.

Crack-arrest holes were drilled so that the edge of the hole would coincide with the corresponding fatigue-crack tip, following the recommendation by Fisher et al. (1990). When two cracks were found closely located to each other, a single crack-arrest hole was drilled to encompass both crack tips. Crack-arrest holes were not drilled at cracks that had stabilized in the unretrofitted configuration. Crack-arrest hole placement in the bottom and top web gaps of Specimen 2 is shown in Figure A.9(a) and (c), respectively. The vast majority of crack-arrest holes that were drilled had a diameter of 21 mm ($^{13}/_{16}$ in.) and were drilled using a hole saw with guide. Smaller crack-arrest holes, with a diameter of 6 mm ($^{1}/_{4}$ in.), were drilled at the top web gap region, at the tips of the horseshoe-shaped crack. The smaller crack arrest holes were used in later trials, to determine if the removal of the crack tips in this manner would be sufficient to prevent crack reinitiation when used in combination with the angles-and-plate repair. This variation of the repair technique was considered to be important because the close proximity between the transverse connection plate and the flange at the web gap region makes it very difficult to drill large-diameter holes at the toe of the welds, and because small crack-arrest holes are much less detrimental to the structural integrity of the girder.
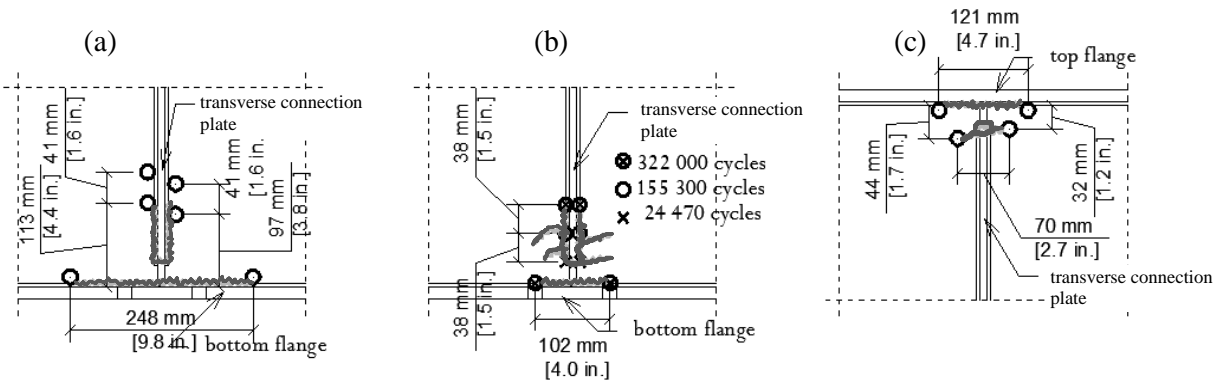
Figure A.9: Crack-arrest holes
(a) Crack-arrest holes in the bottom web gap region of Specimen 2, (b) Crack progression at the bottom web gap region of Specimen 2, unretrofitted (Circles represent crack tip at given number of cycles and not crack-arrest hole), (c) Crack-arrest holes at the top web gap region

A.1.10 Experimental Results

As described in the experimental program section, a total of 14 test trials were performed on three girder subassemblies. Crack progression for the various trials is summarized Tables A.3 and A.4, and illustrated in Figures A.9 to A.12. Figure A.9 (a) and (b) show the location of the cracks, while Figures A.9(b) to A.12 show crack growth as a function of the number of cycles.

Table A.3: Crack Progression

Specimen/ Trial	Retrofit Measure/Observation	Number of Cycles - Trial	Number of Cycles - Specimen	Crack Location and growth, mm (in.)			
				Bottom Horiz.	*Bottom Horseshoe*	*Top Horiz.*	*Top Horseshoe*
1/1	*No Retrofit / Crack initiation*	250,000	250,000	0 (0)	6 (0.3)	0 (0)	0 (0)
1/1	*No Retrofit / Crack growth*	740,000	990,000	6 (0.3)	25 (1)	0 (0)	0 (0)
2/1	*No Retrofit / Crack initiation*	24,460	24,460	0 (0)	6 (0.3)	0 (0)	0 (0)
2/1	*No Retrofit / Crack growth*	490,460	514,920	203 (8)	127 (5)	0 (0)	0 (0)
2/2	*Angles Bottom*	1,225,860	1,740,780	0 (0)	0 (0)	57 (2.3)	25 (1)
2/3	*Angles Bottom & Top*	1,250,740	2,991,520	0 (0)	0 (0)	25 (1)	0 (0)
2/4	*Crack Stop Holes*	39,720	3,031,240	13 (0.5)	70 (2.8)	0 (0)	0 (0)
2/5	*Angles Bottom & Top*	1,238,300	4,269,540	0 (0)	0 (0)	0 (0)	0 (0)
3/1	*No Retrofit / Crack initiation*	73,000	73,000	0 (0)	10 (0.38)	0 (0)	0 (0)
3/1	*No Retrofit / Crack growth*	276,000	349,000	51 (2)	41 (1.6)	0 (0)	0 (0)
3/2	*Angles Bottom*	1,200,000	1,549,000	0 (0)	0 (0)	0 (0)	0 (0)
3/3	*No Retrofit / Crack growth*	71,700	1,620,700	51 (2)	0 (0)	0 (0)	0 (0)
3/4	*Angles Bottom*	1,200,000	2,820,700	0 (0)	0 (0)	0 (0)	0 (0)
3/5	*No Retrofit / Crack growth*	322,000	3,142,700	51 (2)	19 (0.75)	0 (0)	10 (0.38)
3/6	*Angles Bottom*	1,200,000	4,342,700	0 (0)	0 (0)	0 (0)	0 (0)
3/7	*No Retrofit / Crack growth*	275,000	4,617,700	54 (2.1)	13 (0.5)	0 (0)	0 (0)
3/8	*Angles Bottom*	1,200,000	5,817,700	0 (0)	0 (0)	0 (0)	0 (0)

Table A.4: Crack Length Measurements

Specimen/Trial	Retrofit Measure/Observation	Number of Cycles - Specimen	Crack Location and Length, mm (in.)			
			Bottom Horiz.	*Bottom Horseshoe*	*Top Horiz.*	*Top Horseshoe*
1/1	*No Retrofit / Crack initiation*	250,000	0 (0)	6 (0.3)	0 (0)	0 (0)
1/1	*No Retrofit / Crack growth*	990,000	6 (0.3)	31 (1.3)	0 (0)	0 (0)
2/1	*No Retrofit / Crack initiation*	24,460	0 (0)	6 (0.3)	0 (0)	0 (0)
2/1	*No Retrofit / Crack growth*	514,920	203 (8)	135 (5.3)	0 (0)	0 (0)
2/2	*Angles Bottom*	1,740,780	203 (8)	135 (5.3)	57 (2.3)	25 (1)
2/3	*Angles Bottom & Top*	2,991,520	203 (8)	135 (5.3)	84 (3.3)	25 (1)
2/4	*Crack Stop Holes*	3,031,240	216 (8.5)	206 (8.1)	84 (3.3)	25 (1)
2/5	*Angles Bottom & Top*	4,269,540	216 (8.5)	206 (8.1)	84 (3.3)	25 (1)
3/1	*No Retrofit / Crack initiation*	73,000	0 (0)	10 (0.38)	0 (0)	0 (0)
3/1	*No Retrofit / Crack growth*	349,000	51 (2)	51 (2)	0 (0)	0 (0)
3/2	*Angles Bottom*	1,549,000	51 (2)	51 (2)	0 (0)	0 (0)
3/3	*No Retrofit / Crack growth*	1,620,700	102 (4)	51 (2)	0 (0)	0 (0)
3/4	*Angles Bottom*	2,820,700	102 (4)	51 (2)	0 (0)	0 (0)
3/5	*No Retrofit / Crack growth*	3,142,700	152 (6)	70 (2.75)	0 (0)	10 (0.38)
3/6	*Angles Bottom*	4,342,700	152 (6)	70 (2.75)	0 (0)	10 (0.38)
3/7	*No Retrofit / Crack growth*	4,617,700	206 (8.1)	83 (3.25)	0 (0)	10 (0.38)
3/8	*Angles Bottom*	5,817,700	206 (8.1)	83 (3.25)	0 (0)	10 (0.38)
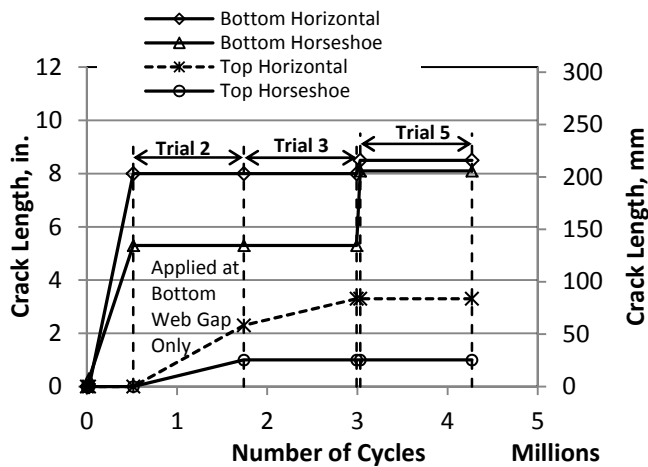
Figure A.10: Crack growth for Specimen 2
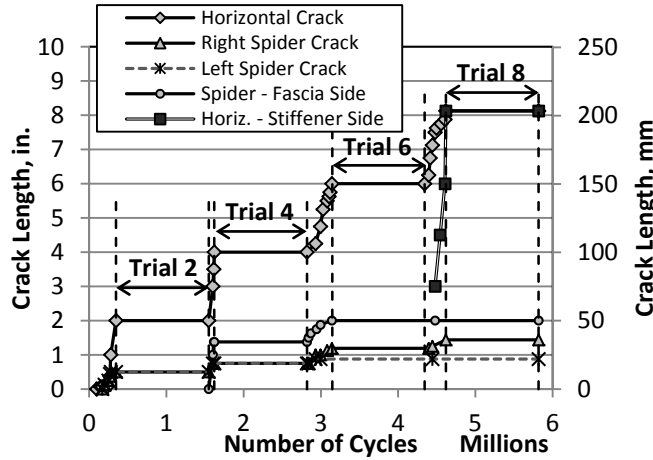
Figure A.11: Web-to-flange weld (horizontal) crack growth for Specimen 3
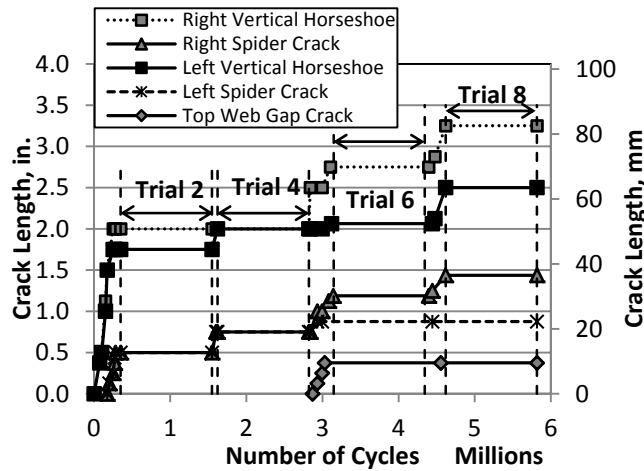
Figure A.12: CP-to-web weld (horseshoe-shaped) crack growth for Specimen 3

Prior to testing Specimen 1, a 38 mm ($1^1/_2$ in.) horizontal crack was fabricated in the bottom web gap region, between the edge of the transverse connection plate and the flange-to-web weld. The crack was fabricated using a rotary tool with a circular saw. The main purpose of the trial conducted with this specimen was to explore the evolution of the crack propagation pattern and to provide data for calibrating the FE models. Test Trial 1 was concluded after 740,000 cycles, and no retrofit measures were evaluated in this specimen. The crack pattern was found to be similar to that found in the bottom web gap region of Specimen 2 [Figure A.9(a)]. A fatigue crack developed at the toe of the CP-to-web fillet weld, similar to the crack that developed at the CP-to-web fillet weld of Specimen 2 [Figure A.9(a)]. Consistent with the results

24

from the FE simulation, the ends of the fabricated horizontal crack grew towards the bottom flange.

Five different test trials were conducted using Specimen 2. Results from the various trials at the measured stress range are plotted with the AASHTO S-N Design Curve (2013) in Figure A.6. The triangle in Figure A.6 represents the number of cycles applied to Specimen 2 during trial 2, with the angles-with-plate retrofit measure on, and without any measurable crack growth. The arrow on top of the triangle in Figure A.6 shows that the trial was stopped after 1.25 million cycles, which exceeded the infinite fatigue life threshold for an AASHTO Fatigue Category A detail. Figure A.10 shows that crack growth in the bottom web gap of Specimen 2 during trials 2, 3 and 5, all lasting approximately 1.2 million cycles and performed with the angles-with-plate retrofit on, was negligible.

Also illustrated in Figure A.6 are the number of cycles corresponding to fatigue-crack initiation (22,700) during Trial 1, and to fatigue-crack re-initiation during Trial 4 (16,000), after the crack-arrest holes were drilled. These results show that the fatigue re-initiation life of the specimen with undersized crack-arrest holes was comparable to the fatigue-crack initiation life. At the end of Test Trial 4, which lasted a total of 39,720 cycles, the horseshoe-shaped crack around the CP-to-web weld in the bottom web gap had grown an additional 70 mm ($2^3/_4$ in.) and the flange-to-web weld crack extended an additional 13 mm ($^1/_2$ in.). The relatively poor performance of the crack-arrest holes can be attributed in part to the large stress range imposed on the web gap region. A large stress range was used in the study to limit the duration of the experiments and to allow a direct comparison with the infinite life limit for AASHTO Category A fatigue details.

A total of eight trials were conducted on Specimen 3 following the same loading protocol used for Specimen 2. Crack length as a function of the number of cycles is presented in Figures A.11 and A.12. The main goal of Specimen 3 trials was to study the effectiveness of the angles-with-plate retrofit measure for different fatigue crack lengths. The first crack, with a length of 10 mm ($^3/_8$ in.), was observed in the toe of the bottom CP-to-web weld at 73,000 cycles. At 150,000 cycles, a 2 mm ($^1/_{16}$ in.) crack was observed at the toe of the bottom flange-to-web weld. The cracks were allowed to grow in the unretrofitted configuration until the horizontal flange-to-web

25

crack reached a length of 51 mm (2 in.) at 349,000 cycles. At this cycle count, spider cracks had branched off from the CP-to-web weld crack in the horizontal direction on either side of the connection plate, and had a length of 13 mm ($^1/_2$ in.).

Test Trials 2, 4, 6, and 8 for Specimen 3 were conducted with the angles-with-plate retrofit measure on, while the remaining trials were conducted in the unretrofitted configuration allowing the fatigue cracks to grow. Crack growth and lengths for each trial are summarized in Tables A.3 and A.4, respectively. For each trial in which the angles-with-plate retrofit was applied to the bottom web gap (2, 4, 6, and 8), the specimen was loaded for approximately 1.2 million cycles, which was equivalent to the infinite fatigue life limit for AASHTO Category A fatigue details for the measured stress range. Figures A.10 and A.11 illustrate that when the retrofit measure was on the specimen, no measureable crack growth was observed at either of the critical locations (the horseshoe-shaped crack around the CP-to-web weld and the horizontal crack at the bottom flange-to-web weld). This trend was confirmed by crack length measurements summarized in Table A.4. After a total of 2,931,200 cycles (during trial 5 of specimen 3) a small crack (3 mm [$^1/_8$ in.]) was found in the top web gap, in the toe of the CP-to-web weld. No retrofit measure was applied to the top web gap of the girder, and by the end of Trial 5 this crack had grown to 10 mm ($^3/_8$ in.). The crack length at the top web gap stabilized and no further growth was observed in Trials 6, 7 and 8 (FigureA.12 and Tables A.3 and A.4).

The trials conducted with Specimen 3 showed that, for the applied stress range and all crack geometries evaluated, the angles-with-plate retrofit measure prevented crack growth in the web gap region that was repaired. This is an important consideration because it simplifies the implementation of this retrofit measure by allowing the use of a single-size configuration for various web gap regions of the same bridge, regardless of crack length.

A.1.11 Conclusions

The research study conducted showed that the angles-with-plate repair was effective in preventing fatigue crack propagation in steel girders damaged by distortion-induced fatigue. Girders in which the angle-with-plates retrofit measure was implemented experienced negligible crack growth under the same load range that caused severe fatigue damage to the web gap region of unretrofitted specimens.

Experimental results from girder subassemblies under fatigue loading were consistent with computer simulations described in Part 8 of this report. Areas in the web gap region of computer models exhibiting the highest maximum principal stress demands correlated closely with the locations in which fatigue cracks were observed in the experiments. The manner in which fatigue cracks propagated during experimental simulations of girder subassemblies was also consistent with the results from the computer simulations. Both computer simulations and girder tests showed that there were two primary crack types that formed in the web gap region: a horseshoe-shaped crack along the toe of the weld between the CP and the girder web, and a horizontal crack along the toe of the weld between the web and girder flange.

Experiments showed that the angles-with-plate retrofit measure was effective in preventing the distortion of the web gap region, drastically reducing the stress demands at critical points. Subassemblies repaired using the angles-with-plate retrofit measure were able to exceed the number of cycles corresponding to infinite fatigue life for AASHTO Category A fatigue details without any measurable crack growth. This result was repeated for girders with various crack lengths, which indicates that, for the range evaluated, the performance of the repair method investigated was not sensitive to the length of the fatigue cracks. Experimental results were consistent with FE simulations described in a companion study, in which calculated stress demands at the critical points of the web gap region were reduced significantly (Appendix A.2).

Although undersized crack-arrest holes were effective for removing the sharp crack tips, experimental results showed that this type of stop-gap measure did not lead to a meaningful increase in fatigue life. This finding is consistent with FE simulations results described in the companion paper, which showed that crack-arrest holes of this size had a small effect on the calculated stress demand in the web gap region. The observed number of cycles to fatigue-crack re-initiation was comparable to the number of cycles to fatigue crack initiation in the unretrofitted configuration, and an order of magnitude lower than the number of cycles without any measurable crack growth undergone by specimens retrofitted with the angles-with-plate repair.

The results from this paper and the companion computational study show that the angles-with-plate repair was very effective in reducing the stress demand at the critical locations of the

27

web gap region, effectively arresting the growth of fatigue cracks in sub-assemblies subjected to very severe cyclic loading. Computer simulations indicate that this type of repair is equally effective in bridge systems as it was in the sub-assemblies evaluated in this study. A separate project is currently underway to corroborate this finding by evaluating the performance of the angles-with-plate retrofit in an existing bridge with distortion-induced fatigue cracks. Additional physical tests of the angles-with-plate retrofit (performed in the test bridge) are described in Appendix A.3 and A.4.

A.1.12 References

AASHTO (2013). *2013 Interim Revisions to the AASHTO LRFD Bridge Design Specifications.* 6th ed. American Association of State Highway and Transportation Officials, Washington, D.C.

ASTM E8/E8M (2009). Standard Test Methods for Tension Testing of Metallic Materials. ASTM International, West Conshohocken, PA.

Cousins, T. E. and Stallings, J. M. (1998). "Laboratory Tests of Bolted Diaphragm-Girder Connections." *Journal of Bridge Engineering*, 3(2), 56-63.

Fisher, J. W., Barthelemy, B. M., Mertz, D. R., and Edinger, J. A. (1980). *Fatigue Behavior of Full-Scale Welded Bridge Attachments*. NCHRP Report 227. Transportation Research Board, National Research Council, Washington, D.C.

Fisher, J. W., Jian, J., Wagner, D. C., and Yen, B. T. (1990). *Distortion-Induced Fatigue Cracking in Steel Bridges*. NCHRP Report 336. Transportation Research Board, National Research Council, Washington, D.C.

Keating, P. B. (1994). "Focusing on Fatigue." *Civil Engineering*, 64(11), 54-57.

Keating, P. B. and Fisher, J. (1987). "Fatigue Behavior of Variable Loaded Bridge Details Near the Fatigue Limit." *Transportation Research Record* 1118, 56-64. Transportation Research Board, National Research Council, Washington, D.C.

Lindberg, A. and Schultz, A. (2007). *Incorporation of Fatigue Detail Classification of Steel Bridges into the Minnesota Department of Transportation Database: Final Report*. Report MN/RC-2007-22. Minnesota Department of Transportation, St. Paul, MN.

Richardson, T. (2012). *Analytical Investigation of Repair Methods for Fatigue Cracks in Steel Bridges*. (Master's thesis). University of Kansas, Lawrence, KS.

Rolfe, S. T. and Barsom, John M. (1977). *Fracture and Fatigue Control in Structures: Applications of Fracture Mechanics*. 1st ed. Prentice-Hall, Englewood Cliffs, NJ.

Appendix A.2: Repairing Distortion-Induced Fatigue Cracks in Steel Bridge Girders using Angles-with-Plate Retrofit Technique, Part II: Computer Simulations

Fatih Alemdar[6]

Temple Overman[7]

Adolfo B. Matamoros[8]

Caroline R. Bennett[9]

Stanley T. Rolfe[10]

A.2.1 Abstract

This paper presents the results from computer simulations of 914 mm (36 in.) deep girder-cross frame subassemblies to study the effects of distortion-induced fatigue and to evaluate the effectiveness of a newly proposed cost-effective retrofit measure. The proposed retrofit measure consists of adding steel angles connecting the girder web and the transverse connection plate (CP), and a steel plate on the back side of the girder web. The retrofit measure is intended to reduce stress demand at the welds, to restrain the web gap region from deforming in the out-of-plane direction, and to distribute lateral forces transferred by cross-frames over a wider region of the web. Parametric studies were carried out to determine the optimal configuration to prevent growth of fatigue cracks of various lengths in the web gap region. It was found that the proposed retrofit measure reduced peak stress demands with respect to the unretrofitted configuration by 50% or more, making it likely that it will prevent fatigue crack re-initiation. The parametric studies showed that the proposed retrofit measure became more effective in reducing the peak stress demand as the stiffness of the elements increased, with the lowest average stress demand occurring when the angles and backing plate were assigned

---

[6] Fatih Alemdar, PhD, Assistant Professor, Yildiz Technical University, Istabul, Turkey

[7] Temple Overman, MS, Bridge Engineer, HNTB Corporation, 715 Kirk Drive, Kansas City, MO, 64105

[8] Adolfo B. Matamoros, PhD, Professor, University of Kansas, 1530 W. 15th St., Lawrence KS, 66045

[9] Caroline R. Bennett, PhD, P.E., Associate Professor, University of Kansas, 1530 W. 15th St., Lawrence KS, 66045

[10] Stanley T. Rolfe, P.E., PhD, A.P. Learned Distinguished Professor, University of Kansas, 1530 W. 15th St., Lawrence KS, 66045

thicknesses equal to 2.67 times the thickness of the web. Experimental verification of this study is presented in Appendix A.1.

A.2.2 Introduction and Background

A web gap region is created when a transverse connection plate is clipped at the top or bottom, leaving a gap between the edge of the connection plate and the unconnected adjacent girder flange (see Figure A.13). The web gap detail, widely used in the United States before the mid-1980s, was implemented in this manner to avoid welding the transverse connection plate to the flange (Castiglioni et al. 1988). This was due to concerns about creating potential for brittle fracture in the flange, a problem that was observed in European bridges early in the last century (Roddis and Zhao 2001).

Figure A.13: (a) Close up of web gap region of bridge in a region of positive moment and (b) Cross-frame-to-web connection

Unforeseen to bridge engineers at the time, cross-frame forces generated by passing traffic induce significant out-of-plane distortion of the web gap. The combination of localized deformations and geometric discontinuities at the web gap result in large stress demands at the transverse connection plate-to-web and web-to-flange welds, which can considerably decrease the fatigue life of bridges (Hassel et al., 2012; Jajich and Schultz 2003; Fisher et al., 1990). Retrofit measures for distortion-induced fatigue damage documented in the literature were developed following two main approaches (Roddis and Zhao 2001; Keating and Fisher 1987; Fisher et al. 1990; Cousins and Stallings 1998): some methods seek to reduce the stress demand

by increasing the flexibility of the transverse connection plate-to-web connection, while others do it by introducing an alternate load path between the transverse connection plate and the girder flange. The flexibility of the web gap region has been increased through several alternatives, including the introduction of a slot at the edge of the transverse connection plate and cropping the connection plate. Adding connecting elements, which increases the stiffness of the connection, is commonly implemented by welding or bolting one leg of a single angle or two legs of a pair of angles to the flange, and the opposite leg(s) to the transverse connection plate. The main drawback of this type of repair is that in many instances having access the top flange requires removal of the concrete deck at the top of cross frame-to-web connections [Figure A.13(b)] (Keating and Fisher 1987; Fisher et al. 1990; Cousins and Stallings 1998). Another problem associated with this type of repair is interference between the retrofit angles and projecting elements of cross-frame members. Such an interference [Figure A.13(b)] requires the removal of welds between the transverse connection plate and the cross-frame members [Figure A.13(a)], which increases the cost of the repair. Also, in some instances the gap between the horizontal member of the cross-frame and the girder flange is large enough that it makes the use of angles impractical for retrofit.

The solution explored in this paper is not affected by those limitations because it relies on strengthening the connection between the transverse connection plate (CP) and girder web, within the web gap region. Because the components are attached with as few as six bolts, the drilling costs are relatively low and there is no need for field welding. These characteristics make this type of repair very economical.

Two baseline cases were considered as a starting point from which to compare the performance of the retrofit that is discussed in the majority of this paper. These two cases were a cracked, unmodified web gap region, and a case in which undersized crack-arrest holes were drilled at the tips of cracks in the web gap region. The term "undersized" is used in this paper in reference to equations for minimum crack-arrest hole diameter proposed by Rolfe and Barsom (1977) and Fisher et al. (1990), which require much larger diameters than those investigated in this study. These equations are discussed in greater detail in Appendix A.1, which describes the experimental study. These two cases have been illustrated before the performance of the retrofit

31

is discussed to provide context to the reader in terms of practical scenarios that may exist before a structural retrofit is applied for distortion-induced fatigue.

A.2.3 Objective and Scope

The main objective of this study was to investigate the performance of a new cost-effective repair method for distortion-induced fatigue cracks in the web gap region of bridge girders. The repair method investigated consists of attaching steel angles to the transverse connection plate and the girder web, and bolting the angles to a steel plate on the opposing side of the girder web. This repair method is referred to throughout the paper as the angles-with-plate repair. It was also desired to consider the fatigue crack re-initiation life of undersized crack-arrest holes in the web gap region when used as a stop-gap measure, without any other form of retrofit. The purpose of this was limited to exploring a baseline scenario that is commonly-implemented by bridge owners. Parametric studies using high-resolution Finite Element (FE) models were used to evaluate the effects of the two retrofit measures on the stress field in the web gap region, and to determine the configuration of the angles-with-plate repair that would result in the lowest the stress demand at the critical points.

Experimental verification of the findings of this study is described in Appendix A.1.

A.2.4 Computer Model Configuration

The computer models were created to resemble as closely as possible the girder-and-cross frame subassemblies tested in the companion experimental study. Given the interactions that exist between primary and secondary actions in a bridge, it is recognized that a complete bridge system provides a far superior platform to evaluate the efficacy of retrofit measures than girder subassemblies. The main advantage of using subassemblies is that experimental studies can be performed at a fraction of the cost of testing a complete bridge system. There is a similar advantage for computer models because smaller subassemblies allow discretizing areas of interest with a larger number of elements. A large-scale computational study on distortion-induced fatigue in steel bridges, comprising more than 1,000 high-resolution simulations of bridge systems with similar girder cross-section dimensions as those evaluated in this study, was carried out by Hassel et al. (2012). The FE simulation results (Figure A.14) from Hassel et al. (2012) (also described in Appendix D) a showed that the stress field in the web gap region of the

subassemblies (Figure A.15) was similar to that found in the web gap region of the two-span continuous model bridge employed by Hassel et al. (Figure A.14b). In both instances, the main areas of vulnerability were at the weld between the transverse connection plate and the girder web, and at the weld between the web and the flange (designated as HSS1 and HSS2, respectively, in Figure16).
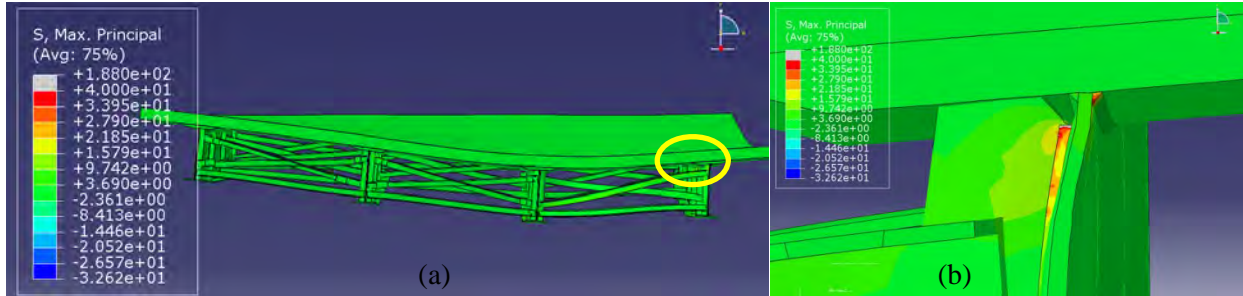
Source: Hassel 2012
Figure A.14: FE Simulation Results
(a) Deflected shape of bridge section in a region of positive moment and (b) Close-up view showing stress demand at the web gap region of the deflected girder
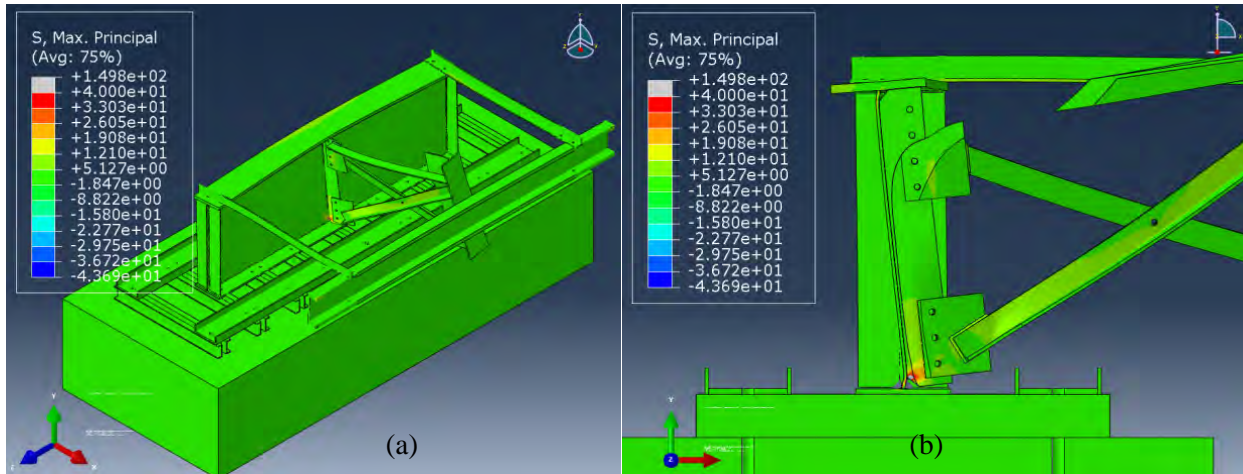
Figure A.15: Deformed configuration of girder specimen
(a) Aerial view (b) Center cut

Figure A.16: Pre-defined paths for sampling of stress demands in the various FE models

Dimensions of the specimens and the measured material properties are presented in Appendix A.1. Linear-elastic FE models were created using eight-node brick elements (C3D8), each with 24 degrees of freedom. Mesh density was determined by performing analyses with various element sizes in the web gap region. The element size adopted in the simulations corresponded to the largest at which the rate of change of the computed HSS with respect to element size became negligible. The number of elements ranged between one and two million, depending on the retrofit measure that was modeled and the configuration of the fatigue cracks. Simulations were performed using the computer program Abaqus (SIMULIA 2008). An 813 mm (32 in.) wide strip with a reduced mesh size was defined in the girder web, centered on the transverse connection plate, spanning from the bottom to the top flange (Figure A.16). The size of the elements in this strip was set to 3 mm (0.1 in) to improve the accuracy of the calculated stress field. A 76 mm (3 in.) wide vertical strip of tetrahedral elements was used to transition from the fine mesh to a 10 mm (0.4 in.) coarser mesh used to model the web of the girder in locations away from the cross frame.

The transverse connection plate was partitioned to allow for varying element types and mesh sizes around the bolt holes and the 32 mm ($1^1/_4$ in.) clipped ends (Figure A.16). A swept hexagonal mesh with 5 mm (0.2 in.) elements was used around the bolt holes, and tetrahedral elements were used in the clipped ends (Figure A.16). Everywhere else in the transverse connection plate, 5 mm (0.2 in.) hexagonal elements were used. A similar meshing technique was used to model the end stiffeners. The hexagonal element size used away from the clipped edges was 8 mm (0.3 in.).

All four web-to-flange fillet welds, which had a size of 5 mm ($^3/_{16}$ in.), were modeled with a triangular cross section using structured hexagonal elements. The five transverse connection plate-to-web fillet welds were also modeled with a triangular cross section, but in this case, using tetrahedral elements (Figure A.16). The fillet welds were placed all around the transverse connection plate, including the top and the bottom, to accurately capture the physical weld geometry of the specimens, and modeled with perfect square corners at the intersections. All welds had a maximum element size of 3 mm (0.1 in.). The modulus of elasticity of the Gr. A36 steel members was defined as 200 GPa (29,000 ksi) and Poisson's ratio was defined as 0.3.

In the physical model, the steel girder was connected to the reaction floor of the laboratory through a series of channels so that the flange would be restrained from out-of-plane motion in the same manner that the axial stiffness of the concrete deck restrains the out-of-plane motion of a bridge girder. The concrete floor (Figure A.15) was simulated in the computer model as a block of elastic material with a modulus of elasticity of 27,780 MPa (4,000 ksi) and Poisson's ratio of 0.2. The concrete mesh consisted of 102 mm (4 in.) brick elements with 16 nodes. Interaction between the concrete floor and the steel elements was simulated using tie constraints and also a contact interaction with a representative coefficient of friction between the two surfaces. The stress field in the web gap region was found to be insensitive to the type of interaction between the concrete floor and the steel elements, so the former approach was adopted in the parametric study because it was more computationally efficient.

Analyses of the subassembly were performed using models in which tensioned bolts were simulated explicitly and also with models in which the bolt force was neglected and the bolts were connected to the steel members with tie constraints. It was found that the computed stress

fields at the web gap region were very similar, with the latter type of model requiring a much lower computational cost. For the same reason, connections between the channels and the bottom flange of the girder were simulated using tie constraints.

The computer model was loaded with a single 22,240-N (5-kip) force, applied to a WT section used to connect the cross frame members to the actuator in the physical model (Figure A.15). This force corresponded to the maximum force applied to the physical models. The WT section was restrained from moving along the longitudinal axis of the girder. The bottom of the concrete block below the specimen was fully fixed, and so were both ends of a channel connecting the two end angles to the reaction frame in the physical model (Figure A.15).

Computed stresses from different models were compared using a Hot Spot Stress (HSS) technique. The adopted HSS technique was used to obtain a more reliable measure of stress demand in areas of the web gap region where there were large stress gradients, such as near welded or bearing connections and geometric discontinuities. The definition of HSS adopted in this study was found to be the least sensitive to mesh size in a convergence study of similar web gap regions conducted by Adams (2009). The study performed by Adams (2009) examined various stress analysis methods, including one-point and two-point extrapolation Hot Spot Stress techniques, and one-plane and two-plane Structural Stress (SS) analyses techniques. Adams found that the HSS techniques studied provided more acceptable results than the SS techniques, on the basis that the HSS results were less mesh-sensitive. The most reliable procedure was found to be a one-point HSS procedure in which stresses were read a distance 0.5t away from the weld toe. This procedure originated from work performed by Maddox (2002).

Figure A.17 presents a comparison of the computed maximum principal stress demand in the web gap region and the physically-observed crack patterns noted in the experimental study. It can readily be seen that the largest maximum principal stress demands in the model correlated very well with locations where cracks formed in the specimens. Therefore, maximum principal stresses were used as a measure of vulnerability to fatigue damage because direct comparisons between computer simulation and experimental results showed that this was appropriate. It is recognized that this is a departure from conventional HSS techniques, such as that suggested by the International Institute of Welding (IIW), wherein direction stresses are extracted. However, it

36

should be noted that directional stresses were also considered in this study, and these did not produce the level of agreement seen between experimental crack formation and computed maximum principal stresses.
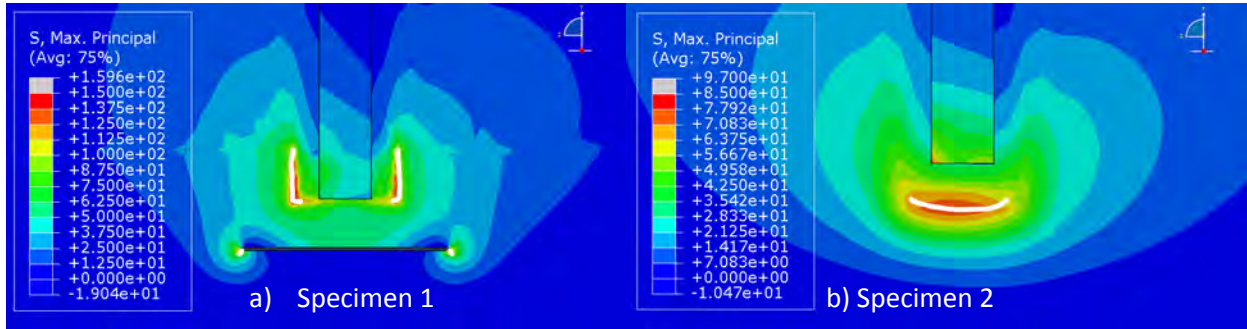
Figure A.17: Observed crack patterns superimposed on the maximum principal stress contours from the simulation models for web gap regions of specimens 1 and 2 (observed cracks shown as white lines) Circular shapes at the tips of the crack in (a) stem from the stress contours at those locations and are not to be confused with crack-arrest holes. Stress contour in (b) corresponds to the configuration without crack-arrest holes.

The HSS was extracted by defining paths at a distance of 5 mm (0.2 in.) away from the weld, a distance equivalent to half the thickness of the web (10 mm [3/8 in.])(Figure A.16). HSS sampling paths were defined only near locations where cracks were observed in the specimens. Path HSS 1 was defined as a horseshoe-shaped path in the bottom web gap of the subassembly (Figure A.16). Path HSS 2 was defined as a horizontal path near the crack that formed in the web-to-flange weld in the bottom web gap of the subassembly (Figure A.16). The J-Integral at the tip of simulated cracks was computed (SIMULIA 2008) as a measure of propensity for crack growth. A total of five contours were evaluated in the calculations, at points evenly spaced through the thickness of the web.

A.2.5 Evaluation of Retrofit Measures

As discussed, two baseline cases were considered, including an unmodified, cracked web gap region, and a case in which the cracked web gap region was modified to have undersized crack-arrest holes. Criteria for determining the minimum diameter of crack-arrest holes are discussed in Appendix A.1. Crack-arrest holes with a diameter of 21 mm ($^{13}/_{16}$ in.), the same

diameter used in the experimental study, were simulated at the tip of the cracks, at the locations shown in Figure A.18b. The location of the crack-arrest holes in the FE models corresponded to the top and bottom web gap locations drilled in Specimen 2 of the experimental study. It should be noted that holes drilled in the girder web away from the CP-to-web weld (Figure A.18b) were used to bolt the angles-with-plate retrofit measure to the girder web and were not intended to prevent crack re-initiation. Because these bolt holes were present in the specimen when it was tested, they were included in the model to account for their effect on the stress field.
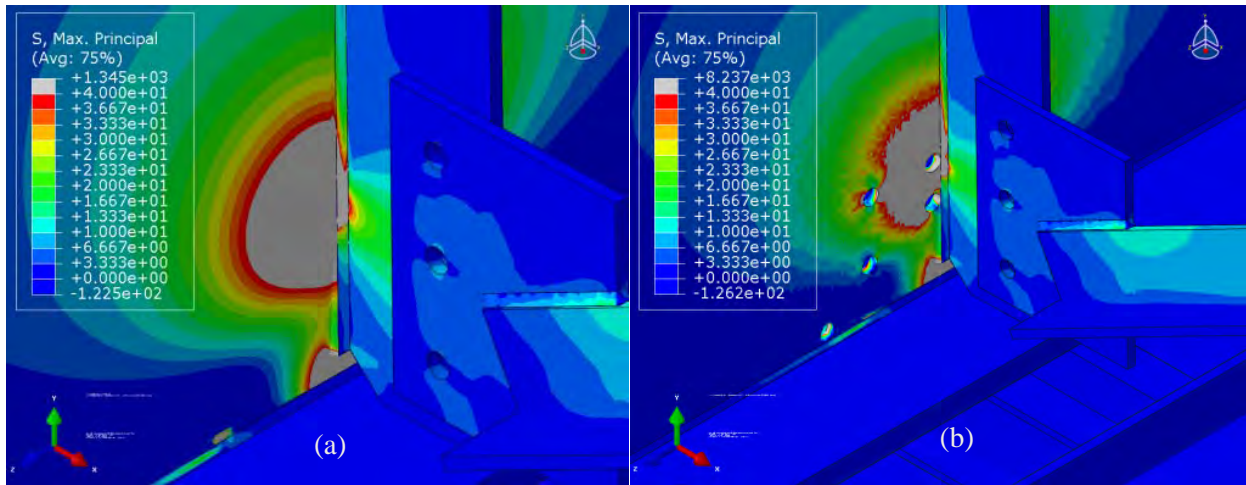
Figure A.18: Stress field in the web gap region of a test specimen with the two fatigue cracks experimentally observed in Specimen 2
(a) Without any retrofit measure; (b) Repaired with the crack-arrest hole configuration implemented in Specimen 2.

Simulations were performed to establish a comparison between an unretrofitted model with two cracks in the bottom web gap region and a model with the same crack pattern but with crack-arrest holes (Figure A.18b). The crack pattern in the model had a 102 mm (4 in.) tall horseshoe-shaped crack around the transverse connection plate-to-web weld (parallel to HSS path 1 in Figure A.16) and a 203 mm (8 in.) horizontal crack at the toe of the flange-to-web weld (parallel to HSS path 2 in Figure A.16) in the bottom web gap of the subassembly. In parametric studies investigating the effectiveness of the proposed retrofit, cracks were modeled explicitly with a thickness of 2.5 mm (0.1 in.). The extended finite element method (XFEM) was used to simulate cracks in models in which the J-Integral was calculated (Richardson, 2012). The

maximum stress demand along path HSS 1 decreased by 27% with the addition of the crack-arrest holes, while the maximum stress demand along path HSS 2 decreased by 16%. The stress fields presented in Figure A.18 show that the reduction in stress demand caused by the presence of the crack-arrest holes was not likely sufficient to prevent the re-initiation of existing fatigue cracks on their own merit.

A.2.6 Angles-with-Plate Repair

This repair technique was developed based on experimental observations from three-point bending specimens with welded connections, as described in Appendix B.2 and B.3. Although the shape of the beam subassemblies was very different from the shape of the three-point bending specimens, computer simulations showed that in both cases there were very high stress demands caused by the geometric discontinuity introduced by the weld. This observation was corroborated by experimental simulations in which horseshoe-shaped cracks originated near the connection transverse connection plate-to-web weld of the beam subassemblies. A simple solution to reduce the stress demand near the welds constitutes the focus of this study. In this case the reduction in stress demand was accomplished by providing an alternate load path using a combination of steel angles and a backing plate.

The main components of the angles-with-plate retrofit measure are shown in Figure A.19b. Diagrams with element dimensions are presented in the companion paper describing the experimental study. Parametric analyses of the angles-with-plate retrofit measure were performed to determine the optimal back plate and angle dimensions. The first parametric study involved varying the thickness of the angles and back plate, while the other dimensions were kept constant. The crack pattern in the model consisted of a 102 mm (4 in.) tall horseshoe-shaped crack and a 203 mm (8 in.) horizontal crack in the bottom web gap of the subassembly, the same pattern used to evaluate the performance of the crack-arrest holes. The back plate and angle thicknesses evaluated were 6 mm ($^1/_4$ in.) (flexible-*f*), 13 mm ($^1/_2$ in.) (medium-*m*), and 25 mm (1 in.) (stiff-*s*), which corresponded to thickness equal to 0.67, 1.33, and 2.67 times the thickness of the web, respectively. Computed HSS demands are summarized in Table, with the naming convention describing the angle (*A*) and back plate (*BP*) in terms of being flexible (*f*), medium (*m*), or stiff (*s*). The last two digits of each specimen name correspond to the length of the back

plate in inches. For example, *s*A-*s*BP18 refers to a retrofit configuration with a 25 mm (1 in.) (stiff-*s*) thick angle and a 25 mm (1 in.) (stiff-*s*) thick back plate with a length of 457 mm (18 in.). The HSS values in Table A.5 show a significant relationship between the thickness of the angles and the level of HSS, with stiffer angles corresponding to the greatest reduction in stress demand. The magnitude of the reduction in stress demand clearly shows that, for the range of thicknesses studied, this retrofit measure significantly reduced the computed stress demand at the critical locations of the bottom web gap region (Figure A.19a vs. Figure A.19c), regardless of connecting element thickness. Stress contours in Figure A19.a and Figure A.19c were chosen so that the colors would correspond to the same stress ranges in both figures. It is clear from the comparison that the reduction in stress demand was very significant and that it occurred throughout the entire web gap region, and not only at the critical points. The following discussion focuses on some trends that are helpful in choosing an optimum solution.

(a)   (b)   (c)
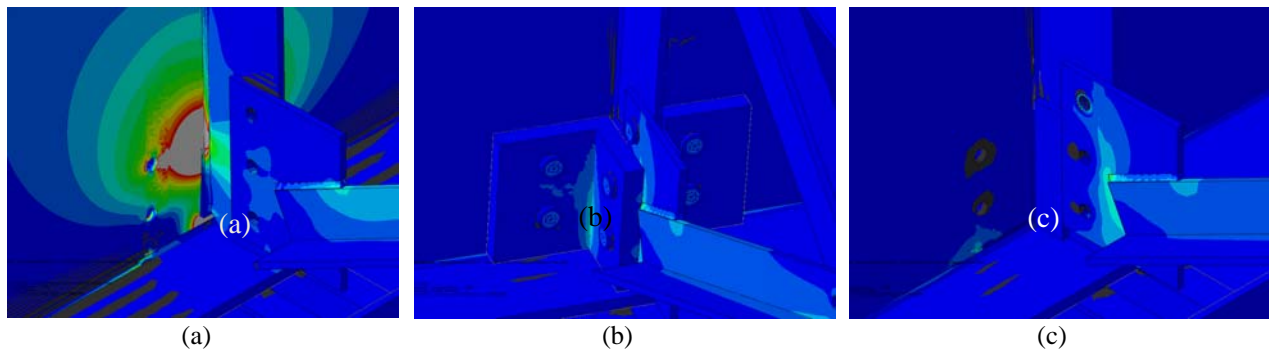
Figure A.19: (a) Computed maximum principal stresses without retrofit, (b) Angle retrofit configuration, (c) Computed stresses with retrofit
Scale is set so that red values are equivalent to 345 MPa (50 ksi) in all figures.

The stress demands in Table A.5 show that, for all back plate configurations, increasing the thickness of the angles led to a significant reduction in the peak stress demand at the path near the horseshoe-shaped crack (HSS1). Increasing the thickness of the back plate did not have a strong influence on the peak stress at the path near the horseshoe-shaped crack. The effect of connecting element stiffness on the peak stress demand at the path near the horizontal crack (HSS2) produced a similar effect, but to a lesser degree (HSS2 values were not as influenced by angle stiffness as HSS1 values were). Increasing back plate and angle stiffness led to decreases

in stress demand for HSS2. If the average of the peak demand at the two HSS paths is used as a measure of stress demand, the configurations with the lowest average stress demands were those with the thickest back plate, with the lowest among those being the configuration with the thickest angles (104 MPa [15.1 ksi]). Configurations with the highest average stress demand were those with the thinnest back plate, with the highest among those being the configuration with the thinnest plate and the thinnest angles (387.5 MPa [56.2 ksi]). These results strongly suggest that a combination of a stiff back plate with stiff angles is the most effective version of this retrofit for reducing stress demand in the web gap region. Use of a flexible combination, or a stiff back plate used with relatively flexible angles is not recommended.

Table A.5: Maximum HSS for Retrofitted Model with 2 Cracks in the Bottom Web Gap Region (Parametric Studies 1 and 2)

Designation	Plate Length, mm (in)	Plate Thickness, mm (in)	Angle Thickness, mm (in)	HSS Path #1 Bottom, MPa (ksi)	HSS Path #2 Bottom, MPa (ksi)
No retrofit	--	--	--	1956.7 (283.8)	739.9 (107.3)
*s*A-*s*BP18	457 (18)	25 (1)	25 (1)	28 (4.1)	180 (26.1)
*m*A-*s*BP18	457 (18)	25 (1)	13 ($^1/_2$)	109 (15.8)	183 (26.5)
*f*A-*s*BP18	457 (18)	25 (1)	6 ($^1/_4$)	465 (67.5)	179 (25.9)
*s*A-*m*BP18	457 (18)	13 ($^1/_2$)	25 (1)	28 (4.1)	201 (29.2)
*m*A-*m*BP18	457 (18)	13 ($^1/_2$)	13 ($^1/_2$)	93 (13.4)	255 (36.9)
*f*A-*m*BP18	457 (18)	13 ($^1/_2$)	6 ($^1/_4$)	450 (65.2)	264 (38.2)
*s*A-*f*BP18	457 (18)	6 ($^1/_4$)	25 (1)	43 (6.3)	225 (32.7)
*m*A-*f*BP18	457 (18)	6 ($^1/_4$)	13 ($^1/_2$)	118 (17.1)	288 (41.7)
*f*A-*f*BP18	457 (18)	6 ($^1/_4$)	6 ($^1/_4$)	433 (62.8)	342 (49.6)
*m*A-*m*BP12	305 (12)	13 ($^1/_2$)	13 ($^1/_2$)	93 (13.5)	253 (36.7)
*m*A-*m*BP18	457 (18)	13 ($^1/_2$)	13 ($^1/_2$)	93 (13.4)	255 (36.9)
*m*A-*m*BP24	610 (24)	13 ($^1/_2$)	13 ($^1/_2$)	90 (13.0)	250 (36.3)
*m*A-*m*BP36	914 (36)	13 ($^1/_2$)	13 ($^1/_2$)	89 (13.0)	252 (36.5)

In general, the parametric study showed that increasing the stiffness of the retrofit elements reduced the stress demand at the transverse connection plate-to-web fillet weld, and reduced the stress demand at the web-to-flange weld. It was found that stresses at the web-to-flange weld were less sensitive to the stiffness of the retrofit elements than the stresses at the connection-plate-to-web-weld. It is important to emphasize that while the effect of stiffness of the angles and the plate had a significant effect on the calculated stress demand, in all instances

41

the calculated stress demands at both the CP-to-web weld (HSS 1) and the flange-to-web weld (HSS 2) were much lower than the values computed for the unretrofitted configuration.

A second parametric study was performed in which the angle and back plate thickness were kept constant at 13 mm ($^1/_2$ in.), while the length of the back plate was changed. For this intermediate (medium-*m*) configuration the thickness of the angles and back plate was 1.33 times the thickness of the girder web. The crack pattern in the model had a 102 mm (4 in.) tall horseshoe-shaped crack and a 203 mm (8 in.) horizontal crack in the bottom web gap of the subassembly, similar to the crack pattern used in the first parametric study. The length of the back plate was set to 305, 457, 610, and 914 mm (12, 18, 24, and 36 in.), which corresponded to 1.5, 2.25, 3, and 4.5 times the length of the horizontal crack used in the evaluation. Shorter lengths were not evaluated because the plate would have been smaller than the footprint of the angles. The results are also summarized in Table A.5. Extremely low levels of variation were found to occur in HSS1 and HSS2 across this parametric study. These results suggest that it is counterproductive to increase the length of the back plate, and that a configuration with a back plate with a length of 1.5 times the length of the horizontal web-to-flange crack provided excellent results while remaining easily manageable during field installation.

A third parametric study was conducted to evaluate the effect of crack length on the likelihood of fatigue damage for the angles-with-plate retrofit measure. HSS values were extracted from analyses of models with varying lengths of the CP-to-web weld and web-to-flange weld cracks and summarized in Table A.6. Configurations evaluated had horseshoe-shaped and horizontal crack lengths of 13 and 13 mm (0.5 and 0.5 in.), 25 and 25 mm (1 and 1 in.), 50 and 50 mm (2 and 2 in.), and 102 and 203 mm (4 and 8 in.), respectively. The last crack configuration, with lengths of 102 and 203 mm (4 and 8 in.), corresponded to the observed crack configuration at the end of the first trial for Specimen 2 of the experimental study, and was the same crack configuration used in the first and second parametric studies. All models had the angles-with-plate retrofit measure implemented with angle and back plate thicknesses of 6 mm ($^1/_4$ in.), 13 mm ($^1/_2$ in.), and 25 mm (1 in.) evaluated for each crack configuration (0.67, 1.33, and 2.67 times the thickness of the girder web, respectively). In all the models of the third parametric study the length of the back plate was 457 mm (18 in.), which corresponds to 2.25

times the length of the horizontal crack. Companion models that included the angle-with-plates

retrofit but that did not include cracks were also analyzed to provide a basis for comparison.

Table A.6: Maximum HSS for Retrofitted Model in the Bottom Web Gap Region (Parametric Study 3)

Designation	Plate Thickness, mm (in.)	Angle Thickness, mm (in.)	HSS Path #1 MPa (ksi)	HSS Path #2 MPa (ksi)	
No retrofit	--	--	231.0 (33.5)	197.2 (28.6)	No Cracks
sA-sBP18	25.4 (1)	25.4 (1)	60.0 (8.7)	102.0 (14.8)	
mA-sBP18	25.4 (1)	12.7 ($^1/_2$)	65.0 (9.4)	103.9 (15.1)	
fA-sBP18	25.4 (1)	6.35 ($^1/_4$)	67.8 (9.8)	103.0 (14.9)	
sA-mBP18	12.7 ($^1/_2$)	25.4 (1)	73.1 (10.6)	106.2 (15.4)	
mA-mBP18	12.7 ($^1/_2$)	12.7 ($^1/_2$)	86.2 (12.5)	111.1 (16.1)	
fA-mBP18	12.7 ($^1/_2$)	6.35 ($^1/_4$)	95.5 (13.9)	110.5 (16.0)	
sA-fBP18	6.35 ($^1/_4$)	25.4 (1)	81.7 (11.8)	107.4 (15.6)	
mA-fBP18	6.35 ($^1/_4$)	12.7 ($^1/_2$)	99.7 (14.5)	114.4 (16.6)	
fA-fBP18	6.35 ($^1/_4$)	6.35 ($^1/_4$)	115.8 (16.8)	127.0 (18.4)	
No retrofit	--	--	1042.3 (151.2)	75.4 (10.9)	13 mm (0.5 in.) horseshoe crack / 13mm (0.5 in.) horizontal crack
sA-sBP18	25.4 (1)	25.4 (1)	193.0 (28.0)	47.9 (7.0)	
mA-sBP18	25.4 (1)	12.7 ($^1/_2$)	453.3 (65.7)	71.6 (10.4)	
fA-sBP18	25.4 (1)	6.35 ($^1/_4$)	740.1 (107.3)	68.1 (9.9)	
sA-mBP18	12.7 ($^1/_2$)	25.4 (1)	377.9 (54.8)	30.0 (4.3)	
mA-mBP18	12.7 ($^1/_2$)	12.7 ($^1/_2$)	604.3 (87.7)	66.1 (9.6)	
fA-mBP18	12.7 ($^1/_2$)	6.35 ($^1/_4$)	832.3 (120.7)	68.0 (9.9)	
sA-fBP18	6.35 ($^1/_4$)	25.4 (1)	481.4 (69.8)	26.1 (3.8)	
mA-fBP18	6.35 ($^1/_4$)	12.7 ($^1/_2$)	679.8 (98.6)	57.1 (8.3)	
fA-fBP18	6.35 ($^1/_4$)	6.35 ($^1/_4$)	882.8 (128.0)	63.7 (9.2)	
No retrofit	--	--	1226.3 (177.9)	292.4 (42.4)	25 mm (1 in.) horseshoe crack / 25 mm (1 in.) horizontal crack
sA-sBP18	25.4 (1)	25.4 (1)	136.8 (19.8)	46.8 (6.8)	
mA-sBP18	25.4 (1)	12.7 ($^1/_2$)	375.9 (54.5)	81.2 (11.8)	
fA-sBP18	25.4 (1)	6.35 ($^1/_4$)	942.4 (136.7)	152.2 (22.1)	
sA-mBP18	12.7 ($^1/_2$)	25.4 (1)	298.0 (43.2)	37.7 (5.5)	
mA-mBP18	12.7 ($^1/_2$)	12.7 ($^1/_2$)	537.6 (78.0)	104.0 (15.1)	
fA-mBP18	12.7 ($^1/_2$)	6.35 ($^1/_4$)	1117.2 (162.0)	193.2 (28.0)	
sA-fBP18	6.35 ($^1/_4$)	25.4 (1)	396.7 (57.5)	63.6 (9.2)	
mA-fBP18	6.35 ($^1/_4$)	12.7 ($^1/_2$)	624.2 (90.5)	126.4 (18.3)	
fA-fBP18	6.35 ($^1/_4$)	6.35 ($^1/_4$)	922.2 (133.7)	213.2 (30.9)	

Table A.6 (Cont.)						
Designation	Plate Thickness, mm (in.)	Angle Thickness, mm (in.)	HSS Path #1 MPa (ksi)	HSS Path #2 MPa (ksi)		
No retrofit	--	--	1998.5 (289.9)	495.7 (71.9)	51 mm (2.0 in.) horseshoe crack	51 mm (2.0 in.) horizontal crack
sA-sBP18	25.4 (1)	25.4 (1)	80.2 (11.6)	123.3 (17.9)		
mA-sBP18	25.4 (1)	12.7 (^{1}/$_2$)	252.5 (36.6)	119.9 (17.4)		
fA-sBP18	25.4 (1)	6.35 (^{1}/$_4$)	827.3 (120.0)	176.7 (25.6)		
sA-mBP18	12.7 (^{1}/$_2$)	25.4 (1)	161.4 (23.4)	33.9 (4.9)		
mA-mBP18	12.7 (^{1}/$_2$)	12.7 (^{1}/$_2$)	469.4 (68.1)	95.5 (13.9)		
fA-mBP18	12.7 (^{1}/$_2$)	6.35 (^{1}/$_4$)	996.7 (144.6)	223.1 (32.4)		
sA-fBP18	6.35 (^{1}/$_4$)	25.4 (1)	221.5 (32.1)	60.8 (8.8)		
mA-fBP18	6.35 (^{1}/$_4$)	12.7 (^{1}/$_2$)	419.4 (60.8)	135.8 (19.7)		
fA-fBP18	6.35 (^{1}/$_4$)	6.35 (^{1}/$_4$)	1094.5 (158.8)	269.7 (39.1)		
No retrofit	--	--	1956.7 (283.8)	739.9 (107.3)	102 mm (4.0 in.) horseshoe crack	203 mm (8.0 in.) horizontal crack
sA-sBP18	25.4 (1)	25.4 (1)	28.1 (4.1)	180.0 (26.1)		
mA-sBP18	25.4 (1)	12.7 (^{1}/$_2$)	109.1 (15.8)	183.0 (26.5)		
fA-sBP18	25.4 (1)	6.35 (^{1}/$_4$)	465.2 (67.5)	178.6 (25.9)		
sA-mBP18	12.7 (^{1}/$_2$)	25.4 (1)	28.4 (4.1)	201.5 (29.2)		
mA-mBP18	12.7 (^{1}/$_2$)	12.7 (^{1}/$_2$)	92.5 (13.4)	254.6 (36.9)		
fA-mBP18	12.7 (^{1}/$_2$)	6.35 (^{1}/$_4$)	449.7 (65.2)	263.6 (38.2)		
sA-fBP18	6.35 (^{1}/$_4$)	25.4 (1)	43.5 (6.3)	225.3 (32.7)		
mA-fBP18	6.35 (^{1}/$_4$)	12.7 (^{1}/$_2$)	117.8 (17.1)	287.6 (41.7)		
fA-fBP18	6.35 (^{1}/$_4$)	6.35 (^{1}/$_4$)	432.8 (62.8)	341.9 (49.6)		

The peak HSS exhibited different trends with respect to crack length along path HSS1 (horseshoe-shaped crack along the toe of the CP-to-web weld) than it did along path HSS2 (horizontal crack along the toe of the web-to-flange weld). HSS1 demand increased significantly with increasing crack length, up to a crack length of 25 to 50 mm (1 to 2 in.), depending upon the stiffness of the retrofit elements, as shown in Figure A.10. These results strongly indicated that the best alternative to reduce the stress demand near the horseshoe-shaped crack at the toe of the CP-to-web weld (path HSS1) was to use the stiffest angle and back plate combination. Excellent levels of stress reduction were found for every crack length studied when the stiff combination was utilized.

For path HSS2 (horizontal crack at the toe of the web-to-flange weld), all combinations of angle and plate thicknesses followed a different trend from that observed for path HSS1, in that HSS2 stress demands generally increased with increasing crack length. The results for HSS2 are also shown in Figure A.10. The results show that for all crack lengths studied, the HSS2

demands in the retrofitted condition are quite low in magnitude. The level of stress reduction noted for HSS2 is lower than noted for HSS1, however, the stress demand in the unretrofitted condition was found to be significantly lower for HSS2 than for HSS1. These results indicate that the retrofit should be expected to provide good performance for mitigating cracking along the flange-to-web weld. An interesting phenomenon was found to occur for short crack lengths (13 mm [$^1/_2$ in.]), in that the unretrofitted and retrofitted demands levels at HSS2 were approximately equal. This indicates that for stress levels that are sufficiently high to produce crack propagation to a length of 13 mm ($^1/_2$ in.), the retrofit is unlikely to arrest crack propagation until it reaches a slightly greater length (> 25mm [1 in.]), at which point the retrofit becomes much more effective. As with any fatigue retrofit, a careful stress demand analysis should be performed to determine the suitability of this retrofit, especially in the presence of web-to-flange cracking.
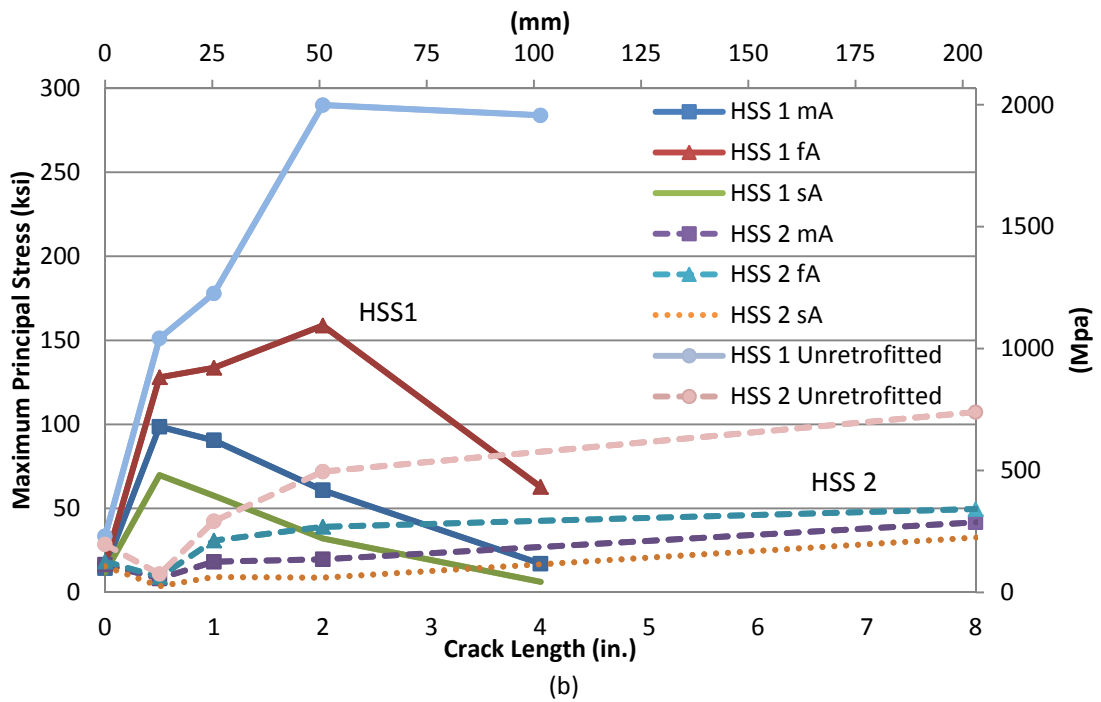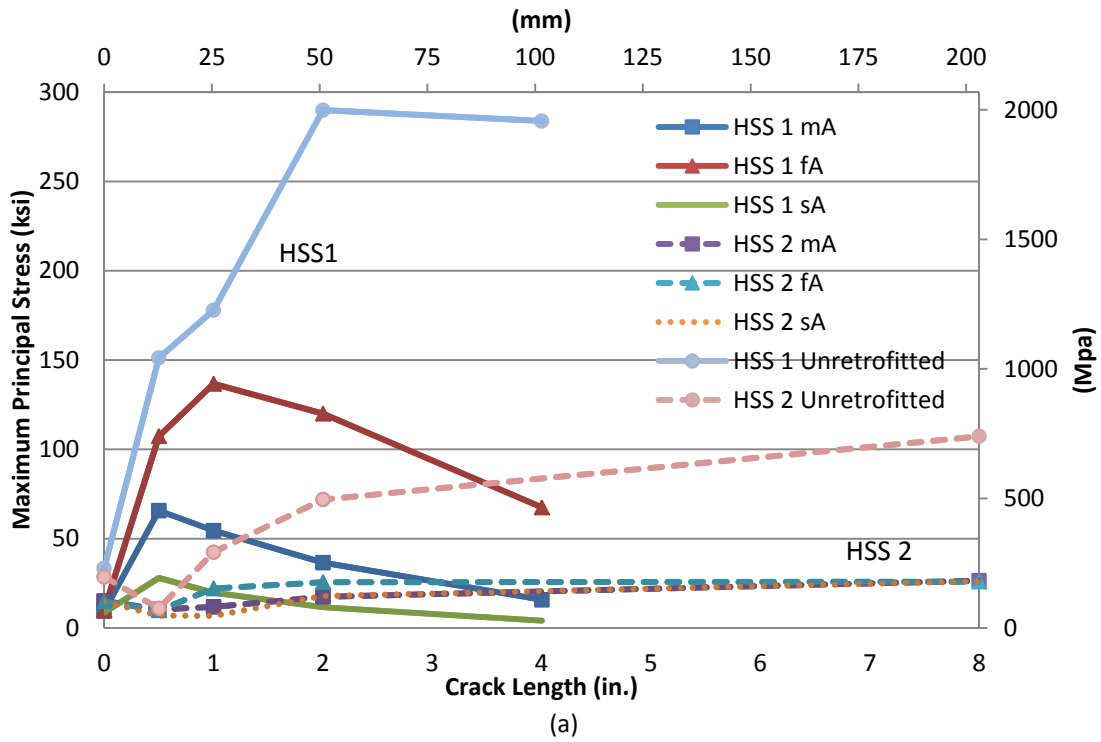
Figure A.20: Peak demand at web gap region vs. crack length for retrofitted specimens (a) HSS for stiff back plate configurations (b) HSS for flexible back plate configurations. Designations are the same used in Table A.5

J-Integral values (Figure A.21) computed from contours surrounding the tip of the horizontal crack at the tension face of the web showed similar trends as observed for the HSS values. The designations *sBP*, and *fBP* in Figure A.21 correspond to stiff back plate and flexible back plate, respectively. The number following the letters in the designation corresponds to the length of the horizontal crack in the model, in units of inches. Calculated *J*-Integral values indicated that retrofitted models with crack lengths of 25 mm (1 in.) and 50 mm (2 in.) had the highest propensity for growth; however, this phenomenon was absent when stiff angles were utilized. It was also found that when stiff angles are utilized, back plate stiffness did not have a large influence on crack growth propensity. When flexible angles were used, the influence of back plate stiffness was greater and the effects of crack length were more pronounced.
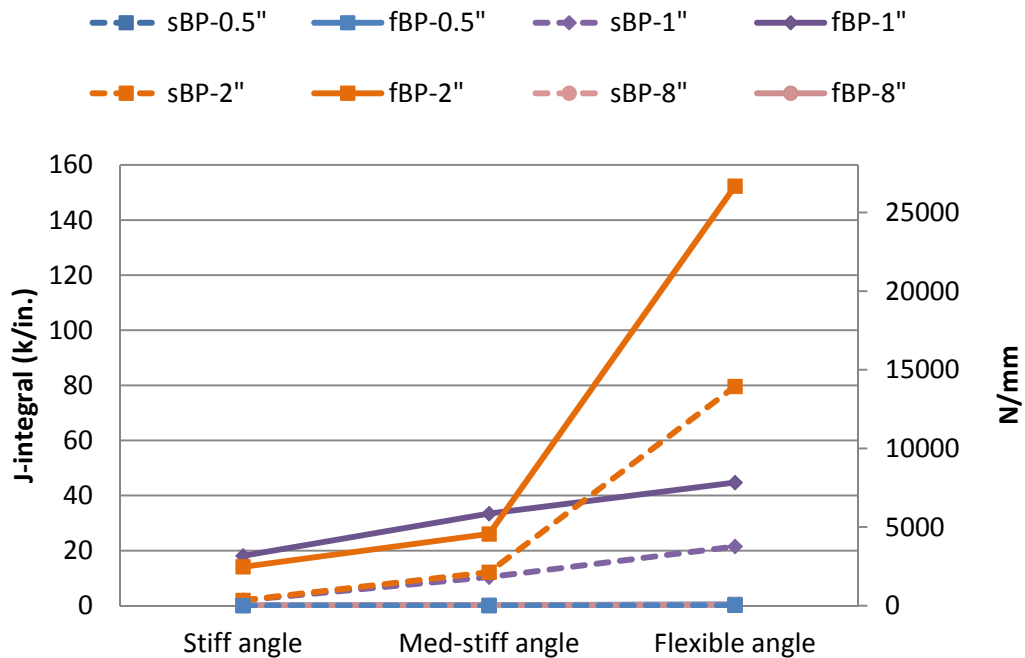
Figure A.21: J-Integral at the tip of the horizontal crack (HSS2 in Figure A.16) vs. angle stiffness for various back plate configurations and crack lengths of retrofitted specimens (designations are the same used in Table A.5)

Results from the parametric study show that the effectiveness of the angles-with-plate retrofit measure, quantified in terms of the HSS and the *J*-Integral, was not very sensitive to crack length when a stiff angles-with-back plate retrofit was used. The retrofit was sensitive to crack length when a flexible angles-with-plate retrofit was used. These results indicate that this type of repair should be effective for cracks with various lengths, with the most effective configurations being those with the thickest connecting elements (the angles, in particular).

When the comparison is carried out in terms of percent reduction in HSS, the effectiveness of the retrofit measure generally increased with crack length. The reduction in HSS1 caused by the retrofit measure was smallest for the configuration without cracks (between 50 and 75%) and became larger as the crack length increased. For HSS2 the trend was similar, with the exception of crack lengths equal to 13 mm ($^1/_2$ in.), as previously discussed.

A.2.7 Conclusions

The computational study showed that the angles-with-plate repair has the potential to be a very effective method to restrain the growth of fatigue cracks in steel girders damaged by distortion-induced fatigue. Areas in the web gap region of computer models that exhibited the highest maximum principal stress demands correlated closely with the locations of fatigue cracks observed in experiments of the companion study. Simulation results showed that the two locations with the highest potential for developing fatigue cracks in the web gap region were the toe of the weld between the CP and the girder web, and the toe of the weld between the web and the flange. The performance of two different mitigation measures intended to prevent further growth of these two types of fatigue cracks was evaluated.

The angles-with-plate retrofit measure was effective in preventing distortion of the web gap region, reducing stress demands calculated at the critical points by an order of magnitude. Finite element simulations showed that stress demands around the connection plate-to-web weld, reinforced with the stiff-stiff version of the angles-with-plate repair, were on the order of 19% of those in the unreinforced configuration for short crack lengths (13 mm [$^1/_2$ in.] or less), and as low as 2% of those in the unreinforced configuration for large crack lengths (102 mm [4 in.] or more). Stress demands at the web-to-flange weld, reinforced with the stiff-stiff version of the angles-with-plate repair, were on the order of 16% of those in the unreinforced condition for

48

short cracks (with the exception of 13 mm [$^1/_2$ in. crack lengths]), and approximately 25 to 30% of those in the unreinforced condition for long cracks. These reductions were significantly greater than the reductions noted for cases in which a more flexible retrofit was used, indicating the importance of using a stiff retrofit.

Computer simulations showed undersized crack-arrest holes had only minimal effect on the stress field surrounding the cracks, implying that the likelihood of fatigue crack re-initiation was very high.

Although the simulation results indicated that the angles-with-plate retrofit measure was effective regardless of connecting element thickness and back plate length, some configurations were found to be significantly more effective than others. Based on the results from the computer simulations it is recommended that angles and back plates with a thickness of at least 2.5 times the thickness of the girder web be employed. It is also recommended that the length of the back plate be at least 1.5 times the length of the horizontal projection of the web-to-flange fatigue crack and that the back plate extends beyond the legs of the angles. In cases in which only the horseshoe-shaped crack has developed in the web gap region, it is recommended that length of the back plate be at least 1.5 times the length of the horizontal projection of the horseshoe-shaped fatigue crack and that the back plate extends beyond the legs of the angles.

Even though the experimental study showed that there was negligible crack growth when the angles-with-plate retrofit measure was implemented, it is recommended that in accordance with sound fatigue repair practice holes be drilled at the tips of the cracks. This is important to remove the damaged material in the fracture process zone and to avoid leaving a sharp tip at the end of the crack, which would make it more likely for the crack to propagate even with the presence of the retrofit measure.

For interior girders of bridges with non-staggered cross frame configurations this type of repair would have to be implemented using angles on both sides of the transverse connection plate. Because this type of connection would have a very different stress field, a repair with angles on both sides of the web requires in-depth experimental and analytical verification that are outside of the scope of this study.

The authors acknowledge that it is very important to thoroughly validate the simulation results before the proposed retrofit measure is widely implemented. A companion paper presents experimental results from girder subassemblies that corroborate the findings from this study (Appendix A.1). Further verification is presented in Appendix A.3 and A.4 of this report through physical and computational simulations of a reduced-scale bridge model, and controlled implementation of the proposed retrofit measure in a bridge in the state of Kansas is being performed under a separate project.

A.2.8 References

Adams, C. (2009). *Finite Element Study of Bridge Details Susceptible to Distortion-Induced Fatigue*. (Master's thesis). University of Kansas, Lawrence, KS.

Alemdar, F., Matamoros, A., Bennett, C., Barrett-Gonzalez, R., and Rolfe, S. (2012). "Use of CFRP Overlays to Strengthen Welded Connections under Fatigue Loading." *Journal of Bridge Engineering*, 17(3), 420-431.

Castiglioni, C., Fisher, J., and Yen, B. (1988). "Evaluation of Fatigue Cracking at Cross Diaphragms of a Multigirder Steel Bridge." *Journal of Constructional Steel Research*, 9(2), 95-110.

Cousins, T. E. and Stallings, J. M. (1998). "Laboratory Tests of Bolted Diaphragm-Girder Connections." *Journal of Bridge Engineering*, 3(2), 56-63.

Fisher, J. W., Jian, J., Wagner, D. C., and Yen, B. T. (1990). *Distortion-Induced Fatigue Cracking in Steel Bridges*. NCHRP Report 336. Transportation Research Board, National Research Council, Washington, D.C.

Hassel, H., Bennett, C., Matamoros, A., and Rolfe, S. (2013). "Parametric Analysis of Cross-Frame Layout on Distortion-Induced Fatigue in Skewed Steel Bridges." *Journal of Bridge Engineering*, 18(7), 601-611.

Jajich, D. and Schultz, A. (2003). "Measurement and Analysis of Distortion-Induced Fatigue in Multigirder Steel Bridges." *Journal of Bridge Engineering*, 8(2), 84-91.

Keating, P. B. and Fisher, J. (1987). "Fatigue Behavior of Variable Loaded Bridge Details Near the Fatigue Limit." *Transportation Research Record* 1118, 56-64. Transportation Research Board, National Research Council, Washington, D.C.

Maddox, S. J. (2002). "Hot-Spot Stress Design Curves for Fatigue Assessment of Welded Structures." *International Journal of Offshore and Polar Engineering,* 12(2), 134-141.

Richardson, T. (2012). *Analytical Investigation of Repair Methods for Fatigue Cracks in Steel Bridges*. (Master's thesis). University of Kansas, Lawrence, KS.

Roddis, W. M. K. and Zhao, Y. (2001). "Out-of-Plane Fatigue Cracking in Welded Steel Bridges: Why It Happened and How It Can Be Repaired." *Welding Innovation*, 18(2), 2-7.

Rolfe, S. T. and Barsom, John M. (1977). *Fracture and Fatigue Control in Structures: Applications of Fracture Mechanics*. 1st ed. Prentice-Hall, Englewood Cliffs, NJ.

SIMULIA (2009). Abaqus, Version 6.8-2. http://www.simulia.com.

Appendix A.3: Experimental Investigation of Distortion-Induced Fatigue Repair in 9.1m (30 ft) Test System

Amanda S. Hartman[11]

Kathleen McElrath[12]

Caroline R. Bennett[13]

Adolfo B. Matamoros[14]

Stanley T. Rolfe[15]

A.3.1 Abstract

With infrastructure in the United States deteriorating at an alarming rate, repair of existing roadway bridges is critical for state highway agencies to responsibly allocate scarce resources. For steel bridges that were constructed prior to the mid-1980s, distortion-induced fatigue cracking can be a significant problem. Retrofit or repair techniques currently used in the field may not completely halt crack growth and/or can be expensive to implement. A distortion-induced fatigue repair technique that is commonly implemented in the field is to provide positive connection between the transverse connection plate and girder flange. However, this technique often requires partial removal of the concrete deck to access the top of the flange to make the connection.

To address these concerns, an innovative retrofit technique developed at the University of Kansas was analyzed to determine its effectiveness as a distortion-induced fatigue repair its suitability for field implementation. A different approach was also taken by the authors where a retrofit termed "angles-with-plate" utilized two angle segments and a backing plate to connect the girder connection plate and the web.

To investigate the performance of this retrofit, a 9.1 m (30 ft) long three-girder test bridge was constructed and tested under fatigue loading to develop, and subsequently repair, distortion-

---

[11] Amanda S. Hartman, PhD, Structural Engineer, Burns and McDonnell, 9400 Ward Pkwy, Kansas City, MO 64114

[12] Kathleen McElrath, Graduate Research Assistant, University of Kansas, 1530 W. 15th St., Lawrence, KS 66045

[13] Caroline R. Bennett, PhD, PE, Associate Professor, University of Kansas, 1530 W. 15th St., Lawrence, KS 66045

[14] Adolfo B. Matamoros, PhD, Professor, University of Kansas, 1530 W. 15th St., Lawrence, KS 66045

[15] Stanley T. Rolfe, PhD, PE, A.P. Learned Distinguished Professor, University of Kansas, 1530 W. 15th St., Lawrence, KS 66045

induced fatigue cracking. A total of 14 test trials were performed with varying load ranges to assess the effectiveness and applicability of the angles-with-backing plate retrofit. In addition to assessing retrofit performance, crack growth as well as girder deflections and strains were monitored. It was found that retrofit application significantly reduced web gap rotation, while the diagonal cross frame angle framing into the top web gap experienced a significant increase in tensile strain. When implemented with crack arrest holes, the angle-with-backing plate performed well at mitigating distortion-induced fatigue cracking in steel girders.

A.3.2 Introduction

During and prior to the 1970s, many steel bridges were constructed without significant knowledge of structural fatigue. Due to several structural failures in Europe when cross frame or diaphragm connection plates were welded to tension flanges in the 1930s (Fisher and Keating 1989), common practice until 1985 was to not weld connection plates to the tension flange. Although the intention of this detailing practice was to prevent similar failures to those that occurred in European steel bridges, this lack of connection initiated an area of significantly high stresses in steel bridge girders leading to rife fatigue cracking in bridges with this detailing. Many steel bridge structures designed and constructed during this time period have exhibited significant fatigue cracking due to distortion-induced fatigue, presenting bridge engineers and management staff with a challenging and expensive situation.

Distortion-induced fatigue commonly occurs at connections of transverse structural members (Roddis and Zhao 2001). Web gaps that exist between connection plates and girder top flanges are the most common location for fatigue cracking. As a bridge experiences traffic loading, the steel girders undergo different levels of deflection. This results in cross frame members inducing secondary, out-of-plane forces on the adjacent girders that are deforming differently. Since the top flange of the girder is restrained from rotation by the concrete deck and the bottom flange is free to rotate, distortion of the web gap region occurs which is shown in Figure A.22. While secondary forces carried by the cross frames may be low in magnitude, they often translate into significant stresses due to the high flexibility of the web gap, and due to the presence of a multitude of stress concentrations in the congested geometry of the web gap region, and fatigue cracking can be expected to occur.
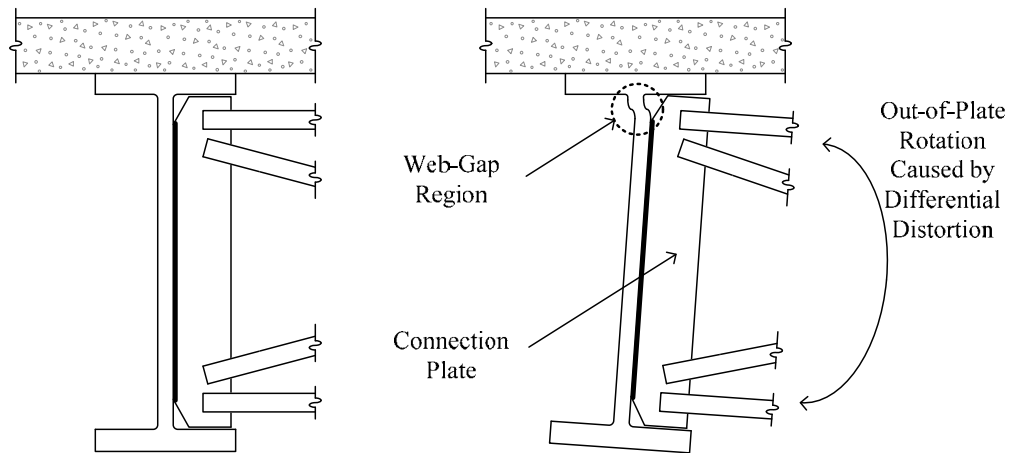
Figure A.22: Out-of-plane rotation causing distortion-induced fatigue

A.3.3 Background

In addition to being a common occurrence in steel bridges, distortion-induced fatigue is also a problem that is both difficult and expensive to repair. There are a number of techniques that can be used to retrofit bridges for distortion-induced fatigue, including drilled crack-arrest holes, cross frame removal, slotting the connection plate, utilizing a back-up stiffener, and connecting the connection plate to the girder's top flange. Each of these techniques have associated advantages and disadvantages, and it is useful to bridge engineers and owners to have multiple options from which to choose.

Crack-arrest holes are often drilled at the tips of sharp cracks to halt crack growth as a first line of defense against fatigue crack propagation; however, "hole drilling alone is not effective at stopping fatigue cracks when the cracks are initiated from out-of-plane distortions" (Grondin et al. 2002). Although crack stop holes may temporarily slow or stop crack growth, they are not a permanent fix for cracking due to distortion-induced fatigue. Instead, crack-arrest holes are often used in conjunction with other retrofit techniques such as slotting or providing an alternate load path via a structural repair.

Cross frame removal is another retrofit option that has been examined for distortion-induced fatigue (Tedesco et al. 1995; Roddis and Zhao 2001). The concept of this technique is to remove the lateral connection between adjacent girders which eliminates out-of-plane forces induced by secondary structural members, thus eliminating distortion-induced fatigue. However,

54

when cross-frames are removed from an existing bridge system, consideration should be given to: (1) effectiveness of the bridge system to laterally distribute live loads; (2) effectiveness of the system to carry wind loading; and (3) future needs regarding deck replacement. While under construction and in negative bending regions post-construction, cross frames provide restraint to prevent lateral-torsional buckling. Due to lateral-torsional buckling considerations, cross frames or other bracing is a necessity during deck replacement and cross-frames generally cannot be removed from negative bending moment regions. Additionally, Tedesco et al (1995) indicated that cross frame removal increases individual girder moment demand by approximately 8 to 14%, due to lower amounts of live load distribution.

Back-up stiffeners are a retrofit scheme that functions by stiffening the web gap region, reducing distortion-induced fatigue effects. Placed on the opposite side of the web from the cross frame connection plate, back-up stiffeners are simply transverse stiffeners that strengthen the web gap and reduce out-of-plane rotation of the web gap region. Although Hassel et al. (2010) concluded that back-up stiffeners can be highly effective in skewed bridge applications with staggered cross frame layouts (discussed in Appendix D), the authors found that these stiffeners are less effective in non-staggered bridges applications where the only potential retrofit locations are on the fascia side of the exterior girders.

Positive connection to the girder flange can be accomplished using several methods. Commonly, angles are used to provide connection between the flange and connection plate by either bolting or welding one leg to the flange and the other to the connection plate (Roddis and Zhao 2003, Fisher et al. 1990). This method was found to be effective at halting fatigue crack initiation and propagation; however, applications of this technique are not without challenges. For example, bolting to the flange is generally preferred over welding due to the greater fatigue sensitivity at welded details. If the web gap being repaired is at the top flange of the girder, application of this technique usually requires removal of at least portions of the concrete deck, bringing about significant traffic disruption and expense.

An alternative retrofit technique to traditional means of positive connection has been the subject of a number of investigative efforts at the University of Kansas. The retrofit described in Appendix A.1 consisted of two angles which attached the connection plate to the girder web. The

55

angles were used in conjunction with a back plate on the opposite side of the girder web to distribute out-of-plane forces over a large area of the web. Since this retrofit did not require any attachment to the flange, it eliminated any need for deck removal and can be installed under traffic. This technique, which was termed the "angles-with-plate" retrofit, was evaluated through a series of tests performed on 2.8 m (9.3 ft) long girder-cross frame subassemblies loaded under a demanding distortion-induced fatigue loading protocol. An analytical investigation was performed in parallel to the physical simulations.

The test set-up used for testing the girder segments (see Appendix A.1) was such that the girder-cross frame subassembly was tested upside-down, with the girder's top flange rotationally restrained to the laboratory strong floor. Cyclic loads were applied through a servo-controlled hydraulic actuator attached to the free end of the cross-frame elements. This test set-up eliminated in-plane bending effects on the test girders and presented a demanding out-of-plane fatigue test. The test set-up used for testing the girder segments is shown again in Figure A.23.
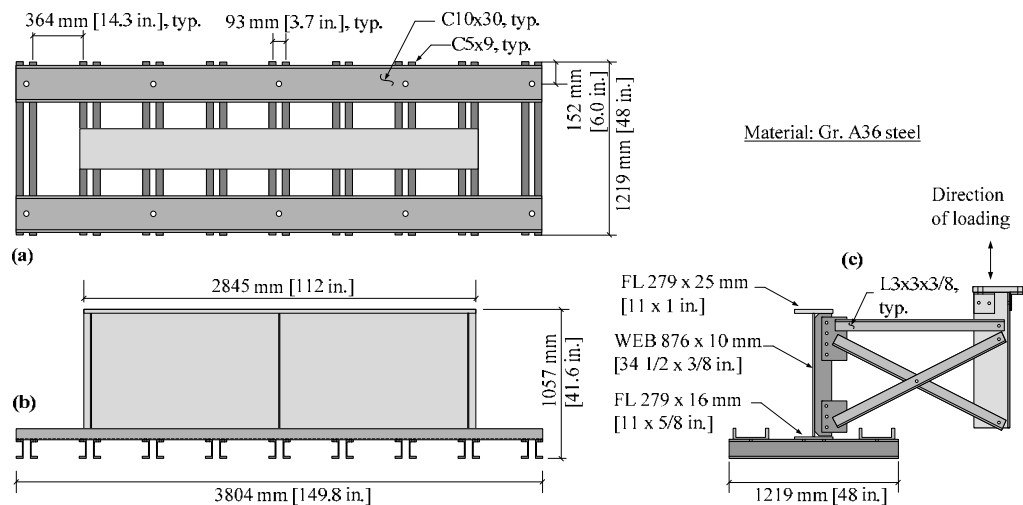
Source: Alemdar et al. 2013(a) and (b)
Figure A.23: Test set-up for 2.8 m (9.3 ft.) girder sub-assembly testing

The test set-up and computational models were used to generate an initial set of data for the angles-with-plate retrofit. This showed that the technique was highly effective under pure out-of-plane fatigue loading, reducing web gap stresses and drastically reducing propensity of crack propagation under distortion-induced fatigue.

56

A.3.4 Objective and Scope

The objective of this study was to investigate the effectiveness of the angles-with-plate retrofit technique reported upon in Appendix A.1 and A.2 of this report in reducing distortion-induced fatigue crack propensity under a more realistic test set-up, wherein both out-of-plane and in-plane effects are considered.

The scope of this study included performing 14 test trials on a three-girder test bridge that was 9.1 m (30 ft) long and included a concrete deck made composite with the girders. Results from a parallel analytical investigation have been presented in a companion paper in Appendix A.4 of this report. Results of these studies are currently limited to straight, non-skewed bridge girders.

A.3.5 Experimental Program

Since the goal of this investigation was to evaluate the effectiveness of the angles-with-plate retrofit in a test that captured both in-plane bending effects and secondary stresses from distortion-induced fatigue, a set-up was constructed that included three 9.1 m (30 ft) long girders connected with X-type cross frames at the two simple support locations and at midspan. A concrete bridge deck was cast in sections and was connected to the girders such that it would act compositely. All loads were applied through a 1470 kN (330-kip) servo-controlled hydraulic actuator. The loading end of the actuator was situated over a steel bearing plate centered on the bridge deck. Details regarding the test set-up are provided in the following sections.

A.3.5.1   Girder Specifications

Test specimen dimensions were primarily based on laboratory space constraints and a sample bridge from American Iron and Steel Institute (AISI) Example 1: Simple-Span Composite I Girder (AISI 1997). Approximately half scale of the AISI sample bridge, the 9.1 m (30 ft.) long girders were comprised of a 16 x 279 mm (5/8 x 11 in.) top flange, 6 x 876 mm (1/4 x 2 ft.-10 1/2 in.) web, and 25 x 279 mm (1 x 11 in.) bottom flange. All girders were supported on rollers to minimize axial forces with a center-to-center span length of 8.7 m (28.5 ft) between supports. Section dimensions and girder span with load placement are shown in Figure A.24. In the laboratory, the longitudinal axis of the bridge system was oriented east-west which defined the exterior girders as being the north and south girders. At the section shown in Figure A.24(a),

57

looking west, the exterior girder shown on the right is the north girder and the left is the south girder.

(a)

(b)
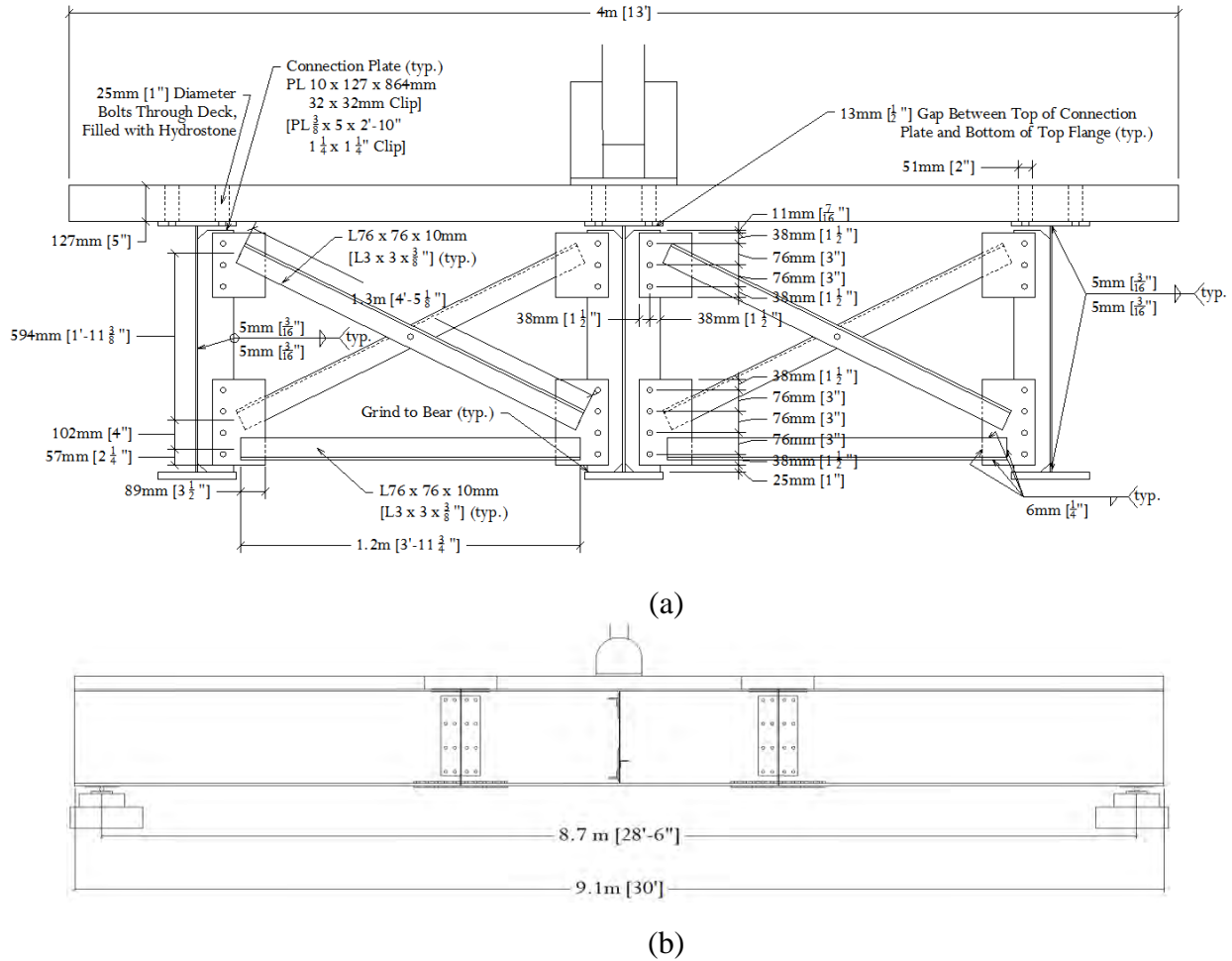
Figure A.24: North and South Girders
(a) Dimensions and schematic of test region cross frames. (b) Girder span and load application.

The concrete deck was cast in five sections; 51 mm (2 in.) diameter circular voids were created during the casting procedure, spaced to provide one bolt on either side of the web at a maximum spacing along the girder flange of 432 mm (1 ft -5 in.). Each portion of deck was cast on using formwork on the ground and then lifted into place after they had been cured. The voids cast into the concrete deck elements matched a hole layout on the top flanges of the girders, providing a location for high-strength structural bolts to be placed through. After the bolts were placed, the remaining void area was filled with Hydrostone. In this manner, horizontal shear

58

transfer was achieved between the steel girders and the concrete deck elements. The compressive strength of the concrete used in the deck was found to range from 267 MPa (3900 psi) to 33 MPa (4800 psi) when tested at 28-days.

A.3.5.2 Loading

Cyclic loading was delivered by a MTS 201.70 actuator (1470 kN (330 kips) capacity in compression) powered by a MTS 505.90 90 GPM pump and controlled with a MTS FlexTest II CTC Controller. A 25 mm (1.0 in.) thick steel plate was centered on the bridge deck, and was grouted in place under the footprint of the actuator. The purpose of the steel plate was to distribute the concentrated compressive force delivered by the actuator. Loading was applied at midspan over the interior girder, as shown in schematic in Figure A.24. The cyclic loading was applied at rates varying between 1.0 to 2.0 Hz depending on the load range being applied.

A.3.5.3 Retrofit Specifications

The retrofit investigated in Trials 2 to 6 contained two angles providing attachment between the connection plate and girder web with a backing plate on the opposing face of the web. Two L152x152x19 mm (L6x6x$^3/_4$ inch) angles were bolted to the connection plate and girder web while a 457x457x19 mm (18x8x$^3/_4$ inch) back plate was used to distribute out-of-plane forces over a large web area, as shown in Figure A.25 schematics.
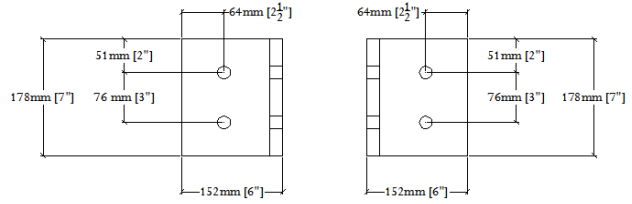
L152x152x19mm
[L6x6x3/4"]
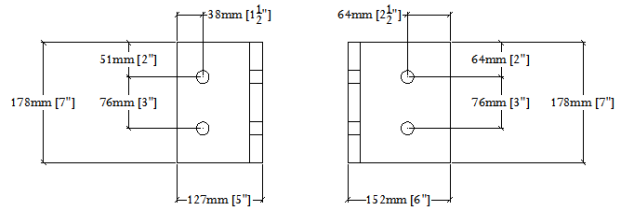
L127x152x19mm
[L5x6x3/4"]

(a)
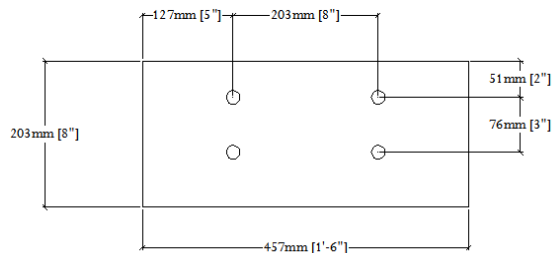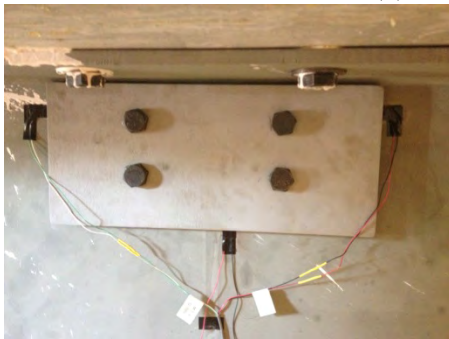
L457x203x19mm
[18x8x3/4"]

(b)

Figure A.25: Retrofit as applied to top web gap in test specimen

Due to fit interferences with the cross frame angles, it was necessary that two retrofit angles each have one leg shortened by 25.4 mm (1 in.). Shim plates were also utilized to avoid weld interference. The bolt layout consisted of a total of six Gr. A325 19 mm ($^3/_4$ in.) diameter slip-critical bolts for each retrofit application.

The retrofit applied in Trial 7 was identical to that used in Trials 2 to 6, except stiffening elements were added to the angle elements of the retrofit, as shown in Figure A.26.

60

Figure A.26: Stiffened angles-with-plate retrofit applied to exterior girders in Trial 7

A.3.5.4 Instrumentation

The test bridge was instrumented such that strain, vertical deflections, and lateral deflections could be measured through the test sequence. Additionally, load and displacement data were recorded from the actuator using the same data acquisition system as was used for all other sensors. Sensors included the following: load cells, linear variable differential transformers (LVDTs), string potentiometers, Bridge Diagnostics, Inc. (BDI) strain transducers, and strain gages. Global bridge response was monitored using load cells, LVDTs, string potentiometers, and strain transducers. Six load cells, one at each girder end, were used to monitor load distribution between girders. Load cells were calibrated using a 6.55V power supply.

LVDTs and string potentiometers were powered using a 15V power supply. Initially, LVDTs were used to monitor vertical girder deflections at midspan as well as lateral displacements for each exterior girder at three different locations along the height of each girder [Figure 27(a)]. Since exterior girder deflections included both vertical and lateral displacements, it was found that the LVDT core could not extend and retract freely which resulted in inaccurate

deflection measurements. Due to this, four string potentiometers [Figure A.27(b)] replaced the original three LVDTs monitoring lateral girder displacements.

(a)   (b)

(1) Fascia Side, Gage Near Flange-Web Weld (Left Side)
(2) Fascia Side, Gage Near Flange-Web Weld (Right Side)
(3) Fascia Side, Gage Behind Transverse Connection Plate
(4) Interior Side, Left Side of Transverse Connection Plate
(5) Interior Side, Right Side of Transverse Connection Plate

(c)
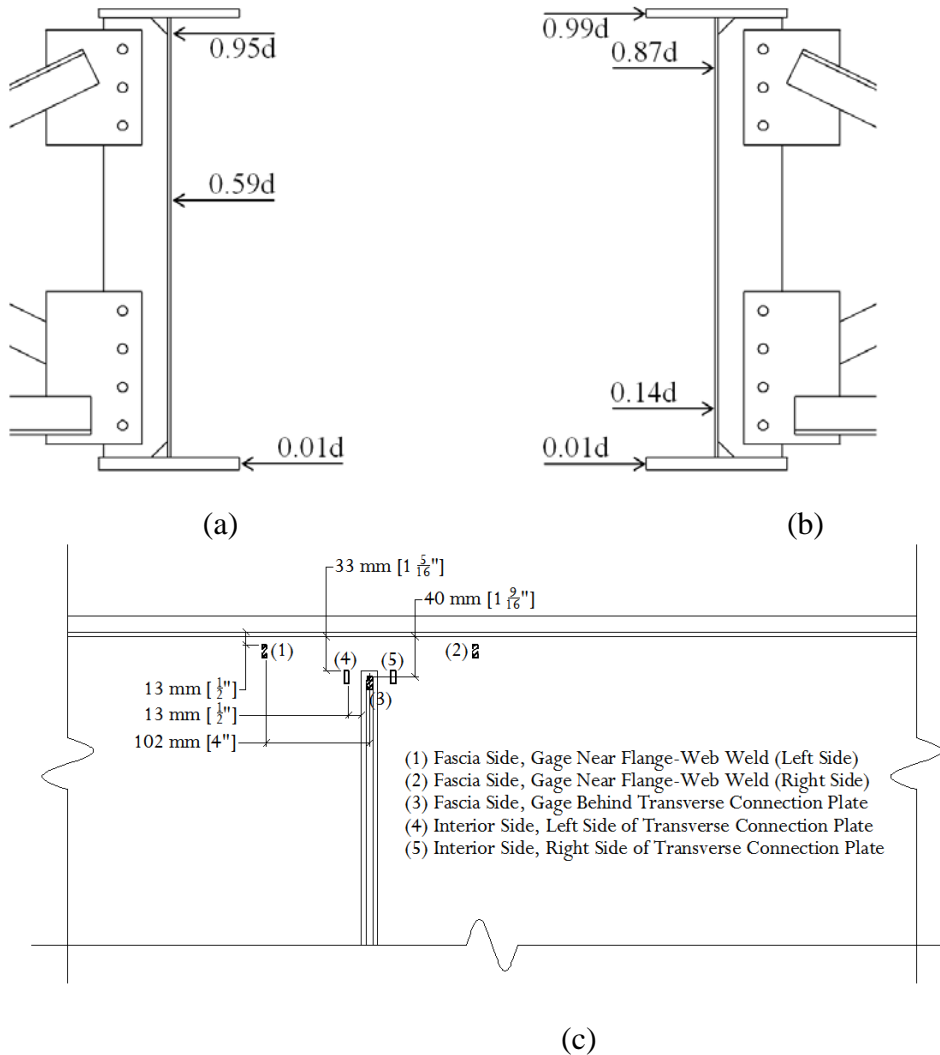
Figure A.27: Instrumentation placements
(a) LVDTs, (b) String potentiometers, and (c) Strain gages

Six Bridge Diagnostics, Inc. (BDI) strain transducers were used in the test set-up. Each girder was instrumented with two strain transducers, one placed at top and bottom of each girder web to monitor in-plane bending strains in the three girders. BDI strain transducers were powered with 5V. To avoid local concentrations due to geometry, these were placed 51 mm (2 in.) below or above the flanges, and were located a longitudinal distance 654 mm (25 $^3/_4$ in.) from the connection plates at midspan.

To monitor strains in the web gap region, bondable strain gages were included in the bridge instrumentation plan. Bondable strain gages were powered directly through the data acquisition system in a quarter bridge configuration with excitation voltages of 2.5V or 3.3V—strain gages into NI-9219 were powered by 2.5V and strain gages into NI-9236 were powered by 3.3V. In total, 20 Micro-Measurements WK-06-250BG-350 gages were placed in web gap regions as shown in Figure 27(c). Additionally, bondable strain gages were placed on each cross frame angle at midspan of the girders oriented along the axis of the cross frame member. On the horizontal angle of the cross frame, the gage was placed mid-span. For the diagonal members which were bolted at mid-span, the gages were placed at the quarter-point of the span nearest the exterior girder.

Due to the scale of the project and large sensor array, synchronizing the data was a critical step. All data were recorded using a single data acquisition system manufactured by National Instruments (NI cDAQ 9188 with NI 9205, NI 9212, NI 9236, and NI 9239 modules). A protocol was written in Labview 2011 to read, compress, and record data in a text file. The quantity of data required an extremely large sampling rate to sufficiently increase the buffer size within the NI cDAQ 9188 chassis. Sampled data were post-compressed to produce an effective sampling rate of approximately 20 samples/second. All appropriate calibration factors were applied within the Labview protocol, such that data written to the measurement file contained appropriate units.

Prior to retrofit application, data were recorded under static load application every 15,000 cycles. Throughout test trials performed on the bridge in the retrofitted state, static data were recorded at the beginning and end of each trial (which usually had a duration of 1.2 million cycles). During data acquisition loading was controlled manually progressing from 0 kN (0 kip) to 356 kN (80 kip) while data were recorded continuously. Raw data were imported into Microsoft Excel and post-processed to examine data at 11 kN (2.5 kip) load increments. As the load range applied to the test bridge was different in various test trials, the maximum load to which data were recorded was increased to 445 kN (100 kip) and then to 534 kN (120 kip), and the corresponding data increment was increased to 22 kN (5 kip).

A.3.5.5   Cracking and Inspection

Crack inspection was performed at regular intervals while the bridge was subjected to cyclic loading. Inspection techniques included photographic and visual inspection as well as evaluation of strain measurement data. Zyglo Penetrant (ZL-27A) by Magnaflux and an ultraviolet flashlight were used to see crack openings and tips. When dye penetrant was sprayed on the region of interest during cyclic loading, surface cracks could be seen pulsing under the ultraviolet light. At each inspection, photographs were taken using a Cannon Rebel XTi DSLR with an 18 to 55mm lens. Early photographic images contained a small scale taped to the girder web used for determining crack length. Later, photographs were scaled to the previous images to verify crack measurements obtained visually and monitor crack growth.

In addition to visual and photographic inspection, strain gages were monitored through static data collection at 15,000 cycles, 20,000 cycles, and 30,000 cycles, and then every 15,000 cycles until retrofitting at 150,000. Strain readings from gages placed on the fascia side directly behind the connection plate [shown in Figure A.27(c)] were compared throughout testing of the bridge in the unretrofitted condition. These gages measured the largest strains and were found to be highly sensitive to cracking in the connection plate-web weld.

As discussed further in the following sections of this paper, it was found that girder cracking first initiated and propagated around the connection plate-web weld in the top web gaps of the south and north girders. These cracks were closely monitored and classified by three different categories: (1) cracks growing down the weld (termed "vertical cracks"), (2) cracks growing out from the weld in the longitudinal direction of the girders (termed "spider cracks"), and (3) cracks extending through the web thickness (termed "through cracks"). Each of these three crack patterns is shown in Figure A.28. Additionally, cracking was found near the flange-web weld; these were termed "longitudinal cracks."
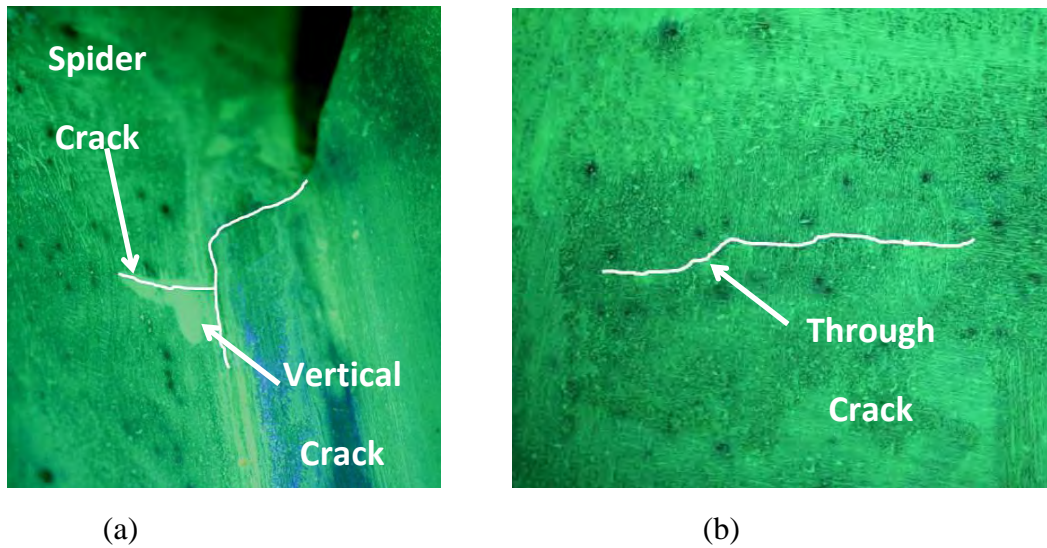
Figure A.28: Crack definition
(a) Interior side of girder web at cross frame connection plate and (b) Exterior or fascia side of girder web.

A.3.5.6   Test Trials

Fourteen test trials were performed on the test bridge which are summarized in Table A.7. For each loading protocol on the bridge system, the two exterior girders (the north girder and the south girder) underwent a test trial. The center girder was not listed as undergoing a test trial, since the center girder did not experience any cracking throughout the test sequence. Trial 1 consisted of an unretrofitted specimen in which cracking was allowed to initiate and propagate until a crack length of 24 mm (1 in.) was achieved. Trials 2, 3, 5, and 6 were indicative of the bridge with the exterior girders in the retrofitted condition (sometimes with the addition of crack stop holes), with each trial having a duration of 1.2 million cycles, with the exception of Trial 4. Trial 4 was the only retrofit trial that did not reach 1.2 million cycles, for reasons discussed further in the following sections.

Table A.7: Specimen Test Trials for North (N) and South (S) Girders with Load Range

Trial	Specimen Description	Target Load Range
1N 1S	Bare specimen	27-267 kN (6-60 kip)
2N 2S	"Angles-with-plate" retrofit applied in top web gap	27-267 kN (6-60 kip)
3N 3S	Same as Trials 2N and 2S: "Angles-with-plate" retrofit applied in top web gap	36-356 kN (8-80 kip)
4N 4S	Small drilled holes with "angles-with-plate" applied in top web gap	44-445 kN (10-100 kip)
5N 5S	Larger drilled hole with "angles-with-plate" retrofit applied in top web gap	44-445 kN (10-100 kip)
6N 6S	Same as Trials 5N and 5S: Larger drilled hole with "angles-with-plate" retrofit applied in top web gap	53-534 kN (12-120 kip)
7N 7S	Stiffened version of angles-with-plate was installed in the top web gap	53-534 kN (12-120 kip)

The load range applied to the test bridge was varied over the course of the testing sequence to create a highly-demanding test of the angles-with-plate retrofit effectiveness at reducing distortion-induced fatigue crack propensity. The load range applied to the bridge in Trials 1S, 1N, 2S, and 2N was 27-267 kN (6-60 kip) which corresponded to a maximum normal bending stress of 29.6 MPa (4.3 ksi) in the bottom flange of the center girder. This load range was found to produce vertical strains of approximately 250 $\mu\varepsilon$ – 850 $\mu\varepsilon$ in the top web gap regions of the south and north girders, and produced a maximum vertical deflection at midspan of 2.0 mm (0.077 in.). Details regarding the strain and deflection measurements under the various load ranges have been provided in Table A.8.

Table A.8: Specimen Trials with Load Range and Bottom Flange Stresses

Trial	Sample Load kN (kip)	Girder Max. Deflection mm (in.)	Girder Maximum Bottom Flange Stress MPa (ksi)	Uncracked Top Web Gap Strain Gages (3)/(4 & 5) (με)	Cracked Top Web Gap Strain Gages (3)/(4 & 5) (με)
1N		0.8 (0.033)	9.7 (1.4)	-705/285-352	-818/252-333
Center	267 (60)	*2.0 (0.077)*	*29.6 (4.3)*	*N/A*	*N/A*
1S		0.8 (0.032)	8.3 (1.2)	-839/522-556	-854/521-556
2N		0.9 (0.034)	9.7 (1.4)	-705/285-352	
Center	267 (60)	*1.9 (0.075)*	*29.6 (4.3)*	*N/A*	
2S		0.8 (0.032)	8.3 (1.2)	-839/522-556	
3N		1.1 (0.044)	13.1 (1.9)	-963/377-468	
Center	356 (80)	*2.3 (0.091)*	*40.0 (5.8)*	*N/A*	
3S		1.1 (0.042)	11.0 (1.6)	-1120/694-742	
4N		1.3 (0.051)	16.5 (2.4)		
Center	445 (100)	*3.4 (0.134)*	*48.3 (7.0)*		
4S		1.4 (0.055)	14.5 (2.1)		
5N		1.4 (0.056)	15.9 (2.3)		
Center	445 (100)	*3.7 (0.145)*	*--*		
5S		1.3 (0.052)	12.4 (1.8)		
6N		1.6 (0.062)	17.9 (2.6)		
Center	534 (120)	*4.5 (0.178)*	*--*		
6S		1.5 (0.059)	15.9 (2.3)		
7N		1.4 (0.054)	15.2 (2.2)		
Center	534 (120)	4.9 (0.193)	--		
7S		1.3 (0.053)	13.1 (1.9)		

All values in Table A.8, with the exception of uncracked strains, are recorded from the end of each trial. Strains in the uncracked north and south girders were only recorded up to a load of 356 kN (80 kip), and strains in cracked north and south girders were only recorded for Trials 1N and 1S since retrofit application caused gages in the top web gap to fail. Maximum girder deflection at mid-span was measured directly using an LVDT under each girder. Strain transducer data were used to determine maximum bottom flange bending stress. For each girder, the two strain transducers were used to develop a strain profile. These were placed in the web; however, with the strain profile, bending strains were extrapolated to the bottom flange (the extreme fiber). Additionally, these strains were not located at midspan so they were modified to represent midspan strains using a linear variation between support and midspan due to single point loading at midspan. Since significant amounts of data were collected, each strain reading is an average of four consecutive data points. All data were averaged in a similar fashion and data for the given maximum load was extracted which resulted in a single set of data for each load.

Three other load ranges were applied in various test trials: 36-356 kN (8-80 kip) (Trials 3S and 3N); 44-445 kN (10-100 kip) (Trials 4S, 4N, 5S, and 5N); and 53-534 kN (12-120 kip) (Trials 6S, 6N, 7S, and 7N). The largest load range used in the test sequence, 53-534 kN (12-120 kip), produced a maximum vertical deflection at midspan under the 53-534 kN (12-120 kip) load range of 4.9 mm (0.193 in.) in Trial 7. An issue with the bottom strain transducer resulted in non-linear data for bending stresses. Extrapolating from previous loading data for the 53-534 kN (12-120 kip) loading, an approximate maximum normal bending stress in the bottom flange of the center was determined to be 57.9 MPa (8.4 ksi).

The load ranges were chosen to be quite large and were significantly higher than what was expected for typical fatigue loadings in an actual bridge structure. Choosing large variation in load range was intended to assess retrofit performance over a full range of load demand that bridge behavior under retrofit application. The authors did not wish to approach the test design by using loadings that would ensure that no crack initiation or propagation would occur under the retrofit. Therefore, it was fully expected that cracking would propagate under the high load demands, even while retrofitted. Changes in crack propagation rates between unretrofitted and retrofitted conditions were therefore key interest to the investigators.

A.3.6 Results and Discussion

Throughout testing, data were recorded through the instrumentation plan discussed and crack growth was monitored and charted. Changes in bridge behavior and crack propagation were used to evaluate the retrofit effectiveness. Cross frame strains and girder lateral deflections helped to establish changes in bridge behavior while crack inspections were used to track crack propagation.

By comparing cross frame strains with cracked and uncracked girders as well as unretrofitted and retrofitted girders, changes in bridge response were observed. Another response that was monitored was the lateral deflections of the north and south girder profiles. Under retrofit application, girder lateral deflections were found to significantly change. In addition to global bridge response, crack initiation was established through strain gage data while crack propagation was monitored through visual and photographic inspection.

A.3.6.1 Girder Cross Frame Strains

Strain measurements on individual cross-frame members at mid-span were monitored to establish the amount of out-of-plane force acting on the web gap as well as to determine the distribution of forces through the cross frame elements. Cross frame labeling notation is shown in Figure A.27 (a) and (b) where angle top (AT) and angle bottom (AB) is where the inclined cross frame angles framing into the top and bottom web gaps, respectively. The horizontal angle in the cross frame is labeled HB (horizontal bottom).

Figure A.28 shows the effects of crack initiation on cross frame strain measurements. Prior to cracking, cross frame members AT and HB for the north and south girders experienced approximately the same strain in tension while AB experienced a similar strain magnitude in compression. Once cracking occurred in the connection plate-to-web weld of each girder, member AT experienced a reduction in strain of approximately 75 με while HB and AB experienced increases in strain of approximately 50 με. Due to cracking in the top web gap, less force was transferred into the cross frame member framing into top web gap, while the remaining members picked up additional load. As crack length increased, cross frame member strain distributions were seen to remain similar, as seen in a comparison of Figure 29 (b) and (c).

Figure A.29 (c) and (d) show the change in strains between unretrofitted and retrofitted conditions after 1.35 million cycles. With the retrofit applied, stiffening the top web gap, inclined cross frame angles framing into the top web gap (AT) experienced an increase in tensile strain of more than 50%. Since the inclined cross frame member framing into the top web gap experienced an increase in strain, both cross frame members framing into the bottom web gap experienced decreases in strain. Inclined cross frame members framing into exterior girder bottom web gaps (AB) experienced a decrease in compressive strains while horizontal members framing into the bottom web gaps (HB) experienced a decrease in tensile strains. Strain increases in element framing into the top web gap does not directly provide any information about propensity for crack growth. It does, however, show that the retrofit allows for significantly more force transfer into the web since the cross frame strains were larger when retrofitted as compared with the unretrofitted condition.
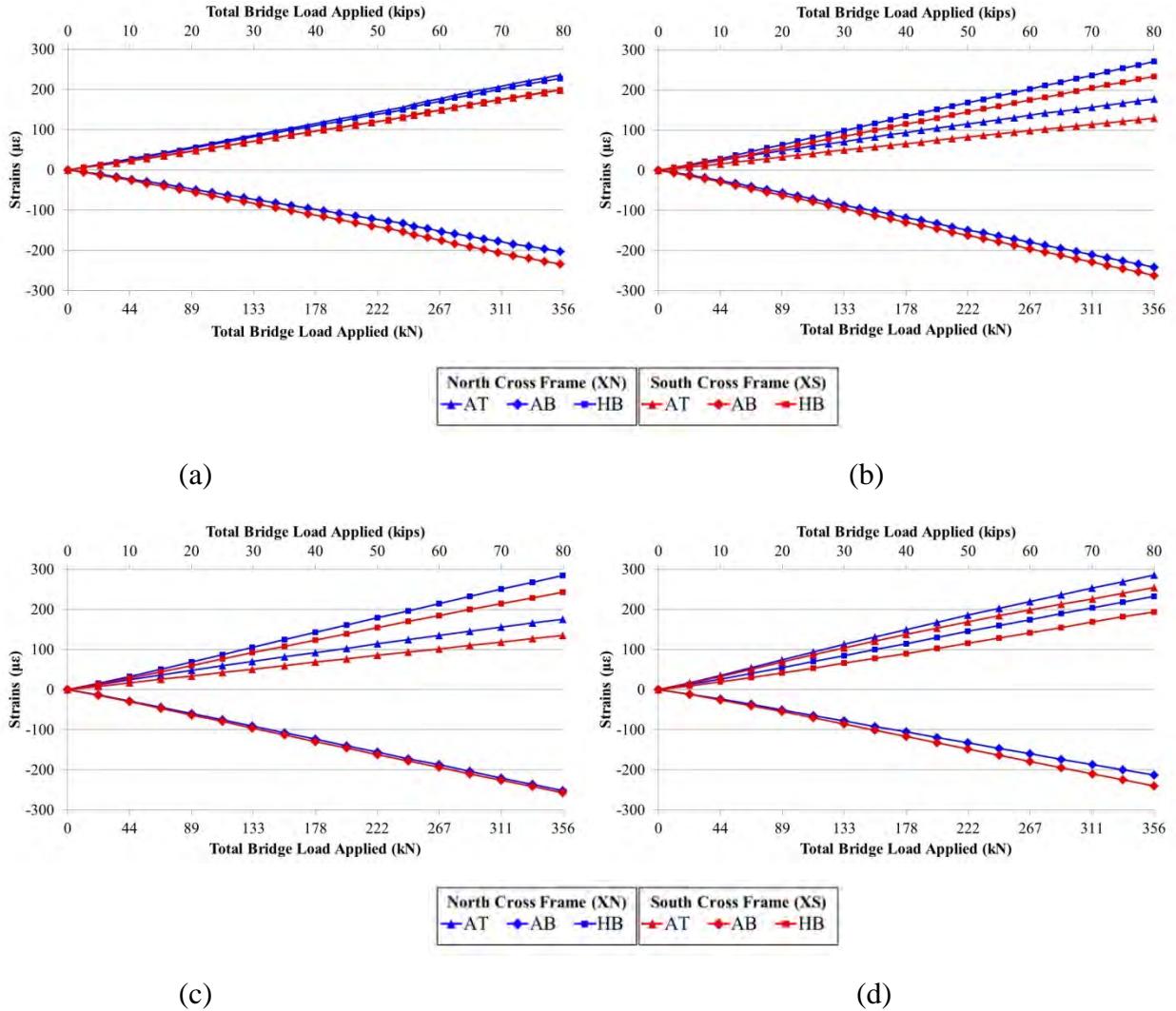
Figure A.29: Cross frame strains
(a) Uncracked, unretrofitted at 0 Cycles, (b) Cracked at 150,000 Cycles, (c) Cracked, unretrofitted at 1.35 Million Cycles, and (d) Cracked, retrofitted at 1.35 Million Cycles.

A.3.6.2   Lateral Girder Deflection

With the initial LVDT locations matching placements used in previous 2.8 m (9.3 ft.) girder sub-assembly testing at the University of Kansas (see Appendix A.1 and A.2), girder lateral deflections at 150,000 total cycles for both pre- and post-retrofit conditions have been presented in Figure A.30.
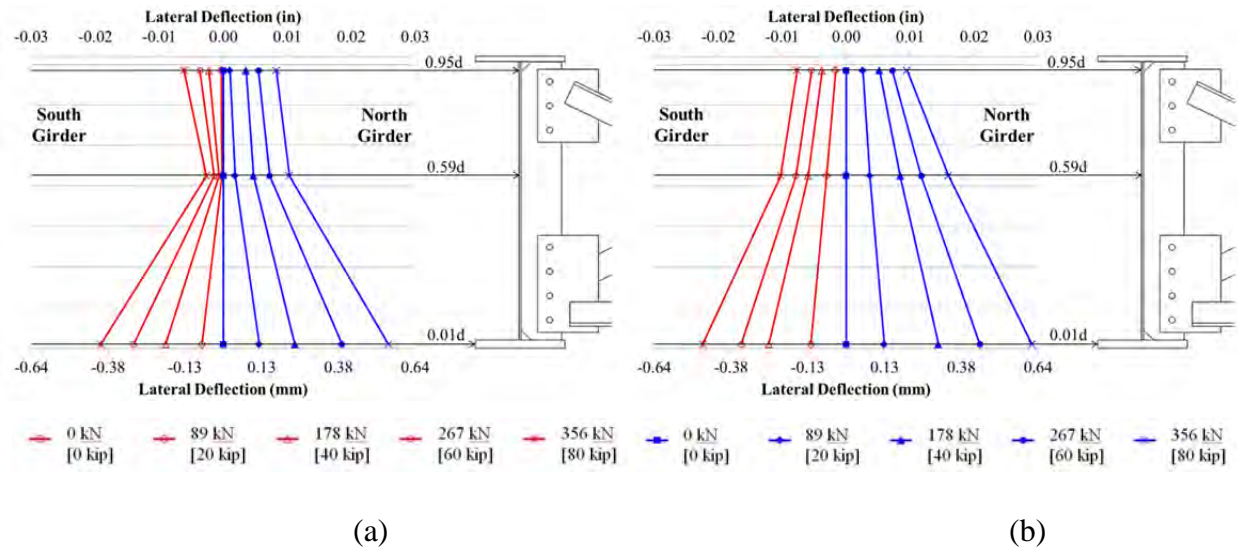
**Figure A.30: Girder lateral displacements at 150,000 cycles
(End of Trials 1S and 1N) For (a) Unretrofitted and (b) Retrofitted conditions**

Lateral girder deflections of the north girder were found to be similar in shape to those obtained from tests of the 2.8 m (9.3 ft.) girder sub-assemblies (see Appendix A.1). South girder deflections were found to behave a little differently than those from the north girder and the girder sub-assemblies tested. Between the top and middle LVDTs, the south girder hinges inward (less displacement) at mid-height while the north girder and component girders experienced increases in lateral displacement. The larger differential displacement between LVDTs placed at the top and mid-height of the south girder may have contributed to more significant crack growth around the connection plate-to-web weld as seen experimentally.

With the initial LVDT placements, little information could be inferred about the top web gap displacements; however, girder deflection was found to be nearly linear when the retrofit was applied [Figure A.30 (b)]. To gain greater information regarding web gap rotations, four string potentiometers replaced the existing three LVDTs. After 1.35 million cycles (end of Trials 2S and 2N), both pre- and post-retrofit girder lateral displacements can be seen in Figure A.31.
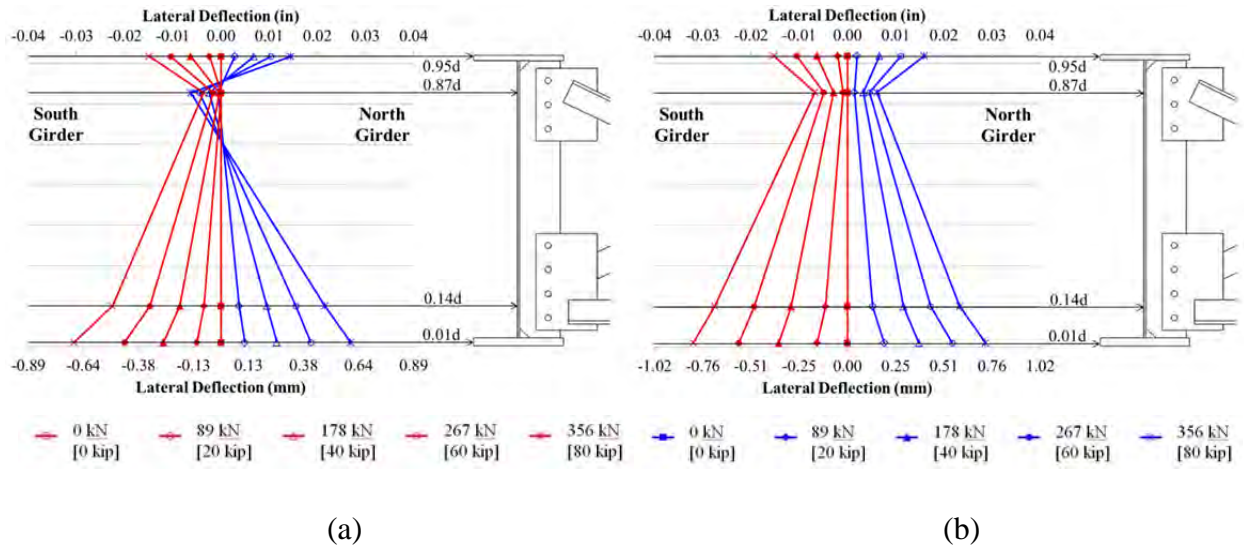
**Figure A.31: Girder lateral displacements at 1.35 Million cycles
for (a) Unretrofitted and (b) Retrofitted conditions**

Revised lateral displacement locations provided an improved description of girder deflections. Without retrofit, significant displacement reversal was found to occur in the top web gap [Figure A.31 (a)] of the north and south girders. Once the retrofit was applied, this reversal was significantly reduced while lateral displacements of girder flanges remained nearly constant. Since web gap rotation is considered to be a driving factor (Jajich and Schultz 2003) in distortion-induced fatigue cracking, reducing web gap rotation was anticipated to reduce fatigue susceptibility.

A.3.6.3   Crack Initiation and Propagation

Crack propagation was of particular importance to the investigators since the primary method for establishing retrofit effectiveness is the ability of the retrofit to significantly slow or halt crack growth. Initially, bondable strain gages placed in the top web gaps on the north and south girders were used to identify potential crack initiation. After initiation was visually confirmed, crack propagation was monitored and charted while the girder was in the unretrofitted condition. Crack lengths were also monitored before and after retrofit applications, providing information regarding crack propagation under the application of the retrofits. Due to the large loads placed on the bridge, change in crack propagation rate was of particular interest. In the following sections crack initiation and propagation have been explained in detail.

72

A.3.6.3.1   Crack Initiation

At the beginning of the test sequence (Trials 1S and 1N), the uncracked, unretrofitted test bridge was cycled between 27-267 kN (6-60 kip) at a frequency of 1 Hz. Visual crack inspections were performed every 5,000 cycles while static data from all instrumentation was recorded every 15,000 cycles. Strain gages placed on the fascia side of the north girder [Gage 3 in Figure A.27 (b)] indicated potential cracking at 15,000 cycles. Figure A.31 displays the increase in strain from -950 $\mu\varepsilon$ to -1225 $\mu\varepsilon$ experienced by the gage of interest.

(a)   (b)
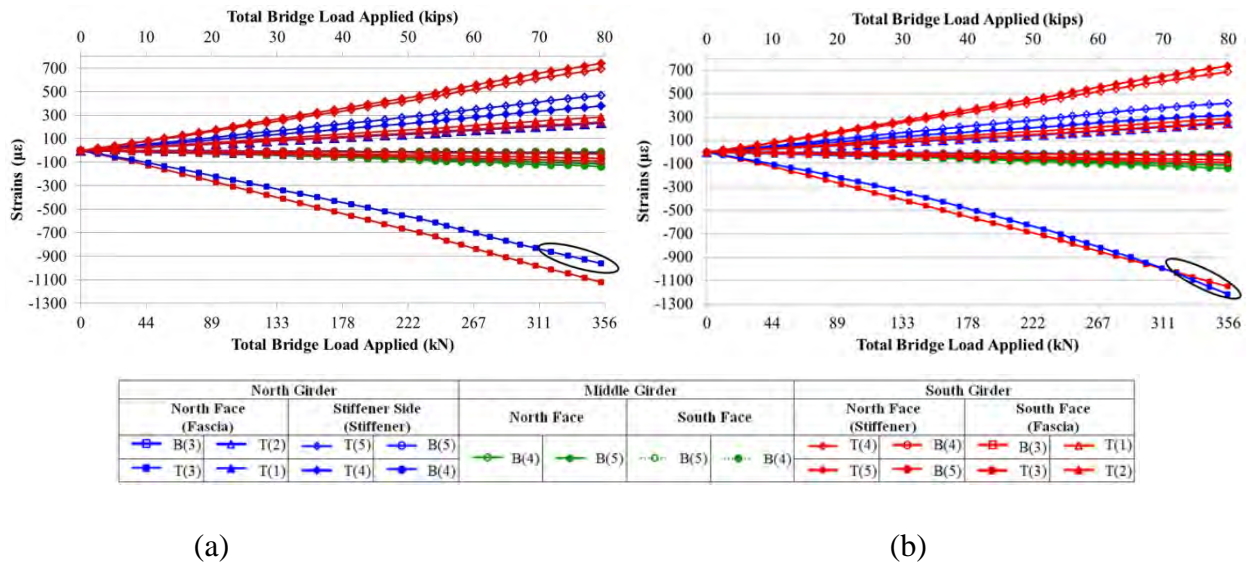
(Top Web Gap Denoted by T in Legend and Bottom Web Gap Denoted By B. Number Denotes Gage Location from Figure A.27(c).)

**Figure A.31: Strains in top web gaps
at (a) 0 cycles and (b) 15,000 cycles**

Although strain gages indicated potential cracking on the north girder, physical inspection found no visible cracking at that point; however, at 20,000 cycles (just 5,000 additional cycles) cracking was visually identified at the connection plate-to-web weld in the north girder. This indicated excellent agreement between the two crack indication / inspection techniques.

A.3.6.3.2   Crack Propagation Pattern

In Trials 1S and 1N, cracking initiated at the weld near the clip in the transverse connection plate. Cracking progressed diagonally down through the weld until reaching the girder web.

73

During Trial 1S, cracking progressed down the weld toe in the south girder until branching out into a spider crack. These spider cracks propagated outward away from the transverse connection plate. On the left side of the transverse connection plate, cracking also progressed down web at the weld toe. North girder cracking progressed slightly differently, in that cracks did not propagate into the web until Trial 2N and did not follow the weld toe. Longitudinal cracks at the flange-web weld were found in Trials 6N and 6S. The point of initiation was unclear for the longitudinal cracking, since the north girder longitudinal cracks were significantly large when discovered at the end of Trial 6N. Table A.9 shows the cracking patterns at the end of Trials 6S and 6N.

Table A.9: Cracking at End of Trial 6 (6,011,097 Cycles)

Left Side of Connection Plate	Right Side of Connection Plate

South Girder

(East)   (West)

North Girder

(West)

(East)
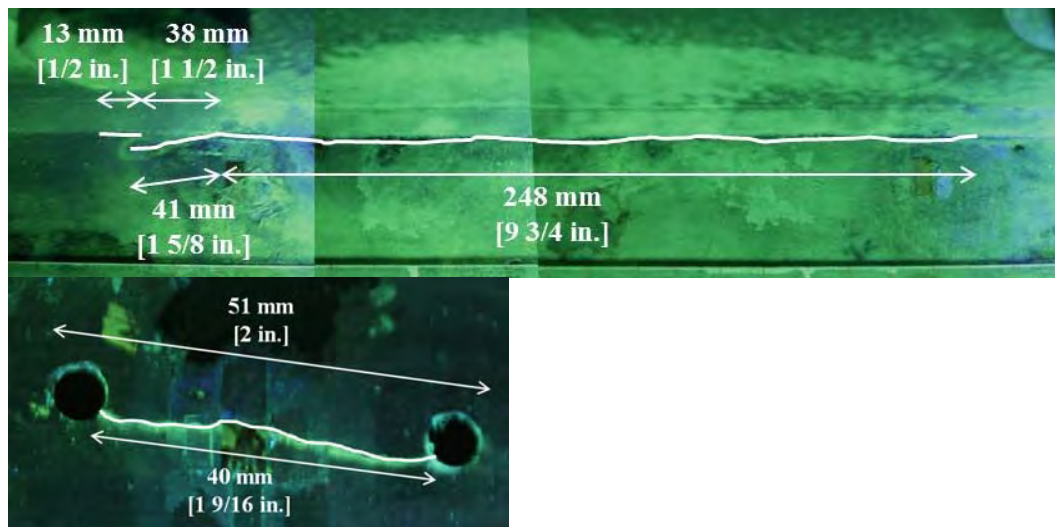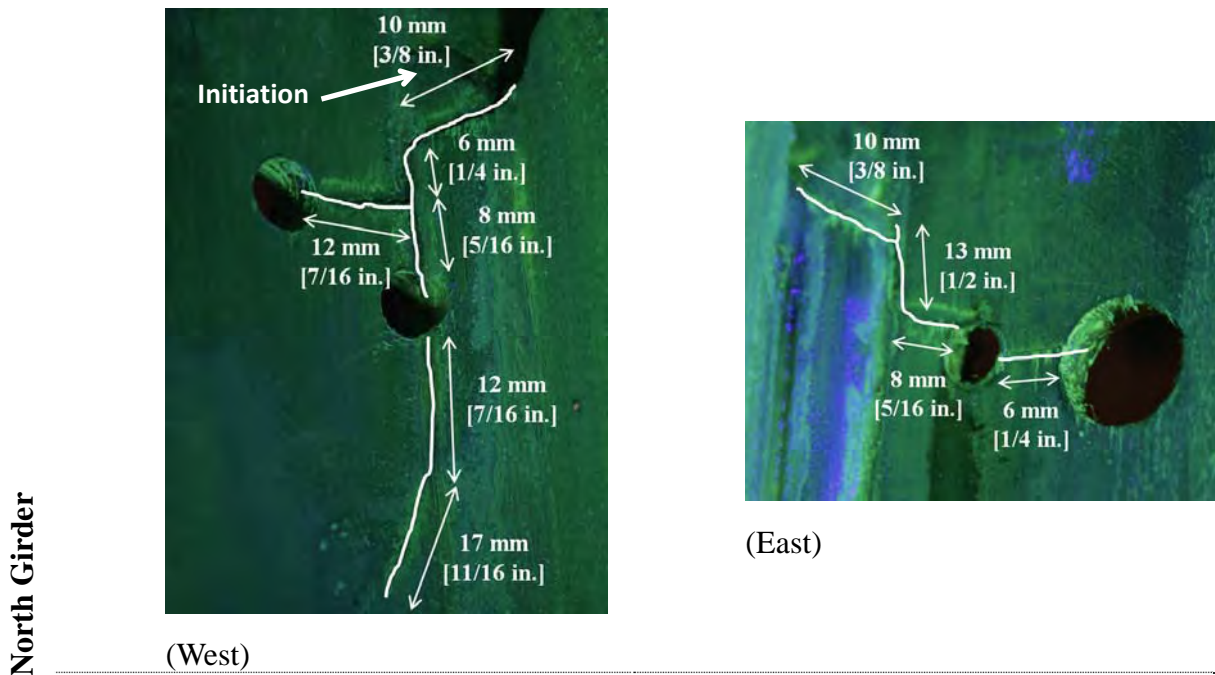
A.3.6.3.3   Trials 1N-6N Crack Growth (North Girder Test Trials)

Crack length is plotted against the total fatigue cycles as shown in Figure A.32. The cracks were each categorized as vertical cracks, spider cracks, through cracks, or longitudinal

cracks. When holes were drilled at crack tips, an instantaneous jump occurred in the graph that is not connected by a line. For locations where a crack grew into an existing crack-arrest hole, only the crack propagation was plotted. As shown in Figure A.32, an instantaneous jump at the end of that test trial is shown with a solid line to denote the difference between drilling a crack-arrest hole and propagating into a pre-existing hole.

Crack Growth - North Girder
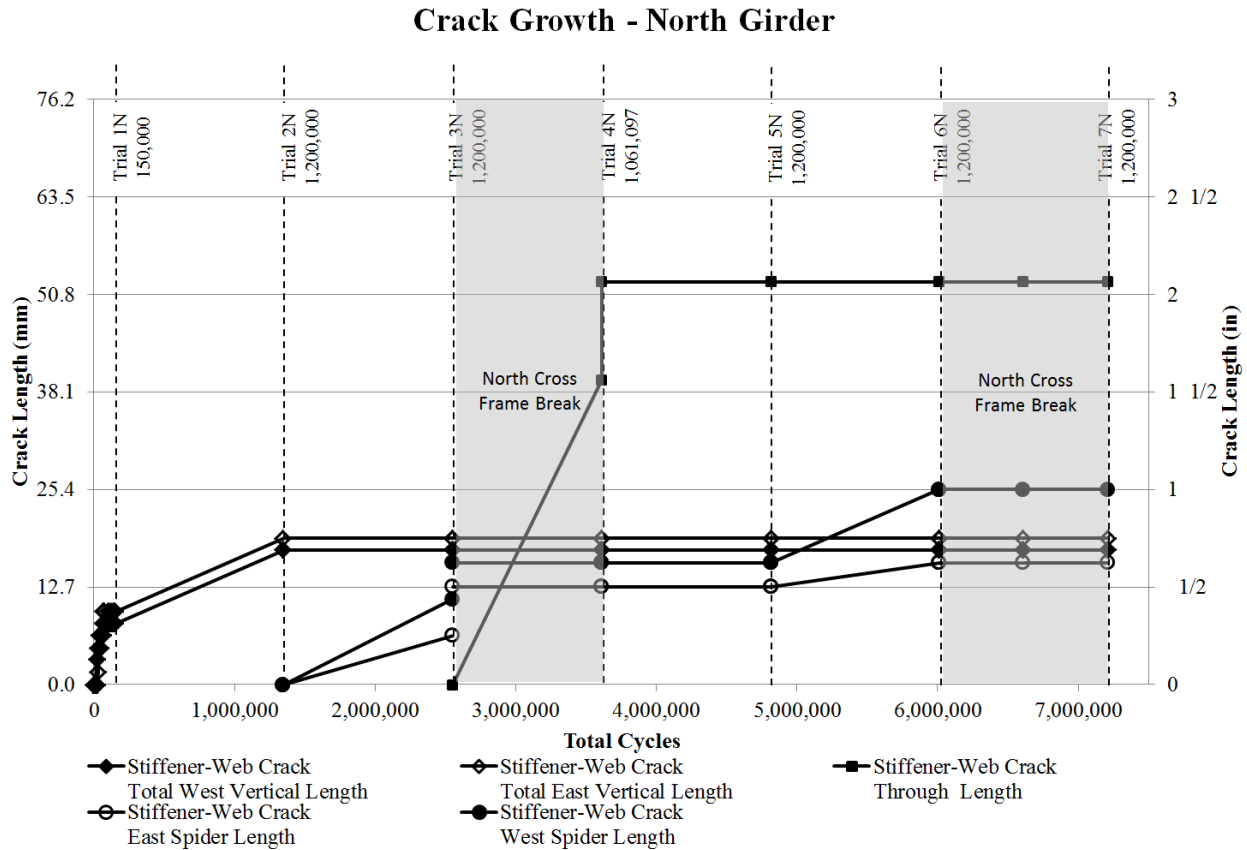
Figure A.32: North girder crack growth around transverse connection plate

Cracking initiated in the north girder at approximately 20,000 cycles during Trial 1N. During Trial 1N, cracking in the north girder reached length of 8 mm ($^5/_{16}$ in.) on the left side (west) and 10 mm ($^3/_8$ in.) on the right side (east) of the transverse connection plate. Both cracks propagated diagonally downward through the weld throat, but did not propagate out into the web. Cracking in the north girder stabilized around 65,000 cycles with no further growth during Trial 1N.

With the angles-with-plate retrofit in place during Trial 2N, north girder cracking lengthened under the retrofit application. Based on the work detailed in Appendix A.1 and A.2 and a detailed finite element study of the 9.1 m (30 ft.) test bridge (presented in Appendix A.4) it is postulated that in this extreme situation where the stress demands are high for a small crack, small amounts of propagation may occur under the retrofit; however, as cracking propagates, this high stress decreases and cracking will slow. Additionally, the load range utilized during testing of the model bridge is greater than would normally be withstood in field applications.

During Trial 3N, cracks again propagated in the north girder. At this point, cracking progressed into the web in the form of a spider crack. Spider crack length out into the web was measured to be 11 mm ($^7/_{16}$ in.) on the west side of the connection plate and 6 mm ($^1/_4$ in.) on the east side of the connection plate. Spider crack dimensions provided are in addition to the cracking that occurred through the weld, which is 18 mm ($^{11}/_{16}$ in.) long on the west side of the connection plate and 19 mm ($^3/_4$ in.) long on the east side of the connection plate.

Small crack arrest holes with a 6 mm ($^1/_4$ in.) diameter were drilled at the crack tips before the start of Trial 4N, and the angles-with-plate retrofit was reapplied and the load range was increased. Approximately 650,000 cycles into Trial 4N, a faint clicking noise was noticed originating from the connection plate in the north girder. After inspection of strain data, no significant change in bridge response was noticed. However, when the bridge was visually inspected at 1.06 million cycles into Trial 4N, the cross frame between the north and middle girders was found to be cracked completely through at the tab plate, as shown in Figure A.33.

Figure A.33: North cross frame failure during Trial 4N

During inspection, there was no evidence of fretting due to the angle-with-plate retrofit. Measured strains in the cross frame element prior to fracture were approximately 375 µε, which, based on modulus of elasticity for steel of 200 GPa (29,000 ksi), correlated with an approximate stress of 75 MPa (11 ksi). It is estimated that the crack started at the bottom corner of the weld toe where the cross frame diagonal member (AT) framed into the tab plate.

Due to the cross frame member failure (member AT) during Trial 4N, the angles-with-plate retrofit was removed and a detailed inspection was performed for the entire test bridge. After inspection, it was noticed that the north girder through-crack developed between the two 6 mm ($^1/_4$ in.) diameter crack-arrest holes. However, the spider cracking had not progressed through the crack arrest holes.

Due to the cross frame failure experienced in Trial 4N, Trial 5N was performed as a repeat of Trial 4N. No crack propagation was experienced during Trial 5N; however, at the end of Trial 6N in which the load was increased, a 298 mm (11 $^3/_4$ in.) longitudinal crack was discovered at the top flange-to-web weld. Prior to Trial 6N inspection, the last inspection was performed at the end of Trial 5N. At this time, no longitudinal crack was reported; however, ridges at the weld toe and very small crack opening displacements impeded crack detection. It should be noted that the loading applied during Trial 6N was expected to be much larger than

78

typical fatigue bridge loading. Due to this, the final trials were believed to have pushed this specimen well beyond most practical applications.

Prior to the start of Trial 7N, 19 mm ($^3/_4$ in.) crack arrest holes were drilled at the crack tips of the 298 mm (11 $^3/_4$ in.) longitudinal crack at the top flange-to-web weld and a stiffened version of the angles-with-plate retrofit was applied. Approximately 150,000 cycles into Trial 7N, the longitudinal crack grew past the crack arrest hole on the west side of the retrofit. An additional 19 mm ($^3/_4$ in.) crack arrest hole was drilled at the tip of the crack. As testing continued, the crack again grew past the additional crack arrest hole. It was decided that the crack was growing too rapidly and crack arrest holes would not contain the longitudinal crack growth at this level of loading. Instead of continuing to drill crack arrest holes, the longitudinal crack at the top flange-to-web weld was welded 300,000 cycles into Test Trial 7N. It was recognized that this impeded the results from Trial 7N, and it should be noted that the welding of the flange-to-web weld crack was performed so that testing on the south girder could continue.

Approximately 1.19 million cycles into Trial 7N, a clicking noise was noticed originating from the center girder. Upon inspection after the trial was completed, it was discovered that the cross frame between the north and middle girders cracked completely through the bottom horizontal angle. The crack occurred on the end of the angle nearest to the middle girder.

A.3.6.4 Trials 1S-6S Crack Growth (South Girder Test Trials)

Cracking experienced around the transverse connection plate in the south girder is shown in Figure A.34. The same crack definitions were applied as those used in the north girder as described in the previous section. Drilled holes are denoted by an instantaneous jump with no line, and cracks that propagated into an existing hole were denoted by an instantaneous jump with a connecting solid line.

Figure A.34: South girder crack growth around transverse connection plate

Cracking in the south girder initiated during Trial 1S at 30,000 cycles in the unretrofitted condition, approximately 10,000 cycles after north girder cracking initiated. South girder cracking propagated through the weld and into the web at a steady rate until about 75,000 cycles. At this time, vertical cracking down the weld toe slowed. The first evidence of spider cracking began at 105,000 cycles. Between 105,000 and 120,000 cycles, the spider cracking propagated through the web, debonding the strain gage (3) on the fascia side of the south girder. This crack initiation was hidden behind the bonded gage and was first noticed at 150,000 cycles. During Trial 1S, a maximum crack length of 25 mm (1 in.) was reached by the vertical cracking on the left side of the connection plate and also in the through-crack length.

During Trial 2S, under application of the angles-with-plate retrofit, cracking on the interior face of the girder did not change; however, fascia cracking increased by a length 6 mm ($^1/_4$ in.). This crack was formed as a through-thickness crack from the spider cracking seen on the

interior side of the girder. The total length of the crack seen on the fascia side was 35 mm (1 $^3/_8$ in.) which correlated with the total projected crack length on the interior side of the girder including the spider crack length (9.5 mm + 6 mm [$^3/_8$ in. + $^1/_4$ in.]), connection plate width (9.5 mm [$^3/_8$ in.]), and weld width (9.5 mm [$^3/_8$ in.]). It is believed that the change in the fascia girder crack length can be attributed to the existing interior crack propagating through the thickness of the girder.

Trial 3S resulted in crack propagation. Spider cracking reached 11 mm ($^7/_{16}$ in.) on the east side of the connection plate and 10 mm ($^3/_8$ in.) on the west side of the connection plate. Vertical cracking on the east side of the connection plate did not propagate during Trial 3S. Through-crack length increased by 5 mm ($^3/_{16}$ in.). At the end of Trial 3S, 6 mm ($^1/_4$ in.) diameter crack arrest holes were drilled at the crack tips of the spider cracks and the vertical crack in the south girder.

Trial 4S, was halted due to north cross frame failure as discussed previously. At the end of Trial 4S, minimal crack growth was seen in the through-web crack on the south girder, while the spider crack on the right side (west side) of the south girder grew through the 6 mm ($^1/_4$ in.) diameter crack stop hole. At the tip of this extended crack, a 13 mm (1/2 in.) diameter hole was drilled for the start of Trial 5S.

Similar to behavior observed in the north girder, cracking did not propagate under the angles-with-plate retrofit during Trial 5S. Increasing the load during Trial 6S resulted in some crack growth. Along the connection plate-web weld, cracking grew down vertically through the 6 mm (1/4 in.) crack stop hole as seen in Table A.9 . Careful inspection of the flange-to-web weld resulted in confirmation of a longitudinal crack detected with 29 mm (1 $^1/_8$ in.) length on the connection plate side of the web. As with the north girder, loading during this test cycle was larger than expected fatigue loading.

Prior to the start of Trial 7S, 19 mm ($^3/_4$ in.) crack arrest holes were drilled as close as possible to the crack tips of the 29 mm (1 $^1/_8$ in.) longitudinal crack at the top flange-to-web weld and the stiffened version of the angles-with-plate retrofit was applied. Due to the size of the crack and its location above the connection plate in the top web gap, it was not possible to drill the crack arrest holes exactly at the crack tips. It was assumed that if the crack grew, it would

grow to the crack arrest holes. Upon completion of Trial 7S, no visual cracking was detected in the longitudinal crack at the top flange-to-web weld. Minimal crack growth occurred in the stiffer-web crack spider I length between crack arrest holes on the fascia side of the south girder.

A.3.7 Conclusions

The objective of this study was to determine the effectiveness of the angles-with-plate retrofit for reducing distortion-induced fatigue propensity when applied to a steel test bridge that included in-plane bending effects as well as out-of-plane effects. The research team's conclusions are as follows:

- Cross frame members framing into the top web gap experienced an increase in tensile strain of more than 50% when the angles-with-backing plate retrofit was applied to a cracked specimen as compared with an unretrofitted cracked specimen. Application of the angles-with-plate retrofit allows more force to be transferred into the web as compared with an unretrofitted condition. Since crack growth was slowed when retrofitted, the angles-with-plate retrofit combats distortion-induced fatigue cracking even though additional force is being transferred into the web.

- Strain gages placed on the opposing web face at the web gap location were found to be good tools with which to detect crack initiation in the web gap region. Significant changes in strain were noticeable just prior to visibly-detectable cracking in the web gap region.

- Measurements taken with LVDTs and string potentiometers showed that out-of-plane web gap rotations were significantly decreased after top web gaps were retrofitted using the angles-with-plates technique, indicating a lower distortion-induced fatigue demand on the web gap region.

- When the angles-with-plate retrofit was applied over top web gap regions with existing sharp cracks, crack growth was significantly slowed. Maximum unretrofitted growth was 25 mm (1 in.) over 150,000 cycles at 27-267 kN (6-60 kip) load while maximum retrofitted growth was 11 mm (7/16 in.) over 1,200,000 cycles at 36-356 kN (8-80 kip) load.

- When the angles-with-plate retrofit was applied over top web gap regions with cracks that had been modified with small crack-arrest holes drilled at the crack tips, crack growth was halted under 44-445 kN (10-100 kip)

loading with a maximum longitudinal bending stress due to fatigue of 48.3 MPa (7.0 ksi).

Given the widespread nature of distortion-induced fatigue in existing steel bridge infrastructure, identification of effective, practical, and inexpensive retrofit techniques are in great demand. The angles-with-plate retrofit tested in a large-scale bridge test set-up under demanding cyclic loads exhibited excellent levels of fatigue crack retardation. The angle-with-plate retrofit is an important development in this area, as it does not require deck removal or flange attachment. Development of this retrofit technique has the potential to greatly streamline the process of repairing steel bridges susceptible to distortion-induced fatigue in a manner that is effective, economical, and easily implementable.

A.3.8 References

Alemdar, F., Nagati, D., Matamoros, A., Bennett, C., and Rolfe, S. (2013a). "Repairing Distortion-Induced Fatigue Cracks in Steel Bridge Girders using Angles-with-Plate Retrofit Technique, Part I: Physical Simulations." *Journal of Structural Engineering*, ASCE, In Press.

Alemdar, F., Overman, T., Matamoros, A., Bennett, C., and Rolfe, S. (2013b). "Repairing Distortion-Induced Fatigue Cracks in Steel Bridge Girders using Angles-with-Plate Retrofit Technique, Part II: Computer Simulations." *Journal of Structural Engineering*, ASCE, In Press.

American Iron and Steel Institute (AISI) Example 1: Simple-Span Composite I Girder (1997). American Iron and Steel Institute, Washington, D.C.

Connor, R. J. and Fisher, J. W. (2006). "Identifying Effective and Ineffective Retrofits for Distortion Fatigue Cracking in Steel Bridges Using Field Instrumentation." *Journal of Bridge Engineering,* 11(6), 745-752.

Fisher, J. W., Jian, J., Wagner, D. C., and Yen, B. T. (1990). *Distortion-Induced Fatigue Cracking in Steel Bridges*. NCHRP Report 336. Transportation Research Board, National Research Council, Washington, D.C.

Fisher, J. W. and Keating, P. B. (1989). "Distortion-Induced Fatigue Cracking of Bridge Details with Web-gaps." *Journal of Constructional Steel Research,* 12(3-4), 215-228.

Grondin, G. Y., Fraser, R., and D'Andrea, M. (2002). "Testing and Evaluation of Fatigue Damaged Girders." *4th Structural Specialty Conference.* Canadian Society for Civil Engineering, Montreal, Quebec.

Hassel, H., Hartman, A., Bennett, C., Matamoros, A., and Rolfe, S. (2010). "Distortion-Induced Fatigue in Steel Bridges: Causes, Parameters, and Fixes." *2010 ASCE/SEI Structures Congress Proceedings,* 471-483.

Jajich, D. and Schultz, A. E. (2003). "Measurement and Analysis of Distortion-Induced Fatigue in Multigirder Steel Bridges." *Journal of Bridge Engineering*, 8(2), 84-91.

Nagati, D. (2012). *Repair of Steel Bridge Girders Damaged by Distortion-Induced Fatigue.* (Master's thesis). University of Kansas, Lawrence, KS.

Overman, T. (2012). *Analytical Investigation of Repair Methods for Fatigue Cracks in Steel Bridges*. (Master's thesis). University of Kansas, Lawrence, KS.

Przywara, J. (2013). *Applications of the Extended Finite Element Method (XFEM) for the Analysis of Distortion-Induced Fatigue Cracking in Highway Bridge Girders*. (Master's thesis). University of Kansas, Lawrence, KS.

Roddis, W. M. K. and Zhao, Y. (2001). "Out-of-Plane Fatigue Cracking in Welded Steel Bridges: Why It Happened and How It Can Be Repaired." *Welding Innovation*, 18(2), 2-7.

Roddis, W. M. K. and Zhao, Y. (2003). "Finite-Element Analysis of Steel Bridge Distortion-Induced Fatigue." *Journal of Bridge Engineering*, 8(5), 259-266.

Tedesco, J. W., Stallings, J. M., and Tow, D. R. (1995). "Finite Element Method Analysis of Bridge Girder-Diaphragm Interaction." *Computers and Structures*, 56(2-3), 461-473.

Appendices A.4: Parametric Analysis of a Retrofit for Distortion-Induced Fatigue in a 9.1 m (30 ft.) Test Bridge

Amanda S. Hartman[16]

Caroline R. Bennett[17]

Adolfo B. Matamoros[18]

Stanley T. Rolfe[19]

A.4.1 Abstract

Developing and testing retrofit techniques to halt distortion-induced fatigue cracking of steel bridge structures can be time consuming and expensive. Finite element modeling is a tool that can be used to reduce the expenses associated with testing such retrofits. In this study, the effectiveness of several existing retrofit techniques was examined for the 9.1 m (30 ft.) test bridge to form a series of baseline values against which to evaluate several variations of the "angles-with-plate" retrofit technique developed and investigated as part of TPF-5(189).

Existing techniques investigated included a full depth back-up stiffener as well as bolted angles providing positive attachment from the connection plate to the girder flange. The research team developed "angles-with-plate" technique uses two angles and a backing plate attached to the girder web (called angles-with-backing plate retrofit). Through finite element modeling, three variations of the angles-with-backing plate retrofit were investigated in which the thickness was adjusted and stiffeners were added to the angles.

During the investigation, two crack patterns were studied with several crack lengths ranging from 25 mm (1 in.) to 203 mm (8 in.). Cracking studied included a horseshoe crack around the connection plate-web weld and a longitudinal crack at the flange-web weld. For the connection plate-web weld, the stiffened angles-with-backing plate provided the largest stress

---

[16] Amanda S. Hartman, PhD, Structural Engineer, Burns and McDonnell, 9400 Ward Pkwy, Kansas City, MO 64114

[17] Caroline R. Bennett, PhD, PE, Associate Professor, University of Kansas, 1530 W. 15th St., Lawrence, KS 66045

[18] Adolfo B. Matamoros, PhD, Professor, University of Kansas, 1530 W. 15th St., Lawrence, KS 66045

[19] Stanley T. Rolfe, PhD, PE, A.P. Learned Distinguished Professor, University of Kansas, 1530 W. 15th St., Lawrence, KS 66045

reduction; however, for the flange-web weld, angles providing positive attachment to the girder flange reduced the stress the most.

A.4.2 Introduction and Background

Many steel bridges built prior to the mid-1980s have experienced distortion-induced fatigue caused by lack of positive connection between connection stiffeners and girder flanges. As differential deflection occurs between adjacent bridge girders, the flexible web gap region experiences repeated out-of-plane rotation which causes fatigue. Several methods have been used to mitigate distortion-induced fatigue cracking including: crack arrest holes, cross frame removal, back-up stiffeners, positive attachment between transverse connection stiffeners and flanges, and slotting the transverse connection stiffener discussed in more detail in Appendix D.

In addition to repair techniques currently in practice, the University of Kansas has developed a new retrofit technique which provides additional positive attachment between the transverse connection stiffener and girder web under TPF-5(189). This technique is termed the "angles-with-plate" retrofit. This retrofit has been shown in previous studies to mitigate crack propagation in a 2.8 m (9.3 ft) girder sub-assembly (see Appendix A.1 and A.2). However, the physical and computational simulations conducted in the girder sub-assembly set-up were representative of a test set-up in which the girder was only subjected to out-of-plane bending effects.

Extensive finite element analyses of these retrofit techniques (of both the more traditional techniques and the newly-developed "angles-with-plate" technique) have been conducted under TPF-5(189). Hassel et al. (2010) used Abaqus v.6.8-2 in which full-scale non-skewed and skewed bridges were evaluated with the following techniques: cross frame removal, back-up stiffeners, positive attachment between connection plates and flanges (using two angles), and slotting the connection plate (described in Appendix D). When the retrofits were applied at every cross-frame location (excluding cross-frame removal), positive attachment between connection plates and flanges were found to provide the largest reduction in stress around the connection plate-to-web weld. However, this study failed to consider hot spot stresses at the flange-to-web weld. Additionally, the newly-developed angles-with-plate retrofit technique was not analyzed in the bridge models studied by Hassel et al. (2010).

In a separate investigation, a series of computational and physical studies were performed aimed at evaluating the performance of the angles-with-plate retrofit when applied on a 2.8 m (9 ft.) long steel girder sub-assembly (see Appendix A.1 and A.2). This assembly was comprised of a girder segment oriented upside-down with the top flange attached to the concrete strong floor. An upward force was applied to the cross frame to imitate an adjacent girder deflecting downward in a real bridge. At the ends of the 2.8 m (9.3 ft.) girder segment, small angles were attached to the flange that was not connected to the laboratory floor at one end, and at the load frame at the other end. This was intended to simulate, in an admittedly rudimentary fashion, the out-of-plane restraint provided by longitudinal girder continuity in a real bridge system as shown in Figure A.35.
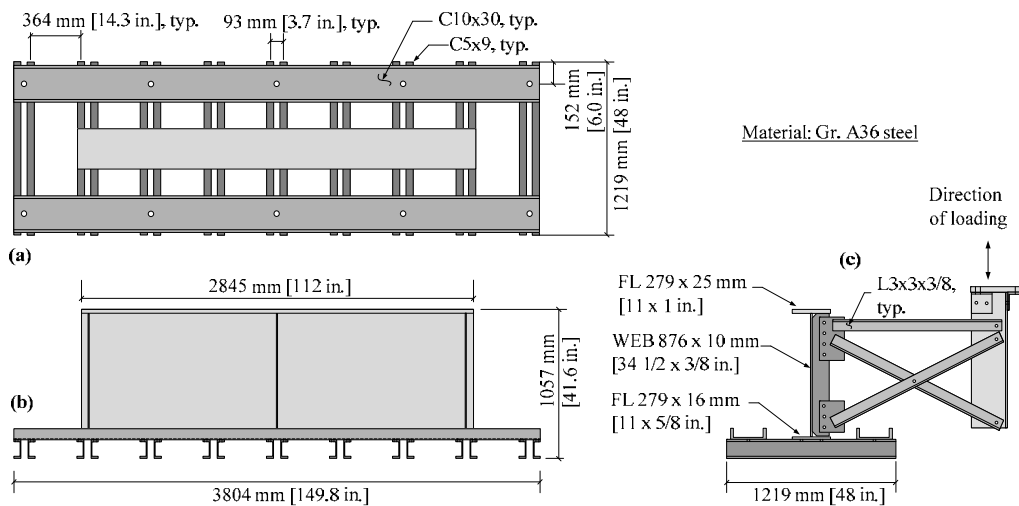
Figure A.35: Girder sub-assembly set-up for 2.8 m (9 ft.) testing and finite element modeling
(See Appendix A.1 and A.2)

In the test set-up, the girder flange connected to the concrete floor was intended to represent the top flange in a real bridge that exhibits no flange rotation (e.g. an extremely stiff concrete deck). Finite element modeling followed the actual sub-girder assembly closely, including the flange restraint mechanism.

In a computational parametric study described in Appendix A.2, the angles-with-plate retrofit and set-up described in Appendix A.1 was studied extensively by varying angle and plate thicknesses. Thickness variations considered for the angle and plate elements included: 6 mm ($^1/_4$

87

in.), 13 mm ($^1/_2$ in.), and 25 mm (1 in.). With a web thickness of 9.5 mm ($^3/_8$ in.), retrofit-to-web thickness ratios of 0.7, 1.3, and 2.7 were examined (see Appendix A.2). For both the flange-to-web weld [Hot Spot Stress Path 2 (HSS2)] and the connection plate-to-web weld [Hot Spot Stress Path 1 (HSS1)], stresses were generally found to increase up to a certain crack length (approximately 50 mm [2 in.]) and then decrease, as shown in Figure A.36. The exception to this was for HSS1 under the stiff-stiff version of the retrofit, which saw minor decreases in stress as crack length increased. Retrofit results are shown for stiff (S-S) angles-with-plate (25 mm [1 in.] thick) and flexible (F-F) angles-with-plate (6 mm [$^1/_4$ in.] thick) combinations.
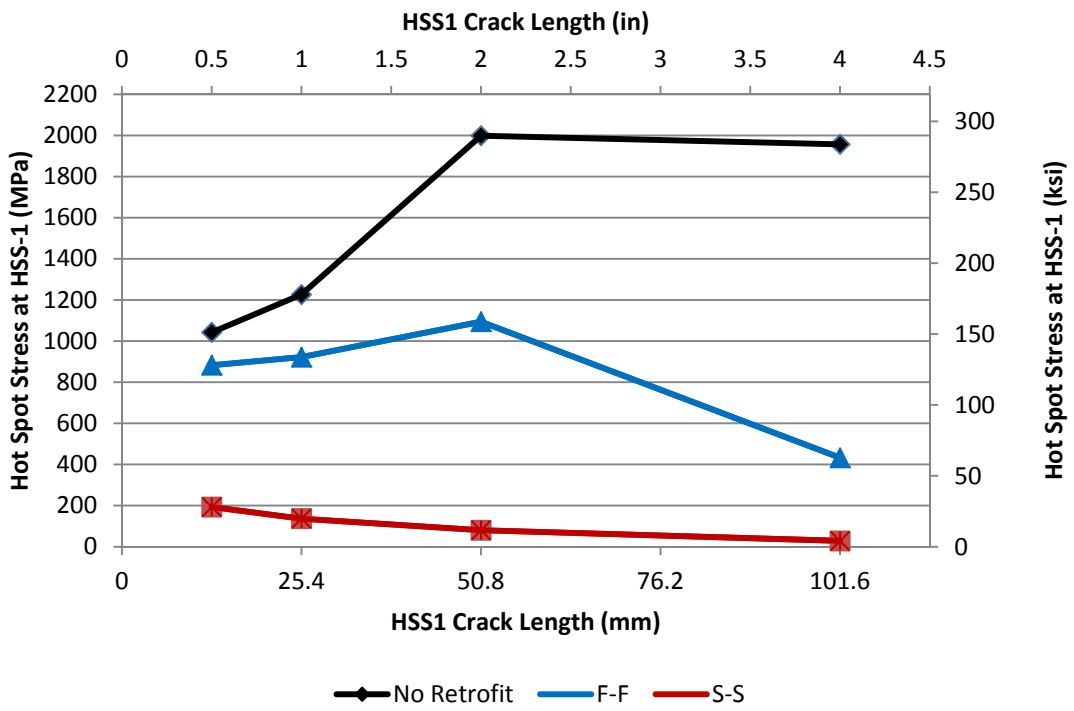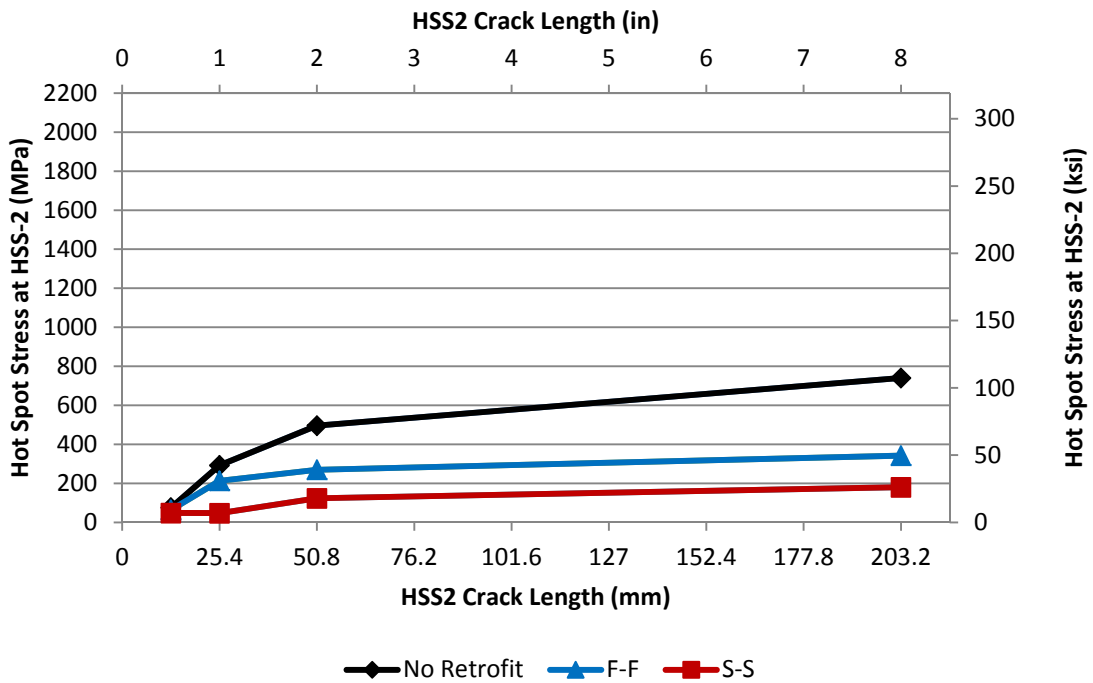
**Figure A.36: Hot Spot Stress
at (a) HSS1 crack and (b) HSS2 crack for no retrofit, F-F retrofit, and S-S retrofit**

The findings described in Appendix A.2 showed that the angles-with-plate retrofit was sensitive to crack type (connection plate-to-web-weld vs. web-to-flange weld), crack length, and retrofit stiffness. It was recommended that stiff versions of the angles-with-plate retrofit be used to achieve optimal performance of the retrofit, regardless of crack length.

Based on the analyses and physical testing outlined in Appendix A.2, it was found that the angles-with-plate measure was effective in preventing distortion of the web gap region, reducing stress demands calculated at the critical points by an order of magnitude. Additionally, experimental testing showed that there was negligible crack growth when the angles-with-plate retrofit measure was implemented in demanding fatigue tests.

A.4.3 Objective and Scope

The primary objective of this study was to analytically evaluate the effectiveness of the new "angles-with-plate" retrofit technique on a 9.1 m (30 ft.) bridge system subjected to both in-plane and out-of-plane bending effects as compared with existing retrofit techniques. The effects crack length on the effectiveness of the angles-with-plate retrofit was investigated, as was the effect of reduced deck stiffness.

The computational simulations presented in this paper corresponded to an experimental test set-up in which a three-girder, 9.1 m (30 ft) long test bridge was tested under fatigue loading. Details regarding the physical tests of the test bridge have been presented in a companion paper (see Appendix A.3).

A.4.4 Finite Element Modeling Methodology

The test bridge geometry described in Appendix A.3 was modeled as faithfully as possible using the commercially-available software Abaqus v.6.10. Screenshots from the bridge model are shown in Figure A.37.
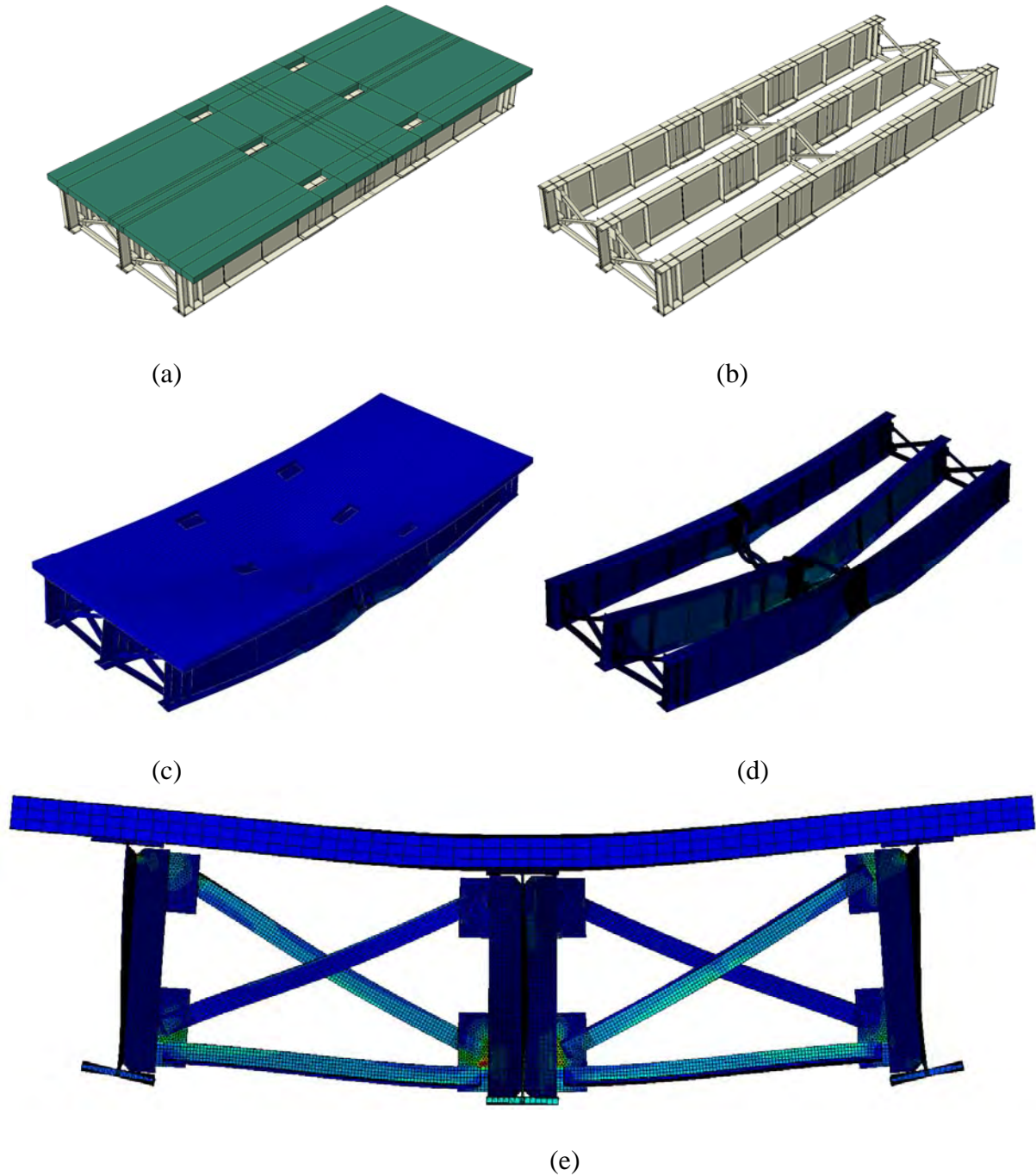
**Figure A.37: Models
(a) Overall model with concrete deck, (b) Overall model without concrete deck, (c) Deflected model with concrete deck, deflection scale=425, (d) Deflected model without concrete deck, deflection scale=425, and (e) Deflected section cut at mid-span, Deflection scale=100.**

Forty-five finite element models were constructed and analyzed as variations of the baseline test bridge geometry. Models included cracked and uncracked conditions in the top web

gap of the exterior (north and south) girders. Cracked models included either a horseshoe-shaped crack or a longitudinal crack. A modeling test matrix is shown in Table A.10.

Table A.10: Finite Element Modeling Matrix for Cracks around Stiffener-Web-Weld

	Model Description / Crack Length	No Crack	25 mm (1 in.)	38 mm (1-1/2 in.)	51 mm (2 in.)	64 mm (2-1/2 in.)	76 mm (3 in.)	101 mm (4 in.)	203 mm (8 in.)
Connection Plate-to-Web Cracks	Unretrofitted condition	X	X	X	X	X	X	X	X
	Reduced deck stiffness with unretrofitted condition				X				
	Broken Cross Frame		X						
	Angles-with-plate repair with 19 mm (3/4 in.) thicknesses		X	X	X	X	X		
	Stiffened angles-with-plate repair with 19 mm (3/4 in.) thicknesses		X	X	X	X	X		
	Angles-with-plate repair with 13 mm (1/2 in.) thicknesses		X	X	X	X	X		
	Traditional angles repair connected to flange with 19 mm (3/4 in.) thickness		X	X	X	X	X		
	Back-up stiffener repair placed on fascia side		X	X	X	X	X		
Flange-to-Web Cracks	Unretrofitted Condition		X		X		X	X	X
	Angles-with-backing plate repair with 19 mm (3/4 in.) thicknesses		X		X		X	X	X

Horseshoe-shaped (U-shaped) cracks were modeled around the connection plate weld toe having leg lengths from 25.4 to 76.2 mm (1.0 to 3.0 in.) and the leg length of the crack was varied in 12.7 mm (0.5 in.) increments. Additionally, two cracks with leg lengths of 101 mm and 203 mm (4.0 in. and 8.0 in.) were also considered. Crack lengths correlated with the vertical

length of each leg of the crack. In separate analyses, longitudinal cracks were placed near the flange-to-web weld. Three longitudinal crack lengths were studied which included: 25 mm (1 in.), 51 mm (2 in.), and 76 mm (3 in.).

All bridge components were constructed in Abaqus v.6.10 using three dimensional elements including mostly hexahedral elements (C3D8R) and some tetrahedral elements (C3D4) for transition regions. Each model contained approximately 3 million elements and 10 million degrees of freedom. A dense mesh was applied to the web gap region while other locations within the bridge contained a coarser mesh as shown in Figure A.38(a). Based on a convergence study performed on the dense mesh region around the connection plate-web weld, the optimal mesh size of the web gap was determined to be 2.5 mm (0.1 in.) [Figure A.38 (b)].

(a)   (b)
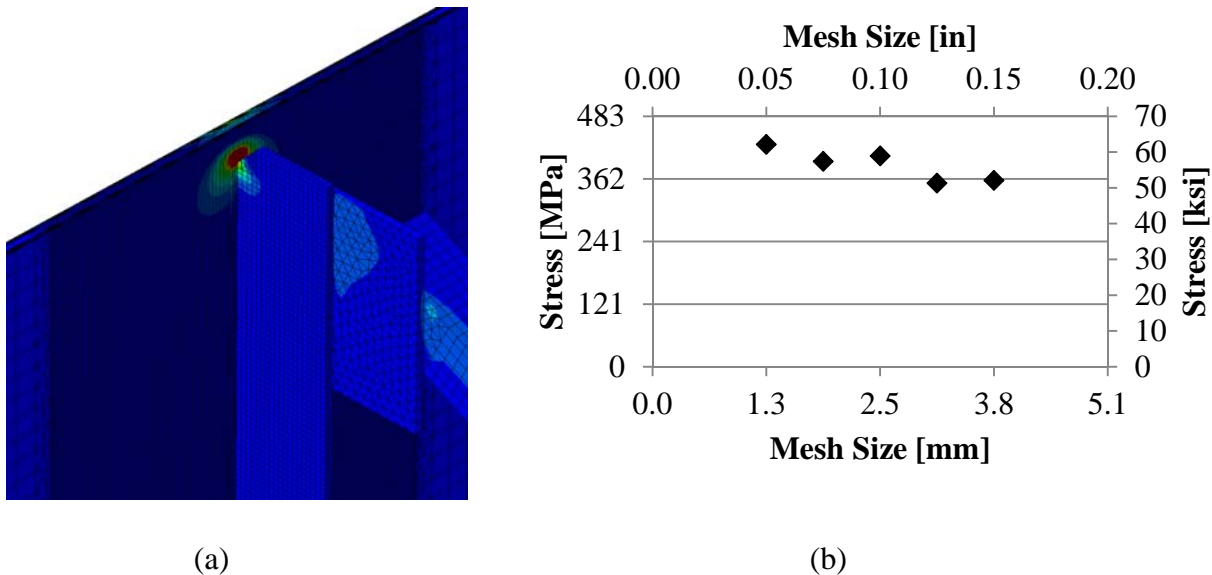
Figure A.38: Mesh
(a) Dense mesh (2.54 mm [0.1 in.]) in web gap region transitions to coarse mesh (25.4 mm [1.0 in.]) and (b) Mesh sensitivity study for changing dense region mesh

Steel and concrete were modeled as linear-elastic materials where the moduli of elasticity for each were taken as 200,000 MPa (29,000 ksi) and 25,000 MPa (3,605 ksi), respectively. Poisson's ratio for steel and concrete were assumed to be 0.3 and 0.2, respectively. For the reduced deck stiffness model, the concrete modulus of elasticity was halved. The entire 9.1 m (30 ft.) test bridge was modeled and assembled in Abaqus v.6.10 using 3D solid elements, including the welds, cross frames, stiffeners, and deck.

Since modeling bolts and bolt tension are computationally expensive endeavors, the base model of the test bridge contained surface-to-surface ties at girder splice locations and cross frame connections. Welds were attached to surfaces using surface-to-surface ties and when appropriate, hard contacts were used to prevent parts from moving through one another during loading.

Retrofitted models required further refinement with regard to bolting. To improve computational efficiency, modeled bolt heads and nuts were tied directly to the surfaces in which they were in contact. All other surfaces contained hard contact interactions with a frictional coefficient of 0.35. All bolts were modeled as 19 mm ($^3/_4$ in.) diameter which was consistent with those used in the physical tests. For models that included application of retrofits, behavior was desired that would replicate the slip-critical bolt conditions implemented in the physical tests. For the slip-critical connection, an initial bolt pretension step was created in the models that induced a bolt load of 125 kN (28 kip) on each bolt using the bolt load function in Abaqus v.6.10.

Static loading applied in the models correlated with the upper bound load of 267 kN (60 kip) from the first test trial in the physical test sequence (Test Trials 1S and 1N). In the models, this load was spread over two areas of 400 x114 mm (15$^3/_4$ x 4½ in.) to represent the application of the load through the two "feet" of the actuator's swivel end. Loading was applied at midspan of the center girder as was done in the physical tests. Due to this load placement, primary regions of interest were found to occur in the top web gaps of the exterior girders. This region of interest was consistent with previous research results obtained for an unstaggered bridge condition in which highest stresses were found to occur in top web gaps for exterior girders (see Appendix D.2) and with the physical test results described in Appendix A.2.

Cracks were modeled using the Extended Finite Element Method (XFEM) in Abaqus v.6.10. Using XFEM, cracks of various shapes could be easily modeled without affecting the mesh in the region of interest. Additionally, cracks could be placed anywhere within elements, not just located at element boundaries. U-shaped cracks (wrapping around the connection plate weld) and longitudinal cracks (along the flange-to-web weld) were modeled using three-dimensional planar elements with a depth larger than the girder web thickness of 6.35 mm ($^1/_4$ in.).

An identified limitation to using XFEM is that only two crack tips can exist for one crack. In experimental testing, cracks were found to often branch out into multiple "spider" cracks. This branching cannot be modeled using XFEM; however, even though branched cracks were found to exist experimentally, generally the vertical portion of the crack was observed to progress down the weld while the branch crack (spider crack) growth slowed (Nagati 2012). As discussed in the companion paper in Appendis A.3, only the east side of the south girder connection stiffener followed this pattern; however, cracking in the test bridge is relatively small [less than 51 mm (2 in.) in the horseshoe-shaped crack]. Due to this, spider cracks were not modeled as they were observed to only temporarily grow until stress concentrations at the weld became larger than the stress concentrations at the spider crack tip. The vertical crack that wrapped around the connection plate-to-web weld was referred to as a horseshoe-shaped crack. In addition to horseshoe-shaped cracking, a separate longitudinal crack was modeled near the flange-to-web weld.

A.4.4.1   *Computing Crack Propensity: Hot Spot Stress Analysis*

Traditionally, in-plane fatigue is classified using nominal stresses; however, the three-dimensional stress state in the web gap region cannot accurately be captured using only nominal bending stress. To capture both normal and out-of-plane stresses, maximum principle stresses were extracted from the models. As discussed in Appendix A.1 and A.2 of this report, it was found that crack growth closely followed maximum principal hot spot as shown in Figure A.39. White lines superimposed on the stress contours in Figure A.39 denote crack growth seen experimentally.
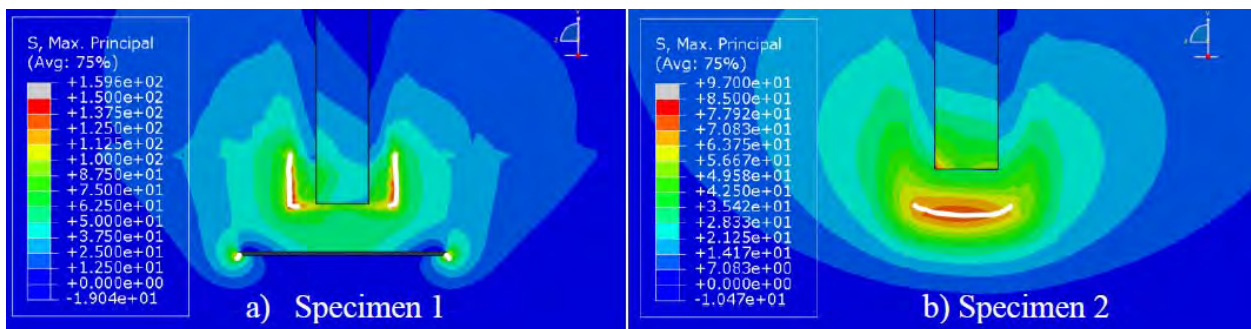
Source: Nagati 2012
Figure A.39: Cracking and maximum principal Hot Spot Stresses

Complicated geometry and stresses in the web gap region made performing accurate comparisons between models a difficult task. A one-point hot spot stress (HSS) procedure was used as the basis for this comparison in which stresses were extracted at a set distance (half the web thickness, 3 mm [$^1/_8$ in.]) from the discontinuity, either a weld or crack. This procedure has been found to be less sensitive to mesh density than extracting maximum stress from the models (Adams 2009). Two hot spot stress paths were chosen for consideration as shown in Figure A.40.

<table>
<tr><td>(a)</td><td>(b)</td></tr>
</table>
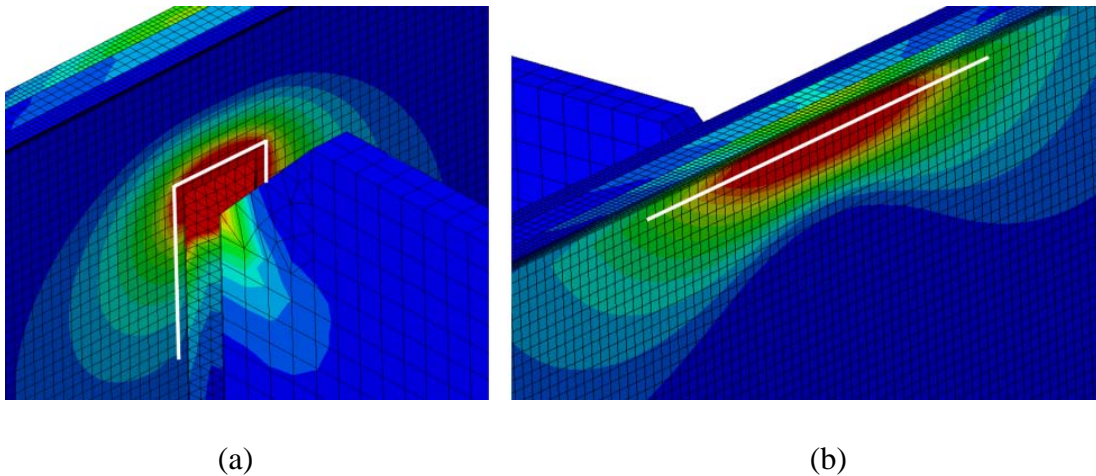
Figure A.40: Hot Spot Stress paths for (a) Interior connection plate side or connection plate-web weld, (b) Exterior fascia side or flange-web weld

A.4.4.2   Description of Retrofits

Three retrofit configurations were investigated in the computational simulations. First, an existing retrofit technique was explored in which positive attachment was provided between the connection plate and top flange using two angles oriented back-to-back. Next, a back-up stiffener technique was studied in which the web gap was stiffened by a secondary stiffener placed on the opposing web face. This retrofit can be applied using either a partial depth or full depth transverse stiffener; however, only a full depth stiffener was studied as it was expected to produce the best result, based upon findings from previous studies (Hassel et. al 2010). Back-up stiffeners were modeled using transverse stiffener dimensions and placed on the girder fascia side. Third, a retrofit in which attachment was provided between the connection plate and web through two angles and a back plate was explored. This last retrofit has been termed the "angles-with-plate" technique and was the subject of investigations described in Appendix A.1 to A.3.

Several variations of the angles-with-backing plate retrofit were explored, in which the thickness of the angle and plate elements were varied (with retrofit-to-web ratios of 2 and 3), and one case in which the angles were modified to include internal stiffeners. Schematics of the retrofits studied are shown in Figure A.41.

Angles:
L152x152 mm (L6x6 in.)
L127x152 mm (L5x6 in.)

Backing Plate:
457x457 mm (18x8 in.)

(a)

Angles:
L152x152 mm (L6x6 in.)
L127x152 mm (L5x6 in.)
Stiffeners:
133x133 mm (5.25x5.25 in.)
108x133 mm (4.25x5.25 in.)
Backing Plate:
457x457 mm (18x8 in.)

(b)

Angles:
L179x179mm (L7x7 in.)

(c)

Back-up Stiffener:
9.5x127x876 mm (3/8x5x34-1/2 in.)
with 32x32 mm (1-1/4x1-1/4 in.)
clip

(d)
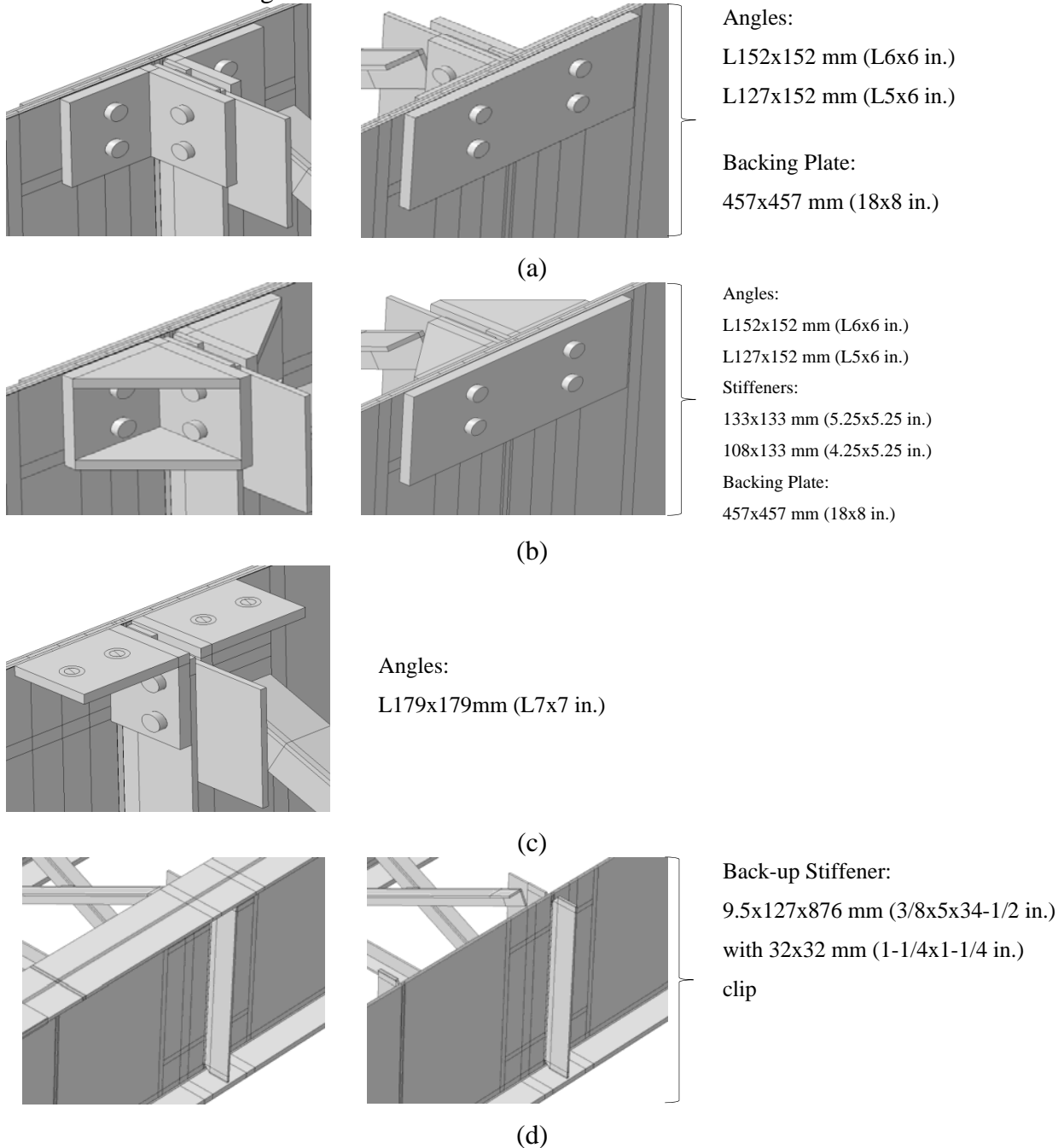
**Figure A.41: Views of various retrofits examined in finite element models
(a) Angles-with- plate retrofit; (b) Stiffened angles-with-plate retrofit; (c) Positive
attachment between transverse connection stiffener and top flange retrofit; and (d) Full
depth back-up stiffener bearing on top and bottom flanges.**

A.4.5 Results

All cracked and/or retrofitted models were normalized based on stress demands computed in the uncracked, unretrofitted finite element model. Although 45 models were analyzed, representative results have been presented in this paper. For the two hot spot stress paths considered, stresses at the connection plate-to-web weld and at the flange-to-web weld were found to be within 3% of one another in the uncracked, unretrofitted bridge model. Since all stresses presented have been normalized to hot spot stress demands from the uncracked, unretrofitted models, new stresses due to cracking and/or retrofitting have been approximately normalized to the same initial hot spot stress value due to this circumstance.

A.4.5.1   Stress vs. Crack Length

For all horseshoe-shaped crack lengths studied, hot spot stress decreased or remained nearly constant as crack length increased for both retrofitted and unretrofitted conditions. The percentage of uncracked hot spot stress due to change in length of the horseshoe-shaped crack has been presented in Figure A.42.
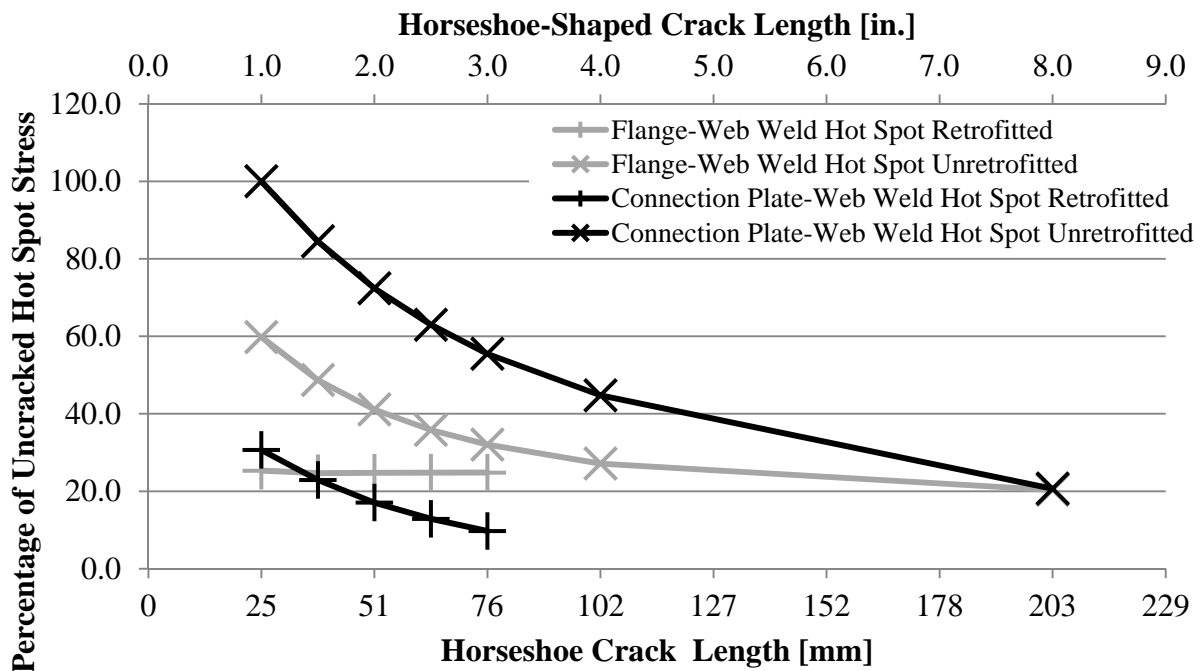
Figure A.42: Percentage of uncracked Hot Spot Stresses with change in horseshoe-shaped crack length for connection plate-web weld and flange-web weld.

Cracks were physically located at the connection plate-to-web weld toe on the web. For both the unretrofitted and retrofitted conditions, hot spot stress at the connection plate-to-web weld decreased as crack length was increased. At the flange-to-web weld in an unretrofitted state, the hot spot stress decreased as the horseshoe-shaped crack length was increased; however, for the retrofitted condition, hot spot stress remained nearly constant.

For the longitudinal flange-to-web crack lengths studied, hot spot stress behavior was found to be similar to that for the horseshoe-shaped cracks. As longitudinal crack length was increased, hot spot stresses for both the flange-to-web weld and connection plate-to-web weld decreased as shown in Figure A.43. Initiation of a 25 mm (1 in.) longitudinal crack provided little reduction in flange-to-web hot spot stress demand, and increased stress demand at the connection plate-to-web weld by approximately 14%. Since both stresses were normalized to similar uncracked hot spot stresses (within 3% of each other), Figure A.43 indicates that once a longitudinal crack initiated, a horseshoe-shaped crack is highly likely to initiate due to increased stresses at the connection plate-to-web weld.
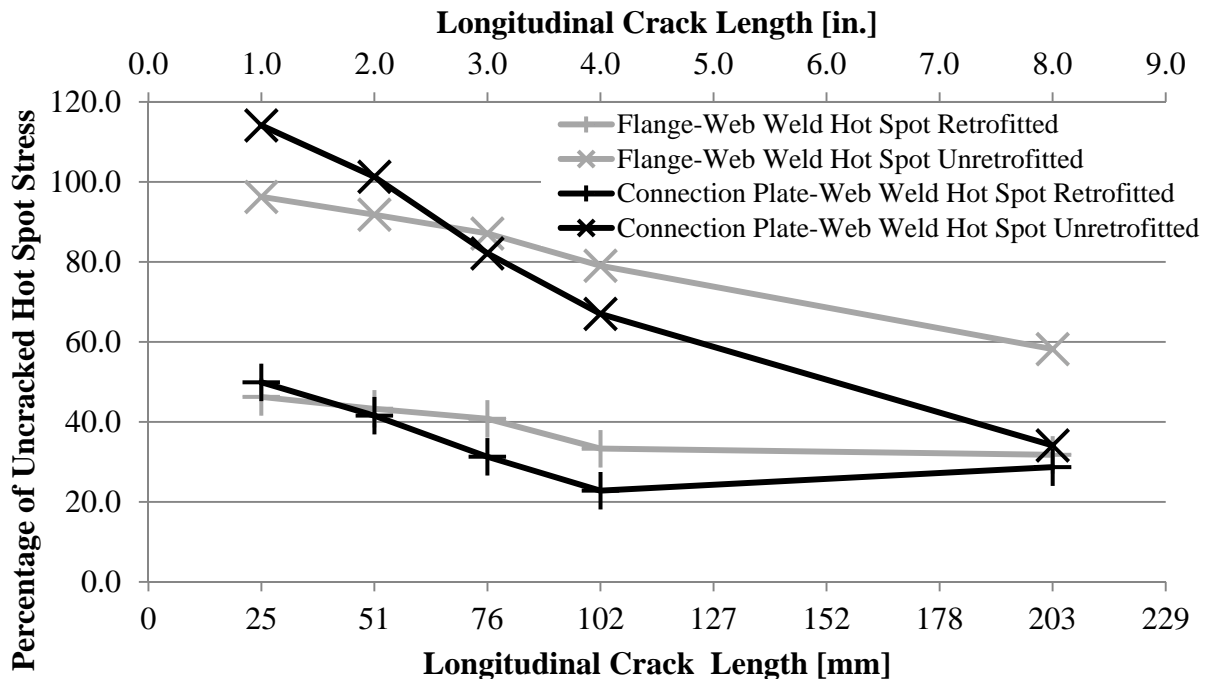
Figure A.43: Percentage of uncracked Hot Spot Stresses with change in longitudinal crack length for connection plate-web weld and flange-web weld

Retrofit effectiveness in the presence of only a longitudinal crack was found to decrease significantly for the connection plate-to-web weld as crack length increased. The reduction in stress from cracked, unretrofitted to cracked, retrofitted for the connection plate-to-web weld was approximately 5% for a 203 mm (8 in.) longitudinal crack and 64% for a 25 mm (1 in.) crack. For the flange-to-web weld location, stress reduction due to retrofitting did not vary significantly with increasing crack length.

The reduction in hot spot stresses as crack length increased is slightly different from the findings form the girder sub-assembly [2.8 m (9.3 ft)] finite element modeling presented in Appendix A.2. For the models of the girder sub-assemblies, crack growth propensity increased as crack length increased, up to a crack length of approximately 50 mm (2 in.). After this point, stress demands tended to decrease for HSS1 and slightly increased for HSS2. As explained in the introduction section, the girder sub-assemblies contained a flange (representing a top flange in a bridge) fixed to a concrete floor. This fixity with a corresponding lack of flange rotation as well as the complete lack of longitudinal bending within the girder, is hypothesized to be the primary cause of the differences in girder performance between the girder sub-assembly tests and analyses and the scaled bridge tests and analyses reported herein.

A.4.5.2 *Effect of Reduced Deck Stiffness*

Reduced deck stiffness was applied to the model to determine the effect of deck stiffness on stress demand in the web gap region. For this condition, only a horseshoe-shaped crack was considered. In both hot spot locations in the top web gap, halving the concrete deck stiffness was found to increase stresses in the web gap region. This increase was approximately 20% of the hot spot stresses computed in a model with full deck stiffness with a horseshoe-shaped crack around the connection plate-to-web weld. Effect of reduced deck stiffness on south girder top web gap stresses can be seen in Figure A.31.
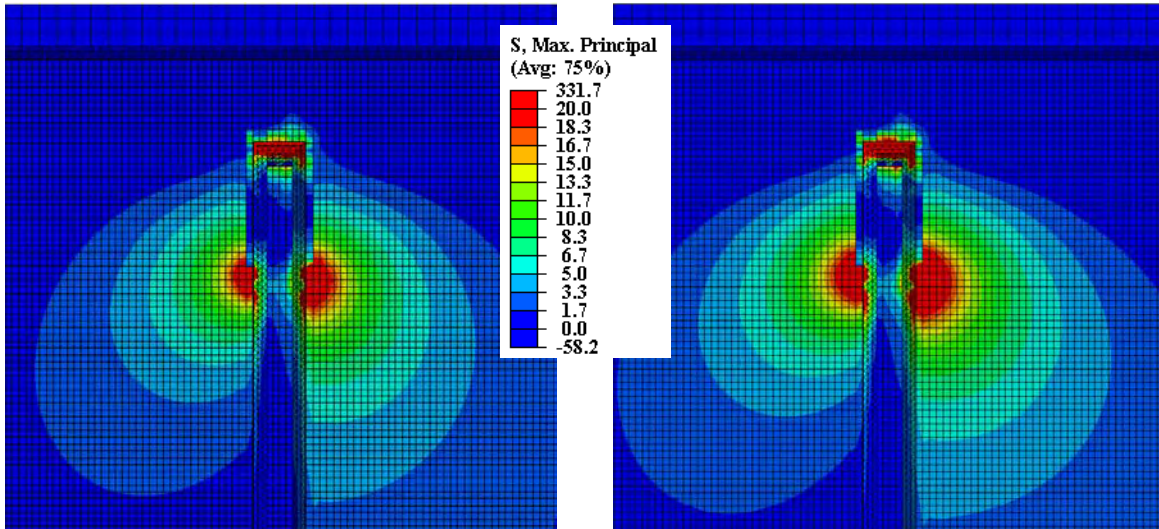
<div align="center">(a)   (b)</div>

Figure A.44: Maximum principal stresses with scale from 0 MPa to 138 MPa (0 ksi to 20 ksi)
(a) Unretrofitted model with normal deck stiffness and (b) Unretrofitted model with reduced deck stiffness and a 51 mm (2 in.) crack. Legend stresses are in ksi

A.4.5.3 Effect of Broken Cross Frame

During experimental testing as outlined in the companion paper (Appendix A.3), the north cross frame at mid-span experienced a fracture through the diagonal member framing into the top web gap of the north girder. The effect of this failure on the bridge system was analyzed in a model of the bridge with a 25 mm (1 in.) horseshoe-shaped crack. In this finite element model, which directly modeled the severed cross frame member where it should have framed into the north girder top web gap, hot spot stresses where the cross frame element previously framed into the girder decreased significantly. This reduction in stresses in the top web gap of the north girder was approximately 77%. At the bottom web gap of the same girder, hot spot stresses more than doubled. This correlated well with the computed maximum principal stress magnitudes in the cross frame members framing into the north girder, which saw a decrease in the broken member and an increase in the horizontal element framing into the bottom web gap. In the south girder, away from the broken cross frame, maximum principal stresses in all cross frame elements decreased. Cross frame stresses can be seen in Table A.11.

<div align="center">101</div>

Table A.11: Cross Frame Element Stresses with 25 mm (1 in.) Horseshoe Crack [MPa (ksi)]

	Angles-and-Plate 19 mm (3/4 in.)			Angles-and-Plate 19 mm (3/4 in.) with Broken Cross Frame Element		
	Maximum Principal	Horizontal	Vertical	Maximum Principal	Horizontal	Vertical
Inclined Cross Frame Element Framing into North Girder Top Web Gap	39 (5.7)	28 (4.1)	8 (1.1)	0 (0.0)	0 (0.0)	0 (0.0)
Inclined Cross Frame Element Framing into North Girder Bottom Web Gap	0 (0.0)	-19 (-2.8)	-6 (-0.9)	0 (0.0)	-23 (-3.4)	-11 (-1.6)
Horizontal Cross Frame Element Framing into North Girder Bottom Web Gap	29 (4.2)	30 (4.3)	0 (0.0)	41 (6.0)	38 (5.5)	0 (0.0)
Inclined Cross Frame Element Framing into South Girder Top Web Gap	37 (5.3)	28 (4.1)	7 (1.0)	24 (3.5)	19 (2.7)	5.5 (0.8)
Inclined Cross Frame Element Framing into South Girder Bottom Web Gap	0 (0.0)	-23 (-3.3)	-6 (-0.9)	0 (0.0)	-19 (-2.8)	-5.5 (-0.8)
Horizontal Cross Frame Element Framing into South Girder Bottom Web Gap	29 (3.9)	29 (4.2)	0 (0.0)	24 (3.5)	24 (3.5)	0 (0.0)

Girder lateral deflections can be seen in Figure A.45. Deflections show as if looking at the girder deflection profiles. The north girder bottom flange moves out toward the right (positive deflection in the plot) and the south girder bottom flange moves out toward the left (negative deflection in plot). The response of the north and south girders in the cracked, unretrofitted condition (25 mm [1 in.] horseshoe-shaped crack) and the response of the girders with the same crack geometry under the angles-with-plate retrofit were found to be symmetric. For the north girder (where the cross frame element was broken), lateral girder deflections were significantly decreased after the cross-frame member was severed, resulting in decreased girder rotation between top and bottom flanges. Additionally, top web gap differential deflection was found to be nearly zero. Different behavior was found to define the south girder after the cross-

frame was severed. In the south girder, top web gap differential deflection was still decreased, but bottom flange deflection increased significantly, resulting in larger girder rotation between top and bottom flanges.
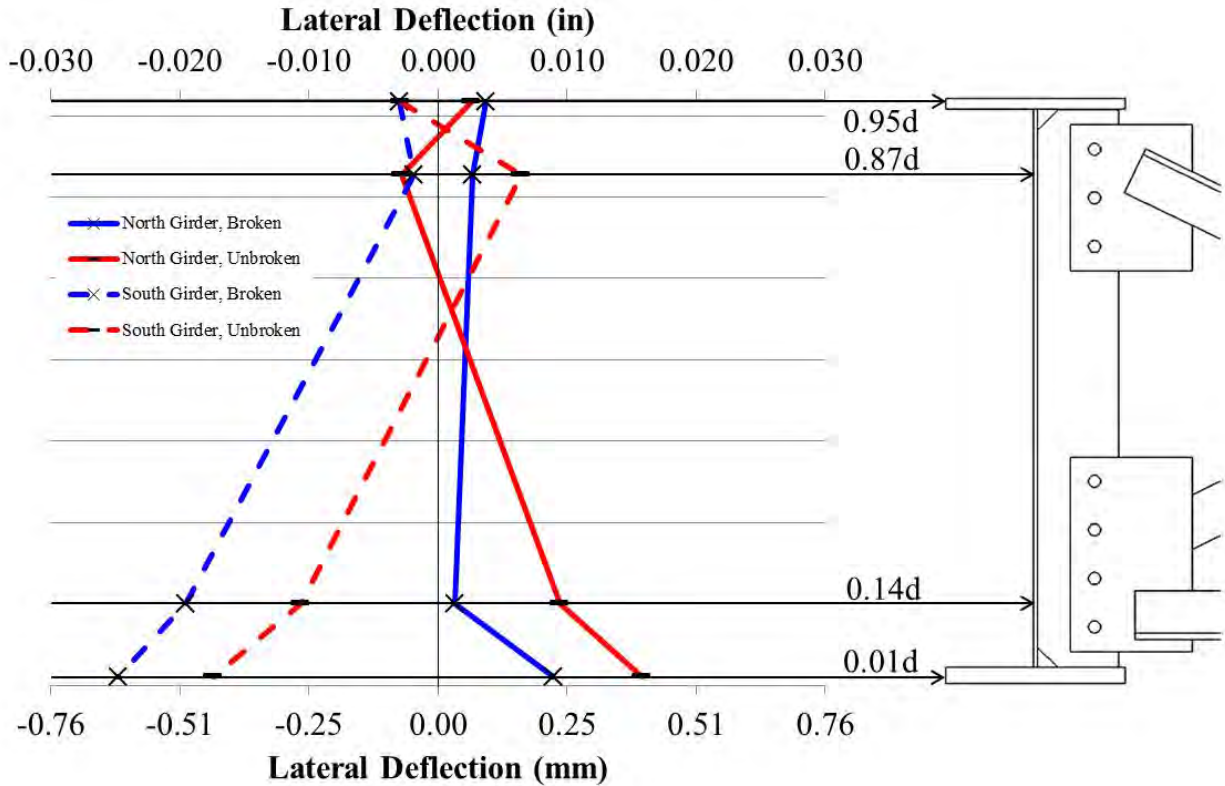
Figure A.45: Girder lateral deflections with unbroken cross frame elements and broken cross frame element framing into the north girder top web gap

Cross section deflected shapes from the FE models have been shown in Figure A.46. These figures provide images for the results outlined in Figure A.45. A localized stress concentration (hot spot) can be seen at the on the tab plate near the end of the inclined cross frame angle as shown in Figure A.46(a). Once the cross frame element is broken, little force exists in the tab plate and therefore little out-of-plane forces are transferred into the north girder top web gap as seen in Figure A.46(b). Symmetric bending was found to occur while both cross frames were fully attached; however, deflections were asymmetric under the broken cross frame condition. For the north girder, slightly more flange rotation and less web rotation as shown in Figure A.46.

103

South Girder   North Girder

(a)

South Girder   North Girder

(b)
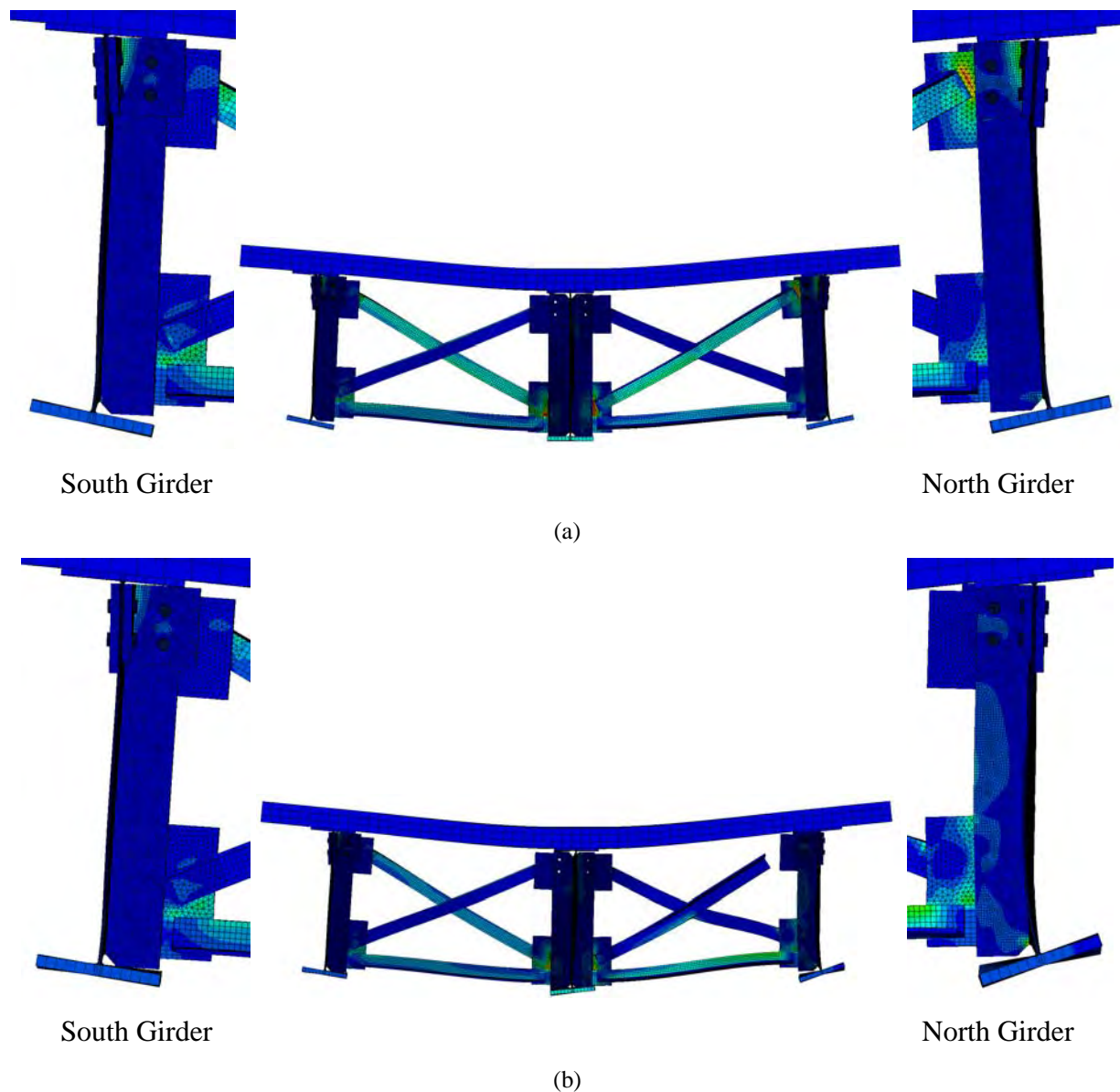
**Figure A.46: Girder deflection profiles
(a) 25 mm (1 in.) cracked and retrofitted model and (b) 25 mm (1 in.) cracked and retrofitted model with broken north cross frame element**

Hot spot stresses were influenced by the broken north cross frame element framing into the top web gap. Stresses extracted from finite element models have been presented in Table A.12. When the north girder cross frame element framing into the north girder top web gap was severed, the hot spot stress at the north girder connection plate-to-web weld decreased by more than 50%. In the north girder bottom web gap, connection plate-to-web weld stress more than doubled. South girder stresses were only slightly affected by the broken north cross frame.

Table A.12: Maximum Principal Hot Spot Stresses with 25 mm (1 in.) Horseshoe Crack [MPa (ksi)]

	Angles-and-Plate 19 mm ($^3/_4$ in.)	Angles-and-Plate 19 mm ($^3/_4$ in.) with Broken Cross Frame Element
North Girder Top Web Gap Connection Plate-Web Weld	71 (10.3)	29 (4.2)
North Girder Top Web Gap Flange-Web Weld	101 (14.6)	37 (5.4)
North Girder Bottom Web Gap Connection Plate-Web Weld	92 (13.4)	191 (27.7)
North Girder Bottom Web Gap Flange-Web Weld	38 (5.5)	77 (11.1)
South Girder Top Web Gap Connection Plate-Web Weld	52 (7.6)	60 (8.7)
South Girder Top Web Gap Flange-Web Weld	102 (14.8)	66 (9.6)
South Girder Bottom Web Gap Connection Plate-Web Weld	97 (14.1)	56 (8.1)
South Girder Bottom Web Gap Flange-Web Weld	41 (5.9)	25 (3.6)

A.4.5.4   Retrofit Comparison

The relative effectiveness of the various retrofits investigated have been presented by showing the stress demands in the web gap region in the retrofitted condition as percentage of the stress demands from the uncracked, unretrofitted condition. All retrofits were analyzed and applied over a horseshoe-shaped crack only. The angles-with-plate retrofit was also analyzed with longitudinal cracks. The percent of uncracked stress in connection plate-to-web weld and flange-to-web weld for changing horseshoe-shaped crack lengths are shown in Figure 41(a) and (b), respectively. For all retrofits considered, the pattern of stress reduction was similar for all crack lengths studied. As crack length increased from 25 mm (1 in.) to 76 mm (3 in.), the percent reduction in hot spot stress decreased for both the connection plate-to-web weld and flange-to-web weld locations. As crack length increases, hot spot stresses decrease as shown in Figure A.41 and A.42. As the retrofit was applied to larger cracks with lower initial stresses, the reduction in stress decreased. Additionally, at a crack length of 76 mm (3 in.), all retrofits

provide a reduction in stress of more than 80%. Continuing to improve on this stress (which is already low) becomes inefficient.
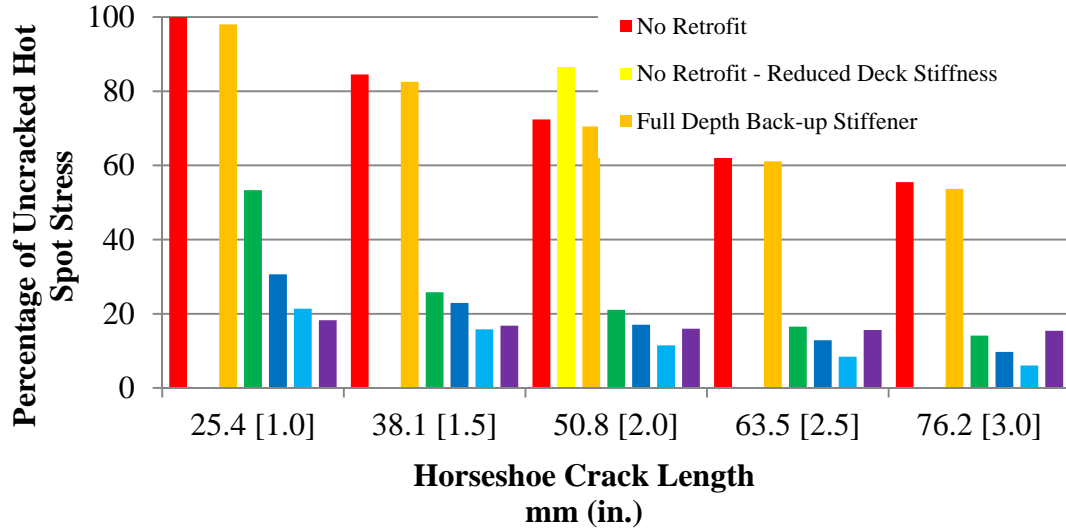
(a)
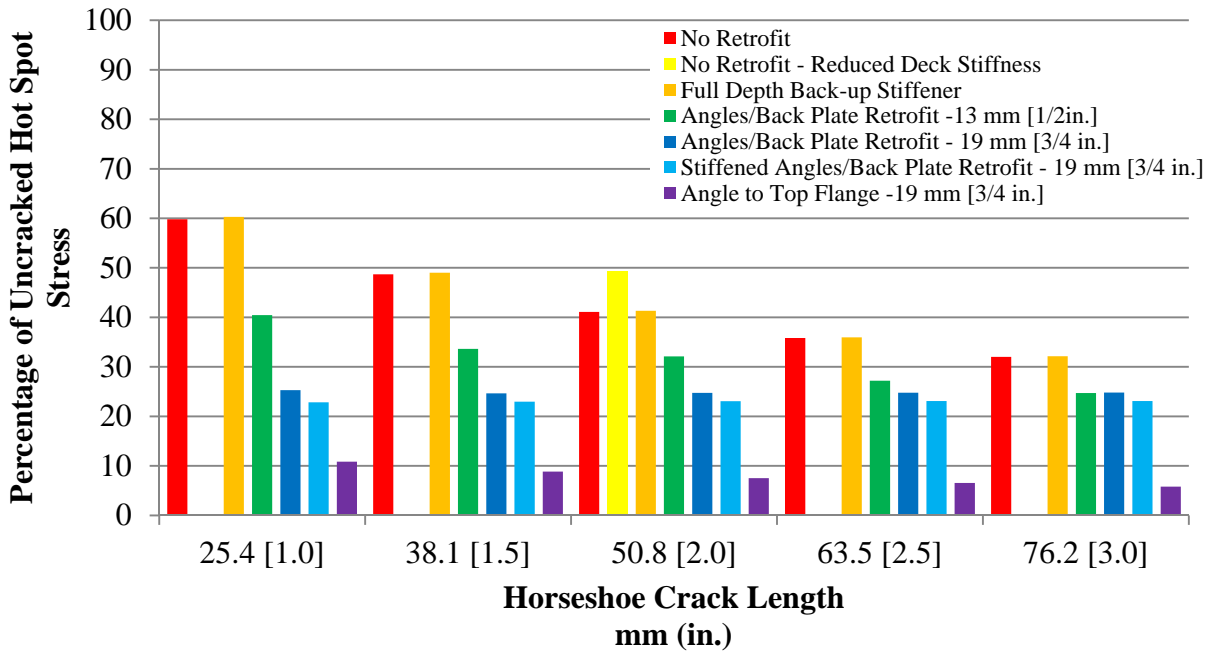
(b)

**Figure A.47: Percent of uncracked stress
at (a) Connection plate-web weld and (b) Flange-web weld for various retrofit techniques
and crack lengths**

Since similar patterns were found for each of the crack lengths investigated, results for a horseshoe-shaped crack length of 51 mm (2 in.) are shown in Figure A.48.
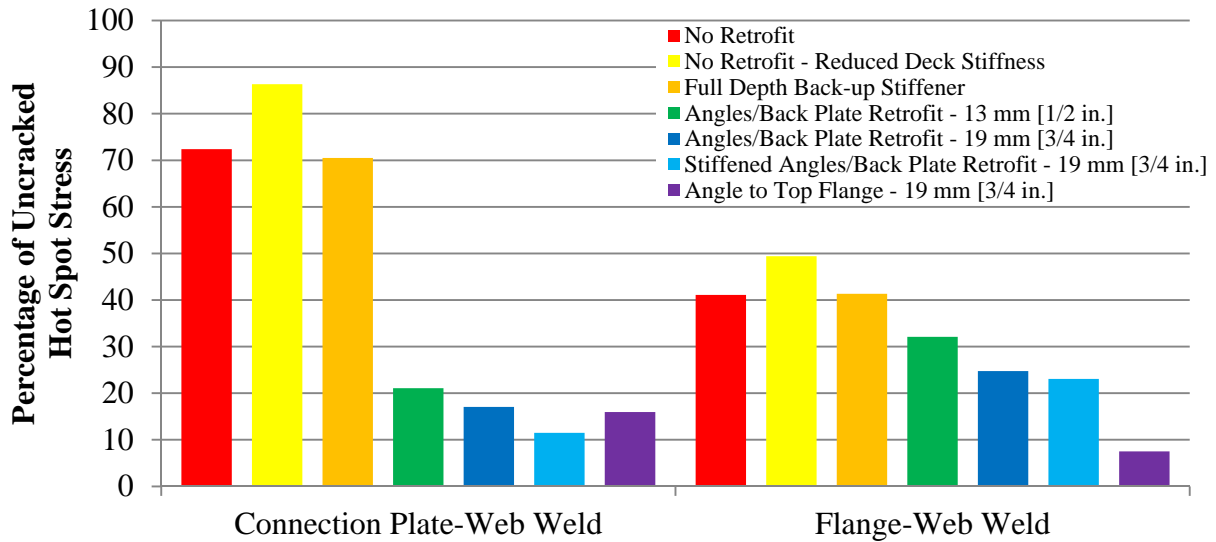
Figure A.48: Percentage of uncracked Hot Spot Stresses for connection plate-web weld and flange-web weld with various retrofit conditions and a 51 mm (2 in.) horseshoe-shaped crack.

As shown, an initial horseshoe-shaped crack length of 51 mm (2 in.) resulted in a connection plate-web weld hot spot stress of approximately 72% of the uncracked state while flange-web weld hot spot stress was approximately 41% of the uncracked state. Retrofit performance was based on additional reduction from the cracked state. As stated previously, initial uncracked hot spot stresses for each location were within 3% of each other. Therefore, all retrofitted hot spot stresses were normalized against a similar value and can be compared directly. In other words, because of this coincidence, a reduction of 10% in the connection plate-web weld is approximately the same as a 10% reduction in the flange-web weld.

Full depth back-up stiffeners provided minimal relief in hot spot stress for both welds of interest. Since the bridge studied was a non-skewed bridge with cross frames placed back-to-back, this corroborates previous findings (Hartman et. al 2010). Excluding back-up stiffeners, all other retrofits resulted in a reduction of stress demand.

Based on all models studied, the best retrofit for reduction of hot spot stress around the connection plate-web weld was found to be the stiffened angles-with-backing plate. For a 51 mm

(2 in.) crack, stiffening the angles resulted in an additional reduction of over 5% when compared with the performance of the unstiffened retrofit; however, adding stiffeners did not significantly improve the stress reduction for the flange-to-web weld. In this location, the additional reduction due to added stiffness was less than 2%.

For the angles-with-plate retrofit, changes in thickness impacted the hot spot stress demand at the two fatigue-susceptible welds. At the connection plate-to-web weld for a 51 mm (2 in.) horseshoe-shaped crack, a retrofit thickness of 13 mm ($^1/_2$ in.) provided a stress reduction of approximately 51%. Increasing the retrofit thickness to 19 mm ($^3/_4$ in.) provided an additional stress reduction of 4%. Similarly for the flange-to-web weld, a thickness of 13 mm ($^1/_2$ in.) decreased stresses by 9% while a thickness of 19 mm ($^3/_4$ in.) decreased stresses an additional 7%. These data support the findings discussed in Appendix A.2. Based on this data, it is estimated that further increasing the angles and plate thicknesses would not continue to provide significant additional reduction in stress—there would be a point in which increasing thickness provides little or no additional benefit.

For the flange-to-web weld, it was found the best performing retrofit was the angles connected with the girder top flange. This retrofit minimized the differential rotation between the girder flange and web, forcing the elements to rotate together rather than separately. This retrofit was also found to perform slightly better than the 19 mm ($^3/_4$ in.) thick angles-with-backing plate retrofit for the connection plate-to-web weld. Although this traditional retrofit indicated good performance, these findings must be balanced against the required additional welding and/or deck removal with traffic disruption for field implementation.

A.4.6 Conclusions

Since many steel bridges built prior to 1985 are in need of repair, it is critical to develop effective retrofit techniques for many different bridge configurations. Finite element simulations can be used to evaluate retrofit effectiveness and can also provide meaningful insight into appropriate retrofit thickness and performance to complement laboratory and/or field implementation. In this study, several retrofits were considered including: full depth back-up stiffeners, angles-with-backing plate (several variations), and angles connected to the top flange.

Additionally, the effect of a broken cross frame element and reduced deck stiffness due to cracking were analyzed. The following conclusions were found:

- Hot spot stresses at connection plate-to-web welds and flange-to-web welds decreased or remained constant as horseshoe-shaped crack length was increased in both unretrofitted models and angles-with-plate (19 mm ($^3/_4$ in.) thickness) retrofitted models.

- Hot spot stresses at connection plate-to-web welds and flange-to-web welds decreased as longitudinal crack length was increased in both unretrofitted models and angles-with-plate (19 mm [$^3/_4$ in.) thickness) retrofitted models. Initiation of a longitudinal crack increased hot spot stresses at the connection plate-to-web weld; therefore, horseshoe-shaped cracking would likely initiate soon after the formation of a longitudinal crack.

- When deck stiffness was halved, hot spot stresses in both the connection plate-to-web weld and flange-to-web weld increased 20%.

- Although the analysis of the cross frame failure did not provide any significant conclusions, changes in bridge response were evident. With the broken north cross frame, the south cross frame and girder did *not* pick up significantly more load in terms of web gap stresses. In fact, web gap stresses actually decreased in the top web gap flange-web weld and the bottom web gap flange-web weld and connection plate-web weld. In terms of stresses, the only location within the bridge that gathered more load was the north girder bottom web gap and horizontal cross frame member in the north cross frame.

- Due to the cross frame failure, slight increases in flange rotation and decreases in web rotation were experienced by the north girder. South girder lateral deflections increased due to north cross frame failure while north girder lateral deflection decreased.

- For all crack lengths studied, the order of retrofit effectiveness remained constant. As crack lengths increased, initial hot spot stresses decreased, resulting in less stress reduction due to retrofitting.

- Both hot spot stresses experienced reduction due to retrofitting. Full depth back-up stiffeners provided minimal stress relief in the system due to bridge configuration.

- Retrofit performance listed in order from most reduction to least reduction was found to be as follows for the connection plate-to-web weld: stiffened angles-with-backing plate 19 mm ($^3/_4$ in.), angles to top flange 19 mm ($^3/_4$ in.), angles-with-backing plate 19 mm ($^3/_4$ in.), angles-with-backing plate 13 mm ($^1/_2$ in.), and full depth back-up stiffener.

- Retrofit performance listed in order from most reduction to least reduction was found to be as follows for the flange-web weld: angles to top flange 19 mm ($^3/_4$ in.), stiffened angles-with-backing plate 19 mm ($^3/_4$ in.), angles-with-backing plate 19 mm ($^3/_4$ in.), angles-with-backing plate 13 mm ($^1/_2$ in.), and full depth back-up stiffener.

- To improve angles-with-backing plate performance, addition of stiffeners to the angles may be a viable option. This may allow for reduction in thickness of angles and backing plate for field implementation.

The sub-assemblies studied in Appendix A.1 and A.2 included only out-of-plane effects and did not capture longitudinal bending effects. In the analyses described in this study, a significant effort was placed in determining at appropriate retrofit technique for a 9.1 m (30 ft.) laboratory test bridge. These models were also used to explain bridge and retrofit behavior.

Based on this investigation, effective retrofits (primarily considering angles-with-plate variations) can be chosen for application on the test bridge. With laboratory test data to validate the results (see Appendix A.3), efforts will then be placed toward field implementation in which the angles-with-plate retrofit will provide an effective and inexpensive technique requiring little-to-no traffic closure.

A.4.7 References

Adams, C. (2009). *Finite Element Study of Bridge Details Susceptible to Distortion-Induced Fatigue*. (Master's thesis). University of Kansas, Lawrence, KS.

Alemdar, F., Nagati, D., Matamoros, A., Bennett, C., and Rolfe, S. (2013a). "Repairing Distortion-Induced Fatigue Cracks in Steel Bridge Girders using Angles-with-Plate Retrofit Technique, Part I: Physical Simulations." *Journal of Structural Engineering*, ASCE, In Press.

Alemdar, F., Overman, T., Matamoros, A., Bennett, C., and Rolfe, S. (2013b). "Repairing Distortion-Induced Fatigue Cracks in Steel Bridge Girders using Angles-with-Plate Retrofit Technique, Part II: Computer Simulations." *Journal of Structural Engineering*, ASCE, In Press.

Hartman, A., Hassel, H., Adams, C., Bennett, C., Matamoros, A., and Rolfe, S. (2010). "Effects of Cross-Frame Placement and Skew on Distortion-Induced Fatigue in Steel Bridges." *Transportation Research Record* 2200, 62-68. Transportation Research Board, National Research Council, Washington, D.C.

Hassel, H., Hartman, A., Bennett, C., Matamoros, A., and Rolfe, S. (2010). "Distortion-Induced Fatigue in Steel Bridges: Causes, Parameters, and Fixes." *2010 ASCE/SEI Structures Congress Proceedings,* 471-483.

Nagati, D. (2012). *Repair of Steel Bridge Girders Damaged by Distortion-Induced Fatigue.* (Master's thesis). University of Kansas, Lawrence, KS.

Przywara, J. (2013). *Applications of the Extended Finite Element Method (XFEM) for the Analysis of Distortion-Induced Fatigue Cracking in Highway Bridge Girders.* (Master's thesis). University of Kansas, Lawrence, KS.

Richardson, T. (2012). *Analytical Investigation of Repair Methods for Fatigue Cracks in Steel Bridges.* (Master's thesis). University of Kansas, Lawrence, KS.

Appendix B: Table of Contents

Appendix B: List of Tables

Appendix B: List of Figures

117

Appendix B: Fiber Reinforced Polymer Retrofit Techniques

Appendix B is organized into six parts, each of which is focused on the development of fiber reinforced polymer (FRP) repair techniques for fatigue. The ultimate goal of the retrofits developed for distortion-induced fatigue (discussed in Appendices B.4 to B.6) was so that they could be applied while a bridge is operating, and without removal of a concrete deck.

Appendices B.1 to B.3 are focused on the development of FRP repairs for tensile loading (B.1) and for in-plane bending loading (B.2 and B.3). Performing these studies before embarking upon development of FRP repair techniques for the more complicated mode of distortion-induced fatigue cracking was a necessary step, resulting in greater understanding of the importance of composite stiffness, bond characteristics, and overlay geometry.

Appendix B.4 to B.6 are focused on applications of FRP for repairing distortion-induced fatigue cracking, and are an outgrowth of the findings discussed in B.1 to B.3. B.4 describes the application of a "composite block" retrofit technique, and B.5 and B.6 describe analytical and physical investigations of sandwich-composite-type repairs for deep web gaps produced under distortion-induced fatigue.

B.1: Use of Carbon Fiber Reinforced Polymer Overlays to Repair Fatigue Damage in Steel Plates under Tension Loading

Fatih Alemdar[1]

Regan Gangel[2]

Adolfo Matamoros[3]

Caroline Bennett[4]

Ron Barrett-Gonzalez[5]

Stan Rolfe[6]

Hao Liu[7]

B.1.1 Abstract

Fiber reinforced polymer (FRP) overlays have been successfully used in the aerospace industry to repair fatigue damage in aluminum plates. With this success there is potential for use of similar FRP overlays to repair fatigue damage in aging steel bridge structures. This study investigated the effectiveness of repairing fatigue damage in steel plate with adhesively bonded carbon fiber reinforced polymer (CFRP) overlays. A total of 15 steel plate specimens with pre-existing fatigue cracks were repaired with varying thicknesses of CFRP overlays to evaluate the effect of the ratio of axial stiffness of the composite to that of the underlying steel, *SR*, on increased fatigue life and decreased applied stress. The results showed that increasing the axial stiffness ratio from 0 to 0.4 could increase the fatigue life by a factor of 10 for the most extreme conditions, and with an optimal axial stiffness ratio infinite fatigue life may be reached. Fatigue life of the steel specimens in this study was found to be dependent on both axial stiffness and

---

[1] Fatih Alemdar, PhD, Assistant Professor, Yildiz Technical University, Istanbul, Turkey
[2] Regan Gangel, MS, Structural Engineer, Burns and McDonnell, 9400 Ward Pkwy, Kansas City, MO 64114
[3] Adolfo Matamoros, PhD, Professor, University of Kansas, 1530 W. 15th St., Lawrence KS, 66045
[4] Caroline Bennett, PhD, PE, Associate Professor, University of Kansas, 1530 W. 15th St., Lawrence KS, 66045
[5] Ron Barrett, PhD, Associate Professor, University of Kansas, 1530 W. 15th St., Lawrence KS, 66045
[6] Stan Rolfe, P.E., PhD, A.P. Learned Distinguished Professor, University of Kansas, 1530 W. 15th St., Lawrence KS, 66045
[7] Hao Liu, MS, Graduate Research Assistant, University of Kansas, 1530 W. 15th St., Lawrence KS, 66045

applied stress range. Results from finite element analyses validated the use of axial stiffness as a design parameter and correlated to the experimental results discussed.

B.1.2 Introduction

A significant number of aging steel bridge structures experience structural problems due to fatigue cracks. One repair technique that has been used by the Kansas Department of Transportation (KDOT) in cases where fatigue cracks have propagated significantly into girder webs is to retrofit the web with a full-depth bolted steel splice at the location of cracking. The intent of the splice is to provide an alternate load path around the damaged web, and it is designed for the full shear demand at that web location. Attaching full-depth splice plates to the damaged web does reduce the stress in the fatigue sensitive area (Roddis and Zhao 2001), however, this is an expensive repair and there is potential that with a full-depth steel splice plate covering the damaged region of a girder any additional crack propagation may be hidden from view and go unnoticed.

A more localized repair utilizing CFRP materials could result in a more cost-effective and inspectable repair. One potential embodiment of this type of repair is a pair of CFRP overlay elements, one bonded to each face of the steel web over the crack with an epoxy resin layer. The CFRP overlays would not need to extend the full-depth of the web; instead, they could "patch" the region over the crack. However, before the potential of any such specific repair geometry can be effectively investigated, fundamental questions must be answered concerning the effectiveness of CFRP overlays in extending the fatigue life of steel plate loaded in tension with a pre-existing fatigue crack. The aim of the research described in this article is to provide fundamental information concerning basic proportions (thicknesses) of CFRP overlays relative to the steel to which they are bonded to effectively slow or halt fatigue crack propagation in the steel under various stress demands. The effect of bond thickness and modulus of elasticity of CFRP on the reduction in stress at critical locations was also evaluated.

B.1.3 Background

A significant amount of research on the use of composite materials has been carried out in the field of aerospace engineering to address fatigue problems in the fuselages of airplanes (Mall and Conley 2009; Umamaheswar and Singh 1999; Schubbe and Mall 1999; Naboulsi and

Mall 1996; Lee and Lee 2004; Liu, Xiao, et al. 2009). The most recent research performed on this topic in the aerospace field has focused on the use of fiber reinforced polymer (FRP) patches to repair fatigue damage in aluminum plates. These studies have shown that FRP plates can reduce stresses in a vulnerable detail significantly if properly proportioned and bonded to the substrate. An experimental study by Mall and Conley (2009) reported that bonding a boron fiber reinforced polymer overlay to only one side of an aluminum specimen increased the fatigue crack propagation life between four and 10 times with respect to the propagation life of an untreated specimen. Wang et al. (2002) also found an increase in fatigue crack propagation life on the order of 10 times in aluminum plates repaired with FRP patches.

In the aerospace field a commonly used parameter for proportioning composite patches for the purpose of repairing fatigue damage is the stiffness ratio:

$$SR = E_{CFRP} \, t_{CFRP} / \, E_s \, t_s \qquad\qquad\qquad \textbf{Equation B.1}$$

where *SR* is the stiffness ratio defined as the ratio of axial stiffness of the composite to that of the underlying steel, E_{CFRP} is the modulus of elasticity of the CFRP, t_{CFRP} is the thickness of the CFRP patch, E_s is the modulus of the steel, and t_s is the thickness of the steel plate. The *SR* parameter is used to determine thickness of FRP needed to repair fatigue-damaged steel plates by assuming that the driving force is redistributed in proportion to the relative axial stiffness of the two materials. For aerospace structures the recommended stiffness ratio is 1.0 (Schubbe et al. 2009). Schubbe and Mall (1999) performed experimental tests on aluminum plates repaired with a bonded composite patch and found that as the stiffness ratio increased, so did the fatigue life of both thin and thick plates. Stiffness ratios of 1.0 and 1.3 were evaluated in that study.

Although the use of CFRP overlays has not been widely implemented in steel structures, several studies have investigated their use to repair fatigue-related damage. Tavakkolizadeh and Saadatmanesh (2003) studied the effectiveness of unidirectional CFRP sheets to improve the fatigue strength of S127x4.5 steel girders with pre-existing notch cracks. The authors reported that the fatigue-crack propagation life of the specimens with CFRP sheets was extended by a factor of approximately three compared with that of control specimens. Liu, Al-Mahaidi, and Zhao (2009) studied the tensile fatigue behavior of notched steel plates strengthened with single-

121

ply CFRP patches. Results showed that single-sided repair extended the fatigue-crack propagation life of the specimen by a factor ranging between 2.2 and 2.7, whereas a double sided repair extended the fatigue-crack propagation life by a factor ranging between 4.7 and 7.9. Roy, Lang and May (2009) performed a study using the same type of materials and procedure used by Liu et al. (2009a and b), and showed similar increases in fatigue-crack propagation life of steel plates repaired with single-sided CFRP patches as seen in Liu, Al-Mahaidi, and Zhao (2009). Bocciarelli et al. (2009) studied the use of double-sided CFRP overlays on uncracked steel plates under fatigue loading and found that failure was precipitated by debonding of the overlays. They also found that the fatigue performance of steel plates reinforced with CFRP plates was comparable to that of steel specimens with welded steel plates.

Kaan et al. (2012) studied the behavior of uncracked plate-coverplate connections repaired with CFRP overlays. Results showed that specimen behavior, according to the AASHTO design specifications, could be improved from a fatigue design Category E' detail to fatigue design Category B' or B detail. In this study, increased fatigue crack initiation life was a direct result of maintaining adequate bond. This study is reported upon in Appendix B.2.

Analytical modeling of CFRP repairs using the Finite Element (FE) method is also an important technique when developing efficient retrofit schemes for steel structures. Researchers (Liu, Xiao, et al. 2009; Lee and Lee 2004) have shown good agreement between the change in stress demand estimated using FE models and experimentally observed changes in fatigue-crack propagation life. In FE models that include a layer of resin between the CFRP overlay and the underlying metal, the potential for debonding can be assessed by comparing the stress demand in the resin with a limiting value. This approach was also adopted in the FE simulations conducted in this study.

B.1.4 Objective and Scope

The overall objective of the research described in this paper was to determine the effectiveness of CFRP overlays to repair existing fatigue damage in steel plate tested under cyclic tensile load. The scope of study included both physical and computer simulations. First, fifteen steel plate specimens were repaired with CFRP overlays of various thicknesses to evaluate the effect of the axial stiffness ratio, *SR*, on fatigue crack propagation life and effective

122

stress range. Second, relationships between the stiffness of the CFRP overlays and steel substrate were identified such that future CFRP repair techniques can be proportioned to effectively slow or halt fatigue crack propagation in the steel substrate. Third, the effect of bond layer thickness and CFRP overlay thickness on the reduction in Hot Spot Stress (HSS) was evaluated using FE models. In this paper, HSS was defined as the stress at a distance half the thickness of the steel plate away from the point of peak stress, which occurred at the edge of the hole (Marquis and Kähönen 1995). HSS was used as an indicator of stress range, and consequently, as a measure of the effectiveness of various composite overlay configurations. This technique has been used in other companion studies aimed at examining fatigue performance and behavior of steel bridges (Hassel 2011; Kaan et al. 2012; Hartman et al. 2010). Finally, the effect of overlay stiffness on fatigue performance determined using the FE method was compared with observations from experimental results. FE simulations and experimental testing were performed on using specimens with the configuration shown in Figure B.1
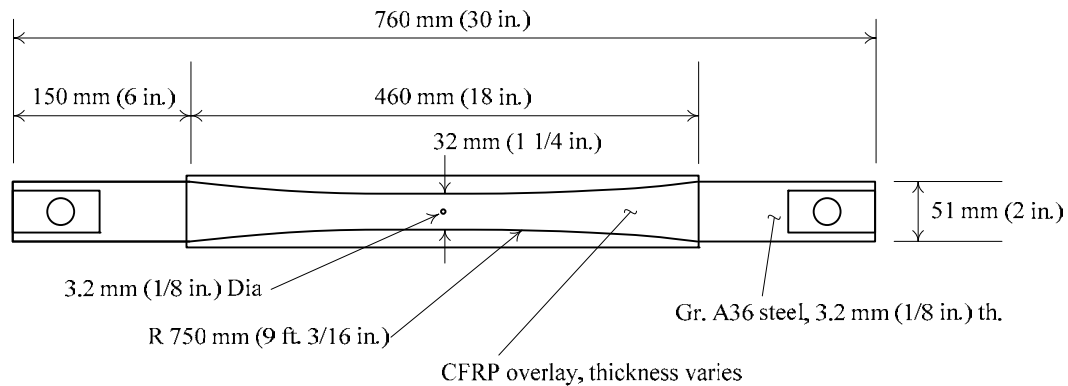
Figure B.1: Tension specimen dimensions [3.2 mm (0.13 in.) thick specimen]

B.1.5 Finite Element Simulations

There are several parameters that can affect the performance of CFRP overlays as a fatigue repair technique for steel plates. A parametric study was carried out to investigate changes in the stress demand in specimens repaired with varying E_{CFRP} and t_{CFRP}. The effects of bond layer properties on peel and shear stress demands were also evaluated.

123

B.1.5.1 Modeling Methodology

Finite element simulations of the specimens tested during the experimental program (Figure B.1) were carried out using the commercially-available finite element analysis software Abaqus version 6.8.2 (SIMULIA 2009). The models consisted of the steel specimen with a modulus of elasticity of 200 GPa (29,000 ksi), overlaid with 6 mm ($^1/_4$ in.) thick, 458 mm (18 in.) long CFRP plates with a modulus of elasticity of 83 GPa (12,000 ksi). The CFRP overlays were attached to each side of the specimen with a 0.6 mm (25-mil) thick resin interface having a modulus of elasticity of 2 GPa (300 ksi). The study was performed by changing a single parameter while maintaining the remaining parameters constant.

FE models were developed using linear-elastic materials, and meshes were assembled using eight-node brick elements. The mesh configuration for the steel specimen part is shown in Figure B.2(a). The mesh was configured using several regions with greater mesh density near the circular opening. The mesh configuration near the opening, presented in Figure B.2(b) and (c), consisted of two concentric circular regions, which allowed gradually increasing element size away from the circular opening. Boundaries between the different regions of the mesh are illustrated in Figure B.2(b). A convergence study was carried out and the results are illustrated in Figure B.2(d). Because the maximum principal HSS near the circular opening was found to be insensitive to mesh size for the range of mesh densities explored, a mesh with a minimum element size of 0.25 mm (0.1 in.), shown in Figure B.2(b), was used in the study.

Interfaces between the steel, resin, and CFRP parts of the model were defined using tie constraints. Motion was restrained at one end of the model while the other end was free to move only in the vertical direction. Two 10.5-kN (2.35-kip) loads were applied in the vertical direction at the unrestrained end, one on each face of the model, simulating as closely as possible the manner in which the text fixture transferred the load from the testing machine. This load corresponded to a nominal testing stress range of 221 MPa (32 ksi), based on the steel net section area.
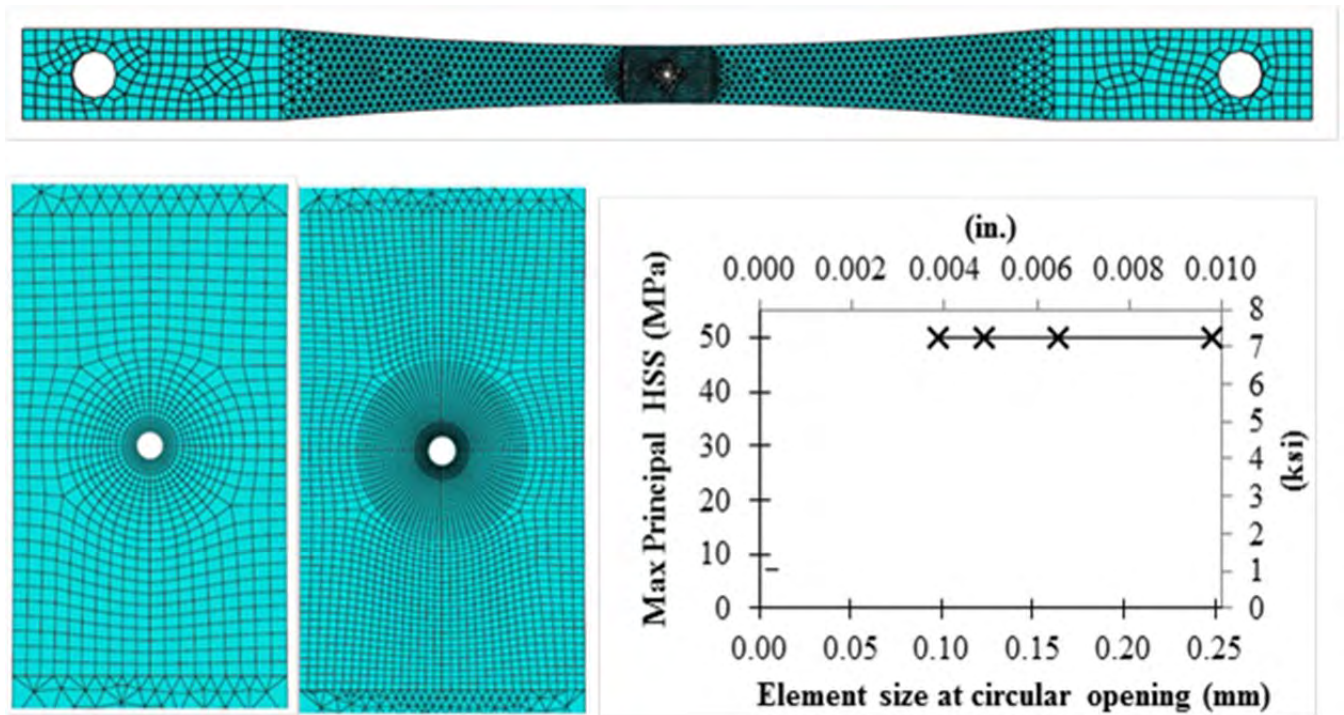
Figure B.2: Finite element
(a) Finite element model mesh (b) Mesh in the vicinity of the circular opening for an element size at the opening of 0.25 mm (0.10 in.) (c) Mesh in the vicinity of the circular opening for an element size at the opening of 0.12 mm (0.05 in.) (d) Effect of element size at the circular opening on maximum principal HSS.

It is recognized that there are studies in which FE simulations of composite repairs have been performed using nonlinear constitutive relationships. Given the objective and scope of this study, a simpler modeling approach was adopted with the goal of limiting the effect of modeling assumptions on the computational results and because the consistency between the experimental findings and simulation results did not warrant increasing the complexity of the computer simulations.

Comparisons of vulnerability to fatigue damage were performed on the basis of the maximum principal HSS as defined in Appendix B.1.4.

B.1.5.2 Effect of the Modulus of Elasticity of the CFRP

Six models were developed to investigate the effect of the modulus of elasticity of the CFRP, E_{CFRP}, on stress imposed on the steel specimen. E_{CFRP} was varied between 27 GPa (3,860 ksi) and 138 GPa (20,000 ksi) in increments of 28 GPa (4,000 ksi). The effect of E_{CFRP} on HSS in the steel specimen is shown in Table B.1. The relationship was found to be parabolic in nature

and inversely proportional, indicating that there was a significant advantage associated with using an overlay, even if E_{CFRP} was relatively low. As Table B.1 shows, HSS dropped by 58% with the introduction of an overlay with a very low modulus (26,600 MPa [3,860 ksi]) when compared with the unreinforced case. This data also shows that increasing E_{CFRP} resulted in diminishing returns, which is important to consider when determining optimal configuration of the overlay. Increasing E_{CFRP} by a factor of five, from 26,000 MPa (3,860 ksi) to 138,000 MPa (20,000 ksi), led to a reduction in HSS by a factor of approximately three. If infinite fatigue or propagation life can be achieved with a relatively inexpensive overlay, there is no economic incentive for using stiffer, and often much more expensive, fibers.

Table B.1: HSS vs. Modulus of Elasticity of the CFRP Overlay (E_{CFRP})

E_{CFRP} MPa (ksi)	0 (0)	26,600 (3,860)	55,200 (8,000)	82,737 (12,000)	110,300 (16,000)	137,900 (20,000)
HSS MPa (ksi)	249 (36)	105 (15)	67 (9.7)	49 (7.2)	39 (5.7)	32 4.7)

B.1.5.3   Effect of the Thickness of the CFRP Overlay

The effect of the CFRP overlay thickness, t_{CFRP}, on HSS was evaluated by varying the CFRP overlay thickness on each side of the steel plate using values of 1.6, 2.4, 3.2, 6.4, and 12.7 mm ($^1/_{16}$, $^3/_{32}$, $^1/_8$, $^1/_4$, and $^1/_2$ in.). Results for these variations are presented in Table B.2. The relationship between t_{CFRP} and maximum principal HSS was found to be inversely proportional and parabolic. The addition of the thinnest CFRP tested, 1.6 mm ($^1/_{16}$ in.) decreased the maximum principal HSS by a factor of two when compared to an unreinforced specimen. Similar to the relationship when E_{CFRP} was varied, increasing t_{CFRP} exhibited diminishing returns.

Table B.2: HSS vs. Thickness of the CFRP Overlays (t_{CFRP})

t_{CFRP} mm (in.)	0 (0)	1.6 (1/16)	2.4 (3/32)	3.2 (1/8)	6.4 (1/4)	12.7 (1/2)
HSS MPa (ksi)	249 (36)	126 (18)	99 (14)	85 (12.3)	51 (7.4)	28 4.1)

B.1.5.4 Ratio of Overlay Axial Stiffness to Steel Axial Stiffness

As discussed in Section B.1.2, one of the design parameters referenced in the literature for proportioning FRP patches is the ratio of axial stiffness of the composite patch to the axial stiffness of the underlying plate (Eq. 15.1). As Eq. 15.1 shows, this ratio may be modified by changing the modulus of elasticity of the FRP, thickness of the FRP, or both. The results presented in Table B.1 and B.2 were used to derive two curves showing the effect of the stiffness ratio SR on the maximum principal HSS in the steel substrate (Figure B.2). For each curve, one of the two parameters (E_{CFRP} or t_{CFRP}) was varied while maintaining the other constant. All other parameters were equivalent to that of the base model.

The results presented in Figure B.3 show that changing SR by changing E_{CFRP} had similar results than changing SR by altering t_{CFRP}. There was a common trend, in that sequential increments in E_{CFRP} and t_{CFRP} resulted in similar reductions of HSS. Therefore, how the axial stiffness parameter was changed did not significantly affect the magnitude of the stress reduction.

The parameter that did have a significant effect on the HSS demand was the SR. Using an SR of approximately 0.41 decreased the maximum principal HSS by a factor of two, when compared with the stress demand in an unreinforced specimen. Increasing the SR of the overlay by a factor of 8 to approximately 3.3 had a much smaller effect, decreasing the maximum principal HSS by a factor of 5. The results in Figure B.3 confirm that the effect of the stiffness ratio on HSS decreased with increasing in stiffness ratio, and that the reduction in HSS had dropped significantly at an SR of 1.0. For these specimens, modeled with a 221 MPa (32 ksi) testing stress range, it is the opinion of the authors increasing SR of the overlay beyond 1.0 has limited benefits.
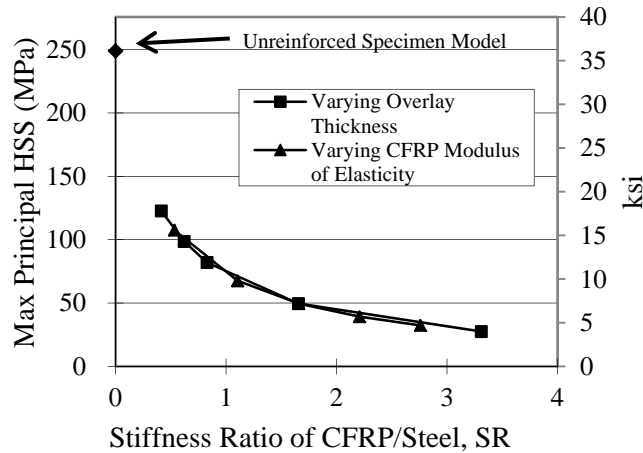
Figure B.3: Effect of stiffness ratio on maximum principal Hot Spot Stress in the steel

B.1.5.5   *Effect of Thickness of Bond Layer*

One of the parameters often neglected in FE simulations of retrofit measures with composite overlays is the flexibility inherent to the adhesive resin used to bond the overlay to the metal substrate. It has often been assumed that the thickness of such a layer is very small, and that there is perfect bond between the composite and the substrate (Sabelkin et al. 2006; Liu, Xiao, et al. 2009; Mall and Conley 2009). Explicit modeling of this layer provides an indication of the average shear demand on the resin and the tensile demand on the resin-steel interface, which can be used to gage the potential for debonding. Because the shear and tensile demands on the resin are affected by the thickness of the resin layer, this is an important parameter to consider in terms of fatigue and fatigue crack propagation life.
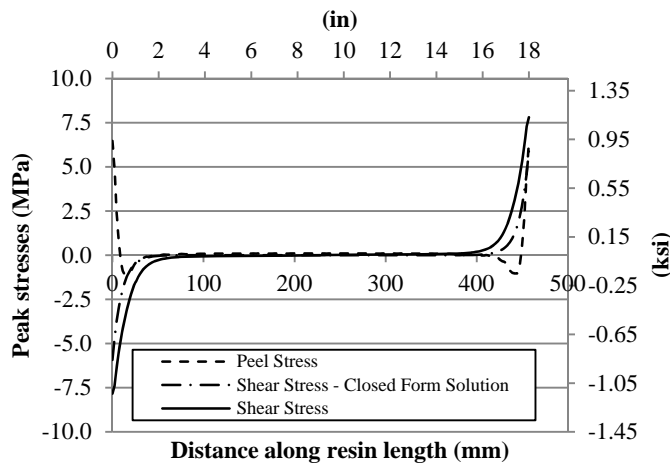
Figure B.4: Peak stresses along CFRP overlay on resin layer end of hole

Five different models were developed to investigate the effect of the thickness of the interface bond layer, t_{resin}, between the CFRP overlay and the steel substrate. The interface layer thickness was varied from 0.6 mm (20 mils) to 5 mm (200 mils). Results discussed by Alemdar (2011) found that the maximum principal HSS was not significantly affected by t_{resin}. However, another important design consideration is the effect of t_{resin} on the stress demand at the resin layer itself. This is important because maintaining bond between the composite and the steel is critical to the successful performance of the retrofit scheme, and higher stress demands increase the probability of fatigue failure at the interface. Figure B.4 shows the stress demand along the resin layer for a model with $t_{resin} = 0.6$ mm (20 mil). A closed-form solution for a plate with constant width and without a circular hole presented by Bocciarelli et al. (2009) is also included for reference. Figure B.4 shows that as expected based from the closed-form solution, the shear and peel stresses (out-of-plane stress) were relatively low along most of the interface. Stress demands were greatest at ends of the interface, which is the location considered to be the most susceptible to failure.

Figure B.5 presents the variation of peak shear and peel stresses as a function of the t_{resin}. Also in Figure B.5 is the closed-form solution presented by Bocciarelli. The results show that increasing t_{resin} from 0.6 mm (20 mil) to 5.0 mm (200 mil) caused a reduction in peak shear demand by approximately 66%. Figure B.5 also shows that the same increase in t_{resin} led to a reduction in peak peel stresses by approximately 50%. The trend observed for the peel stress was different from that observed for the shear stress in that the peel stress demand was relatively insensitive to t_{resin} for thicknesses less than 2.5 mm (100 mil), with a significant reduction in stress for t_{resin} greater than that. These data show that although the thickness of the interface layer may not be relevant to fatigue-crack propagation life due to the negligible effect on the stress range, it is a very important parameter in terms of the bond performance of the interface layer under cyclic loading.
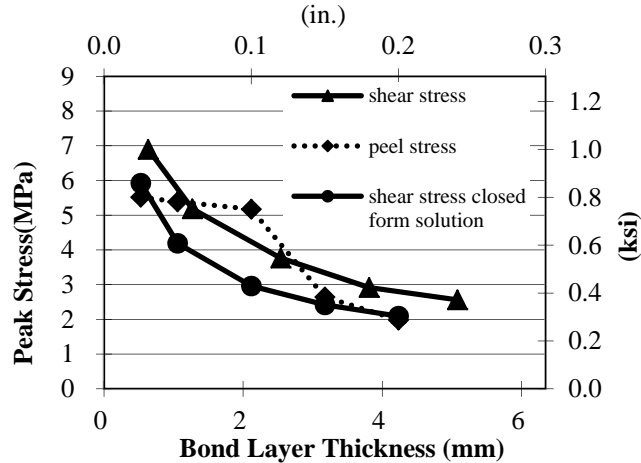
Figure B.5: Peak stress demand on CFRP layer as a function of resin layer thickness

B.1.6 Experimental Program

The primary goal of the experimental program was to evaluate the effect of stiffness ratio on fatigue crack propagation life of steel specimens with pre-existing fatigue cracks repaired using CFRP overlays. Fatigue cracks were propagated on each side of the drilled and reamed hole at the center of the specimen, shown in Figure B.1, until either of the cracks reached a length of approximately 7 mm (0.3 in.). After the initial crack length of 7 mm (0.3 in.) was reached, each specimen was repaired using CFRP overlays. Fifteen specimens were tested, shown in Table B.3.

Of the four parameters in Equation B.7 that could have been varied to alter the stiffness ratio, two were varied in this study: t_{CFRP} and the thickness of the steel plate, t_s. Testing was conducted at stress ranges of 166 MPa (24 ksi), 221 MPa (32 ksi) and 263 MPa (38 ksi), to evaluate effect of *SR* at various stress ranges.

Measured material properties are presented in Table B.4 and B.5. Coupon tests (ASTM 2008) from single-layered specimens showed that E_{CFRP} was approximately 83 GPa (12,000 ksi). Liu et al. (2009a and b) observed in their experiments that after the second layer of CFRP the strain demand quickly dropped; therefore, E_{CFRP} used for the computer simulations was selected to be between measured values for one and three layers. The modulus of elasticity of the 9412 Hysol® resin, E_{resin}, was also measured using coupon tests (Table B.5) performed as prescribed by ASTM (2008). The measured E_{resin} was 2.1 GPa (300 ksi).

130

Table B.3: Specimen Test Matrix and Results

Specimen Designation	Specimen Thickness mm (in.)	CFRP Overlay Thickness mm (in.)	Stress Range MPa (ksi)	Fatigue Crack Propagation Life
F15	3 ($^1/_8$)	1.6 ($^1/_{16}$)	263 (38)	18,900
F3	3 ($^1/_8$)	1.6 ($^1/_{16}$)	221 (32)	60,000
F6	3 ($^1/_8$)	1.6 ($^1/_{16}$)	166 (24)	340,700
Pick12	3 ($^1/_8$)	2.4 ($^3/_{32}$)	221 (32)	271,100
Pick11	3 ($^1/_8$)	3.2 ($^1/_8$)	263 (38)	95,100
F14	3 ($^1/_8$)	3.2 ($^1/_8$)	221 (32)	313,050
F2	3 ($^1/_8$)	3.2 ($^1/_8$)	166 (24)	1,450,095
Pick10	3 ($^1/_8$)	6.4 ($^1/_4$)	263 (38)	282,550
Pick13	3 ($^1/_8$)	6.4 ($^1/_4$)	221 (32)	Run-Out
Pick7	3 ($^1/_8$)	6.4 ($^1/_4$)	166 (24)	Run-Out
F27	3 ($^1/_8$)	12.8 ($^1/_2$)	221 (32)	Run-Out
F4-25	6 ($^1/_4$)	1.6 ($^1/_{16}$)	221 (32)	15,600
F4-21	6 ($^1/_4$)	3.2 ($^1/_8$)	221 (32)	160,150
F4-23	6 ($^1/_4$)	6.4 ($^1/_4$)	221 (32)	571,650
F4-20	6 ($^1/_4$)	12.8 ($^1/_2$)	221 (32)	Run-Out

Table B.4: Measured Material Properties for Continuous CFRP

No. of Layers in Coupon	No. of Coupons	Avg. Modulus of Elasticity *GPa (ksi)*	Std. Dev. *GPa (ksi)*
1	3	85.8 (12,440)	10.0 (1,450)
3	4	75.3 (10,930)	10.9 (1,580)
5	3	61.7 (8,940)	0.3 (42.0)

Table B.5: Measured Material Properties for 9412 Hysol Resin

Coupon Thickness *mm (in.)*	No. of Coupons	Avg. Modulus of Elasticity *GPa (ksi)*	Std. Dev. *GPa (ksi)*
6 (1/4)	6	2.1 (303)	0.2 (25)

131

B.1.6.1   Steel Specimen Dimensions

The specimens were fabricated using grade A36 steel and were either 3 mm ($^1/_8$ in.) or 6 mm ($^1/_4$ in.) thick. For specimens with a thickness of 3 mm ($^1/_8$ in.), the measured average yield strength was 319 MPa (46 ksi), and the measured tensile strength was 381 MPa (55 ksi). For specimens with a thickness of 6 mm ($^1/_4$ in.), the measured average yield strength was 335 MPa (48 ksi), and the measured tensile strength was 495 MPa (72 ksi) (Crain 2010).

Specimen dimensions for 3 mm ($^1/_8$ in.) thick specimens are shown in Figure B.1. There were three dimensions changed for 6 mm ($^1/_4$ in.) thick specimens with respect to those shown in Figure B.1. First, the width at each end was 63.5 mm (2.5 in.) instead of 60.8 mm (2.0 in.). Second, the width at the reduced net section was 44.5 mm (1.75 in.) instead of 31.8 mm (1.25 in.). Third, the diameter of the drilled and reamed hole at the specimen center was equal to the thickness of the specimen, 6 mm ($^1/_4$ in.).

B.1.6.2   Fabrication and Attachment of the Multi-Layered CFRP Overlays

The multi-layered CFRP overlays were pre-fabricated and subsequently attached to the steel specimens. Step-by-step instructions, photographs and diagrams illustrating the fabrication process are presented by Alemdar (2011) and Gangel (2012). Each CFRP overlay consisted of multiple layers of bidirectional pre-impregnated carbon fiber plies. Scotch-Weld Epoxy adhesive (1838 B/A Green) was used between certain layers to ensure that there was a sufficient amount of resin to prevent voids from occurring during the curing process. Table B.6 summarizes the number of carbon fiber plies and Scotch Weld Epoxy adhesive layers used in each CFRP overlay.

The overlays were fabricated using a mold consisting of aluminum plates placed between bolted steel plates. Pre-impregnated carbon fiber plies were cut to dimensions of approximately 457 x 152 mm (18 x 6 in.), which was double the size of the overlays. CFRP sheets were placed on the bottom steel plate of the mold, and were added one layer at a time. A single sheet of Scotch-Weld Epoxy adhesive (1838 B/A Green) resin with the same dimensions was added, following the schedule presented in Table B.6. The overlay was surrounded by an aluminum spacer with a thickness equal to that of the desired overlay thickness. The top steel plate of the mold was then placed on top of the CFRP stack, and pressure was applied by tightening the bolts around the perimeter of the mold to reach the target thickness. Then, the overlay was placed in a

curing oven preheated to a temperature of 175 C (347 *F)*. Overlays were cured inside the mold for three hours, and subsequently allowed to cure at room temperature for 48 hours. After the curing process was completed, the CFRP overlays were taken out of the metal molds and cut to final dimensions of 457 x 64 mm (18 x 2.5 in.) using a diamond saw. Sand paper (grade 400) was used to smooth the edges of the CFRP overlays.

To develop adequate bond, the steel surface was prepared by a process of abrading and cleaning. Abrading consisted of roughening of the surface with a hand grinder to achieve a surface roughness of approximately 0.8 mm (30 mils). After abrading, cleaning of the surface was performed using acetone and methanol. Overlays were attached to the steel specimens using Hysol® 9412 epoxy resin, which has a nominal shear strength of 28 MPa (4 ksi) (Henkel Corporation 2001). The thickness of the Hysol® layer was 0.6 mm (24 mil), maintained during fabrication by using six spacers evenly distributed throughout the interface. Drafting tape surrounding the steel plate was used to prevent leaking of the Hysol® resin, and pressure was applied to maintain t_{resin} = 0.6 mm (24 mils). After two days of room-temperature curing the interface bond layer, the specimen was cleaned of remnant resin using a chisel and a heat gun.

Table B.6: Fabrication of Multi-Layered CFRP Overlays

Overlay Thickness mm (in.)	Single Carbon Fiber Plies	Scotch Weld Epoxy adhesive	Placement of Adhesive
1.6 ($^1/_{16}$)	2	1	After 1st ply
2.4 ($^3/_{32}$)	3	1	After 2rd ply
3.2 ($^1/_8$)	4	2	After 2rd ply
6.4 ($^1/_4$)	8	3	After 3rd and 5th ply
12.8 ($^1/_2$)	16	4	After 4th, 8th, and 12th ply

B.1.6.3   Test procedure

A cyclic tensile load was applied at the ends of the specimen using an MTS closed-loop servo-controlled loading system. The stress range applied to the steel specimen, $\Delta\sigma_{st,}$ was determined based on Equation B.2.

$$\Delta\sigma_{st} = \frac{F_{actuator}}{A_{net,st}} \qquad\qquad \textbf{Equation B.2}$$

where $F_{actuator}$ is the force or load recorded by the actuator, and $A_{net,st}$ is the nominal net cross sectional area of the steel at the reduced cross-section less the area of the drilled hole. These values, although not representative of the peak stress demand, were adopted to simplify the comparison between various specimens. The ratio of minimum to maximum stress was maintained constant at $R = 0.1$. The rate of fatigue crack propagation was evaluated at three different stress ranges, 262 MPa (38 ksi), 221 MPa (32 ksi) and 166 MPa (24 ksi).

The propagation life of the steel specimens used in this study was calculated for different stress range demands based on established theoretical expressions. Theoretical crack lengths at a given number of cycles were determined using the following equation presented by Barsom and Rolfe (1999):

$$\frac{da}{dN} = A(\Delta K)^m \qquad\qquad \textbf{Equation B.3}$$

where A and m are properties constant for a material, ΔK is the stress intensity factor range, a is crack length, and da is the change in crack length. Material constants of $A=3.6 \times 10^{-10}$ and $m=3$ were adopted, which correspond to values for ferrite-pearlite steel (Barsom and Rolfe, 1999). Because fatigue cracks extended from a round hole on a plate with a finite width, ΔK was calculated using the following equation (Barsom and Rolfe 1999):

$$\Delta K = \Delta\sigma \sqrt{\frac{\pi \times a_{avg}}{Q}} \times f\left(\frac{a}{r}\right) x f\left(\frac{a}{b}\right) \qquad\qquad \textbf{Equation B.4}$$

where $\Delta\sigma$ is the applied testing stress range, a_{avg} is the average crack length between incremental calculation steps, Q is the flaw-shape parameter (taken as 1.0 in this case), $f(a/r)$ is a function of the radius of the drilled hole to crack length, and $f(a/b)$ is a function of the crack length to finite width of the tensile specimen. Alemdar (2011) showed that good agreement was

found between the calculated and measured crack progressions for unretrofitted specimens based on Equations B.3 and B.4.

A comparison between observed fatigue-crack propagation rate of the specimens with CFRP overlays and the calculated fatigue-crack propagation rate in unreinforced specimens with low stress demands is presented in Figure B.6. As shown in Figure B.6, the crack propagation rate of a specimen repaired with CFRP overlays subjected to a stress range of 166 MPa (24 ksi) was similar to that of an unrepaired specimen subjected to a stress range of 35 MPa (5 ksi) based on theoretical values. These results indicate that the presence of the overlay resulted in a reduction of approximately 80% in the stress range. The test of the specimen repaired with multi-layered CFRP overlay subjected to a stress range of 166 MPa (24 ksi) was stopped after 4 million cycles, after crack growth started to become noticeable. Had the fatigue crack in this specimen continued to propagate at the theoretical rate for an unreinforced specimen under a stress range of 35 MPa (5 ksi), it would have reached a crack length of 7.6 mm (0.3 in.) at approximately 6 million cycles. A similarly loaded unrepaired steel specimen reached a crack length of 7.6 mm (0.3 in.) at only 50,000 cycles (Alemdar, 2011).
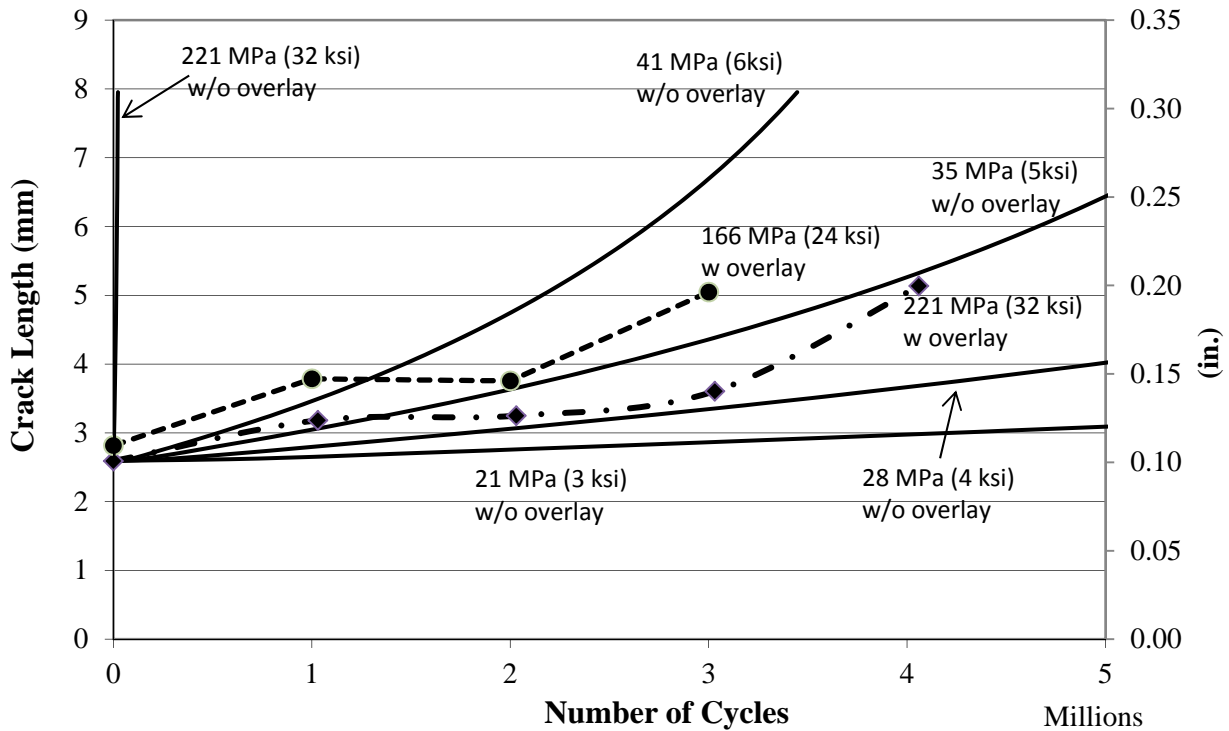
Figure B.6: Crack progression in 3 mm ($^1/_{8\ in.}$) thick specimens
Solid lines are added for comparison and correspond to theoretical crack progressions
calculated using Equation B.4 with material constants of A=3.6x10^{-10} and m=3 for various
stress ranges in a specimen configuration without overlays.

Testing of the remaining specimens with CFRP overlays was carried out without removing the overlays for inspection so that that any cumulative damage to the interface layer and the composite overlay could be directly accounted for in the test results. Each test was terminated after the specimens reached failure or run-out. Failure of these specimens was defined as fatigue crack propagation completely through the width of the steel specimen; however, crack propagation and failure could not be tracked visually due to the bonded overlays. Instead, failure was indicated by a decrease in the percent change in stiffness of the system. The percent change in stiffness was calculated using the following equation:

% change in K = [($\delta L/\delta P$) - K_{max}] / K_{max}   **Equation B.5**

where K is the stiffness of the combined steel and CFRP overlays, δL is the change in load placed on the specimen, δP is the change in position from the testing machine, and K_{max} is

136

the maximum stiffness recorded during testing. Run-out was defined as exceeding the AASHTO S-N curve for a Category A detail at the corresponding nominal stress range (AASHTO 2013).

The relationship between the change in stiffness and the number of cycles for 6 mm ($^1/_4$ in.) thick specimens tested at 221 MPa (32 ksi) are presented in Figure B.7. The relationship between the stiffness and the number of cycles for all the specimens tested in the study is reported by Gangel (2012) and Alemdar (2011).
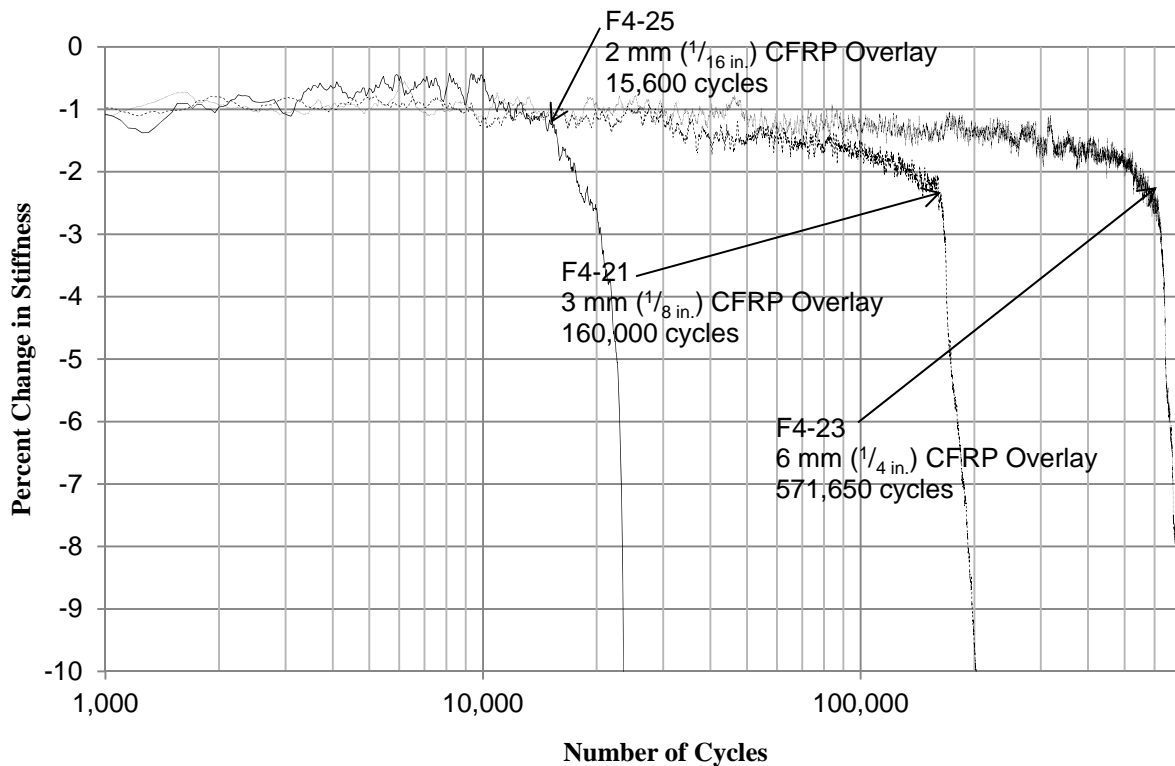
Figure B.7: Percent change in stiffness of 6 mm ($^1/_4$ in.) thick specimens tested at 221 MPa (32 ksi).

B.1.7 Experimental Results

The fatigue-crack propagation life of the steel substrate from an initial crack length of 7.6 mm (0.3 in.) to complete failure in the steel was determined based on the monitored change in stiffness calculated using Equation B.5. For all specimens a significant increase in compliance was observed at a given number of cycles during testing (Figure B.7). Because testing was performed under load control, any increase in compliance had to be caused by softening of the specimens, which is indicative of damage. An increase in compliance could be caused by loss of

bond, damage in the composite overlays, or a reduction in the net cross sectional area of the steel specimen. Because the neither the composite overlays nor the interface layer showed signs of damage or distress, it was hypothesized that gradual increases in compliance were caused primarily by the reduction of the net cross sectional area of the steel specimen. Propagation of the fatigue crack through the entire cross section of the specimen led to 100% of the load being transferred through the composite overlays. This new load path caused a rapid increase in the damage to the overlays in the vicinity of the fatigue crack and to local loss of bond, leading to a large increase in compliance. The number of cycles at which a sudden and significant change in compliance was observed was adopted as the fatigue propagation life for the specimen. Upon the conclusion of testing, the CFRP overlays were removed to inspect the steel specimen and confirm that the fatigue crack had in fact propagated through the entire net section of the steel. The number cycles to failure for each specimen determined in this manner are summarized in Table B.3 and Figure B.8.

For Specimens Pick 13, Pick 7, F27, and F4-20, a significant change in compliance was never observed and these specimens were classified as run-out. The stress reduction in the steel due to the alternate load path provided by the CFRP overlay was sufficient to drive the demand below the fatigue crack propagation threshold (Barsom and Rolfe 1999). The composite overlays were removed for inspection after testing was complete, and it was confirmed that the fatigue cracks had not propagated fully through the steel cross-sections.
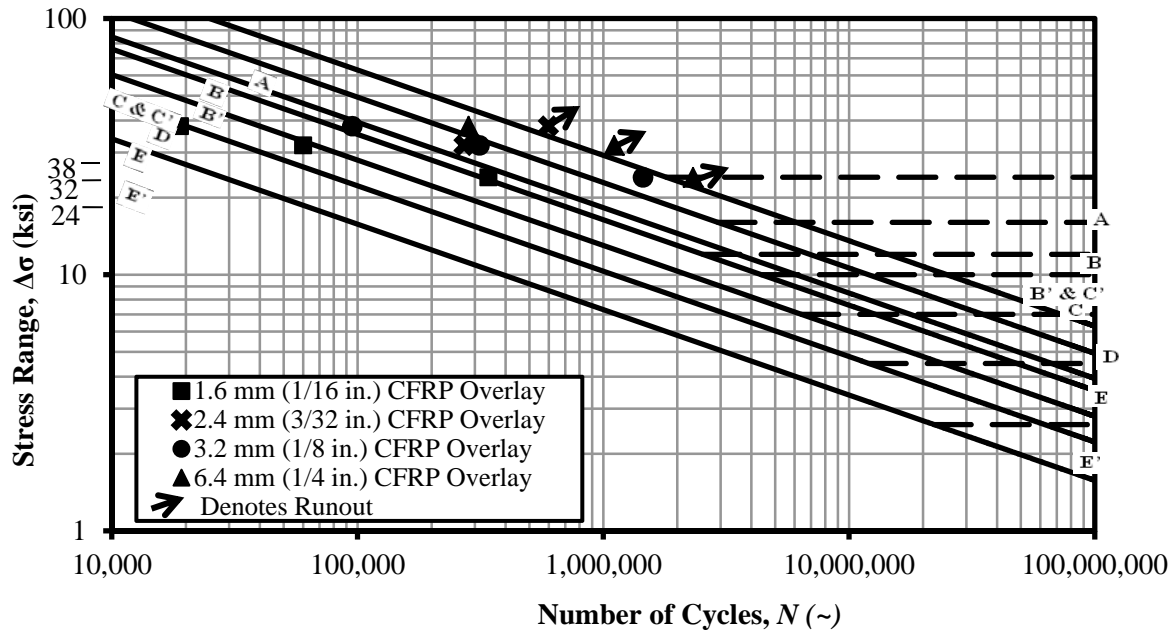
(a)
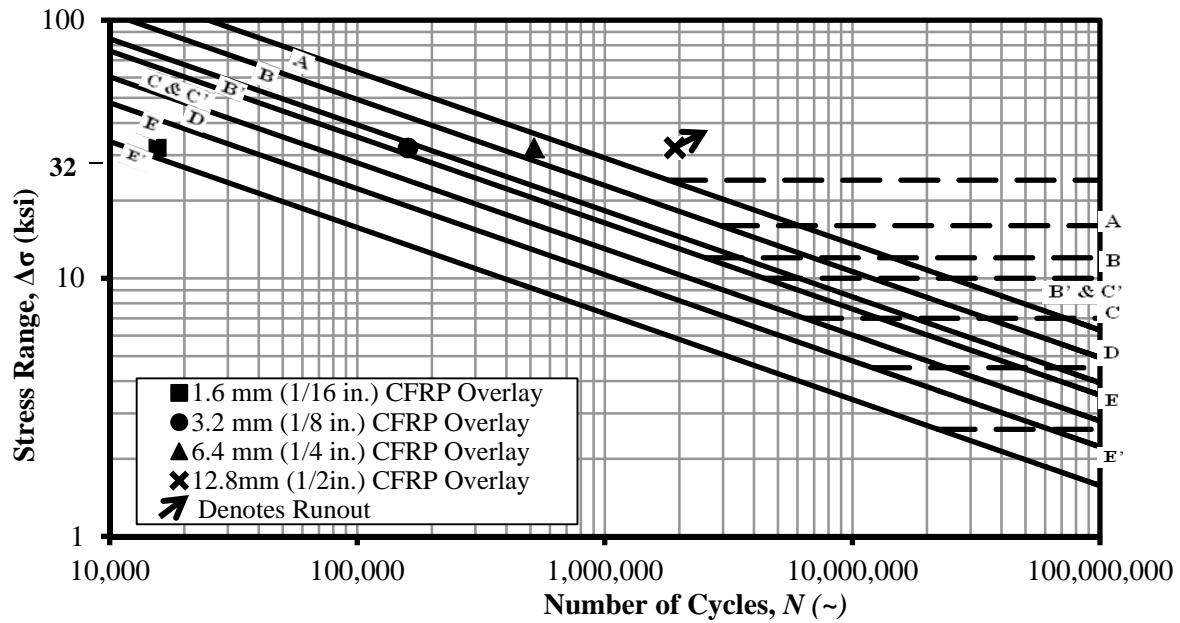
(b)

**Figure B.8: S-N diagram for propagation life
for (a) 3 mm (.12 in.) thick specimens and (b) 6 mm (.24 in.) thick specimens**

139

The fatigue-crack propagation lives determined above were compared on the basis of the axial stiffness ratio. The value of *SR* was determined for each specimen based on $E_{CFRP} = 83$ GPa (12,000 ksi), the measured thickness of the steel, t_s, the CFRP overlay thickness used, t_{CFRP}, and the modulus of elasticity of steel, E_s (200 GPa, 29,000 ksi). Figure B.9 shows the fatigue-crack propagation life of each specimen vs. the stiffness ratio, *SR*. For specimens that reached run-out (the last point of each curve, outside the range of the graph), the number of cycles to failure was extrapolated using accepted models of theoretical crack propagation presented by Barsom and Rolfe (1999). Extrapolated points (not shown) for the four curves were 22.9, 6.8, 3.9, and 3.2 million cycles, corresponding to *SR* values of 1.66, 1.66, 1.66, and 3.2, respectively.

Figure B.9 shows that the effect of the *SR* was dependent on the applied stress range. For a specific stiffness ratio, as the stress range increased the fatigue life decreased, as expected. However, this trend was not proportional. Much greater improvement was observed when the stress range decreased from 221 MPa (32 ksi) to 166 MPa (24 ksi) than when the stress range decreased from 263 MPa (38 ksi) to 221 MPa (32 ksi).
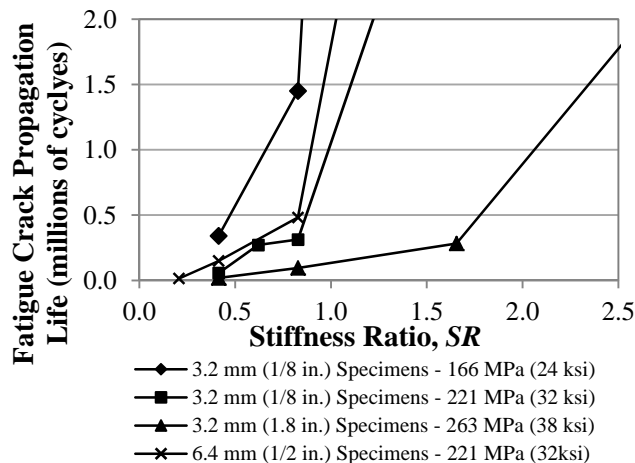
Figure B.9: Fatigue-crack propagation life for all specimens treated with CFRP overlays and an initial crack length of 7 mm (0.3 in.)

Figure B.9 also shows a relationship between propagation life and *SR* that may be approximated as bilinear. For all specimens, the fatigue-crack propagation life increased as the stiffness ratio increased. For each stress range there was a stiffness ratio at which the slope of the

curve had a sudden increase, trending towards infinity. Past this point, small increases in the stiffness ratio resulted in propagation lives that vastly exceeded run-out. It is clear from Figure B.9 that the critical *SR* at which each set of data trended towards infinity increased with stress range. The critical *SR* for specimens tested at stress ranges of 166 MPa (24 ksi), 221 MPa (32 ksi), and 263 MPa (38 ksi) ksi were approximately 0.8, 1.0, and 1.6, respectively, regardless of specimen thickness. These results indicate that as stress range increases, the stiffness ratio must be increased to achieve infinite fatigue life.

Because the critical width of the 6 mm (¼ in.) thick specimens differed from that of the 3 mm ($^1/_8$ in.) thick specimens, failure of the former specimens was taken as the number of cycles at which the crack reached a length of 14 mm ($^9/_{16}$ in.). Therefore, the propagation life used in the comparisons corresponds to the same crack growth for all specimens, regardless of specimen thickness, allowing a direct comparison between the two. A direct comparison between the 3 mm ($^1/_8$ in.) thick and the 6 mm (¼ in.) thick specimens tested at 221 MPa (32 ksi) (Figure B.9) shows that for the same stiffness ratio the thicker specimen had the greater propagation life. However, both specimens had approximately the same critical stiffness ratio.

Given the relatively large initial crack size of 7.6 mm (0.3 in.) relative to the remaining steel net section, control specimens were not tested in this study as their fatigue lives would have been quite low in the unreinforced condition. However, theoretical crack propagation lives for un-retrofitted specimens were determined using Equation B.3. With the calculation of *ΔK* from Equation B.4, the theoretical number of cycles to failure of an unretrofitted specimen can be found from Equation B.3 if the change in crack length (*da*) is set as the distance from an initial crack length of 7.6 mm (0.3 in.) to the edge of the specimen. The results of this theoretical fatigue crack propagation life for un-retrofitted specimens are shown in Table B.7 designated as having a stiffness ratio of 0.

Table B.7: Theoretical Fatigue Life of Un-Retrofitted Specimen and Comparative Increase in Fatigue Life of CFRP Repaired Specimens

Description	Stiffness Ratio	3 mm (1/8 in.) steel specimens			6 mm (1/4 in.) steel specimens		
		Stress Range			*Stress Range*		
		166 MPa (24 ksi)	*221 MPa (32 ksi)*	*263 MPa (38 ksi)*	*166 MPa (24 ksi)*	*221 MPa (32 ksi)*	*263 MPa (38 ksi)*
Theoretical fatigue crack propagation life (cycles) caclulated using Equations 3 and 4	0	6,891	2,907	1,736	10,423	4,397	2,625
Increase in fatigue life from theoretical values to measured values	0.21	--	--	--	--	3	--
	0.41	49.4	19.2	10.9	--	34	--
	0.62	--	93.3	--	--	--	--
	0.83	210.4	107.7	54.8	--	109.5	--
	1.66	run-out	run-out	162.8	--	run-out	--
	3.31	--	--	run-out	--	--	--

After the theoretical fatigue crack propagation life of unretrofitted specimens was calculated for an initial crack length of 7.6 mm (0.3 in.), it was compared with the fatigue crack propagation lives of CFRP repaired specimens, which are presented in Table B.3. The ratio of observed fatigue crack propagation life of the various retrofitted specimens to calculated fatigue life of the unretrofitted specimen is presented in Table B.7. Table B.7 shows that the applied stress range played a crucial role in the level of fatigue life improvement that was achieved through use of CFRP overlays. When the stress range decreased 16%, from 263 MPa (38 ksi) to 221 (32 ksi), the ratio of increase in fatigue crack propagation life was approximately doubled for stiffness ratios of 0.41 and 0.83. The same held true when the applied stress range was decreased form 221 MPa (32 ksi) to 166 MPa (24 ksi). Although this means that a CFRP overlay repair was more effective at a lower stress range, the improvements observed at very high stress ranges are still promising. For a specimen with a thickness of 6 mm ($^1/_4$ in.) tested at a stress range of 221 MPa (32 ksi), the smallest stiffness ratio tested (0.21) the fatigue propagation life increased by a factor of 3 when compared with the theoretical fatigue crack propagation life of an unretrofitted specimen. At 263 MPa (38 ksi) and a stiffness ratio of 0.41, the fatigue life of the

specimen with the same thickness increased by a factor of 10.9. For specimens with a thickness of 3 mm ($^1/_8$ in.), increasing the stiffness ratio to 1.66 at 263 MPa (38 ksi) increased the fatigue life by a factor of 162, when compared with that of an unretrofitted specimen.

Drastic increases in fatigue crack propagation life can be attributed to the reduced applied stress imposed on the steel. The stress ranges corresponding to the fatigue crack propagation lives presented in Table B.3 were determined using the relationships from Equations B.3 and B.4. For example, specimen F15 was tested at a stress range of 263 MPa (38 ksi) based on the measured cross-section of the steel; however, the experimental fatigue crack propagation life presented in Table B.3 corresponds to an effective applied stress range of approximately 118 MPa (17 ksi) based on the measured cross-section of the steel. Figure B.10 presents the effective stress ranges for all steel tensile specimens based on their calculated stiffness ratio. The reductions in stress follow the same patterns determined during the FE analysis and shown in Figure B.3. Both Figures B.3 and B.10 show a relationship between stiffness ratio and stress reduction that is parabolic and inversely related in nature.
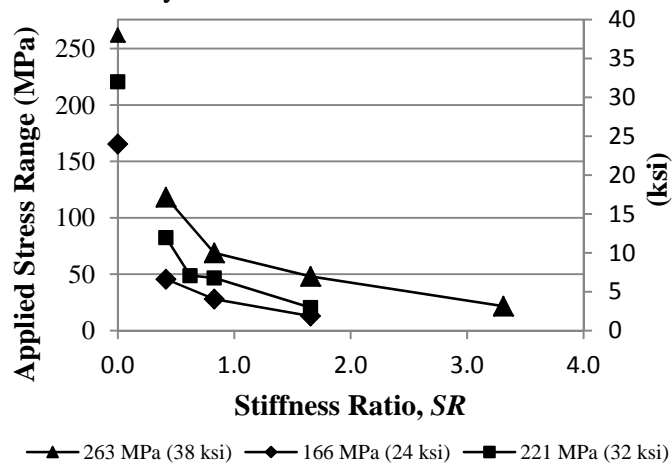
Figure B.10: Equivalent applied stress of all Specimens treated with CFRP overlays and an initial crack length of 7 mm (0.3 in.)

B.1.7.2   Specimen Debond Behavior

Of the 15 specimens tested with initial crack lengths of 0.3 in., only one specimen, F4-20, experienced partial debonding between the steel and CFRP overlays. This specimen represented the thickest steel plate tested, combined with the thickest CFRP overlay tested. This suggests that the combination of very thick components led to independent behavior in terms of deformation,

instead of system deformation. It is hypothesized that this behavior resulted in fatigue crack initiation in the resin layer at the bottom and top of the CFRP overlay, and subsequent crack propagation towards the center of the length of the overlay. The fatigue crack in the bond layer was noticed at a length of approximately 38 mm (1.5 in.). At this point, a steel collar consisting of two steel plates bolted around each end of the specimen was attached to prevent further debonding (Gangel, 2012). The debonding never approached the region of the fatigue crack in the steel since it was arrested with the steel collar installation; therefore, the results from this specimen are presented as comparable to the others in the study.

B.1.8 Conclusions

Results of an experimental and analytical study examining the use of CFRP overlays to repair fatigue cracks in steel plates has resulted in the following conclusions:

- Experimental results showed that as stress range was increased, a greater stiffness ratio was required for the fatigue crack propagation life to tend towards infinity. At 166 MPa (24 ksi), 221 MPa (32 ksi), and 263 MPa (38 ksi) the number of cycles to failure tended towards infinity at stiffness ratios of 0.8, 1.0, and 1.6, respectively.
- Both FE analysis and experimental results showed a diminishing effect on stress demand as the stiffness ratio increased. Based on these results it is the opinion of the authors that the greatest benefit of using overlays to reduce the stress demand is achieved for stiffness ratios below unity.
- Experimental results showed that bonding of pre-fabricated multi-layered CFRP overlays increased the theoretical fatigue crack propagation life of unretrofitted steel specimens by at least three times and up to 162 times before experimental specimens reached run-out.
- The observed increase in fatigue-crack propagation life matched or was significantly higher than values ranging between 3 and 10 reported in previous studies on aluminum plates, steel plates, and steel beams. The main difference between the overlays used in this study and those used in other studies is that the stiffness ratio *SR* was significantly higher in this study than identified in previous literature.

Implications of the fundamental research described herein are significant. Research presented within this article has shown that use of CFRP overlays to repair cracks in steel members can be a highly effective means of reducing the stress demand and greatly prolonging the fatigue-crack propagation life of steel substrate. This work has provided a basis for proportioning CFRP overlays for effectiveness in halting/slowing fatigue crack propagation, based upon nominal stress range and the stiffness ratio between the overlay and the steel.

Future research is advised to better understand the demands upon and the behavior of CFRP overlays bonded to steel substrate. Topics that should be studied include testing thicker steel plates representative of bridge girder webs and investigating wide steel plates with a bonded overlay element of lesser width.

B.1.9 References

AASHTO (2013). 2013 Interim Revisions to the AASHTO LRFD Bridge Design Specifications. 6th ed. American Association of State Highway and Transportation Officials, Washington, D.C.

Alemdar, F. (2011). Repair of Bridge Steel Girders Damaged by Distortion-Induced Fatigue. (Ph.D. dissertation). University of Kansas, Lawrence, KS.

ASTM D3039/D3039M-08 (2008). Standard Test Method for Tensile Properties of Polymer Matrix Composite Materials. ASTM International, West Conshohocken, PA.

Barsom, J. M. and Rolfe, S. T. (1999). "Fatigue and Fracture Behavior of Welded Components." Chap. 10 in Fracture and Fatigue Control in Structures: Applications of Fracture Mechanics. 3rd ed. ASTM, West Conshohocken, PA.

Bocciarelli, M., Colombi, P., Fava, G., and Poggi, C. (2009). "Fatigue Performance of Tensile Steel Members Strengthened with CFRP Plates." Composite Structures, 87, 334-343.

Crain, J. (2010). Fatigue Enhancement of Undersized, Drilled Crack-Stop Holes. (Master's thesis). University of Kansas, Lawrence, KS.

Gangel, R. (2012). Use of CFRP Overlays to Repair Fatigue Damage in Steel Bridge Girders and Components. (Master's thesis). University of Kansas, Lawrence, KS.

Hartman, A., Hassel, H., Adams, C., Bennett, C., Matamoros, A., and Rolfe, S. (2010). "Effects of Lateral Bracing Placement and Skew on Distortion-Induced Fatigue in Steel Bridges," Transportation Research Record 2200, 62-68 Transportation Research Board, National Research Council, Washington, D.C.

Hassel, H. L. (2011). An Analytical Evaluation of Distortion-Induced Fatigue in Steel Bridges. (Master's thesis). University of Kansas, Lawrence, KS.

Henkel Corporation (2001). Loctite® Hysol® 9412 Epoxy Adhesive Product Description Sheet. Retrieved from http://www.henkelna.com/product-search-1554.htm?nodeid=8797873373185.

Kaan, B. N., Alemdar, F., Bennett, C. R., Matamoros, A., Barrett-Gonzalez, R., and Rolfe, S. (2012). "Fatigue Enhancement of Welded Details in Steel Bridges using CFRP Overlay Elements." Journal of Composites for Construction, 16(2), 138-149.

Lee, W. Y. and Lee, J. J. (2004). "Successive 3D FE Analysis Technique for Characterization of Fatigue Crack Growth Behavior in Composite-Repaired Aluminum Plate." Composite Structures, 66(1-4), 513-520.

Liu, H. B., Al-Mahaidi, R., and Zhao, X. L. (2009). "Experimental Study of Fatigue Crack Growth Behaviour in Adhesively Reinforced Steel Structures." Composite Structures, 90(1), 12-20.

Liu, H. B., Xiao, Z. G., Zhao, X. L., and Al-Mahaidi, R. (2009). "Prediction of Fatigue Life for CFRP-Strengthened Steel Plates." Thin-Walled Structures, 47(10), 1069-1077.

Mall, S. and Conley, D. S. (2009). "Modeling and Validation of Composite Patch Repair to Cracked Thick and Thin Metallic Panels." Composites Part A: Applied Science and Manufacturing, 40(9), 1331-1339.

Marquis, G. and Kähönen, A. (1995). Fatigue Testing and Analysis using the Hot Spot Method. VTT Publications no. 239. Technical Research Centre of Finland.

Naboulsi, S. and Mall, S. (1996). "Modeling of a Cracked Metallic Structure with Bonded Composite Patch using the Three Layer Technique." Composite Structures, 35(3), 295-308.

Roddis, W. M. K. and Zhao, Y. (2001). "Out-of-Plane Fatigue Cracking in Welded Steel Bridges: Why It Happened and How It Can Be Repaired." Welding Innovation, 18(2), 2-7.

Roy, M., Lang, C., and May, I. (2009). "Modelling Composite Repairs to Cracked Metal Structures." Proceedings of the Institution of Civil Engineers (ICE)-Structures and Buildings, 162(2), 107-113.

Sabelkin, V., Mall, S., and Avram, J. B. (2006). "Fatigue Crack Growth Analysis of Stiffened Cracked Panel Repaired with Bonded Composite Patch." Engineering Fracture Mechanics, 73(11), 1553-1567.

Schubbe, J. J. and Mall, S. (1999). "Modeling of Cracked Thick Metallic Structure with Bonded Composite Patch Repair using Three-Layer Technique." Composite Structures, 45(3), 185-193.

SIMULIA (2009). Abaqus FEA, Version 6.8.2. Providence, RI. http://www.simulia.com.

Tavakkolizadeh, M. and Saadatmanesh, H. (2003). "Fatigue Strength of Steel Girders Strengthened with Carbon Fiber Reinforced Polymer Patch." Journal of Structural Engineering, 129(2), 186-196.

Umamaheswar, T. V. R. S. and Singh, R. (1999). "Modelling of a Patch Repair to a Thin Cracked Sheet." Engineering Fracture Mechanics, 62(2), 267-289.

Wang, Q.Y., Li, T. and Ning, J. X. (2002). "Fatigue Crack Growth Behavior of Bonded Composite Repairs." Third International Conference on Experimental Mechanics, Proceedings of SPIE 4537.

B.2: Fatigue Enhancement of Welded Details in Steel Bridges Using Carbon Fiber Reinforced Polymer Overlay Elements

Benjamin N. Kaan[8]

Fatih Alemdar[9]

Caroline R. Bennett[10]

Adolfo Matamoros[11]

Ron Barrett-Gonzalez[12]

Stan Rolfe[13]

B.2.1 Abstract

Carbon fiber reinforced polymer (CFRP) overlay elements were developed with the purpose of enhancing the fatigue performance of welded connections in steel bridge girders. Fatigue tests of seven specimens, including four CFRP-strengthened specimens and three control specimens, were performed to quantify the effect of the CFRP overlays on the fatigue crack initiation lives of the welded connections. Results showed that bonding of CFRP overlays significantly reduced the stress demand on welded connections tested at high stress ranges, leading to a large increase of the fatigue crack initiation life. The level of effectiveness of the CFRP overlay elements to extend fatigue crack initiation lives of the tested connections was found to be primarily affected by bond strength under cyclic loading; bond strength was found to be dependent on the composition and thickness of the resin layer used to bond the CFRP to the steel. Using the AASHTO fatigue design curves as a frame of reference, it was found that when an optimal bond composition was employed, reinforcing the welded connections with CFRP overlays led to a change in fatigue performance category from that consistent with Category E to

---

[8] Benjamin Kaan, P.E., M.S., Project Engineer, Thornton Tomasetti, 912 Broadway, Suite 100, Kansas City, MO, 64105

[9] Fatih Alemdar, PhD, Assistant Professor, Yildiz Technical University, Istanbul, Turkey

[10] Caroline Bennett, PhD, PE, Associate Professor, University of Kansas, 1530 W. 15th St., Lawrence KS, 66045

[11] Adolfo Matamoros, PhD, Professor, University of Kansas, 1530 W. 15th St., Lawrence KS, 66045

[12] Ron Barrett-Gonzalez, PhD, Associate Professor, University of Kansas, 1530 W. 15th St., Lawrence KS, 66045

[13] Stan Rolfe, PhD, PE, A.P. Learned Distinguished Professor, University of Kansas, 1530 W. 15th St., Lawrence, KS 66045

run-out at high stress range. An optimal bond composition was identified that resulted in excellent performance under fatigue loading.

B.2.2 Introduction

An emerging fatigue enhancement technique for aging steel bridges is to utilize fiber reinforced polymers (FRP) to reduce stresses at fatigue-vulnerable welded connections. Fiber reinforced polymers (FRP) are an ideal material choice to strengthen welded connections in steel bridge construction due to their high strength and stiffness, low weight, ability to diffuse crack propagation (Meier 1992), and ability to be molded into various geometries. Attaching FRP materials as external overlay elements to steel bridge connections can provide an alternate load path which reduces stress demand at the tip of a crack or at a previously uncracked welded connection. Lower stress demand translates both into increased fatigue crack initiation and fatigue crack propagation life, with the increase in fatigue life being proportional to the reduction in stress range at the fatigue-vulnerable detail.

An investigation is described wherein carbon fiber reinforced polymer (CFRP) materials were used to stiffen welded connections common in welded steel bridge girders. A significant body of research exists investigating the effect of FRP sheets bonded over cracks in plates subjected to tension (Jones and Civjan 2003; Sabelkin et al. 2006; Colombi et al. 2003a; Colombi et al. 2003b). However, welded connections present a significantly more complex stress state than that seen in plates. Therefore, in this study, composite overlays were bonded over welded connections of coverplate specimens with the goal of reducing peak stresses at the weld and extending the fatigue crack initiation life of the welded connection. This paper focuses on the conceptual design and the fabrication aspects of the bond between the overlay and the welded connection, which were validated through experimental testing of the CFRP-stiffened steel specimens under cyclic loading.

B.2.3 Background

Several studies in the literature show that CFRP materials can be used successfully to strengthen structural steel elements (Jones and Civjan 2003; Tavakkolizadeh and Saadamatmanesh 2003; Deng and Lee 2007). For this strengthening technique to be effective, a key aspect is maintaining the bond between the composite materials and the steel. There are a

number of studies that have investigated bond characteristics between FRP and steel under monotonic loading (Sebastian and Luke 2007; Buyukozturk et al. 2004). Experimental work focusing on FRP repairs under fatigue loading has been more the purview of the aerospace industry, which has spent significant resources in developing techniques to address the recurring problem of fatigue cracks in aircraft fuselages (Sabelkin et al. 2006).

The majority of studies in the literature investigating the use of FRP materials to improve fatigue performance focus on methods for improving the fatigue crack propagation life of specimens with various types of pre-existing notches, both in the aerospace and structural engineering fields (Bassetti et al. 2000a, 2000b, and 2000c; Colombi et al. 2003a and 2003b; Tavakkolizadeh and Saadatmanesh 2003; Jones and Civjan 2003; Nozaka et al. 2005a and 2005b; Sabelkin et al. 2006). These studies provide several important conclusions. For example, one of the key findings in the work by Bassetti et al. (2000a, 2000b, and 2000c) was that it is essential for CFRP strips being used for fatigue repair to have a strong and durable bond between the steel and composite such that adequate and reliable load sharing can be accomplished. Bassetti et al. (2000a, 2000b, and 2000c) found that debonding of the composite lessened the effectiveness of the CFRP strips, which in turn accelerated the rate of crack growth and led to further debonding. Internal and external delaminations were common problems experienced in investigations examining use of composite materials applied to steel structural members (Colombi et al. 2003a and 2003b). Often the bond material was not able to sufficiently resist shear stresses to provide continuous load sharing between the bonded materials for a significant number of load cycles. Additionally, Hertzberg (1996) found that once a crack began to form in the bond layer, it tended to propagate quickly due to the brittle behavior of most bond materials at standard testing temperatures.

Other important findings from previous studies were given careful consideration in the development of this experimental program. First, the bond layer between the steel and composite must be comprised of a material that is durable, strong, and able to withstand significant levels of shear stress. Second, it was known that thickness of the bond material greatly affects the extent of load sharing between the steel and composite (Colombi et al. 2003a and 2003b), so further testing should include investigation of multiple bond layer thicknesses.

Third, an increased number of plies in the composite increased the maximum moment the detail could withstand when used as an overlay on a fatigue-vulnerable detail on the flange of a steel girder, and thus decreased the stress demand at the critical location (Nozaka et al. 2005a and 2005b). Fourth, use of finite element modeling as an evaluation tool helped to focus experimental work and pare down the number of variables associated with the use and testing of composite materials (Colombi et al. 2003a and 2003b).

As noted, previous studies focused primarily on using CFRP strips to extend the fatigue crack propagation life of already cracked specimens. Studies investigating the use of composite materials to repair the type of welded connections commonly found in structural steel bridges are very scarce. One of the few studies found is by Nakamura et al. (2009) who successfully used CFRP strips to repair specimens simulating welded web gusset joints. The application investigated in this study is significantly different from others found in the literature because it is focused primarily on increasing fatigue crack initiation life of uncracked specimens with welded connections, in which the composite overlay was used to reduce the stress demand in a region with high stress gradients caused by abrupt changes in geometry. This application is different from the use of composite sheets to repair cracked plates subjected to tension; in the former scenario, the stress field is significantly more complex than that in a plate element, inducing both tension and shear stress demands along the interface bond layer between the overlay and the steel.

B.2.4 Research Plan and Objective

It was quite common for bridge engineers to employ welded coverplates to reinforce steel girder flanges in regions of high moment demand as recently as 40 years ago. Although this retrofit technique is seldom used in the present, its common use in the past created numerous fatigue crack initiation sites, especially for welds at the ends of thick steel coverplates [greater than 20.3 mm (0.80 in)]. This particular type of welded connection proved to be so prone to development of fatigue cracks that AASHTO (2013) categorized it with the worst fatigue grouping, denoted as Category E'. Although the engineering community now recognizes that this type of connection is a poor performer under fatigue loading, many examples can still be found in aging, existing steel bridges.

Effective use of FRP overlays to prevent or repair fatigue damage in steel structures hinges on preventing fatigue failure of the retrofit measure itself. Failure of the type of repair discussed in this paper may occur due to fatigue failure within the overlay or due to bond failure between the overlay and substrate under cyclic loading. Previous efforts by the authors have found that the type of overlays applied were not governed by fatigue strength of the overlay (Alemdar et al. 2009; Alemdar 2010; Kaan (2008) and Kaan, et al. (2008). For this reason, this study focused on evaluating the effect of configuration parameters and fabrication techniques such as bond layer thickness, bond layer composition, and boundary conditions of the bond layer on the bond strength under cyclic loading between composite overlays and the steel substrate.

A plate-coverplate specimen (see Figure B.11 and B.12(a) with fatigue-vulnerable welded connections was chosen for this study, because the goal was to evaluate the bond performance of repairs with CFRP overlays (see Figure B.11(b) and B.12(b) under fatigue loading. This type of specimen was chosen due to the well-documented poor fatigue performance of the welded connections (Albrecht and Lenwari 2007), the common use of coverplates in the past, and the stress demands that the specimen imposes on the bond layer between the FRP and the substrate steel (combined effects of tension and shear).

The research was carried out in the following manner. A suite of finite element analyses were performed to identify parameters critical to the performance of the bond layer under fatigue loading. The shape of the interface bond layer was varied, and the effect on computed shear and peel stress demands was quantified. An experimental program was subsequently carried out to validate results from the analyses, and to investigate the effect of fabrication techniques on fatigue performance of the interface layer.

(A)

CFRP Overlay Element — Gr. A36 Cover Plate — Gr. A36 Flange Plate —

To upper cross-head of test frame

To lower cross-head of test frame

140 mm (5.5 in) 152 mm (6.0 in) 140 mm (5.5 in) 152 mm (6.0 in)

25.4 mm (1.00 in) 25.4 mm (1.00 in)

305 mm (12.0 in) 660 mm (26.0 in) 305 mm (12.0 in)

76.2 mm (3.00 in) 114 mm (4.50 in)

Path A

Path B

Path C

Path D

Bond (resin) layer*

(B)
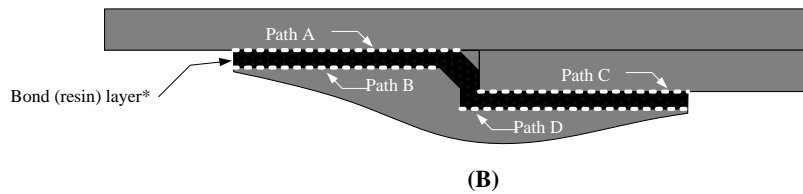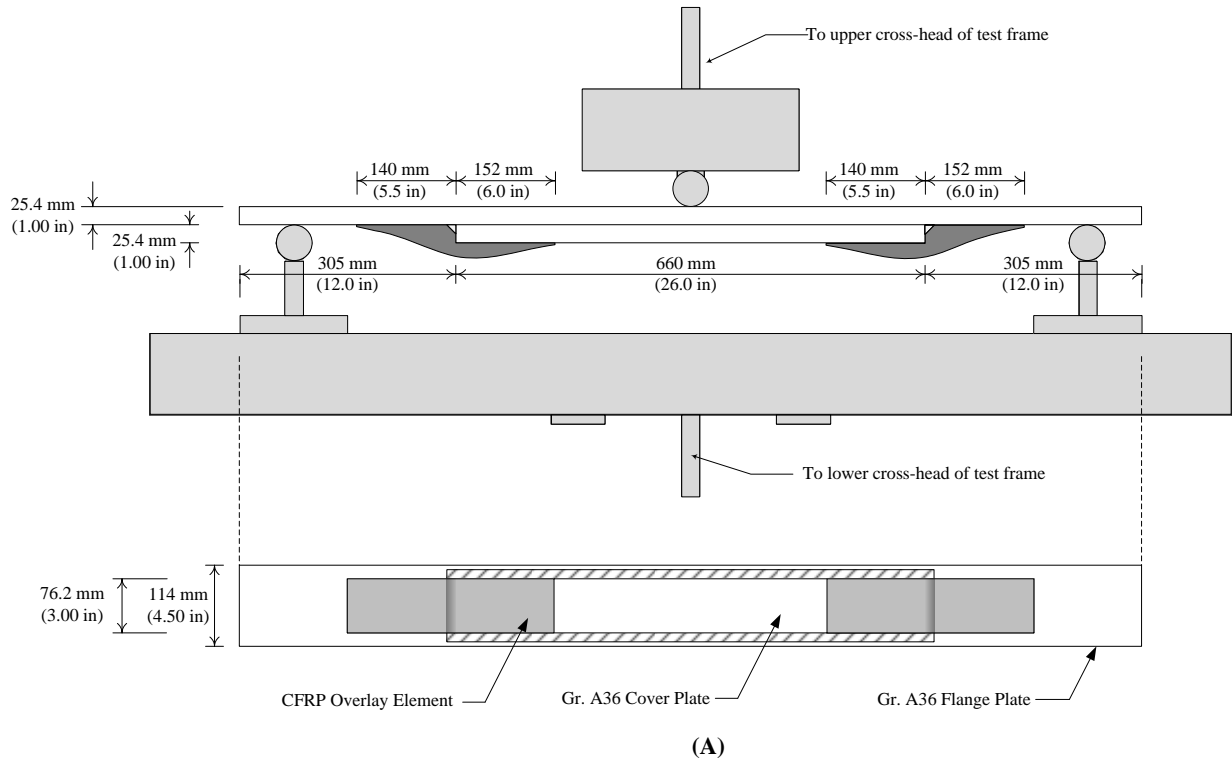
*Exaggerated scale to show detail in bond layer

Figure B.11: (a) Schematic of three-point bending fixture with CFRP-stiffened specimen; (b) Detail of CFRP-resin-steel bond interface

(a)

40 plies bi-directional carbon
fiber, pre-impregnated with
cyanamide-123 epoxy resin
with 5 layers of boron fiber

12.7 mm (0.50 in)

Resin film used
to fill void areas

140 mm
(5.50 in)

12.7 mm
(0.50 in)

140 mm
(5.50 in)
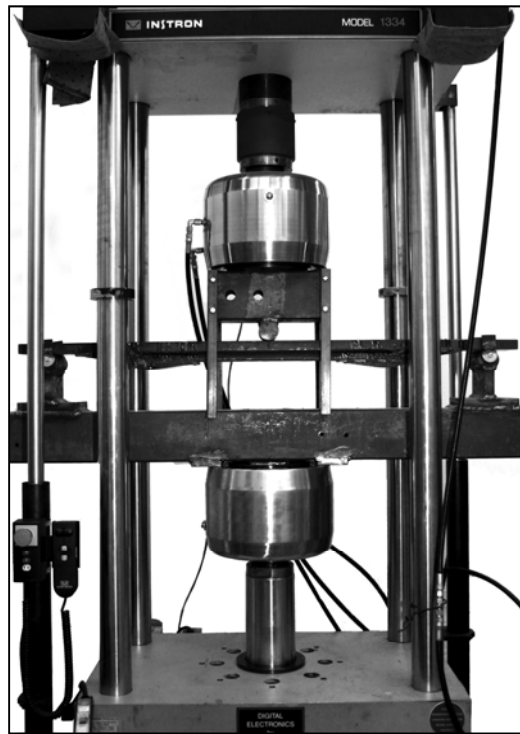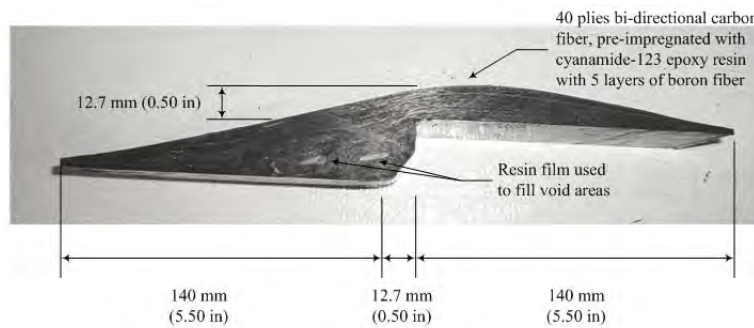
(b)

Figure B.12: (a) View of experimental test set-up; (b) Profile of CFRP overlay element

B.2.5 Analytical Investigation

Finite element analyses were performed to examine the effects of the bond layer thickness and bond layer length on the effectiveness of the CFRP overlay elements. A two-dimensional model of a 25 mm (1.0 in.) wide segment of specimen was created to study the effects of various parameters on fatigue life. Computer simulations were performed using the

finite element analysis software Abaqus (SIMULIA 2009). The steel, weld and composite material were defined as linear elastic materials.

Each component was meshed separately and joined together using interaction surfaces. The connections between the plates and the weld and between the plates and the composite overlays were modeled using tie constraints. A tie constraint is an FE modeling technique that joins two separate surfaces to one another so that they displace together as one piece at the tie(s) location(s). The interface between the flange and coverplate was modeled using hard contact interaction. A pressure load was applied at the midpoint of the top plate to simulate the load acting on the specimen during testing, and an adjustment was made to the applied load to account for the difference between the width of the specimen and the width of the model. Vertical displacement was restricted at the two supports, both located at 76 mm (3.0 in.) from the ends of the specimen, and horizontal displacements were restricted at one end of the model. Six different bond layer thicknesses between the steel and overlay were investigated analytically: 0.3 mm (0.01 in.), 0.8 mm (0.03 in.), 1.3 mm (0.05 in.), 1.7 mm (0.07 in.), 2.5 mm (0.10 in.), and 3.2 mm (0.13 in). Both faces of the bond layer were rigidly tied to the CFRP and the steel, therefore, flexibility exhibited by the bond layer was related to the stiffness of the resin. The modulus of elasticity for the resin material was conservatively taken as 2.8 GPa (400 ksi) within the models, due to inherent variability in resin moduli; the value chosen for the models was taken as higher than the measured modulus (2100 MPa [303 ksi]) and the manufacturer's information (2300 MPa [330 ksi]) since a stiffer interface in the models would result in higher demands on the steel than a more flexible bond could induce. Poisson's ratio was taken as 0.2. Interface surfaces between the resin and the steel and between resin and the composite were modeled using tie constraints. The CFRP modeled in the computer simulations was rectangular in profile, as can be seen in Figure B.13. A broader investigation by the authors has considered effects of CFRP profile shape (Alemdar 2010 and Appendix B.3), and found that CFRP profile shape had very little effect on the stress demands in the bond or steel substrate.

Stress demands between the steel and the interface resin layer, and between the resin layer and the composite overlay, were evaluated by extracting the shear and tensile stresses along paths in the interface between materials. There were four different paths evaluated. These paths,

designated *A* through *D,* are illustrated in Figure B.11(b) and B.13 for one of finite element models that was analyzed.
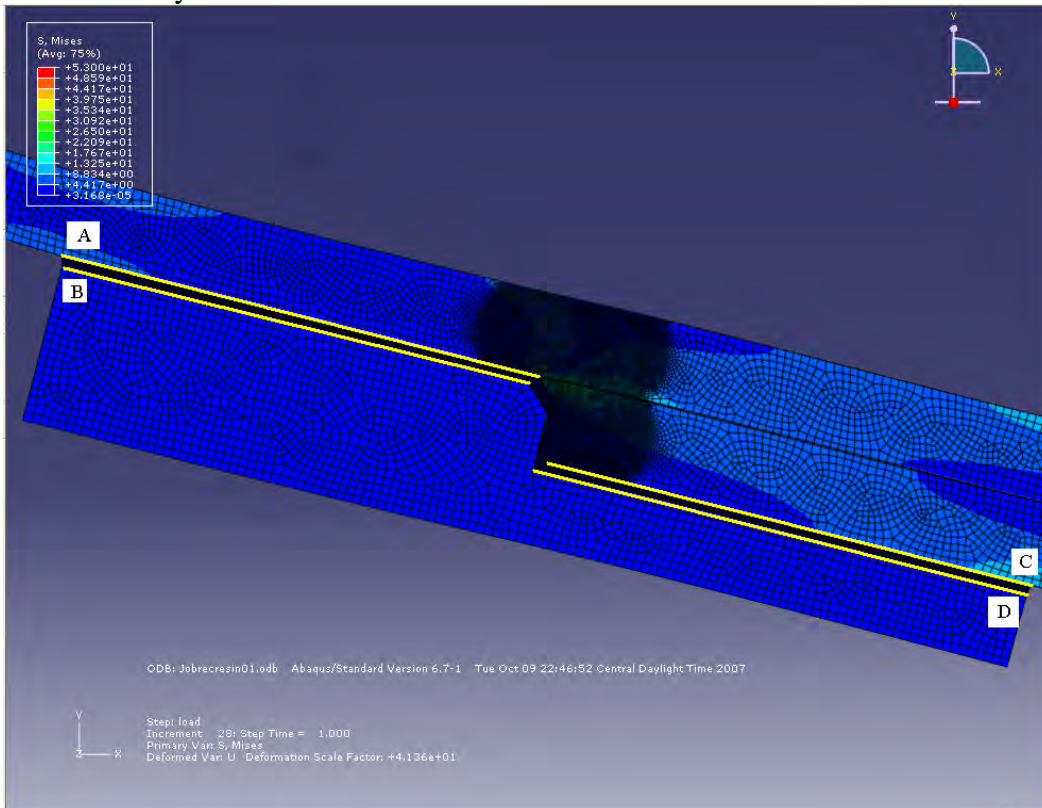
Figure B.13: Stress comparison paths on the resin layer

One of the most important aspects of this type of repair is the effect of the overlays on stress demand at the weld, which is directly proportional to the fatigue crack initiation life of the welded connection. The finite element results (Figure B.14) showed that increasing the thickness of the resin layer resulted in a small reduction on the maximum stress demand on the steel plate at the location of the weld toe, the location of which corresponded to a point approximately 300 mm (11.8 in.) from the edge of the specimen in Figure B.14. The stresses shown in Figure B.14 were extracted from paths *A* and *C* shown in Figure B.11 (b) and B.13, along the surface of the steel. Figure B.14 shows that in the area near the weld, computational models with greater resin layer thicknesses produced higher calculated stress demands than noted for models with less thick resin layers, which indicates that the retrofit measure becomes less effective as the thickness of the resin layer increases.
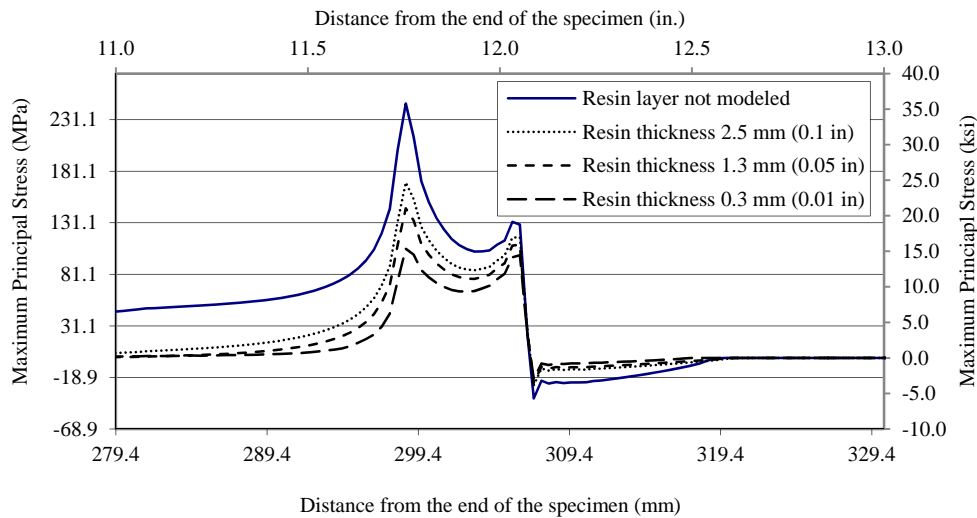
Figure B.14: Maximum principal stress on the steel plate in the area of the weld

Another important factor that affects the fatigue behavior of this type of repair, central to the focus of this study, is the stress demand along the interface between the composite and the steel. Calculated shear and tensile (peel) stresses were computed along the interfaces. The observed stress distribution and magnitudes along the interface between the steel and the resin were very similar for both shear and peel stresses, with peak demands located at the end of the path corresponding to the edge of the overlay and a much smaller peak at the weld toe. The distribution of shear stress along path A (Figure B.13) is shown in Figure B.15. It was found that in the case of the peel stresses, the peak demand at the interface between the steel and the resin (path *A*) was higher than the peak stress demand at the interface between the resin and the composite (path *B)*; this was not unexpected, given the higher stiffness of the steel plate.

Calculated stresses along path *C* were similar in nature, with peak demands occurring at the edge of the overlay and a much smaller peak occurring near the edge of the coverplate. Calculated stress demands along path *A* are presented because the magnitude was higher than the stress demands along path *C*, which is attributed to the greater flexural stiffness of the plate-coverplate segment (path *C*) resulting in lower curvature demands in that segment of the specimen. Due to the similar nature and lower magnitudes of the results for paths C and D to those of A and B, they are not presented here; however, additional results from a broader modeling effort can be found in Alemdar (2010). Results show that the curvature of the specimen

when deformed in bending induced a significant peel stress demand that is not present in composite sheet repairs of plates subjected to pure tension. Also, it should be noted that the type of specimen used in this study is likely to pose a greater peel stress demand on the interface layer than flanges of beams reinforced with cover plates because the curvature demand in the shallow specimen used in this study is likely to be much higher than that in beams.
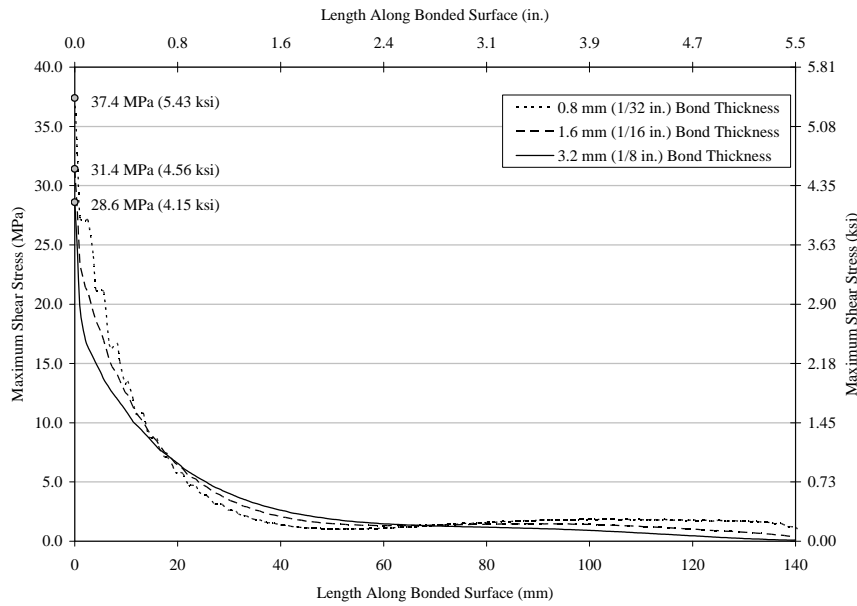
Figure B.15: Calculated shear stress along Path A in Figure B.14 for varied bond thickness

The distribution of the computed stresses suggest that the point along path *A* (Figure B.13) corresponding to the edge of the overlay is critical in terms of fatigue performance because at this location the interface resin layer is subjected to the highest stress demands. For this reason, it is expected that this location will be a trigger point for bond failure under fatigue loading. On the basis of this finding it was decided that one of the parameters of the experimental study should be the geometric configuration of the interface resin layer. It was hypothesized that terminating the interface resin layer directly at the edge of the overlay would be detrimental to fatigue performance because it would couple the location of a discontinuity with the maximum stress demand. For this reason, it was decided to evaluate two different configurations in the experimental phase of the study: a configuration with a resin pool extending beyond the edge of the overlay, and another without it.

Another important consideration related to bond performance under fatigue loading is the effect of the resin layer thickness on peel and shear stresses at the interface. Although the finite element analyses showed that resin layer thickness was likely to have a small effect on fatigue life of the steel substrate, a significant effect on the interface stress demand would have an important effect on the bond strength under fatigue loading. Figure B.15 depicts the shear stress distributions along the bonded surface of the CFRP overlay found for bond thicknesses varying from 0.8 mm ($^1/_{32}$ in.) to 3.2 mm ($^1/_8$ in.). Figure B.15 shows that the shear stress distribution was similar for all thicknesses studied, with the greatest demand found to occur at that the edge of the coverplate. The maximum shear stress demand in the bond layer decreased as the thickness of the layer increased. The trends for the peel stress were similar in nature. The results also showed that stresses in the steel increased as the resin layer thickness increased. As the resin layer becomes thicker, and thus more compliant, more load is transferred through the steel and less stress is resisted by the bond.

The importance of shear stress at the leading edge of the bond layer was further confirmed by experimental observation as the bond failure path propagated to the leading edge through the bond material at an angle of approximately 45º. Therefore, another hypothesis derived from the finite element analyses was that increased bond thickness between the steel and CFRP elements would increase the bond tenacity, while some stiffening capability would be sacrificed. A goal of the experimental testing, in light of this hypothesis, was to determine an optimal bond thickness that provided enough stiffness to the specimen to increase the life of the fatigue-vulnerable welds, while still minimizing shear stress in the bond material, thus minimizing the frequency of debonding of the CFRP-overlay elements from the steel specimens.

B.2.6 Experimental Program

The experimental program consisted of a series of tests of welded coverplate steel assemblies reinforced with CFRP overlays (Figure B.11) subjected to fatigue loading. Each assembly was subjected to cyclic loading until crack initiation was observed in the steel substrate or run-out was achieved. Each time debonding of an overlay was observed, the overlay was removed and the weld was inspected for the presence of fatigue cracks. If fatigue cracks were not observed, the overlay was rebonded and fatigue testing resumed. CFRP overlay elements were

re-used throughout tests when they suffered no visually noticeable internal degradation. Since the fatigue lives of the bond layers were dependent upon study variables, it was felt that using new CFRP overlays after each debond event would add little value, as each overlay would still have been subjected to a different number of fatigue cycles. Therefore, CFRP overlays were regularly inspected during fatigue testing and were replaced when internal degradation was visually observable; this occurred only once throughout the testing program. The number of cycles between the attachment of an overlay and its subsequent debonding is reported as a fatigue test of the interface bond layer, so multiple fatigue bond tests were performed on every coverplate assembly.

The test requirements used in this study were chosen because they are more stringent than real loading in a tension flange. The primary goal of this work was to test the bond durability between the steel and CFRP overlay. The authors have performed numerous tensile fatigue tests of cracked steel specimens with CFRP bonded over the cracked region (Alemdar 2010), none of which experienced bond failure. To better understand bond behavior and durability, and to develop a bond layer with superior fatigue performance demands, a more demanding test set-up was conceived. Additionally, it was considered that this retrofit type may be used in other applications in the future, such as on a girder web or for resisting out-of-plane fatigue loading; both are common situations in which greater interaction between shear and tension would be expected.

The steel specimens to which CFRP overlays were bonded were comprised of two 25.4 mm (1.0 in.) thick plates welded together with a 7.9 mm ($^5/_{16}$ in.) fillet weld. Dimensions of the steel specimen are provided in Figure B.11.

B.2.6.1   CFRP Overlay Elements

The CFRP overlays were engineered to achieve infinite fatigue life under the loading experienced in this study. The detailed process followed for the development and fabrication of the CFRP overlays is discussed elsewhere (Kaan 2008; Kaan et al. 2008). The CFRP overlay elements were constructed by layering 40 plies of bi-directional carbon-fiber fabric pre-impregnated with cyanimide-123 resin in an aluminum mold. Each layer of carbon fiber fabric was cut to a different length such that the final profile of the stack was curvilinear. Five plies of

159

boron-fiber were included in the stack to limit out-of-plane migration of the carbon-fiber layers during the molding process, and several layers of resin film were added to eliminate voids in the CFRP overlay profile.

A heat press was utilized to produce CFRP overlays with good consolidation. Heated platens of the press applied a pressure of 18.0 bar, or 1.80 MPa (260 psi), and a temperature of 177 ℃ (350 ℉) to the overlay elements within the mold for three to four hours until complete cross-linking of the resin was achieved. CFRP overlays produced by this method had a curvilinear profile and curvature and thicknesses that were consistent between overlays. The typical profile of a completed CFRP overlay element is shown in Figure B.12. As discussed, it was determined in an analytical investigation (Alemdar 2010 and Appendix B.3) that stress demands on the bond layer and steel substrate were very similar for rectilinear and curvilinear overlay profiles. Based on this, it appears feasible to use a simpler, rectilinear profile in similar future applications.

An important effect of the relatively large thickness of the overlays was that it significantly increased the moment of inertia of the composite-steel cross section in the vicinity of the fatigue-critical welds, increasing the flexural stiffness of the specimen and reducing deflections. The added material provided an alternate load path that lowered the stress demand at the welds. This approach was considered to be more effective than bonding composite strips to the specimens; while the approach used herein is intended to increase the fatigue crack initiation life by reducing the stress demand on the welds, the latter works essentially by slowing crack growth after cracks form at the toe of the weld. The approach implemented in this study is conceptually different from the use of composite strips evaluated previously, because the overlays were designed to reduce the stresses in an area with a very complex stress field instead of working in direct tension.

B.2.6.2 *Bonding of CFRP Overlays to Steel Specimens*

Because this study investigated the effect of various configuration parameters on the fatigue performance of the bond layer, all parameters unrelated to the configuration and composition of the bond layer were kept constant. All CFRP-stiffened specimens were outfitted with composite overlays manufactured using materials and processes that were as close to

identical as practically possible. The same procedure was followed each time for lay-up, molding, and curing, and the pre-impregnated carbon fiber fabric materials and bonding resin were from the same respective companies throughout the research and testing program.

Bonding of the CFRP overlay elements to the steel specimens was accomplished using Hysol (Loctite 9412), a commercially-available high-grade resin epoxy. The surface of the steel substrate was prepared using a standard hand grinder and degreased using a mild acid solution and isopropyl alcohol. Composite overlay surfaces were roughened using 100-grit sandpaper and were also degreased using isopropyl alcohol. The resin layer was controlled for thickness and uniformity by using spacers, such as small ball-bearings and short lengths of steel rod laid on their sides. After the resin was placed, an additional benefit of the spacers was that clamping force could be applied to the CFRP overlay without displacing the resin. The Hysol layer between the CFRP overlay and the steel substrate was cured at room temperature for a minimum of 48 hours before any load was applied. Four steel specimens were outfitted with CFRP overlay elements, and were subsequently identified as Specimens TRI-04, TRI-05, TRI-06, and TRI-07. Specimen TRI-06 underwent extended testing, referred to as TRI-06-2.

The parameters of the testing program were: thickness of the bond layer, length of the bond layer, and composition of the bond layer. Composition of the bond layer was varied as shown in Table B.8. Based on the finite element analysis results, it was hypothesized that increasing the bond layer thickness between the steel and CFRP would decrease the stiffening effect provided by the CFRP overlay elements as well as decrease the frequency of overlay element debonding. This hypothesis is consistent with findings by Colombi et al. (2003a and 2003b). Specimen TRI-05 had a bond layer thickness of 1.6 mm ($^1/_{16}$ in.), TRI-04 and TRI-07 had bond layer thicknesses of 3.2 mm ($^1/_8$ in.), and TRI-06 had a bond layer thickness of 6.4 mm ($^1/_4$ in.).

Table B.8: Fatigue Testing Program and Results for CFRP-Stiffened Specimens

Specimen	Test Designation	Number of Cycles to Bond Failure	Breather Cloth	Resin Pool	Resin Layer Thickness mm (inch)
TRI 02	C0030-01	275,000	N	N	0.8 ($^1/_{32}$)
TRI 02	C0030-02	900,000	N	N	0.8 ($^1/_{32}$)
TRI 04	C0125-01	529,800	N	N	3.2 ($^1/_8$)
TRI 04	C0125-02	255,750	N	N	3.2 ($^1/_8$)
TRI 04	C0125-03	134,150	N	N	3.2 ($^1/_8$)
TRI 04	C0125-04	71,150	N	N	3.2 ($^1/_8$)
TRI 04	C0125-05	204,500	N	N	3.2 ($^1/_8$)
TRI 04	C0125-06	1,125,300 *	N	N	3.2 ($^1/_8$)
TRI 04	CP0125-01	1,060,950 *	N	Y	3.2 ($^1/_8$)
TRI 04	CP0125-02	722,000 *	N	Y	3.2 ($^1/_8$)
TRI 06	CP0065-01	279,750	N	Y	1.6 ($^1/_{16}$)
TRI 06	CP0065-02	283,900	N	Y	1.6 ($^1/_{16}$)
TRI 06	CP0065-03	239,250	N	Y	1.6 ($^1/_{16}$)
TRI 06	CP0065-04	956,606	N	Y	1.6 ($^1/_{16}$)
TRI 06	CP0065-05	398,596	N	Y	1.6 ($^1/_{16}$)
TRI 05	CPB0250-01	1,205,315	Y	Y	6.4 ($^1/_4$)
TRI 05	CPB0250-02	1,634,756 *	Y	Y	6.4 ($^1/_4$)
TRI 07	CPB0125-01	1,725,900 *	Y	Y	3.2 ($^1/_8$)
TRI 07	CPB0125-02	1,725,900 *	Y	Y	3.2 ($^1/_8$)
TRI 07	CPB0125-03	1,564,300 *	Y	Y	3.2 ($^1/_8$)
TRI 07	CPB0125-04	1,564,300 *	Y	Y	3.2 ($^1/_8$)

Test was stopped without observed debonding

One of the parameters of the testing program was the use of breather cloth within the bonding resin layer. The bonding resin used had a very low initial viscosity which made the process of creating unusually thick bond layers more difficult. Specimen TRI-05 was fabricated to have 6.4 mm ($^1/_4$ in.) thick bond layers, a dimension significantly greater than is commonly used when bonding composites to steel. Therefore, a resin captivation material made from polyester fiber breather cloth was added to the bond layers to keep the resin in place through the mechanism of capillary action. Breather cloth can be obtained in multiple materials, including non-woven polyester and nylon. It is an excellent material for soaking up excess resin and reducing spillage and flow during some layup processes due to its high absorptive capacity, which made it ideal for use in this investigation. The polyester breather fabric used as a resin captivation layer was approximately 2.5 mm (0.1 in.) thick when uncompressed. The addition of

the breather cloth was at first solely a constructability consideration to keep the bonding resin in place while wet. However, as will be discussed, improved performance of specimens that contained the fabric in the bond layer spurred the investigators to include it in subsequent tests. Three layers of the breather fabric were used when constructing 6.4 mm ($^1/_4$ in.) thick bond layers, and two layers were used when constructing 3.2 mm ($^1/_8$ in.) thick bond layers.

Another parameter of the study was the geometric configuration of the resin layer. Results from finite element analyses showed that peak tensile and shear stress demands on the resin layer occurred at the edge of the overlay. The coinciding location of the highest stress demand and the abrupt termination of the interface layer was considered to be potentially detrimental to the fatigue performance of the bond layer. An alternative configuration was evaluated in which the perimeter of the resin layer was extended beyond the perimeter of the overlays through the implementation of a resin pool. The resin pool was trimmed to extend approximately 25 mm (1.0 in.) beyond the ends of the CFRP overlay element. This configuration was conceived so that high stress demands at the end of the overlay would not coincide with the termination of the interface layer and was used in the majority of the stiffened steel specimens. Use of a resin pool began with specimen TRI-04, which had a 3.2 mm ($^1/_8$ in.) thick bond layer. The resin pool was used for part of this test, and implementation began in earnest after its beneficial effects became evident. Therefore, the first few fatigue bond tests (debonds and rebonds) on specimen TRI-04, were performed without a resin pool. All subsequent fatigue bond tests, including all the tests performed on the remaining specimens fitted with overlays (TRI-05, TRI-06, and TRI-07), were fabricated to include a resin pool.

B.2.6.3 Material Properties

Properties of the materials used in the composite overlays and the interface layer are summarized in Table B.9. Coupon tests performed in accordance with ASTM 3039/D 3039M (ASTM 2000) from single-layered specimens showed that the modulus of elasticity of the CFRP was approximately 83 GPa (12,000 ksi). The modulus of elasticity of the 9412 Hysol® resin was 2.1 GPa (300 ksi). The yield strength (F_y) of the steel was found to be 300 MPa (43 ksi), and the tensile strength (F_u) was 490 MPa (71 ksi).

Table B.9: Composite Material Properties

CFRP

Number of Layers in Coupon	Number of Coupons	Avg Modulus of Elasticity GPa (ksi)	Standard Deviation GPa (ksi)
1	3	85.8 (12,400)	10.0 (1,450)
3	4	75.3 (10,900)	10.9 (1,580)
5	3	61.7 (8,900)	0.3 (42.0)

9412 Hysol® Resin

Coupon Thickness mm (in.)			
6.4 (0.25)	6	2.1 (303)	0.2 (25)

B.2.6.4   Fatigue Testing Experimental Setup

Multiple trials on the five CFRP-stiffened steel specimens (Table C.1) were conducted using a three-point bending test fixture to apply fatigue loading (Figure C.1). Cyclic fatigue loads for all specimens were applied such that the minimum load was one-tenth the maximum load ($R = P_{min} / P_{max} = 0.1$). The maximum load applied was 17.1 kN (3.84 kip), which corresponded to a stress range at the weld toes of the transverse welds of the control specimen of 138 MPa (20.0 ksi). Cyclic loading was applied using a sinusoidal function with a constant frequency of 1.5 or 2.0 Hz. Figure B.11 shows a schematic drawing of the three-point bending fixture used in this testing. This test set-up was chosen because of the stringent demands it places on the CFRP bond (tensile and peel stresses), as opposed to a pure tensile fatigue test. Load and deflection data were monitored for each loading cycle, and were saved to a spreadsheet file every 50th cycle for the duration of each test.

Testing on all stiffened specimens progressed until a crack initiated in the steel, one of the composite overlay elements experienced a bond failure, or the total number of applied fatigue cycles reached a minimum run-out threshold of 1.5 Million cycles. This threshold was chosen to define run-out because it corresponded to expected infinite life for a Category B detail subjected to a stress range of 138 MPa (20 ksi) (AASHTO 2013). In the event that a CFRP-overlay element debonded, testing of that specimen was stopped, the CFRP-overlay element was removed, and the weld to which the composite had been bonded was inspected for the presence of a crack using a dye penetrant. If no crack was detected, then the surfaces on both the CFRP-

overlay element and the steel specimen were cleaned and prepared for rebonding. This included

grinding old resin residue off of the steel substrate and bringing the steel back to a shiny,

roughened surface. Similarly, all resin residue was removed from the CFRP overlay by applying

a low amount of heat (150°C [300°F]) and light sanding. After the composite was rebonded,

testing was resumed.

B.2.7 Experimental Results and Discussion

A parameter that was inferred from direct test measurements was the instantaneous

stiffness, or dynamic stiffness of the specimens. Dynamic stiffness is defined herein as the

change in the applied load divided by the change in deflection of the specimen for each recorded

fatigue cycle:

$$K_{dyn} = \Delta P / \Delta y$$ **Equation B.6**

where ΔP = the change in applied load over one fatigue cycle and Δy = the change in

deflection over one fatigue cycle. A decrease in the dynamic stiffness of the specimen served as

an indication of change in specimen response to load. This change was either due to the initiation

and propagation of a crack in the steel or initiation and progression of a debonding failure at

either of the bonded CFRP-overlay element locations. It was not difficult to differentiate between

the two stiffness reduction mechanisms. Changes in stiffness due to crack initiation and

propagation in the steel substrate occurred over multiple hundreds of thousands of cycles, while

changes in stiffness due to debonding occurred in less than ten thousand cycles.

Figure B.16 displays average dynamic stiffness data determined for each of the four

specimens tested, as well as for two control specimens. The values shown were the average of

the dynamic stiffness data recorded at fifty cycle intervals during testing of the specimens. For

the CFRP stiffened specimens, this dynamic stiffness data excluded load cycles in which the

CFRP overlay was undergoing debond, and was thus representative of stiffened specimen

behavior. Where a suffix "-2" is seen added to the designation of a specimen, the stiffness

measurement corresponds to a series of trials with a different interface layer thickness than used

in the first set of trials conducted on the specimen. The average measured dynamic stiffness for the control specimens was 4.76 kN/mm (27.2 kip/in.).

Figure B.16 shows that CFRP overlays had a significant effect on the flexural stiffness of the specimens, with treated specimens having an average stiffness ranging between 10-20% higher than untreated ones. In the case of specimens without breather cloth, Figure B.16 shows that increasing the thickness of the resin layer had a noticeable effect on the average stiffness of the overlay, with the average dynamic stiffness varying inversely proportional to the thickness of the resin layer. For a very thin resin layer (0.8 mm [$^1/_{32}$ in.]) the increase in stiffness brought about by the overlays was 21%. For resin layer thicknesses of 1.6 mm ($^1/_{16}$ in.) and 3.2 mm ($^1/_8$ in.) the increases in dynamic stiffness were 17% and 10% respectively. In the case of specimens with breather cloth, the trend was reversed. For resin layer thicknesses of 3.2 mm ($^1/_8$ in.) and 6.4 mm ($^1/_4$ in.), the respective increases in dynamic stiffness were 16% and 21%. The presence of the resin captivation appears to have significantly increased the stiffness of the interface layer from that of the epoxy resin alone to that of a polyester fiber reinforced polymer material (albeit one with a lower than normal fiber volume fraction). Such an increase would negate the initial hypothesis that the stiffening effect of the CFRP overlays would decrease with increasing bond thickness because the effect of the resin captivation material was not considered in the finite element analyses.
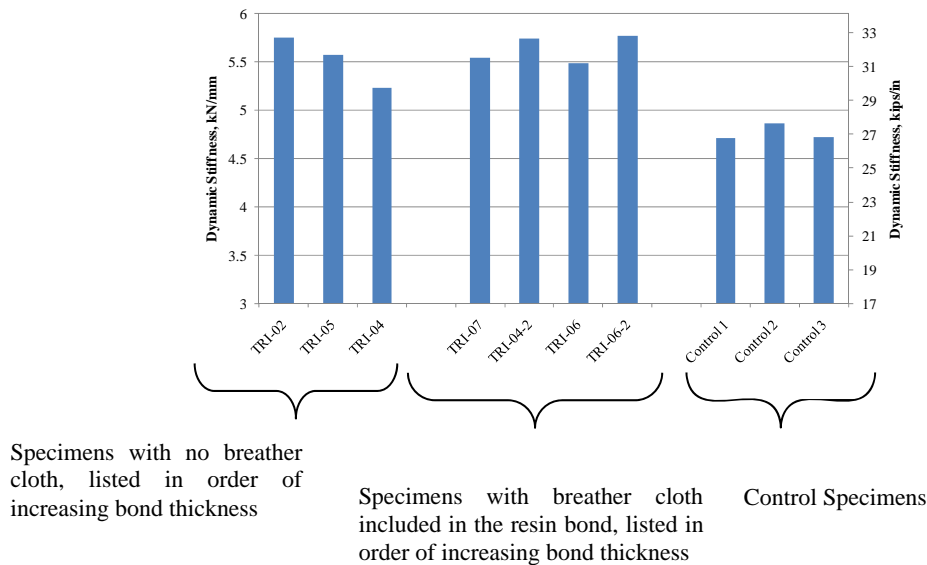
Figure B.16: Measured dynamic stiffness of specimens

Results of fatigue testing are summarized in Table B.8. Each of the four CFRP-stiffened steel specimens exhibited significantly longer fatigue lives than untreated control specimens tested at the same stress range. This effect is illustrated in Figure B.17, which shows the cumulative number of cycles on each specimen in the form of an S-N diagram with the AASHTO (2013) fatigue design curves added for reference. A control specimen tested in work reported by Vilhauer (2007) at a stress range of of 138 MPa (20.0 ksi) demonstrated a fatigue crack initiation life of 350,000 cycles. Because the specimens tested in this study experienced several bond failures, the welds were subjected to a meaningful number of cycles in an unreinforced or partially reinforced configuration. For this reason the cumulative number of cycles to fatigue crack initiation that were observed for each specimen represent only a lower bound to the number of cycles to fatigue crack initiation if bond is maintained throughout the entire test, and are used herein as an approximate gage of the viability of this reinforcing technique.
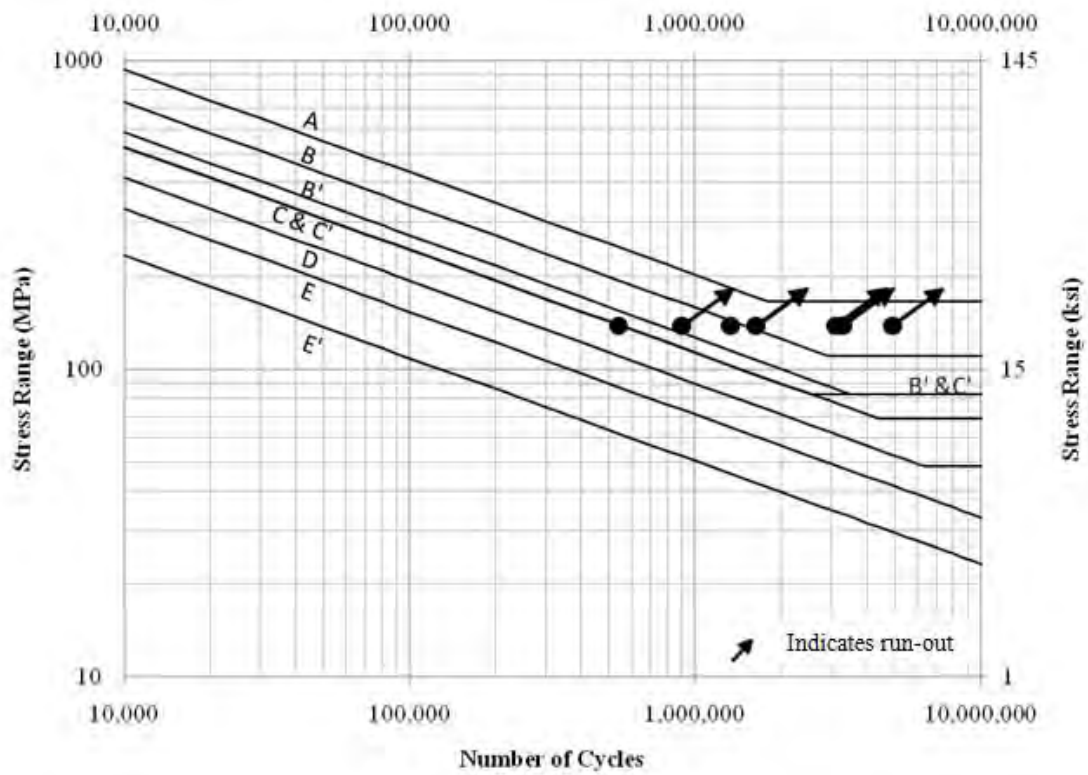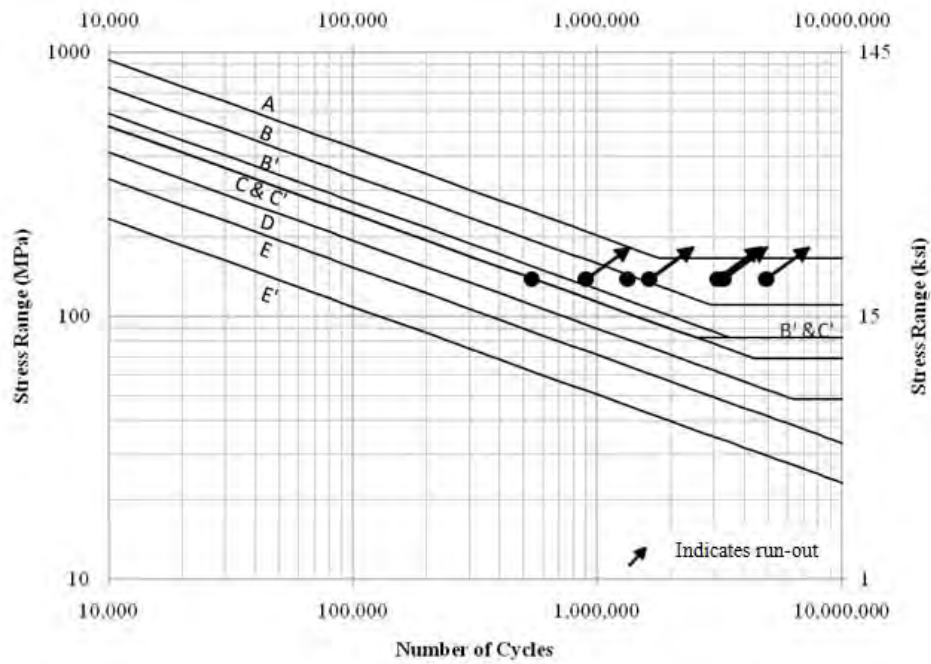
Figure B.17: S-N diagram of fatigue test results for showing the cumulative number of cycles to fatigue-crack initiation for CFRP treated specimens

168

Precisely determining the cumulative number of cycles at which a fatigue crack was found was a difficult task because the overlay obstructed the view of the weld. The procedure followed in this testing program to inspect the welds after debonding events or at set intervals has its limitations. For example, a fatigue crack was discovered upon inspection of specimen TRI-04 after the specimen had been subjected to 1,990,000 cycles. The same weld had previously been inspected and found to have no fatigue cracks at 1,270,000 cycles. Welds were not inspected between examinations because the CFRP overlay element obstructed the view of the welds. There were other factors that affected the cumulative number cycles at fatigue crack initiation shown in Figure B.17.

During testing of specimen TRI-04 it was observed that one of the CFRP overlay elements underwent internal degradation (delamination and cracking) that led to the overlay exhibiting decreased stiffness, which could be visibly discerned. Upon this discovery, noted at 1,125,000 cycles, the degraded overlay was removed, and a new overlay was applied. It is hypothesized that crack initiation was influenced by the degradation of the CFRP overlay element, but the extent of the influence could not be discerned from the data recorded. In addition, TRI-04 experienced the greatest number of debond events for all of the CFRP-stiffened specimens, with a total of six debondments. This relatively high frequency of debonding likely coincided with TRI-04 undergoing a greater number of cycles in the unstiffened configuration than the other specimens. Given the very small size of the crack upon discovery [approximately 1.6 mm (0.06 in.)], it was surmised that initiation occurred after the 1.5 Million cycle run-out threshold, however evidence to support or dispute this hypothesis was not available. Thus, the only definitive conclusion that can be presented is that TRI-04 did not exhibit crack initiation until after it was subjected to 1,270,000 cycles. Although there were limitations associated with the cumulative number of cycles at fatigue crack initiation, it is indisputable that measured values were representative of a large improvement over the fatigue performance of the control specimens. Furthermore, fatigue crack initiation was not observed at all in CFRP-stiffened specimens TRI-05, TRI-06, and TRI-07 when tested at a weld toe stress range of 138 MPa (20 ksi). This underscored the finding that while bond was maintained between the CFRP overlay

169

element and the steel, the increased stiffness at the fatigue-vulnerable welded connection prevented fatigue crack initiation. In terms of the cumulative number of cycles to fatigue crack initiation specimens TRI-04, TRI-05, TRI-06, and TRI-07 exhibited behavior at or above the curve expected for an AASHTO Category B' detail, and Specimens TRI-05, TRI-06, and TRI-07 exhibited behavior at or above the curve expected for an AASHTO Category B detail. The control specimen tested by Vilhauer (2007) exhibited behavior corresponding to AASHTO fatigue design category D.

B.2.7.1 Effects of Bond Thickness and Composition on Carbon Fiber Reinforced Polymer Overlay Effectiveness

Results from specimens TRI-04-2, TRI-06, TRI-06-2, and TRI-07 were especially significant, as they showed that a bond layer as thick as 6.4 mm ($^1/_4$ in.) did not reduce the effectiveness of the CFRP overlay in extending the fatigue crack initiation life of the weld, when breather fabric was incorporated into the resin bond. These results suggest that the flexibility of the bond layer, demonstrated experimentally in Figure B.15 did not have a significant effect on the stress demand at the weld toe and consequently was not large enough to affect the fatigue crack initiation life of the treated specimens.

The effect of the configuration of the interface resin layer on bond life is illustrated in Figures B.18 and B.19. Figure B.18 shows the bond life of trials with a resin layer thickness of 3.2 mm ($^1/_8$ in.). Trials with a resin pool and breather cloth are designated CPB0125, trials with a resin pool and without breather cloth are designated CP0125, and trials with neither breather cloth nor resin pool are designated CO125. The results show that adding a resin pool resulted in a significant improvement in bond life, which confirms the hypothesis formulated on the basis of the finite element results. While one C0125 specimen did outperform the CP0125 group by a minimal amount, the average fatigue life for the C0125 specimens (386,775 cycles) was considerably less than that of the CP0125 specimens (891,475 cycles). Figure B.18 also shows that the best overall performance was obtained for trials that had both a resin pool and breather cloth.

Figure B.19 shows the bond life of trials with different resin layer thickness and all other configuration parameters being the same (without a resin pool and without breather cloth). Trials

170

designated C0030 had an interface layer thickness of 0.8 mm ($^1/_{32}$ in.) while trials designated C0125 had an interface layer thickness of 3.2 mm ($^1/_8$ in.). The results show a great degree of scatter with no discernible effect of layer thickness on bond life. When comparing Figures B.18 and B.19 it is clear the presence of a resin pool and the use of breather cloth lead to a large improvement in bond life, and also reduce the degree of scatter. The experimental results as a whole indicate that fabrication considerations, such as the presence of breather cloth in the resin layer or a resin pool, had a much greater effect on the bond life of the resin layer under fatigue loading than the thickness of the resin layer.
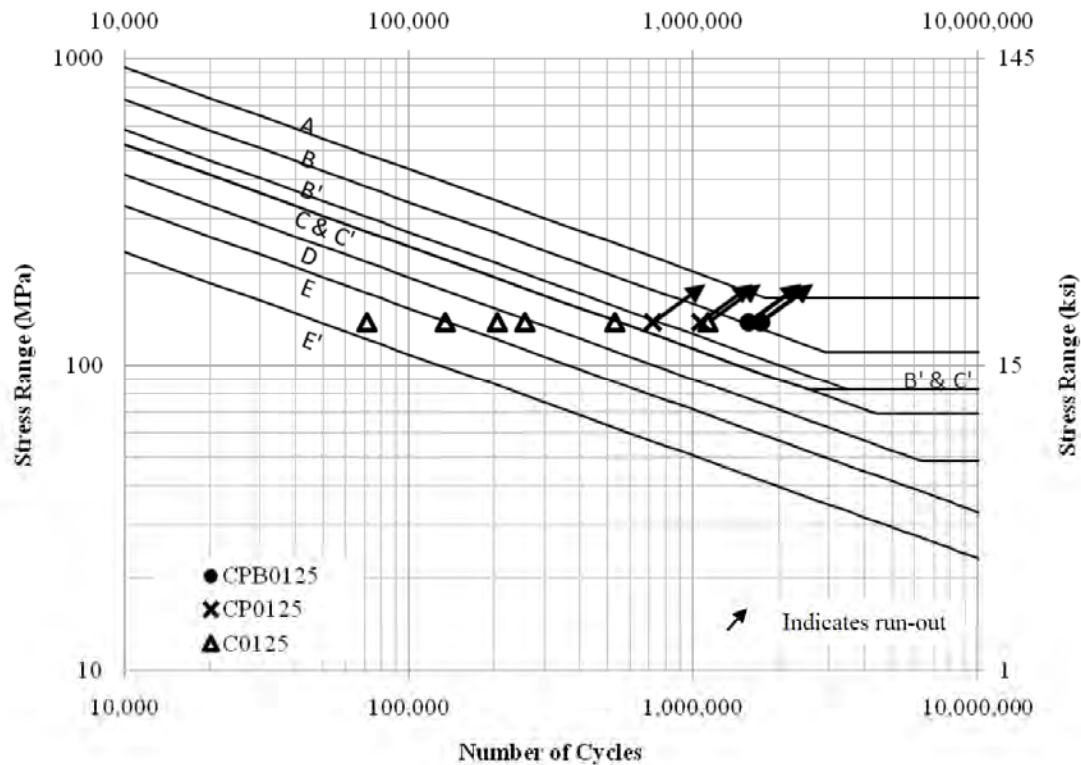
Figure B.18: S-N diagram of fatigue test results for test trials with a bond layer thickness of 3.2 mm ($^1/_8$ in.)

One of the most important findings of this study was the outstanding bond life of trials with breather cloth present within the resin bond tested at a nominal weld toe stress range of 138 MPa (20.0 ksi). Previous studies on the use of composites as fatigue enhancement tools have

struggled to overcome the hurdle of repeated debond events, therefore, this was an important finding.
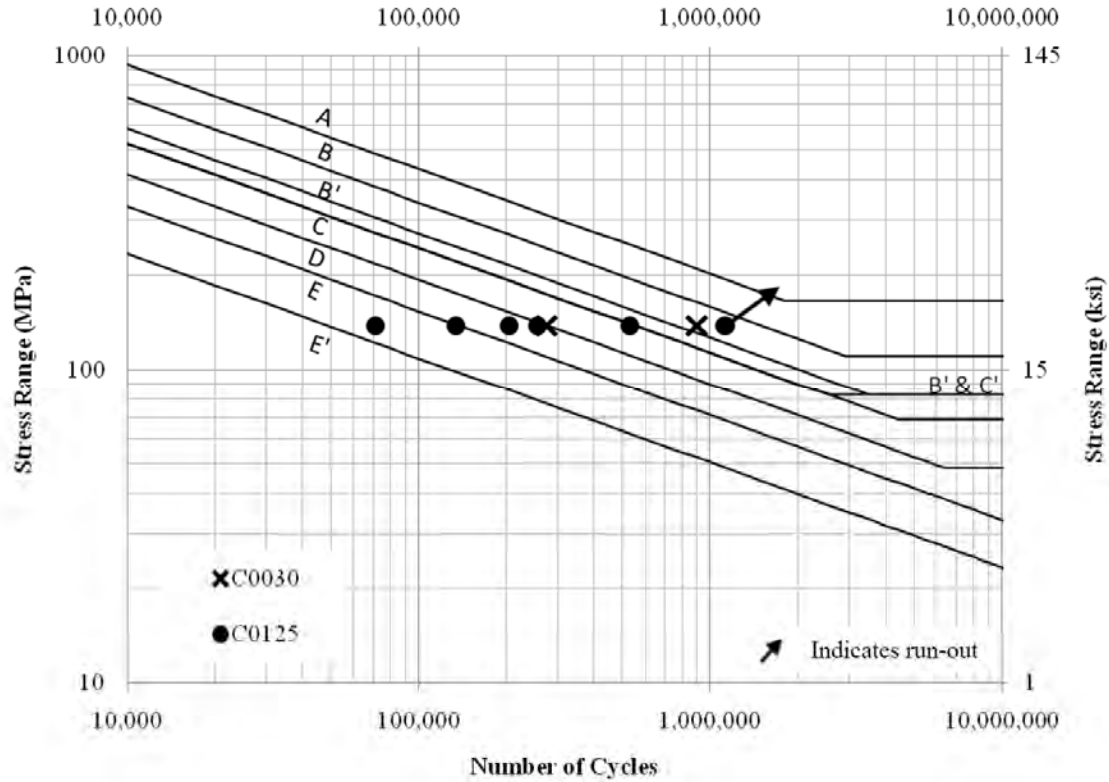
Figure B.19: S-N diagram of fatigue test results for specimens without a resin pool and without breather cloth

B.2.8 Conclusions

Testing of steel specimens in which plate-coverplate welded connections were reinforced with CFRP overlay elements resulted in the following conclusions:

- The bonding of CFRP overlay elements over plate-coverplate connections increased the stiffness and reduced the stress demand at fatigue-vulnerable welds, improving the fatigue performance of the connections by inhibiting crack initiation.
- In specimens in which the CFRP overlay elements debonded and were re-attached, performance according to the AASHTO design specifications improved from fatigue design Category E' to fatigue design Category B'

172

(specimen TRI-04) and fatigue design Category B (Specimens TRI-05 and TRI-06).

- The increase in fatigue crack initiation life brought about by the use of CFRP overlays was contingent upon maintaining the bond between the composite overlays and the steel, and upon maintaining the internal integrity of the composite overlays.
- Addition of polyester fibers for the purpose of resin captivation within the interface layer led to large increases in bond life between the CFRP overlays and the steel, exceeding the infinite fatigue threshold of the AASHTO fatigue design curves for the stress range evaluated in the study.
- Extending the resin layer beyond the edge of the overlay by forming a resin pool led to significant improvements in bond life.

Based on observations of the tests and finite element analyses performed, it is recommended that a fibrous resin captivation layer and an extended interface layer be used during implementation of this repair technique for maintaining adequate bond under cyclic loading. The experimental results also showed that an interface resin layer with a thickness of 6.4 mm ($^1/_4$ in.) and a resin captivation layer comprised of polyester breather cloth provided the best balance of stiffness and bond tenacity for the CFRP overlay elements studied. Results showed that use of CFRP materials to improve the fatigue performance of existing structures is a promising and viable technology.

The research reported herein was aimed at investigating factors that determine bond durability between CFRP and steel under a demanding fatigue test set-up, as satisfactory bond performance has historically been a major hurdle to successfully using CFRP as a fatigue retrofit in steel structures. The findings and recommendations of this study are a contribution aimed at overcoming that important hurdle. While this study was not aimed at capturing field conditions, it has removed obstacles to achieving that end. Therefore, one important aspect of future research is a thorough examination of practical matters associated with field application practices and optimizing the CFRP overlay configuration for field implementation. Research should be performed to investigate the applicability of CFRP composite materials for fatigue enhancement of a broader range of geometries, which may guide researchers to consider the practical benefits of very thick bond layers to accommodate dimensional tolerances and different material

application systems, including spray techniques. Further investigation of the effect of the fibrous resin captivation layer on the bond strength of resin epoxy as well as effects of extending the resin pool should also be performed.

B.2.9 References

AASHTO (2013). 2013 Interim Revisions to the AASHTO LRFD Bridge Design Specifications. 6th ed. American Association of State Highway and Transportation Officials, Washington, D.C.

Albrecht, P. and Lenwari, A. (2007) "Fatigue-Proofing Cover Plates." Journal of Bridge Engineering, 12(3), 275-283.

Alemdar, F. (2010). Use of Composite Materials to Repair Steel Structures Vulnerable to Fatigue Damage. (Master's thesis). University of Kansas, Lawrence, KS.

Alemdar, F., Kaan, B., Bennett, C., Matamoros, A., Barrett-Gonzalez, R., and Rolfe, S. (2009). "Parameters Affecting Behavior of CFRP Overlay Elements as Retrofit Measure for Fatigue Vulnerable Steel Bridge Girders." Second International Conference on Fatigue and Fracture in the Infrastructure, Philadelphia, PA, July 26-29, 2009.

ASTM D3039 (2000). Standard Test Method for Tensile Properties of Polymer Matrix Composite Materials. ASTM, West Conshohocken, PA.

Bassetti, A., Nussbaumer, A., and Hirt, A. (2000a). "Crack Repair and Fatigue Life Extension of Riveted Bridge Members using Composite Materials." Bridge Engineering Conference (IABSE), Sharm El-Sheikh, Egypt, vol. I, 227-238.

Bassetti, A., Nussbaumer, A., and Hirt, A. (2000b). "Fatigue Life Extension of Riveted Bridge Members using Prestressed Carbon Fibre Composites." Steel Structures of the 2000s (ECCS), Istanbul, Turkey, 375-380.

Bassetti, A., Nussbaumer, A., and Colombi, P. (2000c). "Repair of Riveted Bridge Members Damaged by Fatigue using CFRP Materials." Advanced FRP Materials for Civil Structures, Bologna, Italy, 33-42.

Buyukozturk, O., Gunes O., and Karaca, E. (2004). "Progress in Understanding Debonding Problems in Reinforced Concrete and Steel Members Strengthened Using FRP Composites." International Journal of Construction and Building Materials, 18(1), 9-19.

Colombi, P., Bassetti, A., and Nussbaumer, A. (2003a). "Analysis of Cracked Steel Members Reinforced by Pre-stressed Composite Patch." Fatigue & Fracture of Engineering Materials & Structures, 26, 59-66.

Colombi, P., Bassetti, A., and Nussbaumer, A. (2003b). "Crack Growth Induced Delamination on Steel Members Reinforced by Prestressed Composite Patch." Fatigue & Fracture of Engineering Materials & Structures, 26, 429-437.

Deng, J. and Lee, M. (2007). "Behavior Under Static Loading of Metallic Beams Reinforced with Bonded CFRP Plate." Composite Structures, 78, 232-242.

Hertzberg, R. W. (1996). Deformation and Fracture Mechanics of Engineering Materials. 4th ed. John Wiley & Sons, New York, NY.

Jones, S. and Civjan, S. (2003). "Application of Fiber Reinforced Polymer Overlays to Extend Steel Fatigue Life." Journal of Composites for Construction, 7(4), 331-338.

Kaan, B. (2008). Fatigue Enhancement of Category E' Details in Steel Bridge Girders using CFRP Materials. (Master's thesis). University of Kansas, Lawrence, KS.

Kaan, B., Barrett, R., Bennett, C., Matamoros, A., and Rolfe, S. (2008). "Fatigue Enhancement of Welded Coverplates Using Carbon-Fiber Composites." 2008 ASCE/SEI Structures Congress Proceedings, 1-8.

Meier, U. (1992). "Carbon Fibre-Reinforced Polymers: Modern Materials in Bridge Engineering." Structural Engineering International, 2(1), 7-12.

Nakamura, H., Jiang, W., Suzuki, H., Maeda, K., and Irube, T. (2009). "Experimental study on repair of fatigue cracks at welded web gusset joint using CFRP strips." Thin-Walled Structures, 47(10), 1059-1068.

Nozaka, K., Shield, C., and Hajjar, J. (2005a). "Design of a Test Specimen to Assess the Effective Bond Length of Carbon Fiber-Reinforced Polymer Strips Bonded to Fatigued Steel Bridge Girders." Journal of Composites for Construction, 9(4), 304-312.

Nozaka, K., Shield, C., and Hajjar, J. (2005b). "Effective Bond Length of Carbon-Fiber-Reinforced Polymer Strips Bonded to Fatigued Steel Bridge I-girders." Journal of Composites for Construction, 10(2), 195-205.

Sabelkin, V., Mall, S., and Avram, J. B. (2006). "Fatigue Crack Growth Analysis of Stiffened Cracked Panel Repaired with Bonded Composite Patch." Engineering Fracture Mechanics, 73(11), 1553-1567.

Sebastian, W. and Luke, S. (2007). "Interface Failure Mechanics of Elastically (Advanced Composite) Reinforced Steel Members." Journal of Structural Engineering, 133(5), 683-694.

SIMULIA (2009). Abaqus FEA, Version 6.8.2. Providence, RI. http://www.simulia.com

Tavakkolizadeh, M. and Saadatmanesh, H. (2003). "Fatigue Strength of Steel Girders Strengthened with Carbon Fiber Reinforced Polymer Patch." Journal of Structural Engineering, 129(2), 186-196.

Vilhauer, B. (2007). Fatigue Behavior of Welded Connections Enhanced by UIT and Bolting. (Master's thesis). University of Kansas, Lawrence, KS.

B.3: Use of Carbon Fiber Reinforced Polymer Overlays to Strengthen Welded Connections under Fatigue Loading

Fatih Alemdar[14]

Adolfo Matamoros[15]

Caroline Bennett[16]

Ron Barrett-Gonzalez[17]

Stanley Rolfe[18]

B.3.1 Abstract

This study evaluates the performance of various methods to prevent and repair fatigue damage in welded connections, a recurring problem that affects a significant number of steel bridges in the national inventory. Experimental tests and analytical simulations were carried out to investigate the fatigue performance of coverplate specimens in which the welded connections were reinforced with carbon fiber reinforced polymer (CFRP) overlays. Some of the overlays were continuous-fiber type, and others utilized spray-on chopped fibers. Specimens were loaded in three-point bending induced by a cyclic load to evaluate the change in fatigue-crack initiation life of the welded connections caused by the attachment of the CFRP overlays.

Test results showed that when bond between the CFRP overlays and the steel was maintained, the reduction in stress demand was sufficient to extend the fatigue life of the welded connections from AASHTO fatigue category E in the unreinforced configuration to the infinite fatigue life range. Test results also showed that the fatigue strength of the bond layer was drastically improved by introducing breather cloth material within the bond layer.

---

[14] Fatih Alemdar, PhD, Assistant Professor, Yildiz Technical University, Istanbul, Turkey

[15] Adolfo Matamoros, PhD, Professor, University of Kansas, 1530 W. 15th St., Lawrence, KS 66045

[16] Caroline Bennett, PhD, PE, Associate Professor, University of Kansas, 1530 W. 15th St., Lawrence, KS 66045

[17] Ronald Barrett, PhD, Associate Professor, University of Kansas, 1530 W. 15th St., Lawrence KS, 66045, USA, Email: barrettr@ku.edu

[18] Stan Rolfe, PhD, PE, A.P. Learned Distinguished Professor, University of Kansas, 1530 W. 15th St., Lawrence, KS 66045

B.3.2 Introduction

A significant number of studies have been performed, mostly in the aerospace field, to investigate the use of fiber reinforced polymers (FRP) to repair metal plates with fully developed fatigue cracks (ie. Sabelkin et al. 2007; Schubbe and Mall 1999; Tavakkolizadeh and Saadatmanesh 2003). In most instances discussed in the literature, pre-existing cracks or notches are covered with one or a few layers of composite sheets to effectively reduce the rate of crack growth. There are very few studies (Nakamura et al. 2009) investigating the use of composite materials to repair or strengthen welded connections. Because welded connections are very common in existing bridge structures, and because the implementation of repairs in this type of connections is often challenging due to limitations imposed by complex geometry, the use of composite materials presents a new alternative that significantly expands the tools available to bridge engineers.

In terms of linear elastic fracture mechanics theory, there are essentially three alternatives to improve fatigue life, if material properties remain the same (Barsom and Rolfe 1999): to reduce the initial flaw size, to reduce the stress range, or to induce a residual stress field that will cause the area subjected to fatigue loading to be in compression.

Repair methods such as laser peening and ultrasonic impact treatment improve fatigue life by reducing the initial flaw size and introducing a residual stress field. Other repair techniques, such as bolting, and attachment of FRP overlays, increase fatigue life by reducing the stress demand. There are many examples in the literature that show the effectiveness of FRP materials when used to repair existing notches or cracks. For example, (Tavakkolizadeh and Saadatmanesh 2003) concluded that the use of FRP sheets to repair notched beam flanges led to significant improvements in fatigue life. Because FRP repairs work by reducing the stress range experienced in the metal substrate, this method should be effective before and after crack initiation, so long as bond between the FRP and the underlying metal is maintained.

The focus of the present study builds upon work performed by Kaan (2008) reported upon in Appendix B.2 and Vilhauer (2010) by examining the effectiveness of various configurations of CFRP overlays, and comparing their performance to other methods of fatigue retrofitting, including ultrasonic impact treatment and weld grinding. Two types of CFRP

overlays are considered in the present work: those made using conventional lay-up techniques, and those created using a spray-on method (chopped fiber overlays). Parameters influencing the performance of the overlays are provided significant attention in the present work, such as geometric properties of the overlay, modulus of elasticity of the CFRP, thickness of the resin layer used to attach the CFRP overlay to the steel surface, and the presence of an unbonded region (gap) in the direct vicinity of the weld. Finally, in the present work, fatigue life of the bond layer between the CFRP overlays and the substrate is closely differentiated from the fatigue life of the retrofitted steel specimens.

B.3.3 Background

Several studies conducted in the past (Nakamura et al. 2009; Tavakkolizadeh and Saadatmanesh 2003), including recent experimental work from the study reported on in Appendix B.2 welded steel connections, show that bonding FRP sheets or overlays can be a very effective technique to improve fatigue-crack initiation life and fatigue-crack propagation life in steel bridge components. This study focuses on the repair of welded cover plate connections that have thick cover plates, which are known to be vulnerable to fatigue damage (Albrecht and Lenwari 2007), using prefabricated CFRP overlays. This particular type of connection was chosen because its geometry falls within the worst fatigue category in the AASHTO LRFD Bridge Design Specification (2013), Category E', and consequently allows for the evaluation of strengthening techniques that bring about large increases in fatigue life. Additionally, this geometry induces both shear and peel stresses on the bond layer, which are hypothesized to be critical stresses in a FRP-type repair for distortion-induced fatigue.

A thorough review of experimental work carried out to characterize the fatigue performance of welded cover plates in steel beams, including several retrofit techniques, is presented by Albrecht and Lenwari (2007). Experimental data presented by Albrecht and Lenwari (2007) in their review showed that three techniques: end bolting, splicing, and bonding of the cover plates with an epoxy adhesive, resulted in large increases in fatigue life, pushing the beams to the infinite fatigue life range.

The present study is a continuation of studies carried out by Vilhauer (2010), Petri (2008) and Kaan (2008), evaluating the performance of various repair and retrofit measures for welded

connections. Vilhauer (2010) tested 17 steel welded cover plate specimens (Figure B.21) to investigate the performance of several fatigue strengthening methods. The specimens used by Vilhauer (which had the same dimensions as those used in this study) each consisted of two steel plates connected all-around with an 8 mm (0.3 in.) shielded metal arc (SMAW) fillet weld. One of the plates had dimensions of 1270 mm x 114 mm x 25 mm (50 in. x 4.5 in. x 1.0 in.), while the other had dimensions of 660 mm x 76 mm x 25 mm (26 in. x 3.0 in. x 1.0 in.) Both plates were Grade A36 steel. The specimen was supported in the vertical direction at a distance of 76 mm (3.0 in.) from both edges of the larger plate. Vilhauer (2010) evaluated three different fatigue strengthening methods: ultrasonic impact treatment (UIT), a post-installed fully-tensioned structural high-strength bolt, and a combination of the two techniques. Vilhauer (2010) found that specimens in which the welds were treated with UIT were able to reach infinite fatigue life when tested at a stress range of 138 MPa (20 ksi).
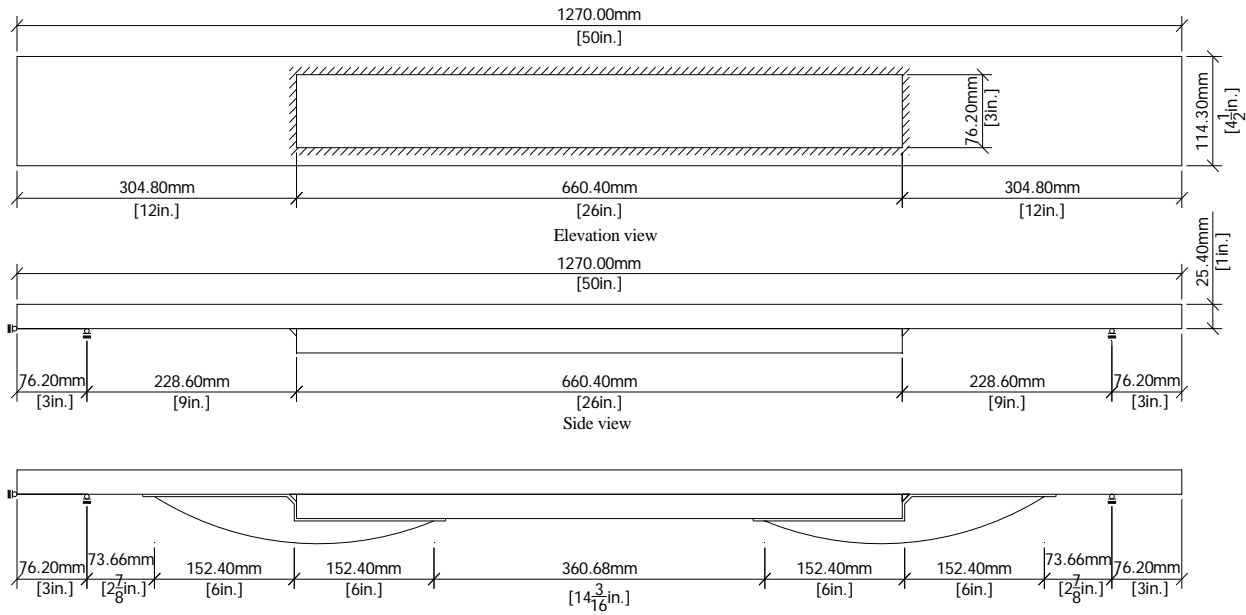
Figure B.20: Three point bending specimens
(a) Without CFRP retrofit (Vilhauer 2010); (b) With CFRP retrofit applied (Kaan 2008)

Kaan (2008) studied the use of CFRP overlays for increasing fatigue crack initiation life. Kaan (2008) conducted experiments with two different types of prefabricated overlays: Type I and Type II. Type I overlays were fabricated by placing successive layers of bidirectional woven

179

carbon-fiber ply until the desired geometry was achieved. Type II overlays were developed to obtain greater consolidation and uniformity than achieved in Type I overlay elements. Type II overlays were comprised of 36 plies of bidirectional woven carbon fiber plies (pre-impregnated with cyanamide-123 resin) and four plies of boron fiber. In testing that utilized Type I overlays, fatigue failure occurred through the composite material, instead of the bond layer or the welded connection.

The results of multiple test trials carried out by Kaan (2008) on four different fatigue specimens reinforced with Type II CFRP overlays are presented in Table B.10. Although the test results showed that the fatigue-crack initiation life of the welded connections increased when the specimens were reinforced with CFRP overlays, repeated bond failures between the CFRP and the steel occurred. When debonding of the overlay occurred, the specimen was subjected to fatigue cycles in the unreinforced configuration until debonding was noticed through inspection; in these cases, the CFRP overlay was reattached to the steel specimen after subsequent inspection for cracks. After multiple debonding failures, the steel substrate was subjected to a significant number of load cycles in the unreinforced configuration, placing it at greater risk for developing a fatigue crack. For this reason, these tests provide meaningful information about the effect of the interface layer configuration on the bond life under fatigue loading and also showed that use of the overlays led to an increase in the fatigue-crack initiation life of the welded connections; however, the tests do not present an appropriate measure of the magnitude of the increase in fatigue life of the welded connection when bond between the CFRP overlay and the steel substrate is maintained throughout the test.

Table B.10: Experimental Results of Three Point Bending Tests Performed by Kaan (2008) and Vilhauer (2010) All specimens tested at a stress range of 138 MPa (20 ksi)

Type of Treatment	Specimen Desig.	Resin Thickness, mm (in)	Duration of test, No. of cycles	No. of cycles to crack initiation	Average number of cycles to CFRP debonding	No. of debonds	Reference
CFRP	TRI 02	0.76 (0.030)	900,000	460,000	588,000	2	Kaan (2008)
CFRP	TRI 06	1.65 (0.065)	1,554,656	N/A	431,500	5	Kaan (2008)
CFRP	TRI 04	3.18 (0.125)	2,051,800	1,329,800	239,070	6	Kaan (2008)
CFRP	TRI 05	6.35 (0.250)	1,634,756	N/A	1,205,000	1	Kaan (2008)
None	Cntrl_03			500,000			Vilhauer (2010)
None	Cntrl_05			350,000			Vilhauer (2010)
UIT	Uit_02			5,000,000			Vilhauer (2010)
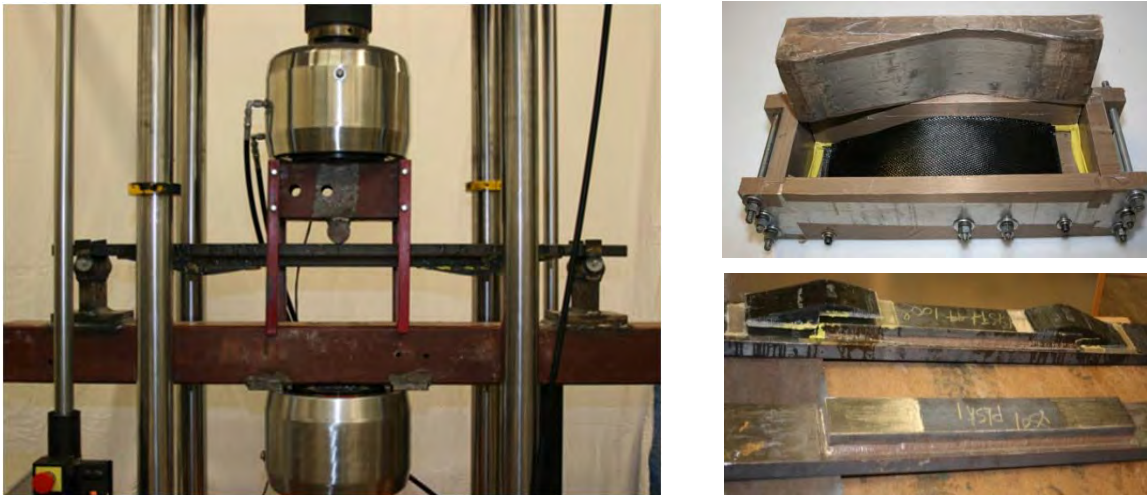
Figure B.21: Three point bending specimens (a) Test setup; (b) CFRP overlay in fabrication mold; (C) Unreinforced and reinforced specimens side by side.

The two main conclusions from the tests performed by Kaan (2008) reported upon in Appendix B.2 were that the use of CFRP overlays led to a significant increase in fatigue-crack initiation life of the welded connections, and that maintaining the bond between the CFRP and the steel substrate was a critical factor to achieving the largest possible increase in fatigue-crack initiation life.

B.3.4 Objective

The primary objective of this study was to investigate the effectiveness of CFRP overlays as a fatigue strengthening method (attaching overlays before crack initiation) for welded connections, and to compare its effectiveness to that of other methods used to strengthen welded connections. A second objective was to determine the effectiveness of CFRP overlays in reducing fatigue-crack propagation rate when used as a repair method (attaching overlays after crack initiation).

To meet both objectives, three-point bending welded cover plate specimens were tested in fatigue under a constant stress range. Pre-fabricated CFRP overlays were bonded to the ends of the cover plates both prior to loading and after fatigue cracks were observed in the welds.

To complement the experimental study, a suite of finite element analyses were performed to characterize the stress field in the region surrounding the weld toe, and to quantify the effect of the characteristics of the overlay on the stress demand.

B.3.5 Finite Element Simulations

The stress distribution in specimens tested by Vilhauer (2010) and Kaan (2008) was studied by Petri (2008) with 3D analyses performed using the finite element software Abaqus V.6.8 (SIMULIA 2009). Models were created using linear elastic material models for the steel and composite materials, and a mesh consisting of 20-node brick elements. The interface between the two plates was modeled as a contact surface, and analyses were performed with a various assumptions about the interaction between the plates, ranging from a frictionless surface to a fully attached surface. The welds were modeled as separate parts and rigidly connected to the plates using the tie constraint technique in Abaqus (SIMULIA 2009). The analyses showed that attaching CFRP overlays to a welded steel cover plate connection would result in a significant reduction of peak stress at the toe of weld, which was consistent with the increase in fatigue life observed experimentally by Kaan (2008).

Deflected shapes and computed maximum principal stresses under the peak load from the various computational models analyzed by Petri are shown in Figure B.22. The stress fields show that the composite overlays were effective in reducing the high stress demands that occurred at the weld toe of the unreinforced specimen, and in distributing those stresses over a much greater

182

area. A comparison of Figures B.22 (b), (c) and (d) shows that the there was a spike in stress field near the edge of the CFRP overlay closest to the end of the specimen, and that the magnitude of the spike decreased as the length of the overlay increased. Due to the spike in the stress field this point is of critical importance to maintain the bond between the FRP overlay and the substrate steel, particularly in the case of shorter overlays. Additional finite element simulations were conducted as a part of this study. 2D finite element models were developed in Abaqus v.6.8.2 (SIMULIA 2009) using linear elastic material properties and 4-noded plane strain elements. The 2D model captured a 25 mm (1.0 in.) mid-width strip of the specimen. Twenty different models were analyzed to provide the basis for a parametric study. Parameters investigated included the geometric profile of the overlay, its length, thickness (Figure B.23), modulus of elasticity of the CFRP, thickness of the resin layer used to attach the CFRP overlay to the steel surface, and the presence of an unbonded region (gap) in the direct vicinity of the weld. Each parameter was varied while maintaining the others constant. The reference values for the modulus of elasticity of the composite and the thickness of the resin layer were 26.5 GPa (3850 ksi) and 6.4 mm (0.25 in.), respectively, and the modulus of elasticity of the resin was 3.5 GPa (500 ksi). The different geometric profile parameters that were investigated are shown in Figure B.23
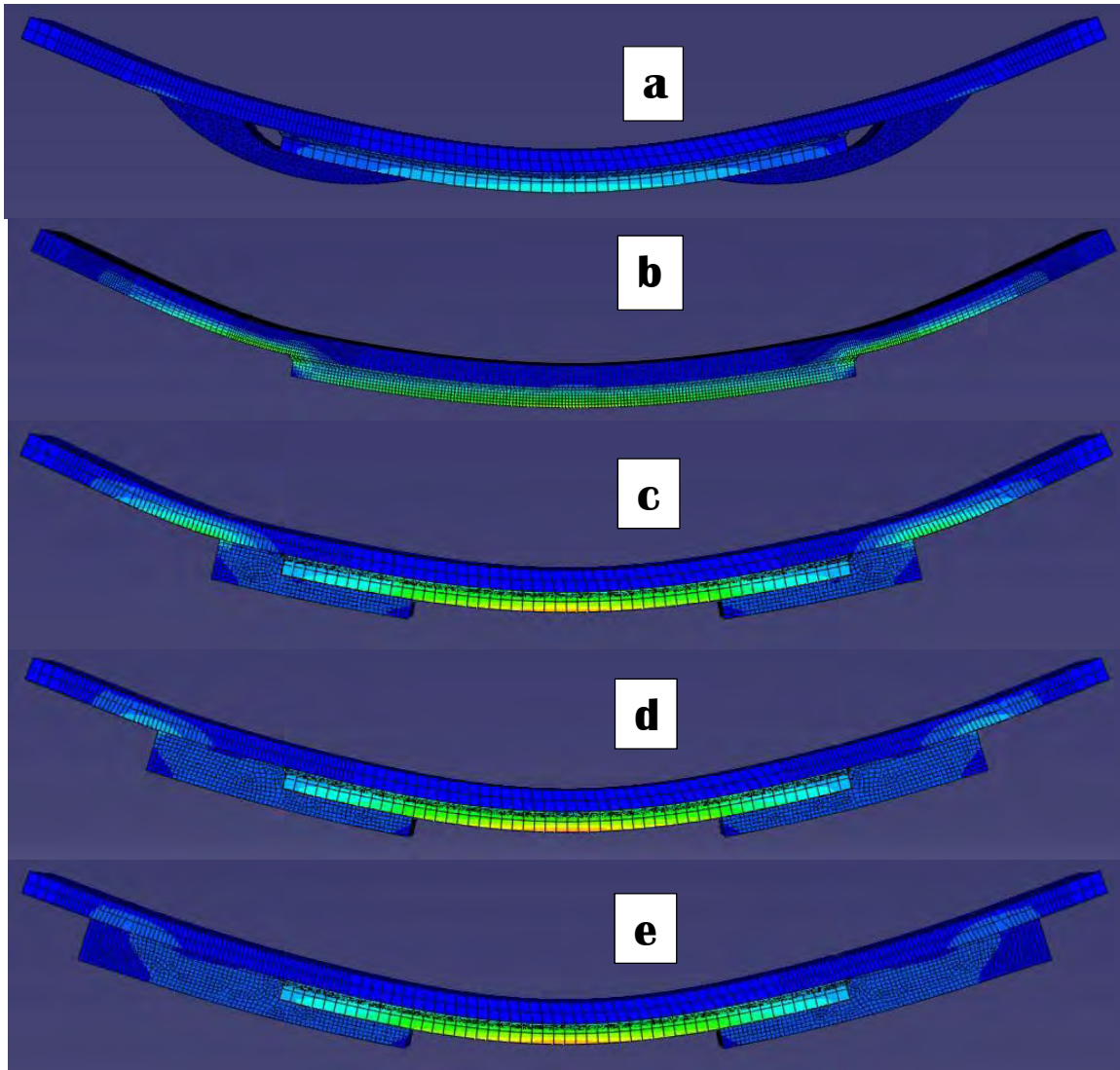
**Figure B.22: Elevation view showing maximum principal stress
(a) control specimen; (b) specimen with smooth-shaped composite overlay; (c) short rectilinear composite overlay; (d) rectilinear composite overlay; (e) long rectilinear composite overlay**

Figure B.23 a) Rectangular, Standard — 144mm [$5\frac{11}{16}$in.], 8mm [$\frac{5}{16}$in.], 152mm [6in.], 48mm [$1\frac{7}{8}$in.], 23mm [$\frac{7}{8}$in.]

b) Curved without gap — 144mm [$5\frac{11}{16}$in.], 8mm [$\frac{5}{16}$in.], 152mm [6in.], 48mm [$1\frac{7}{8}$in.]

c) Rectangular, Short — 68mm [$2\frac{11}{16}$in.], 8mm [$\frac{5}{16}$in.], 152mm [6in.], 48mm [$1\frac{7}{8}$in.], 23mm [$\frac{7}{8}$in.]

d) Curved with gap — 102mm [4in.], 51mm [2in.], 152mm [6in.], 48mm [$1\frac{7}{8}$in.]

e) Rectangular, Long — 221mm [$8\frac{11}{16}$in.], 152mm [6in.], 48mm [$1\frac{7}{8}$in.], 23mm [$\frac{7}{8}$in.]

f) Rectangular with gap — 102mm [4in.], 51mm [2in.], 152mm [6in.], 48mm [$1\frac{7}{8}$in.], 23mm [$\frac{7}{8}$in.]

Figure B.23: Configuration of CFRP overlays evaluated in the analytical model

The parametric study was intended to determine the optimum configuration of the CFRP overlay and to investigate how effective the overlay would be in decreasing the peak stress demand at the weld toe. Computed stress fields in the vicinity of the weld for the unreinforced and reinforced (Figure B.23b) configurations are presented in Figure B.24. The 2D simulation results were consistent with those obtained by Petri (2008) in that the addition of the overlay resulted in a significant reduction in the peak stress demand at the weld toe (on the order of 80% for the overlay configuration shown in Figure B.23(d). These simulation results were also consistent with the increments in fatigue life increase observed by Kaan (2008).
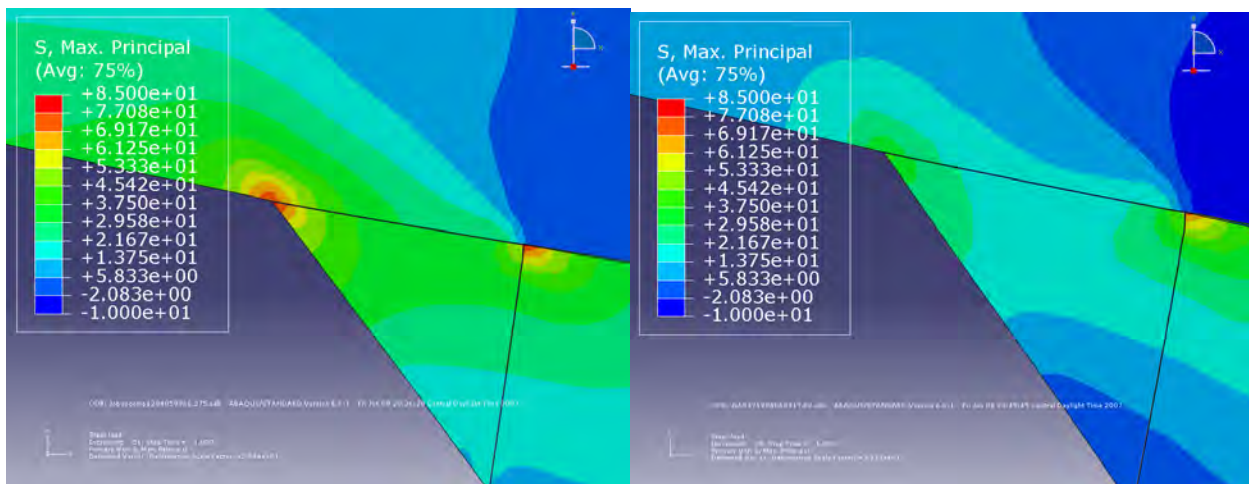
Figure B.24: Elevation view showing maximum principal stress
(a) Control specimen; (b) Specimen with smooth-shaped composite overlay (overlay not shown for clarity)

185

The finite element analyses also showed that the reduction in the maximum principal stress was not as significant at the root of the weld as it was at the toe of the weld. Unreinforced specimens in which cracks were allowed to propagate until structural failure of the specimen exhibited crack initiation at the toe of the weld, consistent with the computed stress field for the unreinforced configuration shown in Figure B.24. In the case of reinforced specimens, tests conducted by Kaan in which debonding took place showed that the fatigue behavior after debonding was similar to that of unreinforced specimens, with cracks initiating at the toe of the weld and propagating through the plate from that location. In specimens in which debonding of the overlays did not take place, the specimens did not develop visible cracks by the time the infinite fatigue life range was reached. Given the configuration of the specimens it was not possible to inspect the back of the welds for cracks, so the only conclusion that could be drawn about the behavior at the root of the weld was that either the reduction in stress demand at the root of the weld was sufficient to achieve infinite fatigue life, or that if fatigue cracks developed at this location, the reduction in the stress demand was sufficient to delay the propagation of those cracks so that there were no visible signs of damage or measurable changes in the stiffness in the specimens when the infinite fatigue life range was achieved.

The suite of finite element simulations performed in this study evaluated the effect of the following parameters: geometric configuration of the overlay, thickness of the interface bond layer, and the modulus of elasticity of the composite. The 2D simulations showed that the geometric profile of the CFRP overlay did not have a significant effect on the calculated stress demand at the weld toe, whereas the presence of a gap between the weld and the CFRP overlay did have a notable effect. This is illustrated in Figure B.25 and B.26, which present the computed longitudinal stress along a path on the surface of the bottom steel plate. The observed trends in the calculated longitudinal stress and the maximum principal stress were similar in nature, so the directional stress presented in the figures was chosen on the basis of clarity.

In Figures B.25 and B.26, the spike in stress observed at a distance of approximately 298 mm (11.8 in.) from the edge of the specimen corresponds to the location of the toe of the weld, while the root of the weld was located at approximately 307 mm (12.1 in.) from the edge of the specimen. The distance from the edge of the specimen shown in the two figures corresponds to

186

the "true distance" measured in the computed deformed configuration. This causes as slight offset in the locations of the toe of the weld and the root of the weld in the curves shown in Figures B.25 and B.26. Results were plotted using this coordinate system to facilitate observing similarities and differences between the curves.

Figure B.25 shows that a curved and a rectilinear CFRP overlay configuration were equally effective in reducing the peak stress demand at the toe of the weld. Figure B.27 shows that the most effective retrofit scheme involved bonding the overlay up to the location of the weld, which resulted in a reduction on the peak stress demand at the weld toe on the order of 80%. When the analysis was performed leaving a gap near the weld toe [configuration shown in Figure B.23(d)] the reduction in peak stress demand at the weld toe was still very significant, on the order of 60%, but the efficiency of the repair was diminished. The analyses showed that within the evaluated range of values, other parameters related to the shape of the CFRP overlay, such as length and the thickness of the overlay, did not significantly affect stress demand at the toe of the weld.
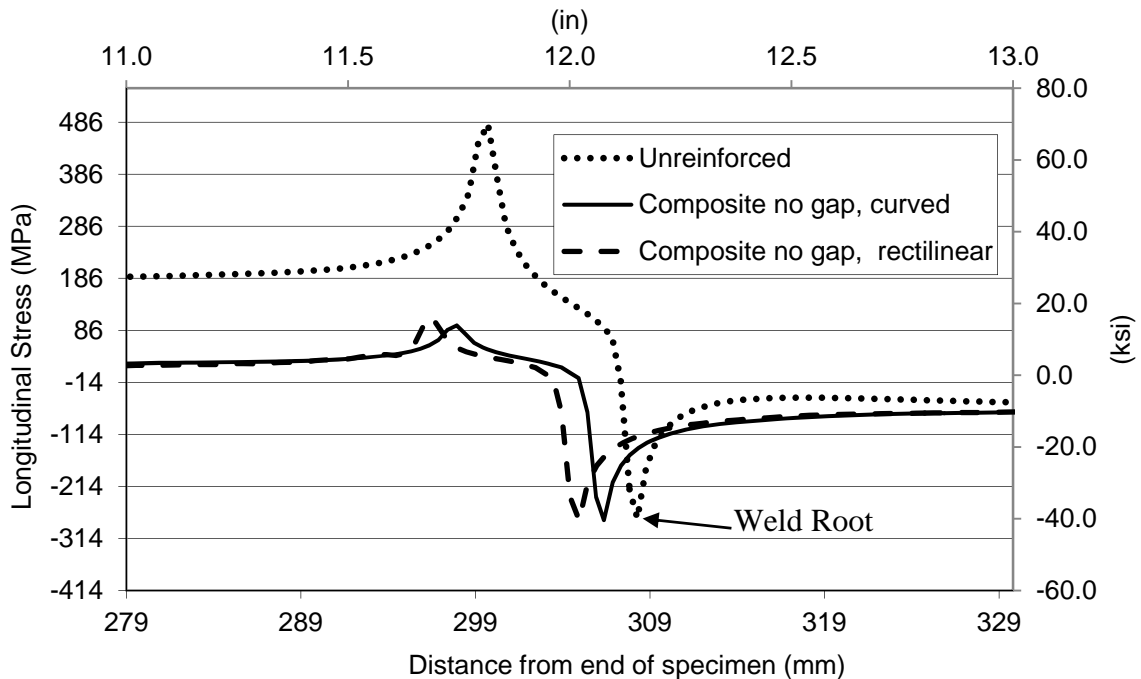
Figure B.25: Effect of composite overlay shape on longitudinal stresses in the area of the weld
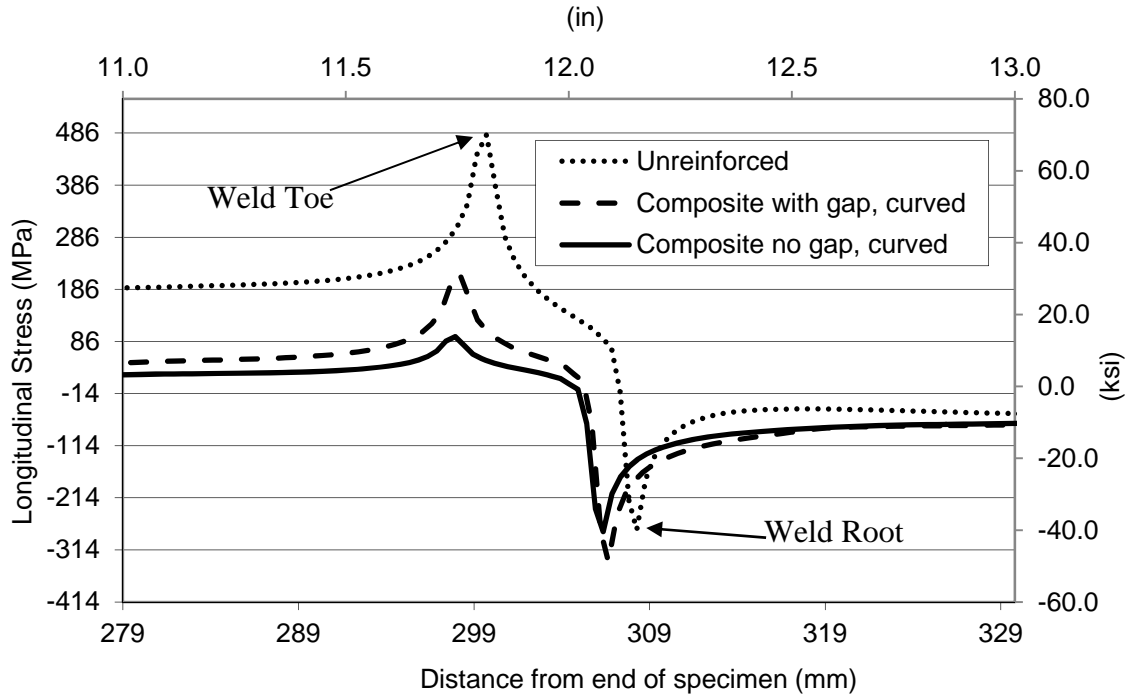
Figure B.26: Effect of the presence of an unbonded gap over the weld on the longitudinal stresses in the area of the weld

Of the remaining parameters, the modulus of elasticity of the composite and the thickness of the interface bond layer had the most significant effect on the stress demand at the weld toe. The effect of the modulus of elasticity of the CFRP overlay is illustrated in Figure B.27.

A reference value of 26.6 GPa (3,860 ksi) was adopted for the modulus of elasticity based on experimental measurements performed on the composite material used to fabricate the overlays used in this study. A suite of FE analyses were performed in which the CFRP modulus of elasticity ranged between 60% of the reference value (16 GPa [2,315 ksi]) and 400% of the reference value (106 GPa [15,430 ksi]). Results presented in Figure B.27 are for the overlay configuration shown in Figure B.23(b).

Figure B.27 shows that equal successive increments in the modulus of elasticity of the CFRP overlay resulted in decreases in stress demand. These results suggest that prefabricating the overlay to achieve higher fiber contents, as was done in this study, improves the effect of the repair on the fatigue life of the welded connection. The results also suggest that, for the analyzed overlay configurations, paying a premium for very stiff fibers may not bring about a meaningful increase in fatigue life beyond that achievable with conventional fibers.

188

The effect of the thickness of the interface layer is illustrated in Figure B.28, which shows that explicitly modeling the flexibility of the interface layer resulted in a lower stress demand at the weld toe, likely due to the effects of bending on the overlays. When the interface layer was modeled, increasing the thickness of the overlay resulted in a slight increase in the peak stress demand at the weld toe. This indicates that a thicker interface layer is less effective in reducing the peak stress demand at the weld toe than a thinner interface layer. However, the analyses also showed that peak shear and peel stress demands at the interface between the composite and the bond layer exhibited the opposite trend. Figure B.29 shows that as the thickness of the interface decreased (which reduces the calculated stress demand at the weld toe), both the calculated peak shear and peel stress demands increased, which can be expected to have a detrimental effect on bond strength under cyclic loading.
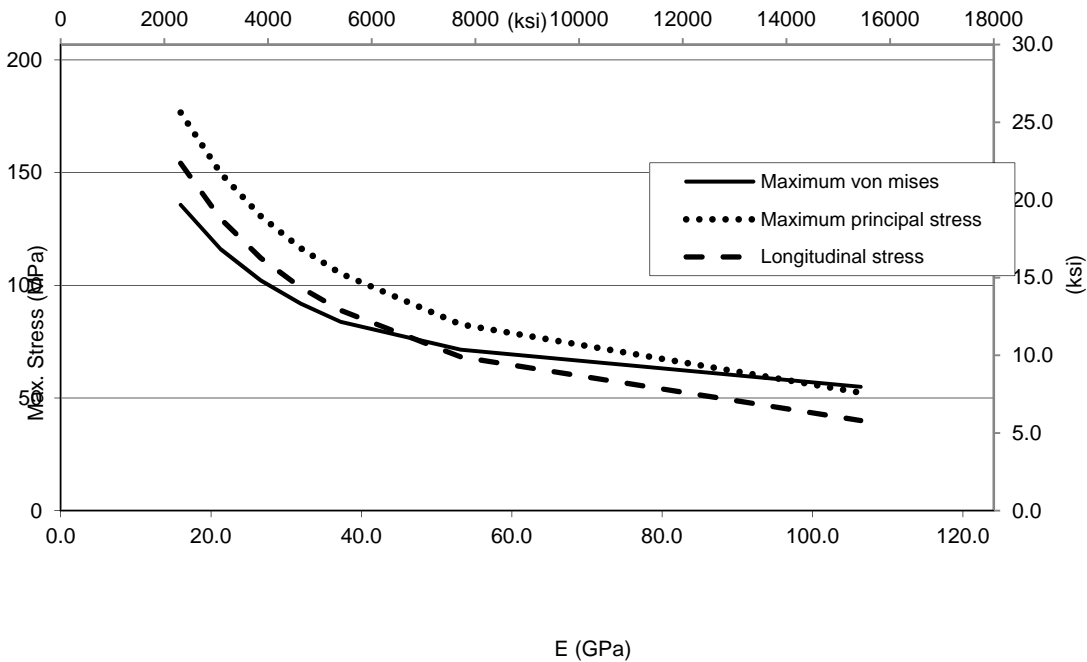
Figure B.27: Effect of composite overlay stiffness on maximum stress demand at the weld toe
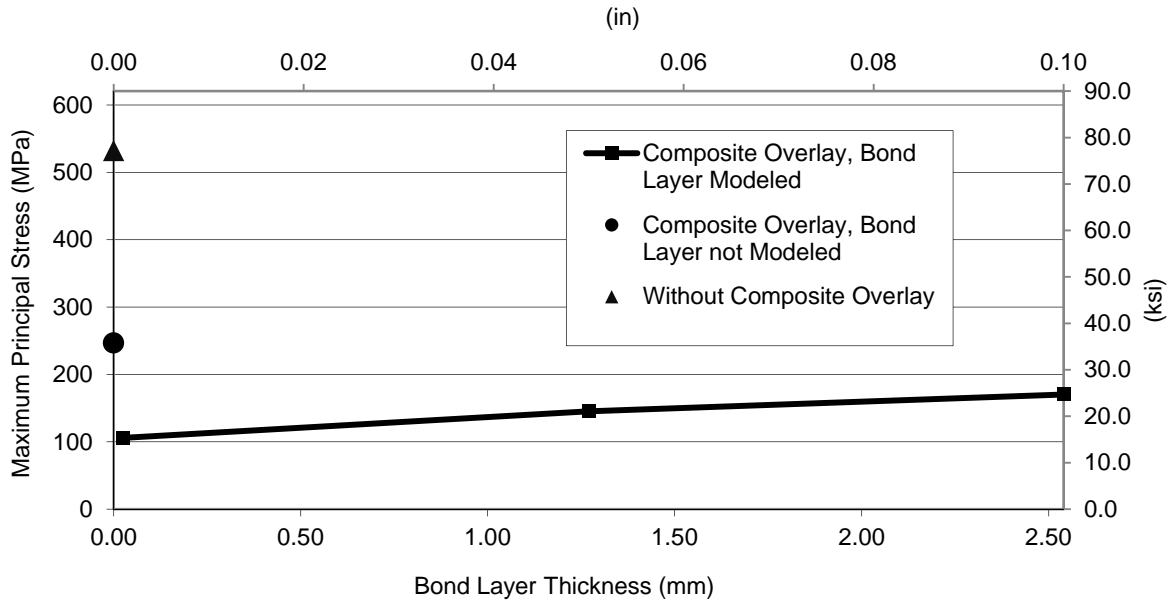
Figure B.28: Maximum principal stress on the steel plate in the vicinity of the weld as a function of the thickness of the bond layer
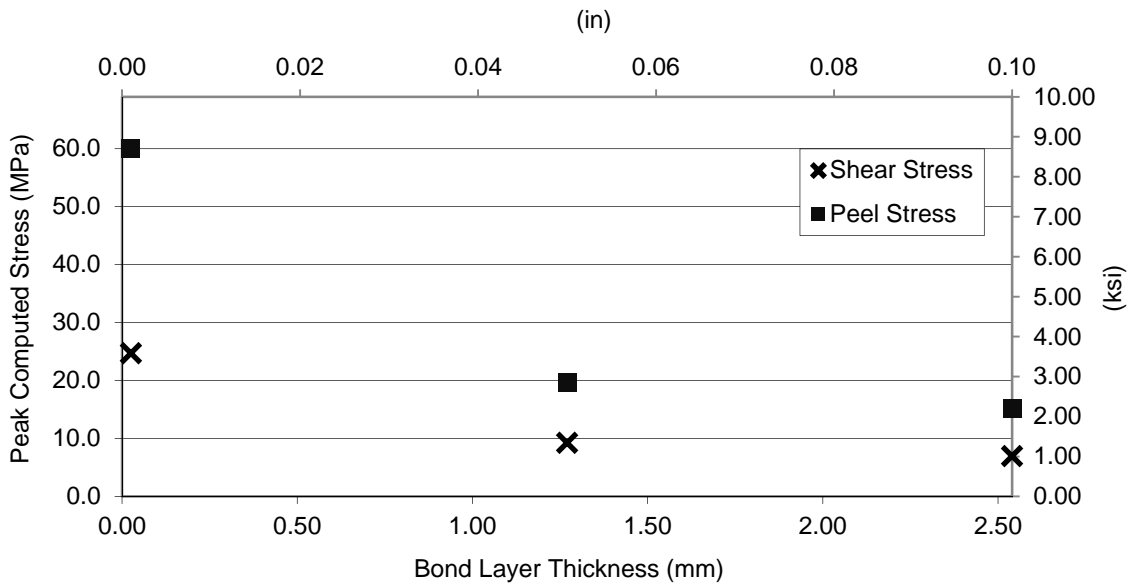
Figure B.29: Maximum computed stress at the interface between the composite and the bond layer

B.3.6 Experimental Analysis

The experimental program consisted of a series of welded cover plate specimens loaded in three point bending and subjected to cyclic loading under a constant stress range (Figures B.20 and B.21). The three point bending specimens were comprised of two plates with identical dimensions as those studied by Vilhauer (2010) and Kaan (2008), and previously described in the background section. The specimens were restrained from vertical motion at points 76 mm (3.0 in.) from the edges of the larger plate. The smaller plate was attached to the larger plate with a continuous 8 mm ($^5/_{16}$ in.) fillet weld all around the perimeter of the smaller plate. The effect of weld imperfections on the fatigue performance of the repair methods was not a parameter investigated in the study. An effort was made to ensure that all welds in the specimens were similar in nature by having all welding performed by the same fabricator using the same technique under similar conditions. The welds were of good quality with no visible signs of undercut at the toe of the weld and had a slightly convex profile.

The experimental matrix is summarized in Table B.11. As shown, three different types of treatments were utilized, including three different types of composite overlays. To establish a frame of reference based on the type of geometric discontinuity, the welded connection between the two plates was classified as an AASHTO Category E' detail (AASHTO 2013). According to the AASHTO design curves, the nominal stress range for a Category E' detail should be maintained below 31.0 MPa (4.50 ksi) in the area of the weld to ensure that cracking will not initiate under fatigue loading. Loads were selected to achieve a high stress range of 138 MPa (20.0 ksi) at the transverse welds, at the location of the weld toes. The ratio of maximum to minimum load was selected as $R = 0.1$. The maximum load was 17.1 kN (3.84 kips) and the minimum load was 1.70 kN (0.38 kips).

Three specimens were strengthened with prefabricated multi-layered CFRP overlays, and were designated TRI 04, TRI 06, and TRI 07. Multi-layered CFRP overlays were prefabricated following the same procedure used by Kaan (2008) for Type II overlays. The dimensions of CFRP overlay were 300 mm x 76 mm x 38 mm (12 in. x 3.0 in. x 1.5 in). The shape of CFRP was curved in profile, without leaving any gap between weld and the CFRP [Figure B.23(b)].

Breather cloth approximately 2 mm (0.1 in.) thick was embedded within the resin layer to improve bond behavior under cyclic loading.

Table B.11: Experimental Matrix

Specimen ID	Stress Range MPa (ksi)	Thickness of Bond Layer * mm (in.)	Treatment Type	Fiber Type
TRI 04	138 (20)	6.4 ($^{1}/_{4}$)	CFRP Overlay	Carbon
TRI 06	138 (20)	6.4 ($^{1}/_{4}$)	CFRP Overlay	Carbon
TRI 07	138 (20)	3.2 ($^{1}/_{8}$)	CFRP Overlay	Carbon
CHP1	138 (20)	None	Chopped Fiber	Carbon
CHP2	138 (20)	6.4 ($^{1}/_{4}$)	Chopped Fiber	Carbon
CHP3	138 (20)	6.4 ($^{1}/_{4}$)	Chopped Fiber	Glass
GRND 1	193 (28)		Smoothed Weld	
GRND 2	193 (28)		Smoothed Weld	
GRND 3	193 (28)		Smoothed Weld	
GRND 4	193 (28)		Smoothed Weld	
Control (TRI 08)	138 (20)			

$*$ *when multiple bond layer configurations were used in the same specimen, value shown is for configuration with breather cloth*

Of the three specimens treated with muli-layered CFRP overlays, two (TRI 06 and TRI 07) were intended to study the effectiveness of CFRP overlays for preventing fatigue damage in the area near the weld toe. The remaining specimen (TRI 04) was used to investigate the effectiveness of the CFRP overlays to repair a connection with a pre-existing fatigue crack in the weld. One of the uncracked specimens (TRI 07) had never been loaded before, while the other two specimens (TRI 04 and TRI 06) had already been subjected to fatigue loading by Kaan (2008).

In addition to the specimens described above, three specimens were treated with chopped fiber overlays. The chopped fiber overlays were fabricated using an external mixing spray machine (a non-atomized resin LEL chopper system commercialized by BINKS). The spray machine utilized a vinyl ester resin with Norox MEKP-925 catalyst and graphite fiber yarn. Prior to spraying the composite material, the surface of the steel substrate was abraded using an angle grinder and cleaned with acetone and isopropyl alcohol. After cleaning, the fiber-resin mix was sprayed in layers approximately 3 mm ($^{1}/_{8}$ in.) thick and compacted using a hand tool. Overlay CHP 1 had the configuration shown in Figure B.23(a) while the shape of overlays CHP

2 and CHP3 was similar to that of the prefabricated multi-layered CFRP overlay [Figure B.23(b)]. All overlays used in the testing program are shown in Figure B.30. After spraying was completed, the specimen was cured at room temperature for two days, after which the remnant resin was cleaned from the steel substrate. In the specimen designated CHP 2, a breather cloth layer was placed on the surface of the steel and saturated with resin before spraying the combined resin-chopped graphite fiber mix. In the specimen designated CHP 3, the breather cloth was soaked with Hysol® resin and cured for two hours at room temperature before a resin-chopped glass fiber mix was sprayed.

All other specimens tested were not treated with composite overlays. An additional control test (TRI 8) was performed to complement the data set developed by Vilhauer (2010) on identical specimens (Table B.10). The remaining specimens without overlays (GRND 1 through GRND 4) were treated by smoothing out the roughness of the surface of the welds using an angle grinder. When the smoothing process was finished, the surface of the weld was approximately flat, and formed an angle of approximately 45 degrees with respect to the surface of both plates. After grinding, the surface of the weld was cleaned with a steel brush to ensure imperfections from the welding process had been removed. This process was repeated until no imperfections were visible. The two goals of the weld treatment were to ensure that there was a smooth transition between the weld and the plate at the weld toe, and to significantly reduce the initial size of the weld flaws created during the welding process.

Figure B.30: Composite overlays used in the study

Measured material properties are presented in Table B.12. Coupon tests performed in accordance with ASTM 3039/D 3039M (ASTM 2000) from single-layered specimens showed that the modulus of elasticity of the CFRP was approximately 83 GPa (12,000 ksi). The modulus of elasticity of the 9412 Hysol® resin and of the chopped fiber composite were also measured using coupon tests (Table B.12) as prescribed by ASTM 3039/D 3039M (ASTM 2000). The measured modulus of elasticity of the resin was 2.1 GPa (300 ksi). The yield strength of the steel was found to be 300 MPa (43 ksi), and the tensile strength was 490 MPa (70.9 ksi).

Table B.12: Material Test Results

CFRP	Number of Layers in Coupon	Number of Coupons	Avg Modulus of Elasticity GPa (ksi)	Standard Deviation GPa (ksi)
	1	3	85.8 (12,438)	10.0 (1,445)
	3	4	75.3 (10,926)	10.9 (1,581)
	5	3	61.7 (8,944)	0.3 (42)
9412 Hysol® Resin	Coupon Thickness mm (in.)			
	6.4 (0.25)	6	2.1 (303)	0.2 (25)
Chopped fiber (Graphite Fiber)	4.8 (0.19)	7	14.1 (2,052)	6 (866)
Chopped fiber (Glass Fiber)	5.6 (0.22)	1	1.4 (202)	--

B.3.7 Results from Three-point Bending Specimens under Fatigue Loading

There were two common modes of fatigue failure observed in the tests carried out by Vilhauer (2010), Kaan (2008) and those performed as part of this study: fatigue failure of the bond layer between the composite and the steel, and fatigue failure of the welded connection. For this reason the results are interpreted in terms of two different types of fatigue tests, those related to the fatigue life of the bond layer (Table B.13, and those related to the fatigue life of the welded connection (Table B.14).

Table B.13: Fatigue Life of Bond Layer for Various Bonding Techniques

Test Designation	Resin Layer Thickness, mm (in.)	Number of Cycles to Bond Failure †
C0030-01	0.76 (0.03)	275,000
C0030-02	0.76 (0.03)	900,000
C0125-01	3.18 ($^1/_8$)	529,800
C0125-02	3.18 ($^1/_8$)	255,750
C0125-03	3.18 ($^1/_8$)	134,150
C0125-04	3.18 ($^1/_8$)	71,150
C0125-05	3.18 ($^1/_8$)	204,500
C0125-06	3.18 ($^1/_8$)	1,125,300*
CP0125-01	3.18 ($^1/_8$)	1,060,950*
CP0125-02	3.18 ($^1/_8$)	722,000*
CPB0250-03	6.35 ($^1/_4$)	1,318,900*
CPB0250-04	6.35 ($^1/_4$)	1,318,900*
CPB0250-05	6.35 ($^1/_4$)	1,547,850*
CPB0250-06	6.35 ($^1/_4$)	1,547,850*
CP0065-01	1.59 ($^1/_{16}$)	279,750
CP0065-02	1.59 ($^1/_{16}$)	283,900
CP0065-03	1.59 ($^1/_{16}$)	802,900
CP0065-04	1.59 ($^1/_{16}$)	153,706
CP0065-05	1.59 ($^1/_{16}$)	637,846
CPB0250-07	6.35 ($^1/_4$)	1,550,450*
CPB0250-08	6.35 ($^1/_4$)	1,550,450*
CPB0250-01	6.35 ($^1/_4$)	1,205,315
CPB0250-02	6.35 ($^1/_4$)	1,634,756*
CPB0125-01	3.18 ($^1/_8$)	1,725,900*
CPB0125-02	3.18 ($^1/_8$)	1,725,900*
CPB0125-03	3.18 ($^1/_8$)	1,564,300*
CPB0125-04	3.18 ($^1/_8$)	1,564,300*

*Test was stopped without observed debonding after number of cycles exceeded infinite fatigue life
† All tests performed at a stress range of 138 MPa (20 ksi)

Table B.14: Experimental Results of Three Point Bending Tests

Specimen Designation	Stress Range MPa (ksi)	Bond Layer Thickness mm (in.)	Number of Cycles *	No of Cycles to Crack initiation	Operator
TRI 02	137.9 (20.0)	0.76 (0.03)	900,000	N/A	Kaan (2008)
TRI 04	137.9 (20.0)	3.18 ($^1/_8$)	4,918,550 †	N/A	Kaan (2008)-Alemdar
TRI 05	137.9 (20.0)	6.35 ($^1/_4$)	1,634,756	N/A	Kaan (2008)
TRI 05	137.9 (20.0)	6.35 ($^1/_4$)	1,634,756	N/A	Kaan (2008)
TRI 06	137.9 (20.0)	1.59 ($^1/_{16}$)	3,105,106	N/A	Kaan (2008)-Alemdar
TRI 06	137.9 (20.0)	1.59 ($^1/_{16}$)	3,105,106	N/A	Kaan (2008)-Alemdar
TRI 07	137.9 (20.0)	3.18 ($^1/_8$)	3,290,200 ‡	N/A	Alemdar
TRI 07	137.9 (20.0)	3.18 ($^1/_8$)	3,290,200 ‡	N/A	Alemdar
TRI 08	137.9 (20.0)			355,450	Alemdar
GRND 1	193.1 (28.0)			391,000	Alemdar
GRND 2	193.1 (28.0)			1,200,000	Alemdar
GRND 3	193.1 (28.0)			950,000	Alemdar
GRND 4	193.1 (28.0)			600,000	Alemdar
UIT 02	193.1 (28.0)			1,300,000	Vilhauer (2010)
UIT 03	193.1 (28.0)			2,100,000	Vilhauer (2010)
UIT 01	137.9 (20.0)		5,000,000	N/A	Vilhauer (2010)
Cntrl_05	193.1 (28.0)			80,000	Vilhauer (2010)
Cntrl_06	193.1 (28.0)			50,000	Vilhauer (2010)
Cntrl_04	137.9 (20.0)			350,000	Vilhauer (2010)

† After 1.3 mil cycles and at the end of the test overlays were removed to measure crack length
‡ After 1.5 mil cycles and at the end of the test overlays were removed to inspect for the presence of cracks
* Specimens that achieved runnout

Debonding of the overlay under fatigue loading occurred in a relatively rapid manner (Kaan, 2008). Bond layers were periodically examined by visual inspection and by monitoring the stiffness of the specimen computed on the basis of the applied load and the vertical displacement at the center. Failure of the bond layer typically initiated at the edge of the overlay closest to the end of the specimen and propagated through the bond layer towards the toe of the weld (Kaan, 2008). Welds were inspected for the presence of cracks with dye penetrant using the technique adopted by Vilhauer (2010). Cracks typically initiated at the weld toe, near the center of the weld, and propagated towards the edge of the specimen.

B.3.8 Fatigue Strength of the Bond Layer

The study by Kaan (2008) showed that composite overlays can effectively prevent fatigue failure of the welded connection, but to do so, it is essential to avoid failure of the bond layer due to fatigue. The effect of various bonding techniques on the fatigue strength of the bond layer are shown in Figure B.31, and test results are summarized in Table B.13. Designations for the experiments carried with multi-layered CFRP overlays were defined in terms of the thickness of the bond layer. In specimens in which multiple bond failures took place the overlay was reattached to the same cover plate specimen after each failure event. Overlays were inspected and re-used if undamaged. Specimens without breather cloth and resin pool (tested by Kaan [2008]) are designated by the letter C, specimens with a resin pool extending beyond the edge of the overlay (Kaan 2008) are designated by the letters CP, those with breather cloth and a resin pool (tested as part of this study) are designated CPB, and the three specimens with chopped fiver overlays (also tested as part of this study) are designated by the letters CHP. A resin pool was created by leaving a gap of at least 13 mm ($^1/_2$ in.) between the edge of the overlay and the edge of the resin layer used to attach the overlay to the steel. A detailed step-by-step description of the fabrication process is given by Kaan (2008). The number in the designation of specimens with multi-layered overlays represents the thickness of the bond layer in units of in. $x\ 10^3$.

The term run-out is used in this paper in reference to specimens that achieved a large number of cycles, near to or exceeding the infinite fatigue life threshold specified by the AASHTO fatigue design curves, after which testing was discontinued. In most instances reported in this paper specimens that achieved run-out also exceeded the infinite fatigue life threshold for the corresponding AASHTO fatigue design category and stress range without developing observable fatigue cracks. The results show that with one exception all specimens with multi-layered overlays that were bonded using breather cloth achieved run-out at a very high stress ranges without failure of the bond layer. This is in direct contrast with the trials without breather cloth carried out by Kaan (2008). For example, a fatigue test reported by Kaan (2008) performed on a steel specimen with CFRP bonded to it without breather cloth cycled 1.33 million cycles before crack initiation; however, the CFRP overlays debonded six times during the test. Each time debonding occurred, the CFRP overlay was completely removed from the specimen and

rebonded. The thickness of the resin layer was 3 mm ($^1/_8$ in.). Fatigue tests performed utilizing breather cloth embedded in the resin bond layer of the same thickness (3 mm [$^1/_8$ in.]) sustained 3.3 million cycles without any observed debonding between the CFRP and steel. After 1.5 million cycles, the CFRP overlay was removed, and the steel substrate was inspected for cracks. No cracks were discovered. In specimens without breather cloth the average fatigue life of the bond layer with a thickness of 2 mm ($^1/_{16}$ in.) was 431,000 cycles, while the average fatigue life for bond layers with a thickness of 3 mm ($^1/_8$ in.) was 240,000 cycles. The coefficients of variation were 0.64 and 0.74, respectively. The scatter of the results can be appreciated in Figure B.31. The fact that the trend opposes the results from the finite element analyses and the degree of scatter were indicative that fabrication problems in the bond layer induced significant variability in the results and severely affected the fatigue-crack initiation life of the bond layer. A detailed description of the type of fabrication problems encountered and the effect of breather cloth on the quality of the bond layer is presented elsewhere (Alemdar et al., 2011).

Of the three specimens reinforced with chopped fiber overlays, the best results were obtained with test CHP2, in which a layer of breather cloth was first saturated with the same resin used in the chopped fiber composite, and later sprayed with the resin-fiber mix. Test CHP1, in which the chopped fiber mix was sprayed directly on the steel surface, had very weak bond strength under fatigue loading. This was also the case for test CHP3, in which a layer of Hysol® with embedded breather cloth was adhered to the steel prior to spraying with the resin-fiber mix. In this case, failure occurred at the interface between the Hysol® and the sprayed fiber composite. Results from the sprayed fiber specimens indicate that this method of fabrication of the overlay has merit as a repair technique, with the most promising results exhibited by the bond technique used in test CHP2. However, refinements to the bonding technique are still needed in order to achieve bond performance necessary to reach the infinite fatigue life threshold of the welded connection.
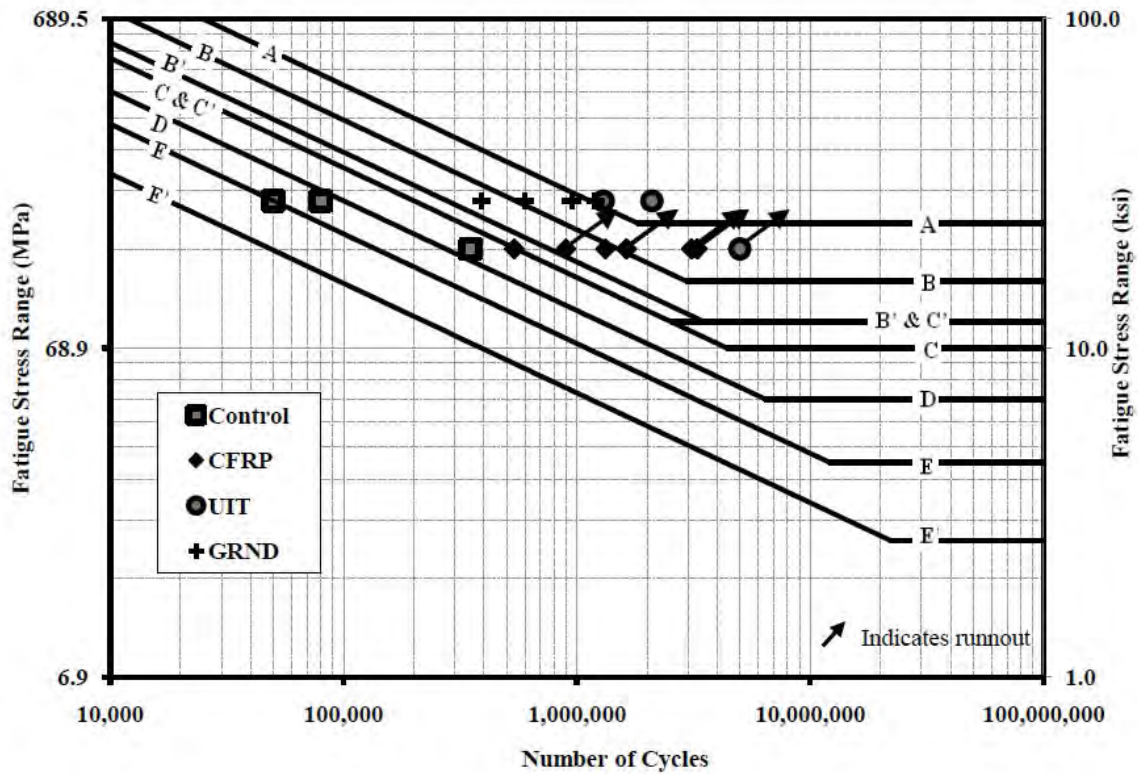
Figure B.31: Fatigue life of welded connections for various types of treatments

B.3.9 Fatigue Crack Initiation Life of the Welded Connections

The tests performed with breather cloth in the bond layer showed that by implementing this fabrication technique the bond layer could achieve run-out under very high applied stress range. Having addressed the bond problem under fatigue loading, the remaining research problem was whether the reduction in stress demand afforded by the composite overlays would be sufficient to extend the fatigue life of the welded connections to the infinite range, as suggested by the results from the finite element analysis. To address this question, two specimens were strengthened with CFRP overlays using breather cloth within the resin layer. The first, designated as TRI 06 in Table B.11 and B.15, had been previously loaded with 1.6M cycles without developing observable fatigue cracks (Kaan, 2008). Testing conducted during the initial 1.6M cycles included a resin layer 2 mm ($^1/_{16}$ in.) thick, without breather cloth. Subsequent testing performed on TRI 06 used a resin layer 6 mm ($^1/_4$ in.) thick with breather cloth embedded within the bond layer. The specimen was tested under fatigue loading with the same protocol

described in Kaan (2008). After 1.55M cycles, the test was stopped, and the composite overlay removed to inspect the weld for crack initiation. No cracks were observed.

The second specimen, designated TRI 07, was treated with a CFRP overlay and breather cloth and had not been loaded prior to this study. The thickness of the resin layer was 3 mm ($^1/_8$ in.) and it had embedded breather cloth. This specimen was subjected to the fatigue loading protocol for a total of 3.29M cycles. After first 1.50M cycles, the test was paused and the overlays were removed to inspect for fatigue cracks. After inspection, the overlays were reattached and the specimen loaded until a total of 3.29M cycles were reached. The final inspection showed that the specimen had not developed any detectable fatigue cracks.

To gage the effectiveness of the CFRP overlay repair technique, results from specimens reinforced with composite overlays were compared with improvements in fatigue life associated with other repair techniques evaluated using the same type of specimens. Results are summarized in Table B.14 and presented in Figure B.32. Specimens that were treated by smoothing of the welds are designated GRND, specimens in which the welds were treated with UIT are designated UIT, and control specimens are designated Cntrl.

On average, control specimens tested at a stress range of 193 MPa (28 ksi) had a fatigue-crack initiation life of 65,000 cycles. Specimens with smoothed welds tested at the same stress range had an average fatigue life of 785,250 cycles with a coefficient of variation of 0.46. This weld treatment technique resulted in a very significant increase in fatigue life, on average raising the fatigue performance from AASHTO fatigue design Category E to AASHTO fatigue design Category B. However, it should be noted that if the same statistical approach used to derive the AASHTO fatigue design curves is followed, the high variance of the results would lead to a much more modest increase in fatigue category. Figure B.32 shows that treating the specimens with composite overlays or treating the weld with Ultrasonic Impact Treatment were equally effective, extending fatigue life to run-out in both instances.
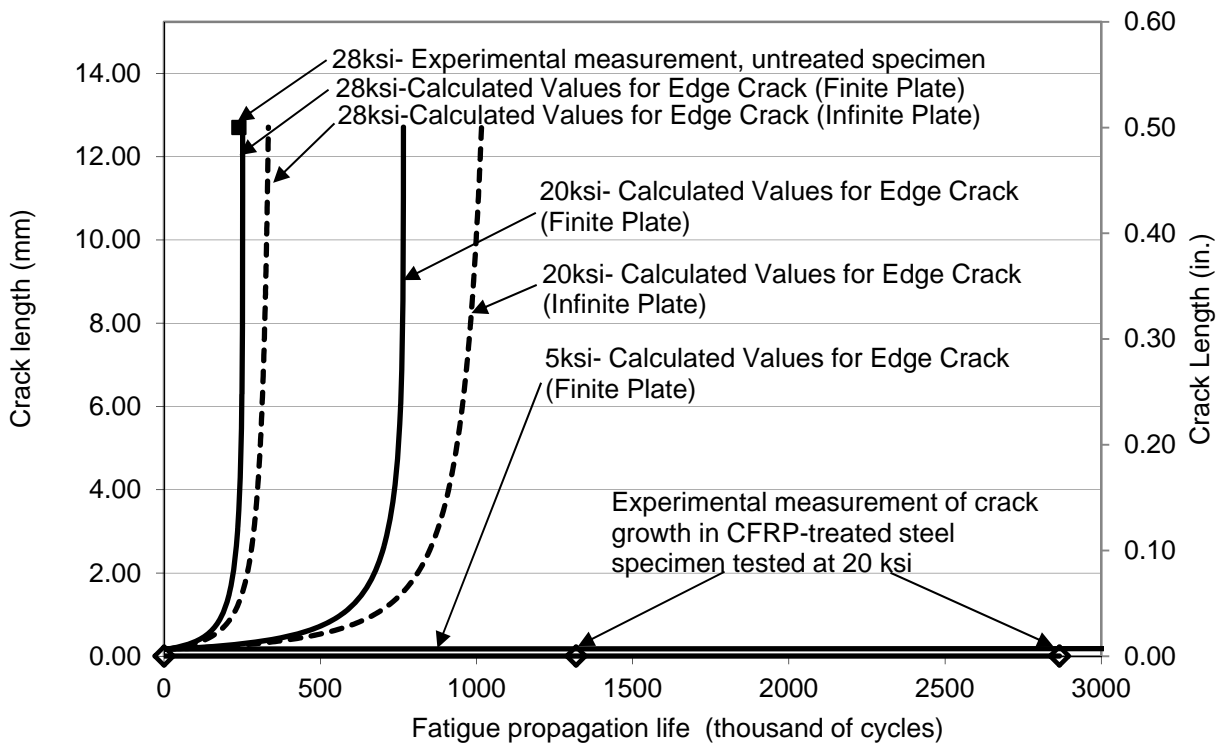
Figure B.32: Theoretical and experimental propagation life of untreated and CFRP retrofitted three-point bending specimens

B.3.10 Fatigue-Crack Propagation Life of the Welded Connections with CFRP Overlays

One of the specimens, designated TRI 04, was previously tested by Kaan (2008) and developed a fatigue crack after 1.36M cycles. This specimen was repaired with CFRP overlays with breather cloth embedded in the resin layer. The fatigue crack, detected using dye penetrant after testing by Kaan (2008), was approximately 2 mm ($^1/_{16}$ in.) long in the width direction. This pre-cracked specimen was reinforced with CFRP overlays with a 6 mm ($^1/_4$ in.) thick resin layer, and subjected to additional fatigue loading. After 1.3M cycles into the additional testing, the CFRP overlays were removed to inspect for fatigue cracks. After inspection, the overlays were reattached and the specimen loaded until a total of 2.88M cycles were reached. A caliper measurement taken during final inspection showed that the crack length was approximately the same, within the accuracy of the caliper.

It is meaningful to compare experimental results to theoretical fatigue life predictions. Theoretical calculations of fatigue-crack propagation life were performed using two different

underlying assumptions: (1) a surface crack in an infinite plate, and (2) an edge crack in a finite plate. The theoretical model based on the assumption of an edge crack in a finite plate (Rooke and Cartwright 1976) captured the known thickness and known width of the steel specimen. It assumed a semi-elliptical edge crack subjected to uniaxial tensile stress. These calculated values were compared with experimental measurements of crack length at a known number of fatigue cycles after crack initiation. This theoretical calculation, based on the assumption of an edge crack in a finite plate, yielded the closest match to experimental results obtained by Vilhauer (2010) using a control specimen. The experimental results obtained by Vilhauer, taken from a specimen subjected to a stress range of 193 MPa (28.0 ksi), are shown for reference in Figure B.32. Other theoretical models that were considered (e.g. surface crack in a finite plate) produced results that lay between those of the surface crack in an infinite plate and the edge crack in a finite plate. Therefore, for clarity, only the former and latter theoretical crack growth computed values are presented in Figure B.32. Theoretical crack propagation rates were examined at various stress ranges, with the aim of determining the actual stress range the welded connection was subjected to when CFRP overlays were bonded to the specimens. It was found that the experimental crack lengths measured in steel specimens retrofitted with CFRP overlays (shown in Figure B.32 as diamond symbols) were in close agreement with the theoretical crack growth estimates for a bare steel specimen subjected to a 34.5 MPa (5.0 ksi) stress range. Therefore, this exercise suggests that a Category E' specimen with CFRP overlays bonded to it and tested at a stress range of 138 MPa (20.0 ksi) may be expected to perform similarly to an identical bare steel specimen tested at a stress range of 34.5 MPa (5.0 ksi), suggesting a reduction of 80% in the stress demand, which is consistent with results from the finite element analyses. While negligible crack growth was observed after 2.88 M cycles, the estimated fatigue-crack propagation life of an untreated specimen subjected to a similar stress range was 766,000 cycles.

B.3.11 Conclusions

There are several techniques that may be used to increase the fatigue crack initiation life in welded connections. Options for reducing crack growth rate in welded connections are much more limited, due to difficulties presented by complex geometry that often exists at fatigue vulnerable connections. This study focused on the use of CFRP overlays to repair and strengthen

welded connections of structural steel members. It was found that using CFRP overlays was highly effective both as a preventive measure to extend the fatigue-crack initiation life of welded connections and as a repair measure to reduce the stress demand in welded connections below the crack propagation threshold. An improvement in fatigue-crack initiation life of at least 9 times was recorded for specimen TRI 06, and at least 9.5 times for specimen TRI 07, when compared with the fatigue-crack initiation life of untreated steel specimens tested at the same stress range. Composite overlays were as effective as other established repair methods such as UIT (ultrasonic impact treatment), which have been shown to provide significant improvements in fatigue-crack initiation life [14x, reported by Vilhauer (2010)].

The CFRP-retrofitted pre-cracked specimen sustained an additional total of 2.88M cycles after crack initiation without any measurable crack growth. This test showed that the CFRP overlays were able to reduce the stress range at the critical point of the welded connection below the crack propagation threshold.

Given the relatively simple bonding techniques employed, it is anticipated that with the proper level of training, this repair technique will be equally effective under field conditions, although it is recognized that there are some important considerations to be addressed before it is practical to do so with confidence.

B.3.12 References

 AASHTO (2013). *2013 Interim Revisions to the AASHTO LRFD Bridge Design Specifications.* 6th ed. American Association of State Highway and Transportation Officials, Washington, D.C.

Albrecht, P. and Lenwari, A. (2007) "Fatigue-Proofing Cover Plates." *Journal of Bridge Engineering*, 12(3), 275-283.

Alemdar, F., Matamoros, A., Bennett, C., Barrett-Gonzalez, R., and Rolfe, S. (2011). "Improved Method for Bonding CFRP Overlays to Steel for Fatigue Repair." *2011 ASCE/SEI Structures Congress Proceedings*,133-144.

ASTM D3039/D3039M (2000). Standard Test Method for Tensile Properties of Polymer Matrix Composite Materials. ASTM, West Conshohocken, PA.

Barsom, J. M. and Rolfe, S. T. (1999). *Fracture and Fatigue Control in Structures: Applications of Fracture Mechanics*. 3rd ed. ASTM, West Conshohocken, PA.

Kaan, B. (2008). *Fatigue Enhancement of Category E' Details in Steel Bridge Girders using CFRP Materials*. (Master's thesis). University of Kansas, Lawrence, KS.

Nakamura, H., Jiang, W., Suzuki, H., Maeda, K., and Irube, T. (2009). "Experimental Study on Repair of Fatigue Cracks at Welded Web Gusset Joint using CFRP Strips." *Thin-Walled Structures,* 47(10), 1059-1068.

Petri, B. (2008). *Finite Element Analysis of Steel Welded Coverplate Including Composite Doublers*. (Master's thesis). University of Kansas, Lawrence, KS.

Rooke, D. P. and Cartwright, D. J. (1976). "The Compounding Method Applied to Cracks in Stiffened Sheets." *Engineering Fracture Mechanics,* 8(3), 567-573.

Sabelkin, V., Mall, S., Hansen, M. A., Vandawaker, R. M., and Derriso, M. (2007). "Investigation into Cracked Aluminum Plate Repaired with Bonded Composite Patch." *Composite Structures,* 79(1), 55-66.

SIMULIA (2009). Abaqus FEA, Version 6.8.2. Providence, RI. http://www.simulia.com

Schubbe, J. J. and Mall, S. (1999). "Investigation of a Cracked Thick Aluminum Panel Repaired with a Bonded Composite Patch." *Engineering Fracture Mechanics,* 63(3), 305-323.

Tavakkolizadeh, M. and Saadatmanesh, H. (2003). "Fatigue Strength of Steel Girders Strengthened with Carbon Fiber Reinforced Polymer Patch." *Journal of Structural Engineering,* 129(2), 186-196.

Vilhauer, B. (2010). "Fatigue Behavior of Welded Connections Enhanced with UIT and Bolting," Accepted for publication, Engineering Structures.

B.4: Composite Block Retrofit for Repairing Distortion-Induced Fatigue Damage at Cross-Frame Connection Plates

Say Hak Bun[19]

Caroline R. Bennett[20]

Adolfo Matamoros[21]

Ron Barrett-Gonzalez[22]

Stan Rolfe[23]

B.4.1 Abstract

This paper presents a study in which composite material was used as a retrofit measure to extend the fatigue life of steel bridges susceptible to distortion-induced fatigue. The composite repair developed was a combination of West System™ two-part epoxy and mat fiberglass. Results from both a physical application and computational simulations showed that the retrofit was effective in slowing crack propagation rates.

B.4.2 Introduction and Background

Some common retrofits used to mitigate distortion-induced fatigue cracking are drilling crack-arrest holes, grinding (and sometimes welding) cracks, and attaching steel overlay elements. The retrofit measure introduced in this research paper differs from these methods in that it involves the use of fiber reinforced polymer (FRP) materials (i.e., composite materials) to enhance the fatigue life of steel bridge girders susceptible to distortion-induced fatigue. FRP materials may be an attractive retrofit approach in some cases because they can be pre-formed or cast-in-place to accommodate a wide range of different geometries at complicated connections details.

The composite material used in this research was comprised of fiberglass materials and an epoxy resin binding agent. There are many different choices regarding the composite material

---

available to use for this purpose. The epoxy resin chosen for this study was a West System™ two-part epoxy. The West System™ two-part epoxy is widely available, relatively inexpensive, and is most often used in boat-building and repair applications. This epoxy was chosen for use in this study as it was known to have high strength, low cost, and fatigue resistance under impact damage. In addition to the epoxy, mat-type fiberglass was chosen as the other primary component in the FRP material to comprise the composite block retrofit in this research.

B.4.3 Objective and Scope

The primary objective of this research was to investigate the effectiveness of a fiberglass composite block retrofit technique when used to increase the distortion-induced fatigue life of steel bridge girders in web gap regions. This study included a physical test of the FRP composite block applied to a girder segment tested in distortion-induced fatigue and a corresponding finite element analysis. The girder tie-down system used in this study was modeled using the commercially-available computer application, Abaqus v6.10.2 (SIMULIA 2010), to compare the stress state in the web gap region before and after the retrofit was applied.

B.4.4 Research Approach

A comprehensive approach was used to determine the effectiveness of the fiberglass composite block retrofit, relying on the results both from Finite Element Analysis (FEA) and experimental testing. Because application of this FRP composite block was performed as a pilot study to determine the feasibility and effectiveness of such a retrofit for repairing distortion-induced fatigue damage, this test was performed on a girder segment, rather than on the three-girder test bridge. Alemdar (2011) and Hassel (2011) at the University of Kansas have shown the validity of the test set-up used in the laboratory test program through comparison with highly detailed 3D FEA of full bridge systems.

B.4.4.1   Finite Element Analysis

The girder tie-down system used in the physical tests (the test set-up is described in detail in Appendices A.1 and A.2 of this report) and the concrete floor in the laboratory were modeled using the commercially-available software, Abaqus v6.10.2, to analyze the variation of stresses at the web gap regions on the girder's web. To mimic the laboratory test set-up, the actuator was restrained in the model from moving in both longitudinal and lateral directions of the girder. The

concrete floor was modeled as a fully fixed support, which eliminated any strong axis bending of the girder. The material properties assigned in the FE model are listed in Table B.15, and an overall view of the model is shown in Figure B.33

Table B.15: Material properties used in FE model

Type of Material	Poisson's Ratio	Modulus of Elasticity Mpa (Ksi)
Concrete	0.2	27,800 (4,000)
Steel	0.3	200,000 (29,000)
Composite	0.1	34,500 - 69,000 (5,000 - 10,000)
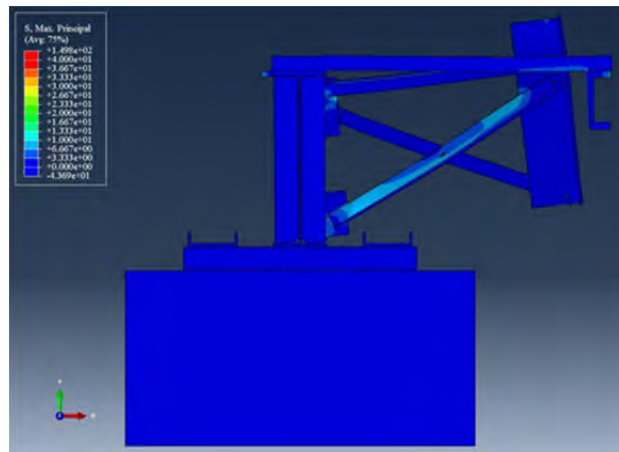
Figure B.33: Side view of the test assembly

Maximum principal stresses were computed along two paths in the models designated as Hot Spot Stress 1 (HSS1) and Hot Spot Stress 2 (HSS2); these stresses were computed at a distance of 5 mm ($^3/_{16}$ in.) from the stiffener-to-web weld and flange-to-web weld, respectively (Figure B.34). The two cracking patterns modeled were intended to mimic two common modes of distortion-induced fatigue cracking that commonly occur in web gap regions, commonly referred to as horseshoe-shaped and horizontal cracks. The HSS1 crack pattern is intended to be indicative of the hot spot stress along a horseshoe-shaped crack (along the connection plate-to-web weld), whereas HSS2 is indicative of the hot spot stress along a horizontal crack (along the web-to-flange weld). Two cracks were modeled using the Extended Finite Element Method

(XFEM); a horseshoe-shaped crack at the web-to-connection plate weld and a horizontal crack at the web-to-flange weld. The web-to-stiffener weld crack had a length of 102 mm (4 in.), and the web-to-flange weld crack was 204 mm (8 in.) long.
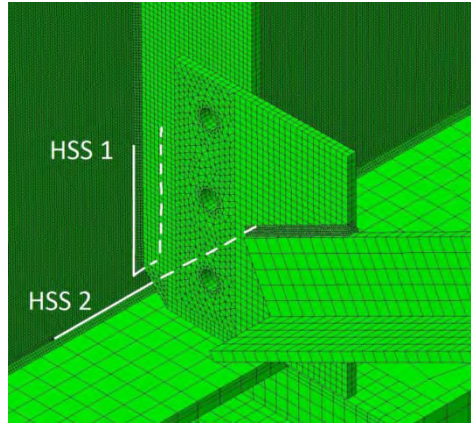
Figure B.34: Paths that stresses were sampled from within the FE models

The composite block was modeled as a retrofit in models that included cracked girder geometry. The block was assigned dimensions of 114 x 114 x 127 mm (4.5 x 4.5 x 5.0 in.) and was modeled as attached to both sides of the connection plate in the bottom web gap (Figure B.35). To simulate a perfect bond between the composite block and steel surfaces, tie constraints were used to connect the composite block surfaces to the girder's web, bottom flange, and connection plate. An upward load of 22.2 kN (5 kip) was applied to the actuator in the model to simulate the loading applied in the experimental tests.
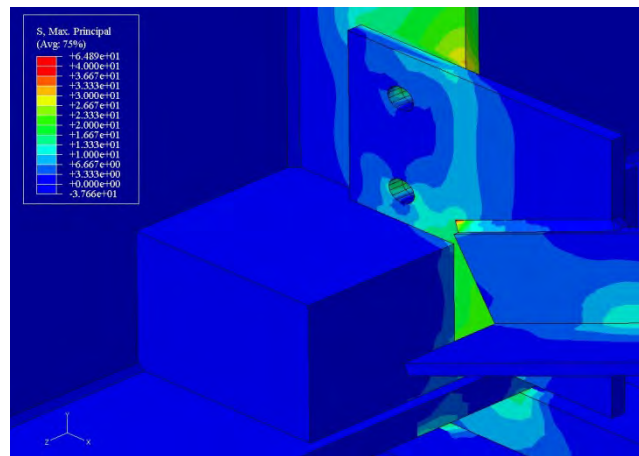
Source: Richardson 2012
Figure B.35: View of the composite block retrofit

209

A 2.8 m (9.3 ft) long built-up steel girder was connected to the concrete laboratory floor through a series of C5x9 channels post-tensioned to the 3 ft thick concrete floor as shown in Figure B.36. The subassembly was tested upside-down such that laboratory concrete floor simulated the lateral stiffness provided by a concrete deck on a bridge. The top flange of the test girder was restrained by the presence of a L3x3x$^3/_8$ angle on each end of the girder. Full-depth stiffeners were provided at the girder ends to prevent web instability at those regions. The subassembly was tested by applying and upwards (tensile) cyclic load that ranged from 2.2-kN (0.5-kip) to 25.3-kN (5.7-kip) on a WT section that connected to the cross-frame (Figure B.37).
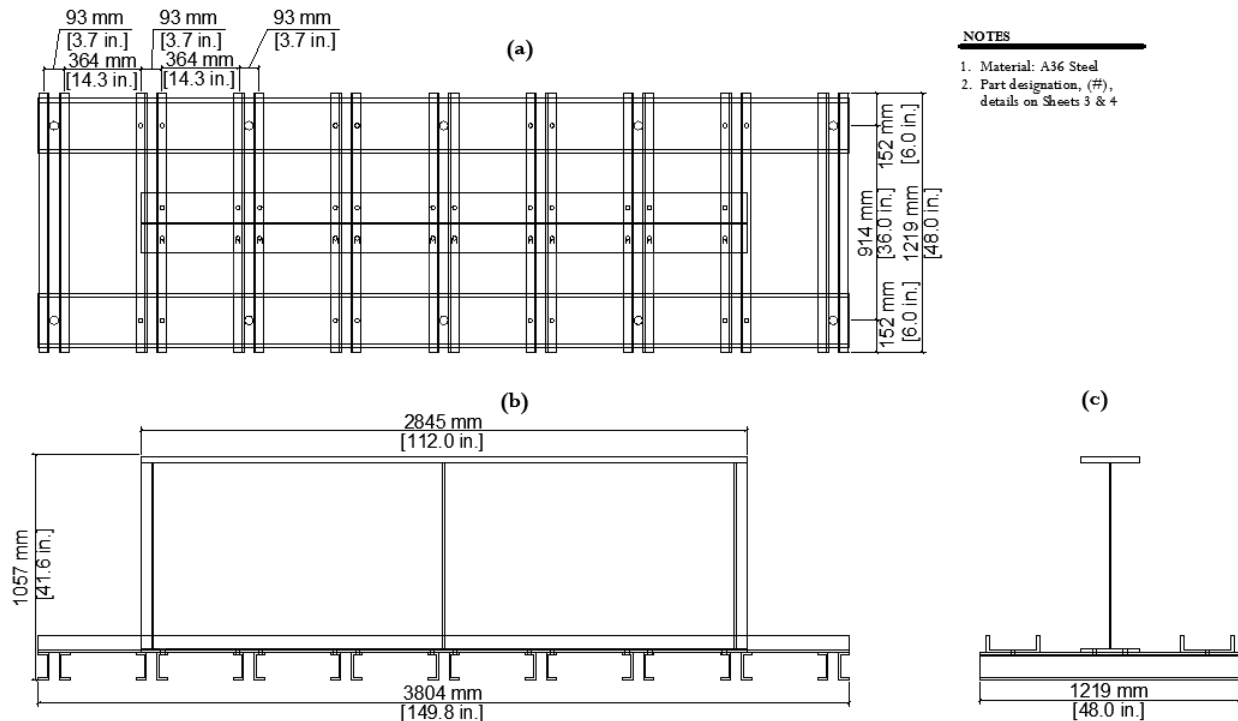
Figure B.36: Girder specimen
(a) Plan view; (b) Elevation view; (c) Section view

Figure B.37: View of the test set-up

B.4.4.3   Specimen Dimensions and Material Properties

The built-up steel girder used in the experimental study was 2.8 m (9.3 ft) long and 918 mm (36-in) tall. The web had cross-section dimensions of 10 x 876 mm ($^3/_8$ x 34½ in.). The bottom and top flanges had cross-sections of 279 x 25 mm (11 x $^5/_8$ in.) and 279 x 25 mm (11 x1 in.), respectively. The web, bottom flange and top flange all had a yield strength of approximately 345 MPa (50ksi). At each end of the girder, there were two stiffeners welded to the web and flanges. A connection plate was welded to the web at the mid-length location of the girder. The four stiffeners were 876 mm (34½ in.) tall, 127 mm (5 in.) wide, and 10 mm ($^3/_8$ in.) thick. The connection plate was 873 mm (34$^3/_8$ in.) tall, 127 mm (5 in.) wide and 10 mm ($^3/_8$ in.) thick. All stiffeners had a cropped end of 32 mm (1¼ in.), and the weld thickness was 10 mm ($^3/_8$ in.). The built-up girder was attached to the laboratory concrete floor through a series of C5x9 channels. A cross-frame was used to connect the connection plate and a WT. The cross-frame was made up of three L76x76x10 mm (L3x3x$^3/_8$ in.) angles, of which two were in an X-configuration, and one was used as a horizontal member. The upwards load was applied on the WT by a servo-controlled actuator.

B.4.4.4   Instrumentation

The test girder was instrumented with three linear variable differential transformers (LVDTs) and seven strain gages (Figure B.38). Two strain gages were placed at the top and bottom web gaps where cracks were expected to initiate. The three LVDTs were used to measure the out-of-plane deflections at three different locations along the height of the girder.
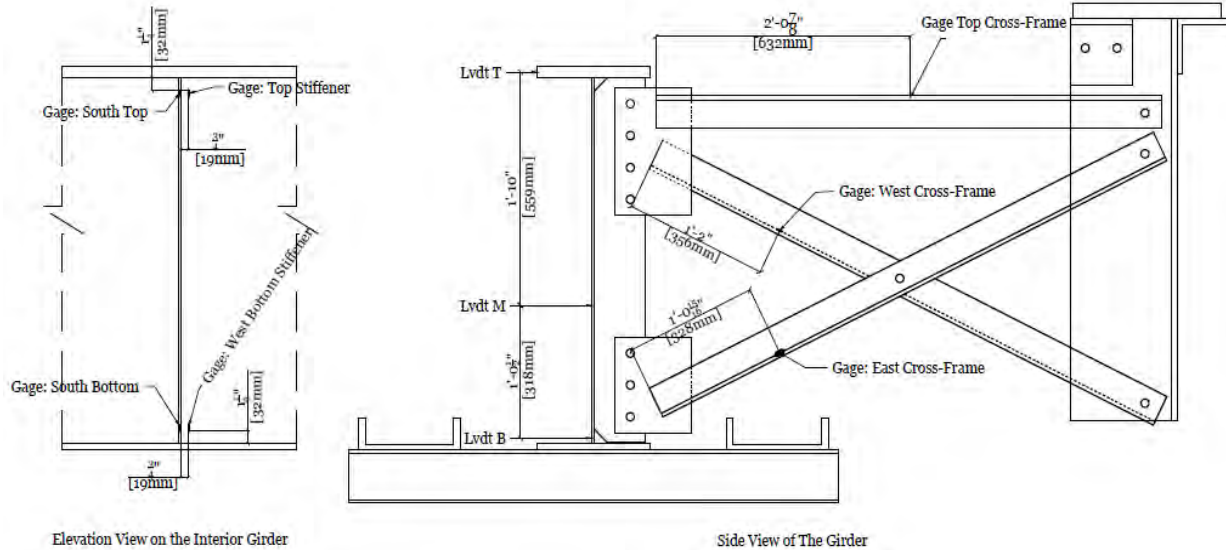
Figure B.38: Instrumentation used on the 9.3 ft girder specimen

B.4.4.5   Experimental Program

The girder subassembly was tested under a cyclic tensile force (the force was applied upwards at the WT- connected to the cross-frame) ranging from 2.2 kN (0.5 kip) to 25.3 kN (5.7 kip). The test was divided into two trials; Test Trial 1 was performed on the girder subassembly without any applied retrofit, followed by Test Trial 2 in which composite block retrofit was applied to the girder subassembly. In Trial 1, a web-to-connection plate crack was initiated and propagated to a length of 57 mm (2¼ in.), at which point the composite retrofit was applied to the girder. The cracking presented as a "horseshoe-shaped" crack around the connection plate-to-web weld (Figure B.41). Before the retrofit was applied, the girder subassembly was inspected every one thousand cycles using ultraviolet (UV) light and dye penetrant. Once the desired crack length was achieved, the composite block retrofit was cast on the interior face of the girder on both sides of the connection plate (Figure B.39).

After the composite retrofit was installed, the girder subassembly was tested for an additional 1.2 million cycles (Trial 2). At the end of Trial 2, the composite blocks were removed, and the girder subassembly was then inspected for any possible crack growth.

Figure B.39: Interior view of the girder
a) Prior to casting the West System™ two-part epoxy. b) View of the cured composite blocks

B.4.4.6   Composite Block Fabrication Processes

The composite block retrofit technique described in this paper was developed to take advantage of the fact that the FRP composite materials are light, corrosive resistant, inexpensive, and shapeable. Two composite blocks were cast in-place at the bottom web gap where the peak stress demands were located. The composite was comprised of West System™ two-part epoxy (West System™ 105 Epoxy Resin and West System™ 206 Slow Hardener) and conventional mat fiberglass. The West System™ two-part epoxy was mixed using WEST 105 resin and WEST 206 hardener at a ratio of 5:1. The West System™ 206 Slow Hardener exhibited a pot life of 25 minutes, which means that the chemical reaction in the epoxy will occur after this time frame, at which point the mix would no longer be workable.

The composite block was developed to hold the cracked surfaces together and to provide shear resistance while subjected to cyclic load. The mat fiberglass helped by providing some additional stiffness to the epoxy, and by adding cohesion to the mix. The fiberglass had the advantages of being lightweight, inexpensive, having moderate compressive and tensile

213

strengths, and being resistant to both impact damage and cyclical loading. The mat fiberglass, which consists of glass fibers randomly laid across each other, was made cohesive by a styrene binder when used in conjunction with the resin.

The fabrication process used to create the composite blocks was as follows. First, to meticulously prepare the steel surfaces, paint in the areas to be bonded was removed by sandblasting, and then cleaned using a degreasing agent prior to casting the composite. Then, two wooden molds were created and placed on each side of the connection plate to form two rectangular molds, each with a dimension of 165 x 121 x 254 mm ($6^1/_2$ x$4^3/_4$ x 10 in). The molds were firmly held in position through use of 19 mm (¾ in.) threaded rods, as pictured in Figure. The threaded rods were tightened to the snug-tight condition. Next, the West System™ epoxy and mat fiberglass were combined to make 0.0102 m^3 (0.36 ft^3) of composite. The composite blocks were composed of approximately 30% mat fiberglass and 70% West epoxy. The fiberglass content was first placed inside the molds, then the two-part epoxy was added to the molds. Finally, the composite blocks were left to cure at room temperature for 24 hours before fatigue testing was performed. It should be noted that no connection beyond that of naturally-occurring adhesion during the curing process was provided between the FRP block and the bottom flange of the test girder.

Figure B.40: Materials used in the FRP block
(a) West System™ two-part epoxy; (b) Mat fiberglass

B.4.5 Results

Results of the physical testing showed that the distortion-induced fatigue life of this girder was improved significantly. The crack propagation rate was slowed significantly when compared to the crack growth rate observed in the test girder without the retrofit. Figure B.41(a) presents the crack pattern that was recorded during the inspection directly before applying the composite block retrofit (after Trial 1 was completed and before Trial 2 was completed), and Figure B.41(b) presents the crack pattern recorded after Trial 2 was completed with the retrofit. It can be seen that the only crack that initiated after application of the retrofit was a small spider crack on the right side of the connection plate.
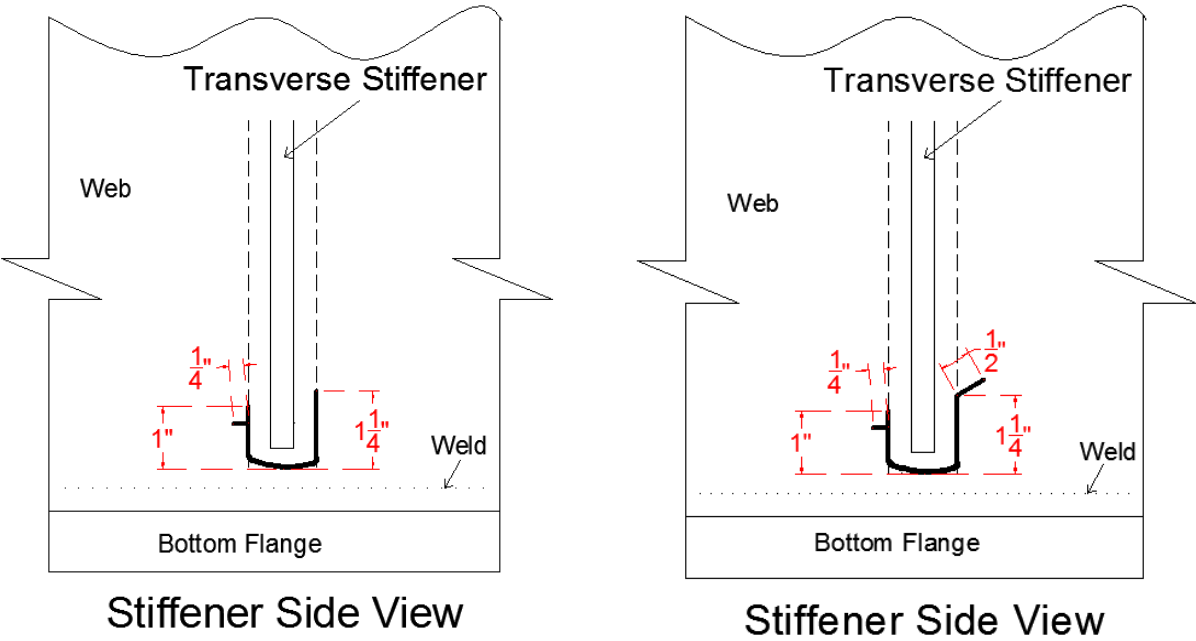
Figure B.41: Recorded crack patterns
(a) after Trial 1 (without FRP block retrofit); (b) After Trial 2 (with FRP block retrofit)

Figure B.42 presents the crack propagation history of the specimen for Trial 1 (unretrofitted) and Trial 2 (retrofitted). It is readily apparent that over the course of 1.2 million test cycles in the retrofitted condition that the girder experienced very low levels of crack propagation.
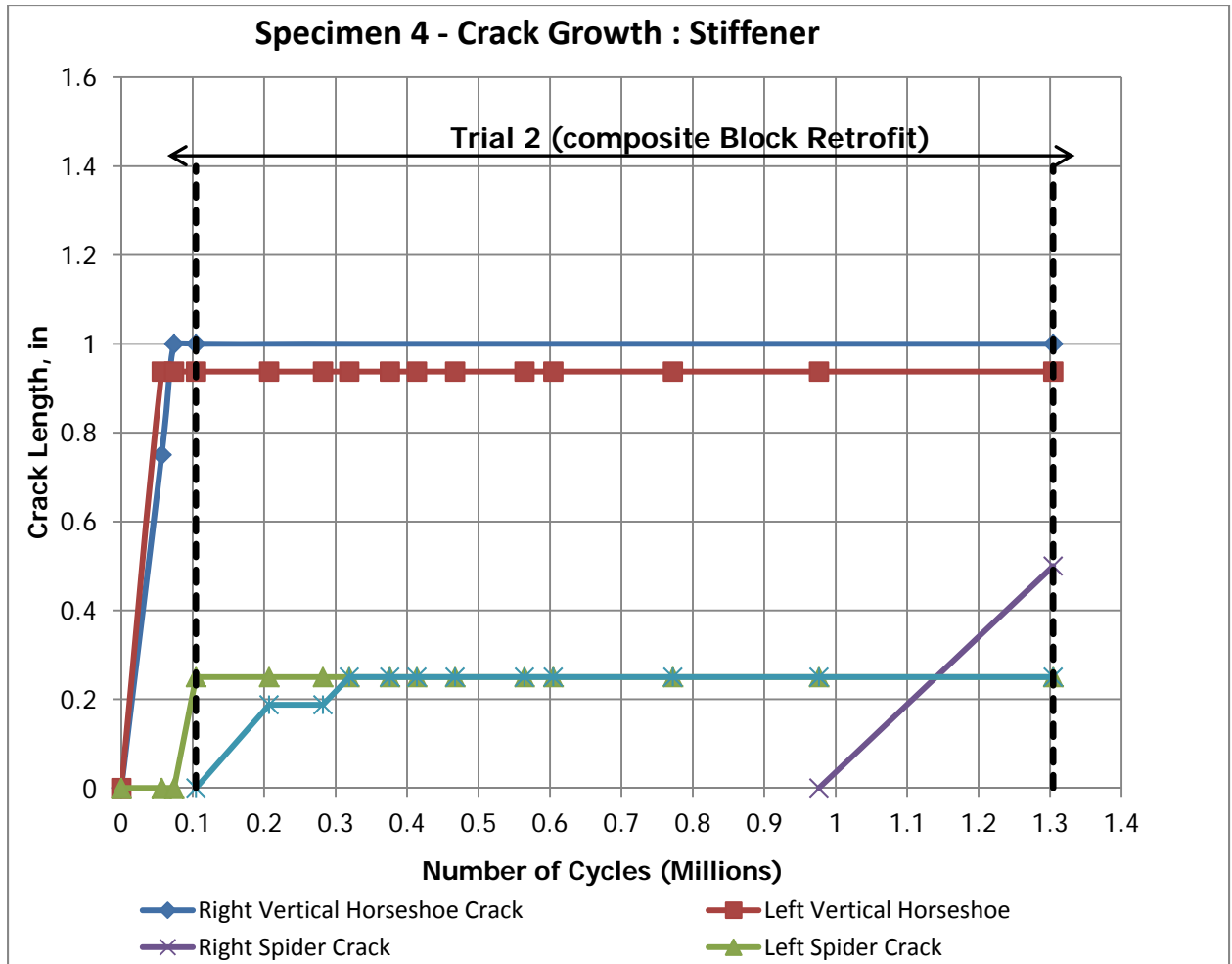
Figure B.42: Graph of crack length vs. cycle count

In the FE model of the specimen retrofitted with the composite block (Richardson 2012), the peak stress demand surrounding the connection plate-to-web weld (HSS1) was found to have decreased by 99%, and HSS2 was decreased by 96%. J-Integral values were also compared, and are shown in Table B.16. The values in Table B.16 indicate that the propensity for crack growth after application of the composite block was extremely small, close to zero. It should be emphasized that debonding between the FRP block and the steel surfaces was noted during Test Trial 2 of the physical testing. Given that the FEA results reported here are only expected to be accurate if the bond is perfectly maintained between the FRP and the steel, these analysis results should be viewed as one extreme end of potential behavior, and are not indicative of the testing

performed in Trial 2 of this test sequence. It is expected that the physical test performed is more indicative of the type of behavior that can be expected for this type of retrofit.

Table B.16: J-Integral comparison

All simulations contained a 102 mm (4 in.) web-to-stiffener weld crack and a 204 mm (8 in.) flange-to-stiffener weld crack (Richardson 2012)

Retrofit	*J*-Integral for 102 mm (4 in.) web-to-stiffener weld crack	*J*-Integral for 204 mm (8 in.) flange-to-stiffener weld crack
No Retrofit	0.41	0.58
Composite Block	1.6 E^{-3}	1.2 E^{-4}

Inclusion of the composite block retrofit slightly decreased the measured out-of-plane deflections of the girder, as shown in Figure B.43.
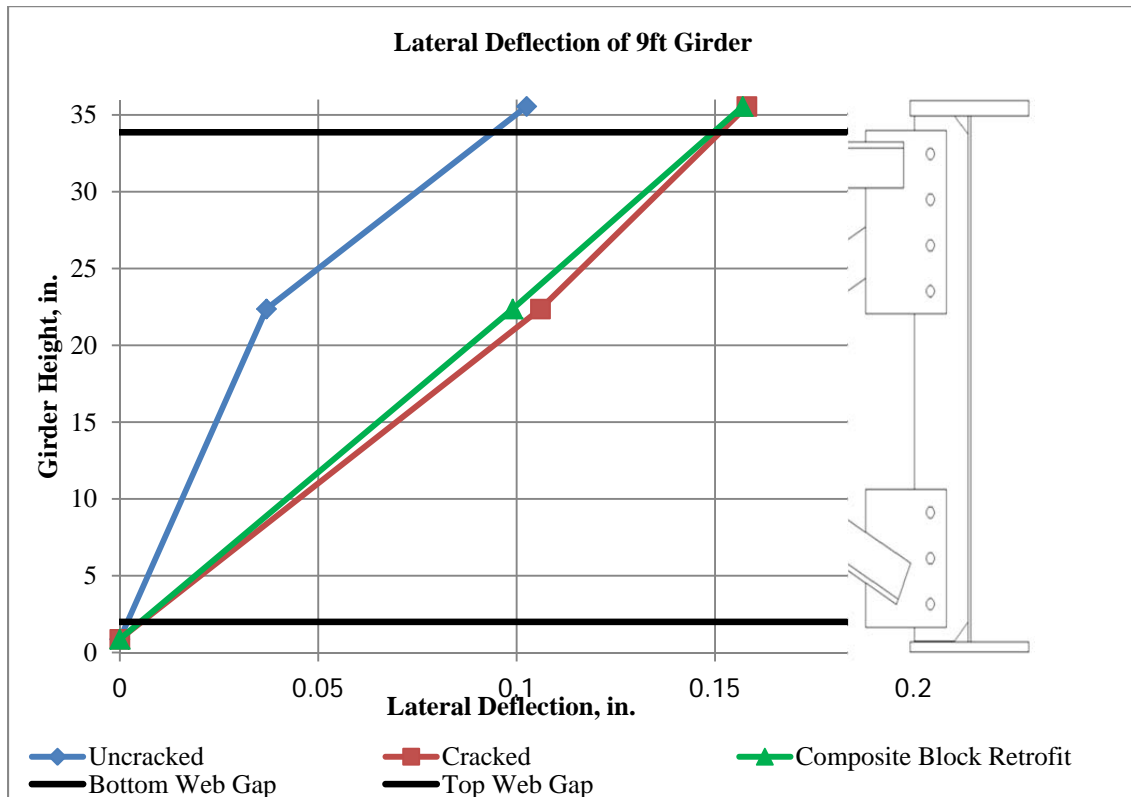
Figure B.43: Lateral deflection of the girder

B.4.6 Conclusions

The research presented in this paper was carried out to evaluate the effectiveness of a FRP composite block retrofit in mitigating distortion-induced fatigue damage in steel girder bridges. Results from physical testing showed that the retrofit was successful in drastically slowing crack propagation and initiation in the retrofitted web gap. Finite element analyses indicated the potential for excellent levels of fatigue performance improvement under perfect bond between the FRP and the steel. It is notable that although perfect bond was certainly not maintained between the FRP and the steel in the physical test, significant levels of fatigue performance were still obtained.

B.4.7 References

Alemdar, F. (2011). *Repair of Bridge Steel Girders Damaged by Distortion-Induced Fatigue*. (Ph.D. dissertation). University of Kansas, Lawrence, KS.

Hassel, H. L. (2011). *An Analytical Evaluation of Distortion-Induced Fatigue in Steel Bridges*. (Master's thesis). University of Kansas, Lawrence, KS.

Richardson, T. I. (2012). *Analytical Investigation of Repair Methods for Fatigue Cracks in Steel Bridges*. (Master's thesis). University of Kansas, Lawrence, KS.

SIMULIA (2010). Abaqus FEA, Version 6.10-2. Providence, RI. http://www.simulia.com.

WEST SYSTEM (2013). 105 Epoxy Resin®/206 Slow Hardener® Technical Data Sheet. http://www.westsystem.com/ss/assets/Product-Data-PDFs/TDS%20105_206.pdf

B.5: Use of Sandwich-Type Steel/Carbon Fiber Reinforced Polymer Repair for Girders Loaded in Distortion-Induced Fatigue: Computational Simulations

Regan Gangel[24]

Caroline R. Bennett[25]

Adolfo Matamoros[26]

Ron Barrett-Gonzalez[27]

Stan Rolfe[28]

B.5.1 Abstract

Fatigue damage is a common problem in steel girder bridges built prior to the mid-1980s. The location in which damage is likely to occur and the type of damage pattern are affected by the bridge geometry and loading conditions. In this study the propensity for damage under the combined effects of girder bending and cross-frame loading, as well as the pattern of damage that is to be expected were evaluated by performing a suite of finite element analyses.

After fatigue damage is detected, some repair or retrofit method must be implemented to prevent further fatigue crack propagation and protect the structural integrity of the bridge. Three repair methods were evaluated to determine the reduction in stress demand that each method produced at two critical locations. The three methods evaluated were: (1) drilling of crack-stop holes at crack tips, (2) attachment of bolted full-depth steel splice plates to the damaged web, (3) and attachment of adhesively bonded carbon fiber reinforced polymer (CFRP) overlays reinforced by bolted steel cover plates. Results of finite element analyses show that while both the full-depth steel splice plates and CFRP assemblage showed large reductions in stress, the later outperformed the other repaired methods and had the best potential for preventing further fatigue crack growth.

[24]Regan Gangel, MS, Structural Engineer, Burns and McDonnell, 9400 Ward Pkwy, Kansas City, MO

[25] Caroline Bennett, PhD, PE, Associate Professor, University of Kansas, 1530 W. 15th St., Lawrence KS, 66045

[26] Adolfo Matamoros, PhD, Professor, University of Kansas, 1530 W. 15th St., Lawrence KS, 66045

[27] Ron Barrett-Gonzalez, PhD, Associate Professor, University of Kansas, 1530 W. 15th St., Lawrence KS, 66045

[28] Stan Rolfe, PhD, PE, A.P. Learned Distinguished Professor, University of Kansas, 1530 W. 15th St., Lawrence, KS 66045

B.5.2 Introduction

B.5.2.1 Problem Statement

Steel girder bridges built prior to the mid-1980s were commonly designed without positive attachment between connection stiffeners and the tension flange (Hassel 2011). Unfortunately an outcome of this detailing practice was the fabrication of a large number of connections likely to develop distortion-induced fatigue damage in this region of the girder web, known as the *web gap*. Fatigue cracks in the web gap region are common in bridges of this era, requiring some repair or retrofit measure. AASHTO has since rectified this issue in new bridge construction by specifying that all connection stiffeners be welded or bolted to both the top and bottom flange of the girder if they are subsequently attached to a diaphragm, cross-frame, or floorbeam (AASHTO 2013). Implementing this type of connectivity in existing bridges would likely prevent further fatigue damage, but a bolted retrofit requires the removal of part of the bridge deck to make attachment to the top flange.

Because removal of the bridge deck can be costly in terms of the retrofit itself and traffic interruptions it causes, a repair or retrofit not involving its removal is preferred. Two such methods are the drilling of a crack-stop hole at the tip of fatigue cracks and attaching steel splice plates over the damaged region (Dexter 2004). Crack-stop holes have been shown to prevent crack re-initiation in plates with notches subjected to direct tension. Equations to determine the diameter of the crack-stop hole needed to prevent further crack growth have been developed based on tensile fatigue tests. One such equation, Equation B.7, was proposed by Barsom and Rolfe (1999):

$$\frac{\Delta K}{\sqrt{\rho}} < 10\sqrt{\sigma_{ys}} \qquad\qquad\qquad \textbf{Equation B.7}$$

which can be rearranged as:

$$\rho > \left(\frac{\Delta K}{10\sqrt{\sigma_{ys}}}\right)^2 \qquad\qquad\qquad \textbf{Equation B.8}$$

where ΔK is the stress-intensity factor range, σ_{ys} is the yield strength of the material, and ρ is the notch tip radius.

Equation B.8 indicates that the hole diameter required to prevent crack re-initiation is proportional to the stress intensity factor range and inversely proportional to the yield strength of the steel. One of the main drawbacks of this repair method is that expressions such as Equation B.8 were based on experimental data from specimens subjected to fracture Mode 1 displacements (Barsom and Rolfe 1999), while the stress fields in web gap regions are much more complex and impose mixed fracture mode displacements. The other drawback of using crack-stop holes is that often times the calculated diameter of the hole needed to prevent crack re-initiation is rather large, or large relative to the available space in the web gap region, making it impossible or impractical to implement. undersized holes will prevent fatigue crack propagation temporarily but often lead to re-initiation and further growth. Crack re-initiation is a major concern because it will require additional repairs and threaten the structural integrity of the member and potentially the bridge.

Retrofitting a bridge with full-depth steel splice plates over the damaged area stiffens the cracked girder web and restores the properties of the web to pre-cracked conditions (Roddis and Zhao 2001). The main drawback for bridge engineers is that this type of repair covers the crack, making it difficult to inspect existing cracks for propagation or initiation of new cracks without removal of the entire splice during inspection. Given these limitations, an alternative method to repair fatigue damage was investigated and their expected performance compared with that of existing repair and retrofit measures.

B.5.2.2 Objective

The first objective of this study was to evaluate various combinations of bending and out-of-plane load demands on the magnitude and orientation of the stress field in the web gap region of steel girders. High-resolution computer simulations were carried out to investigate the effect of loading conditions on the location and type of fatigue damage most likely to occur in steel bridge girders.

The second objective of the study was to evaluate the performance of three different repair methods for girders with large cracks caused by distortion-induced fatigue. Effectiveness of the repair methods was quantified on the basis of the computed reduction in stress demand with respect to companion models of unrepaired girders with a simulated crack. The three repair

221

methods evaluated were: (1) drilling crack-stop holes of varying diameter at the crack tips, (2) attaching bolted splice plates over the full depth of the girder, and (3) attaching a repair assemblage consisting of bonded carbon fiber reinforced polymer (CFRP) overlays reinforced with bolted steel cover plates. High-resolution finite element models of a simply-supported, full-depth steel bridge girder were used to investigate both objectives.

B.5.3 Background

B.5.3.1   Fatigue Crack Locations

Fatigue damage caused by distortion-induced fatigue in welded plate girder bridges is most often observed in the web, between transversely welded structural components (floor beams, diaphragms, or cross-frames) and an adjacent flange (Fisher and Mertz 1984). Within this web gap region there are three types of cracks that are most commonly found. They are: (1) a horizontal crack oriented parallel to the web-to-flange weld along the weld toe, designated as Type 1, (2) a horse shoe shaped crack originating in the web gap region and propagating outward into the web, designated as Type 2, and (3) a vertical crack originating in the web gap region following the weld toe of the stiffener-to-web weld, designated as Type 3 (Fisher and Mertz 1984). The crack type designations, shown in Figure B.44, will be used throughout this study.
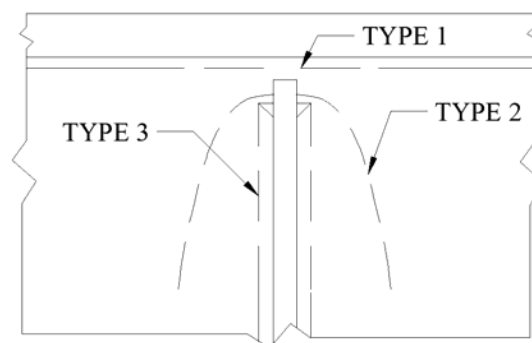
Figure B.44: Typical fatigue crack locations and types

A case study of a Kansas Department of Transportation (KDOT) bridge constructed in 1977 found cracks of Type 1 and 2 in the web gap adjacent to the top flange in positive and negative flexure (Roddis and Zhao 2003). Cracking near the top flange was attributed to the composite action of the slab, which restrains rotation in the top flange of the girder but not in the

bottom flange. The bridge studied was a two-girder non-skewed bridge (Roddis and Zhao 2003). Two other non-skewed bridges evaluated for fatigue damage, the Belle Fourche River Bridge and Chamberlin Bridge over the Missouri River (Fisher and Mertz 1984), also had the majority of fatigue damage occur in the positive moment region, in the web gap adjacent to the compression flange. The fatigue cracks were recorded as through-thickness cracks. (Fisher and Mertz 1984).

Type 2 cracks have also been found to propagate deep into the web of steel girder bridges, as was observed in a Maryland highway bridge investigated by Zhou and Biegalski (2010). This skewed continuous steel girder bridge had web fractures initiating near the tension flange and extending the entire depth of the web. Fatigue cracks of this magnitude are not common, but do occur and pose a serious threat to the structural integrity of a bridge.

Parametric studies completed at the University of Kansas investigated the likely regions where fatigue damage would occur in bridges with varying skew angle and cross frame placement (see Appendix D). It was found that in all bridge configurations studied, fatigue cracks were most likely to form in the positive moment region. Reports of fatigue cracks mainly in the negative moment region have been documented (Khalil et al. 1998). The study reported on in Appendix D.2 found that fatigue cracks in the negative moment region are more likely to occur if the bridge is skewed and also concluded that fatigue cracking was most likely to occur in the top web gap region of the exterior girder when the cross frames were placed parallel to skew. This behavior was found to change when skewed and staggered cross-frames were used, in which case the critical crack location moved from the top to the bottom web gap.

B.5.3.2 Common Fatigue Repair Techniques

When cracking is discovered in welded steel girder bridges, the fatigue detail is most often retrofitted to prevent further propagation and possible failure. Currently, one of the most common retrofit or repair technique is drilling a hole at the tip of the fatigue crack in the girder web. The radius of this crack-stop hole theoretically needed to prevent crack re-initiation can be calculated using Equation B.7.

In many instances, because of the crack location and the geometric constraints in the web gap region, it is not physically possible to drill a hole with the diameter calculated using Equation B.7. The only alternative is to drill an undersized crack-stop hole, which will likely

lead to the re-initiation of cracks and the need for drilling more crack-stop holes. Even when a relatively large crack-stop hole is drilled, crack re-initiation is still probable. Zhou and Biegalski (2010) investigated the use of a 51 mm (2.0 in.) crack stop-holes along predicted fatigue crack paths using the Finite Element method. They found that implementing this crack-stop hole along the expected fracture path increased the web flexibility and produced high stresses in the surrounding area under both in-plane and out-of-plane girder loading (Zhou and Biegalski 2010).

A repair technique used when large fatigue cracks propagate deep into the girder web is bolting steel cover plates to both sides of the web over the cracked region. This type of repair creates an alternate load path through the web, lowering the stress demand at the tip of the fatigue crack, prolonging the fatigue life of the girder (Roddis and Zhao 2001). The drawback to this repair method is that the steel plate covers the entire depth of the web. If any further crack propagation does occur, it will go unnoticed during inspections unless the entire retrofit is removed, or the crack propagates outside the footprint of the retrofit.

B.5.3.3   *Carbon Fiber Reinforced Polymer Overlays*

There has been a significant amount of research on the use of fiber reinforced polymer (FRP) overlays to repair fatigue damage in aircraft fuselages (Mall and Conley 2009; Umamaheswar and Singh 1999; Schubbe and Mall 1999; Naboulsi and Mall 1996; Lee and Lee 2004; Liu, Xiao, et al. 2009) and aluminum plate (Mall and Conley 2009;Denney and Mall 1997, Sabelkin et al. 2006). In a study conducted by Mall and Conley (2009), the fatigue life of 6 mm ($^1/_4$ in.) thick aluminum plate was extended by a factor of four compared with that of an unrepaired plate. A comparable study by Denney and Mall (1997) found that the fatigue life of 1 mm (0.04 in.) thick aluminum plate was extended by a factor of 10 compared with that of an unrepaired plate. Currently, adhesively bonded FRPs are used in the repair of fuselages and structural components of airplanes (Sabelkin et al. 2006).

The positive results generated by research in the aerospace industry have spurred the use of FRP overlays to repair fatigue damage in steel plates. The most commonly used composite material in research investigating the repair of fatigue damage in steel plates is carbon fiber reinforced polymer (CFRP). CFRP overlays have the advantage that the coefficient of thermal expansion of carbon closely matches that of steel. Materials with similar coefficients of thermal

expansion produce a more effective repair, whereas a mismatch in coefficients of thermal expansion could cause the opening of a fatigue crack and subsequent reduction in fatigue life (Sabelkin et al. 2007).

Lui et al. (2009) found that the fatigue life of steel plates could be increased by a factor of 7.9 when repaired with adhesively bonded CFRP overlays. They also found that the fatigue life was greatly increased when the CFRP overlays were attached to both sides of the steel plate when compared with a single-sided repair technique, because the stiffening of only one side introduced out-of-plane bending stresses.

B.5.4 Parametric Analysis of Factors Effecting Susceptibility to Fatigue Damage

Under normal loading conditions, bridge girders are subjected to both out-of-plane forces from cross-frames and in-plane bending from gravity loads. The effect of various combinations of these two types of loads were studied using Finite Element models to determine if either load increased the stress demand in the web gap regions where fatigue cracking is likely to occur or caused the location of the critical stress demand in the web gap region to change. The angle between the out-of-plane cross-frame force and the horizontal was varied between 0 and 45 degrees, simulating X-type cross frames with various girder spacing. The gravity load producing in-plane bending was varied to create a longitudinal bending stress in the top flange ranging between 35 and 138 MPa (5 and 20 ksi), to simulate cross-frame locations at various stations along the girder length.

B.5.4.1   Girder Section Geometry

The effects of in-plane bending and cross frame loading were studied on a single 3.0 m (10.0 ft) wide by 1524 mm (60 in.) deep steel girder section, shown in Figures B.45 and B.46. The simply-supported girder was comprised of a web, top and bottom flanges, and a single connection stiffener welded to the web at mid-span on what will be referred to as the interior side the web. The opposite side of the web is referred to as the fascia side of the web. In this simplified girder model no bridge deck was included. The depth of this section was chosen to represent a reasonable girder depth for a multi-girder highway overpass. The length of the girder section was chosen to be twice the girder depth. The connection stiffener welded at mid-span was truncated 6 mm (0.25 in.) from the face of each adjacent flange. A 25 mm (1.0 in.) clip

produced a web gap region of 35 mm (1.38 in.). At each end of the girder a 13 mm (0.5 in.) thick steel transverse stiffener was attached over the entire depth of the girder, shown in Figure B.45, but removed from Figure B.46. The end stiffeners were attached to both the top and bottom flange and the entire depth of the web. All girder dimensions are shown in Figures B.45 and B.46.
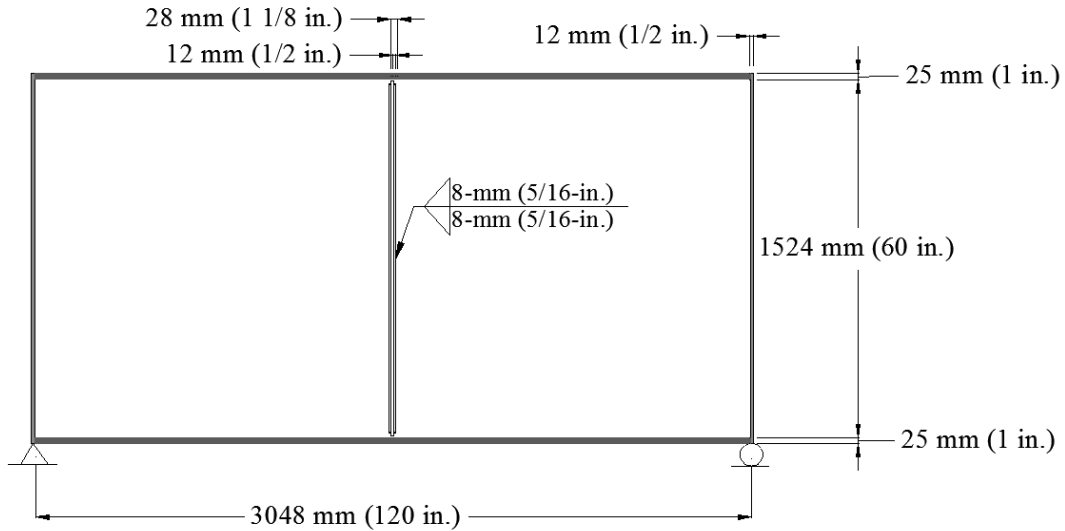
Figure B.45: Plan view of girder section
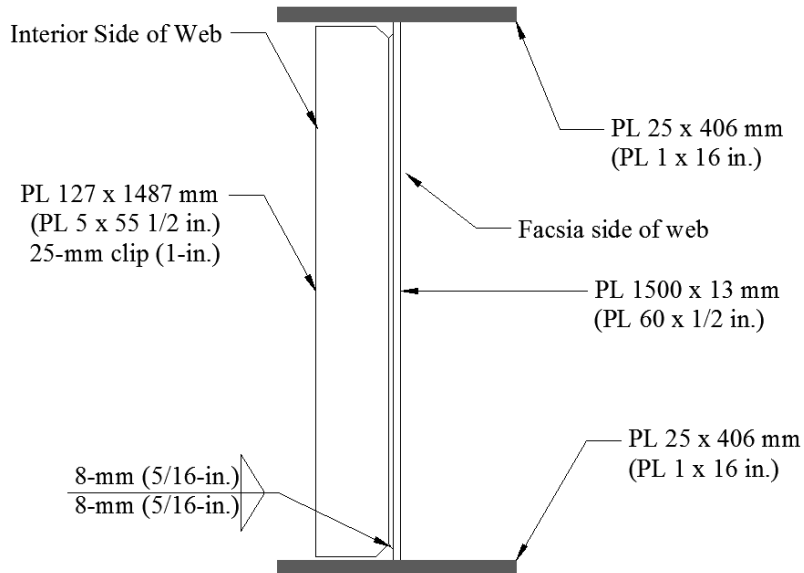
Figure B.46: Girder cross section

226

B.5.4.2   Parameters Considered

The effects of cross-frame loading and bending moment on the stress field at the web gap were analyzed separately. Cross-frame forces were modeled as point loads placed at mid-thickness of the connection plate. A 22-kN (5-kip) load was placed near both the top and bottom of the connection plate. The load near the top of the connection plate was placed in tension while the load near the bottom was placed in compression to match cross frame forces calculated using full-scale bridge models by Hassel (2011) and Roddis and Zhao (2003). In the study by Hassel (2011) the calculated compression force was approximately 1.5 times greater than the tension force. A finite element analysis was completed on the girder section, shown in Figure B.45, to determine the effect on the stress field due to the disproportionate loading scenario. Although stress values were slightly higher near the welds in the bottom web gap (as would be expected) there were no significant differences in the stress fields between the two models. For this reason it was decided that all analyses would be performed with cross-frame forces of equal magnitude.

The 22-kN (5-kip) forces were oriented at angles of 0, 5, 10, 15, 20, 25, 30, 35, and 45 degrees with respect to the horizontal axis. The angle with respect to the horizontal was maintained equal for the tensile and compressive force. The load placement in the vertical direction along the connection stiffener was changed in each model so that the projection of the cross-frame force would pass through the same point in the web gap for each model. This was done to ensure that the effects of forces placed at higher angles were not underestimated. The force parallel to the horizontal was placed 13 mm ($^1/_2$ in.) from the top (or bottom) of the connection stiffener. For each increment in angle with respect to the horizontal axis of 5 degrees, the load was moved approximately 12 mm (0.45 in) toward the neutral axis of the girder section. Figure B.47 shows a schematic of the load placements.
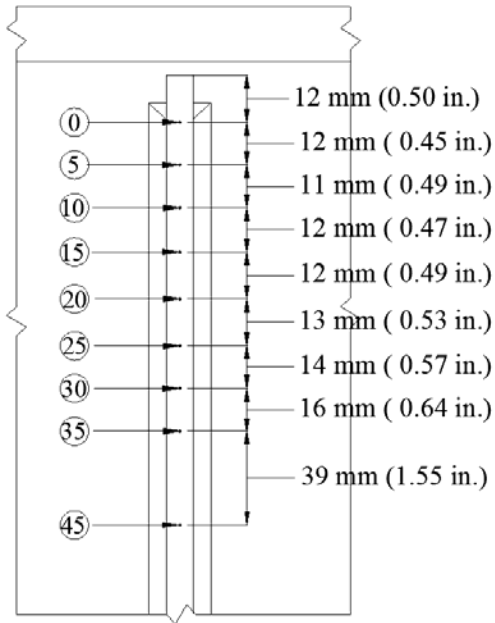
Figure B.47: Placement of loads at varying degrees from horizontal

The bending stress demand was simulated by applying a uniform pressure load to the top flange of the girder. Initially the pressure load was applied to the entire surface of the top flange; however, this caused the ends of the top flange to bend downward in a manner that would not occur in a bridge because of the attachment of the top flange to the bridge deck. To avoid this distortion, the pressure load was applied along the full length of the top flange but was concentrated along the width of the web. This load distribution produced a more reasonable bending shape. Two different gravity loads were compared. The first induced a 35 MPa (5 ksi) longitudinal stress in the top flange, which would be expected under typical truck loads in a long span bridge. The second gravity load induced a 138 MPa (20 ksi) longitudinal stress in the top flange, which represents an extreme and live load level.

The effects of combined in-plane bending and out-of-plane cross-frame loading were then evaluated using the combinations given in Table B.17. This was done to determine if one parameter dominated the behavior when applied simultaneously.

228

Table B.17: Load combinations used to test effect of cross-frame force and bending

Load Combination	Angle of Cross-Frame Force with Respect to the Horizontal	Longitudinal Bending Stress
1	0 degrees	35 MPa (5 ksi)
2	0 degrees	138 MPa (20ksi)
3	35 degrees	35 MPa (5 ksi)
4	35 degrees	138 MPa (20 ksi)

B.5.4.3   Finite Element Modeling

A linear-elastic Finite Element (FE) model of the 3.0 m (10 ft) bridge girder section was constructed in Abaqus v6.10.2 (SIMULIA 2010) using three-dimensional elements. Meshes were assembled using 8-node brick elements for the majority of the model. Small areas of tetrahedral meshing were used near the non-square edges of the connection stiffener. All parts of the girder section were composed of steel modeled with a modulus of elasticity of 200 GPa (29,000 ksi) and Poisson's ratio of 0.3. A maximum mesh size of 6 mm ($^1/_4$ in.) was used for all steel parts. Parts were attached using surface-to-surface tie constraints. Only the weld attaching the connection stiffener to the web was modeled explicitly. All other welds were not modeled explicitly, with the corresponding elements connected directly to each other using tie constraints. A mesh size of 5 mm (0.2 in.) was used for the weld and its material properties matched those of other steel parts.

Simply-supported boundary conditions were created by applying translational restraint along the narrow bottom edge of each end stiffener. This allowed the stress demand to be transferred in such a way that the critical region of the web, at mid-span near the connection stiffener, was not affected by irregularities caused by boundary conditions. The outermost side of each end transverse stiffener was also restrained from movement in the out-of-place direction.

B.5.4.4   Hot Spot Stress Analysis

The potential for fatigue damage of the various loading combinations and retrofit measures was evaluated in terms of the calculated Hot Spot Stress (HSS). This method was chosen as the basis of comparison because it reduces the effect of the mesh configuration in areas of high stress located near geometric discontinuities, such as the connection stiffener-to-web

weld. To determine the peak HSS, maximum principal tensile stress demands were extracted along a path located half the width of the web thickness 6 mm ($^1/_4$ in.) from the geometric discontinuity corresponding to the intersection of the weld and the web.

For each model that was analyzed, two separate HSS paths were investigated. The first HSS path was defined around the toe of the connection stiffener-to-web weld and the maximum principal stress demand extracted from that path was designated HSS#1. This stress demand would be indicative of the potential for initiation or re-initiation of fatigue cracks of types 2 and 3. The second HSS path was defined along the flange-to-web weld and the maximum principal stress extracted from this path was designated HSS#2. Both HSS paths are shown in Figure B.48, along with the mesh configuration. For loading scenarios that did not evaluate in-plane bending, HSS#1 and HSS#2 were determined for both the top and bottom web gaps on both sides of the web. Because the bending moment induced by the gravity load produced tension in the bottom web gap, HSS#1 and HSS#2 were only extracted in the bottom web gap, on both sides of the web.
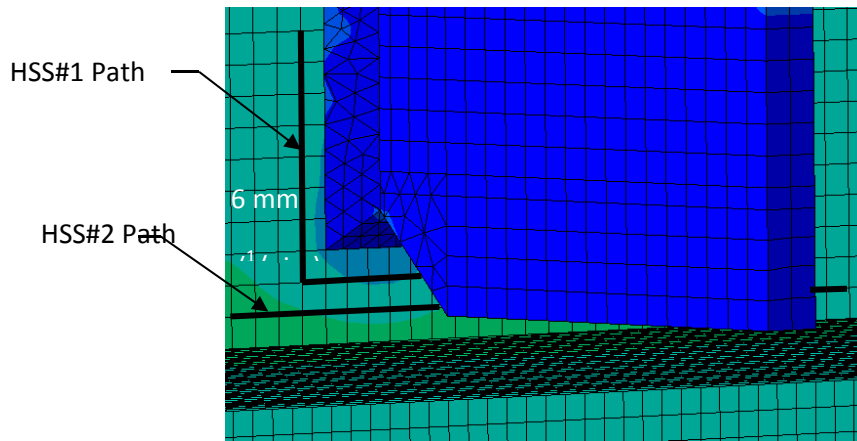
Figure B.48: Schematic of hot spot stress paths

B.5.4.5   *Results of Parametric Analysis*

Among the FE models with various cross-frame configurations the highest web gap stress demands were found for the model in which the cross-frame force acted parallel to the horizontal. All HSS#1 and HSS#2 magnitudes decreased in both the top and bottom web gap as the angle at which the cross-frame force acted was increased. Increasing the angle to 35 degrees from the horizontal decreased HSS#1 by a maximum of 23% and decreased HSS#2 by a

maximum of 15% (both in the top web gap on the fascia side of the web). Although the magnitudes of the maximum principal tensile stress changed with varying angle, no significant changes in the shape of the stress field and consequently the expected location of the fatigue cracks were found. For all variations of cross-frame force the maximum HSS was found to be HSS#1 in the top web on interior side of the web. These results indicate that under cross-frame loading only, expected to take place in regions of bridges near girder inflection points, fatigue crack initiation would be expected to occur first along the connection stiffener-to-web weld in the top web gap.

Subjecting the simply-supported girder model to pure bending caused tensile stresses in the web at the bottom web gap, and compressive stresses at the top web gap. The compressive stresses at the top web gap reduced the likelihood of fatigue damage by reducing or eliminating stress fluctuations in the tension range, making the bottom web gap the region of interest in evaluating the potential for fatigue damage. Even though in long-span bridges a large fraction of the gravity load is not cyclic in nature and consequently has no effect on the stress range, tensile stresses due to gravity do exacerbate the potential for fatigue damage by placing the web in tension prior to tensile load fluctuations caused by traffic directly in the girder and indirectly through the cross frames.

When the longitudinal bending stress in the top flange was increased from 35 MPa to 138 MPa (5 ksi to 20 ksi) the magnitude of HSS#1 and HSS#2 were both increased by approximately 300% on both sides of the web. These results clearly show that as the ratio of live to dead load increases in the bridge so does the potential for fatigue damage in the web gap regions. While the calculated change in demand constitutes a dramatic increase the increase in bending stress (or increase in the ratio of live to dead load) had a negligible effect on the shape of the stress field and consequently the locations where fatigue cracks were most likely to initiate. For models with varying bending stress, the critical location was found to be HSS#1 in the bottom web gap, on the fascia side of the web.

When the effects of bending and cross-frame loading were analyzed together, the fatigue critical location associated with bending stress controlled (HSS#1 in the bottom web gap on the fascia side of the web). This indicates that under combined loading conditions, expected to take

231

place in positive moment regions of girders subjected to significant live loads, bending stress played a more significant role in the potential for fatigue damage. In fact, when a bending stress of 138 MPa (20 ksi) was applied, corresponding to a very high ratio of live to dead loads, the HSS in this location was comparable between models of all varying cross-frame forces and angles.

B.5.5 Parametric Analysis of Fatigue Repair Measures

After a fatigue crack is discovered in a steel bridge structure, it is imperative to implement some measure to repair fatigue damage and protect the structural integrity of the bridge. This study used the Finite Element models discussed above to evaluate three methods of repairing fatigue damage. The methods evaluated were: (1) drilling crack-stop holes of varying diameter, (2) applying full-girder-depth steel splice plates over the region of the web with fatigue damage, and (3) applying a carbon fiber reinforced polymer (CFRP) overlay over a localized region surrounding the fatigue crack tip.

B.5.5.1   Girder Section and Crack Geometry

All repair methods evaluated in this study were applied to the girder section shown in Figures B.45 and B.46. Also, all repairs were applied to cracks of Type 2 shown in Figure B. 44. If left unrepaired or repaired insufficiently, horse-shoe shaped cracks of this type have the potential to propagate deep into the girder web (Zhou and Biegalski 2010). Each repair method was implemented on a through-thickness fatigue crack that had propagated $^1/_8$ of the depth of the web. Repair methods were also evaluated in models with simulated fatigue cracks that had propagated $^1/_4$ of the depth of the web to determine if there were any implications of retrofitting cracks of different lengths. While in most instances regularly scheduled bridge inspections will allow finding fatigue cracks before they reach this depth, there are documented cases. Each model was loaded with 22-kN (5 kip) tension and compression cross-frame force at an angle to 35 degrees from the horizontal and a gravity load which produced a 35 MPa (5 ksi) bending stress in the top flange. Specifics about how the loading and how it was applied are discussed above. From the discussion on loading conditions given, cross-frame forces at an angle of 35 degrees from the horizontal was chosen because they represent a typical girder spacing of a multi-girder highway overpass. An induced bending stress of 35 MPa (5ksi) was chosen as it

232

represents the induced bending that would be expected in a long-span bridge from typical truck loads.

For this pre-determined fatigue crack type, there were two possible locations for crack initiation, the top and bottom web gaps. For the reasons cited above, analyses focused on the stress demands at the bottom web gap. To reinforce that this is the location of expected fatigue damage, preliminary models were loaded with cross-frame forces acting at 35 degrees from the horizontal and an applied gravity load inducing a longitudinal stress of 138 MPa (20 ksi) in the top flange. The Extended Finite Element Method (XFEM) modeling technique was used to simulate pre-existing horse shoe cracks in the bottom web gap. This modeling technique allowed simulating crack propagation following paths of high stress demand. A refined mesh with a maximum mesh size of 1 mm (0.05 in.) was used in a region near the crack. A 25 mm (1 in.) length of tetrahedral meshing was used to transition between mesh sizes.

Significant crack propagation was not observed in the XFEM models under the prescribed loading conditions. The stresses demands at the ends of the horse-shoe crack were found to be higher in the bottom web gap region than in the top web gap. Fatigue cracks of this nature, in the bottom web gap of the positive moment region, were found to be most likely to occur in a bridge configuration with staggered cross frames in the study by Hartman et al. (2010). If a segment of bridge girder between two adjacent cross-frames of a full bridge model is considered (Figure B.49), the ends of the girder segment are pulled by cross-frames in one direction while the middle of the segment is pulled in the opposite direction by the staggered cross-frame (Hartman et al. 2010). The simply-supported model used in this study behaved in a similar manner. Each end of the girder segment was restrained from out-of-plane motion while the center of the girder segment was pulled in the out-of-plane direction by the simulated cross-frame forces. For the evaluation of three different repair techniques, cracks of pre-defined length were placed in the bottom web gap.
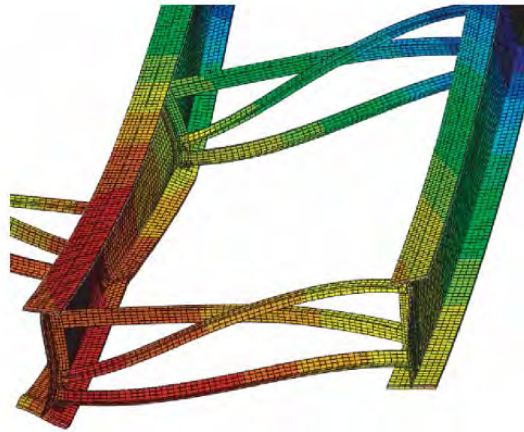
Source: Hartman et al. 2010
Figure B.49: Schematic of staggered cross-frame bridge configuration

B.5.5.2   Repair Methods Evaluated

Currently, the use of crack-stop holes is a common method to repair fatigue damage in older steel girder bridges that experience distortion induced fatigue damage. As previously discussed, expressions like Equation B.7 were derived based on experimental data from fatigue specimens subjected to fracture mode 1 displacements. To gain a better understanding of the effect of crack-stop holes on the potential for crack re-initiation under the stress conditions in the web gap region, models with pre-defined cracks and various crack-stop hole diameters were evaluated. A test matrix for all models with crack-stop holes is presented in Table B.18. Those models listed in Table B.18 that do not have a crack-stop hole are the un-retrofitted cracked models which were used as basis of comparison between different repair methods. The reduction in stress demand for each repair method was calculated based on the maximum HSS demand extracted from each of the models.

Expressions to calculate the minimum crack-stop hole diameter such as Equation B.7 were developed based on tensile fatigue tests, therefore, an evaluation of the effect of crack-stop hole diameter on stress demand was also performed using a girder web under pure tension loading. The girder web dimensions were consistent with those shown in Figures B.45 and B.46. The left end of the girder was restrained against translational motion while a distributed load of 207 MPa (30 ksi) was applied to the other end, placing the web in pure tension. Both a horse-

shoe shaped crack and a straight vertical crack were tested under pure tension for completeness, however, only one crack geometry was evaluated per model. Figure B.50 shows boundary conditions, crack locations, and loading for models tested under pure tension loading.

Table B.18: Test matrix for models testing effect of crack-stop holes

	Crack Size Hole Diameter mm (in.)					
	None	12 ($^1/_2$)	19 ($^3/_4$)	25 (1.0)	51 (2.0)	102 (4.0)
Horse-Shoe Crack 1/4 depth of web Combined Loading	x	x	x	x	x	
Horse-Shoe Crack 1/8 depth of web Combined Loading	x	x	x	x	x	
Horse-Shoe Crack 1/4 depth of web Pure Tension Loading	x		x		x	x
Straight Crack 1/4 depth of web Pure Tension Loading	x		x		x	x

Note: only 1 crack type was evaluated per model
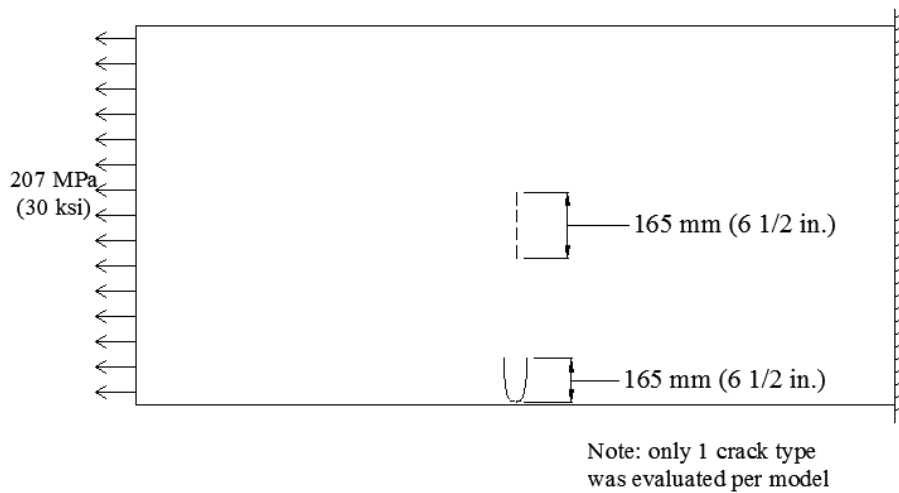
Figure B.50: Boundary conditions and loading for models evaluating effect of crack-stop holes under pure tension loading

The second repair method evaluated was the attachment of 13 mm ($^1/_2$ in.) thick steel splice plates along the full depth of the girder, as shown in Figure B.51. Because crack-stop holes are an accepted and widely used fatigue repair technique, the system included the drilling of a 19 mm ($^3/_4$ in.) crack-stop hole in the web at each tip of the fatigue crack. Two splice plates

measuring 127 x 1473 mm (5.0 by 58.0 in.) were attached to the interior side of the web, one on each side of the stiffener. Because there was no transverse stiffener on the opposite side of the web, a single splice plate measuring 283 x 1473 mm (11.1 x 58.0 in.) was attached there. Each splice plate was terminated at a distance of 25 mm (1.0 in.) from the adjacent flange to prevent the splice plate from restraining the motion of the flange. Splice plates were attached using high-strength 19 mm ($^3/_4$ in.) tensioned bolts spaced at 102 mm (4.0 in.). The horizontal spacing of bolts is shown in Figure B.51. Each bolt was tensioned to 125 kN (28 kip) following the stipulations in AASHTO (2010) Table 6.13.2.8-1. When attached to the web, the steel splice plates completely covered all the fatigue damage, except for the initiation site. They also covered the area where any further crack propagation would occur, making inspection impossible without removal and reattachment of the repair.
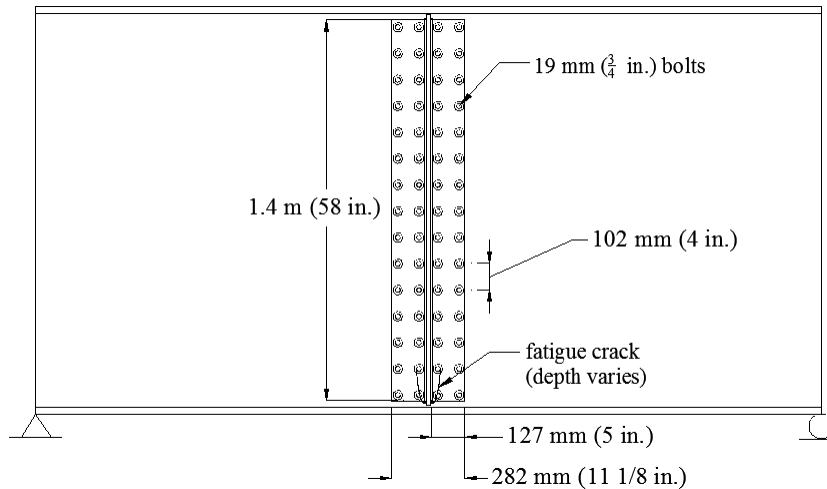
Figure B.51: Full-depth splice plate fatigue damage repair

The CFRP repair assemblage evaluated in this study was created to be representative of fabrication methods under field conditions. The use of CFRP overlays to repair fatigue damage in steel structures has not been widely tested on full-scale models. Research at the University of Kansas has evaluated the use of adhesively bonded CFRP overlays to reduce the fatigue-crack propagation rate in tensile specimens with pre-existing fatigue cracks (Alemdar 2011; Gangel 2012). The experiments showed that for a given stress range, an optimized thickness could be

found for the CFRP overlay based on the ratio of the axial stiffness of the CFRP overlay to the axial stiffness of the underlying steel. Because the stress demand in the web gap region is difficult to define and because an additional steel plate was used over the CFRP to prevent debonding of the repair, an optimized thickness for the CFRP overlay could not be determined based on the previous experimental research. Although the results were not directly comparable, they did provide a useful frame of reference. Based on the observed performance of the tensile specimens with overlays (see Appendix B.1) a CFRP overlay thickness of 6 mm ($^1/_4$ in.) was adopted in this study.

As with the full-depth splice plate repair, the system included the drilling of a 19 mm ($^3/_4$ in.) crack-stop hole in the web at each tip of the fatigue crack. The assemblage then consisted of a 6 mm ($^1/_4$ in.) thick CFRP overlay adhesively bonded to the web. A 13 mm ($^1/_2$ in.) steel cover plate covering the CFRP overlay was bolted to the web, as shown in Figure B.55, to provide a uniform compression force on the overlay and prevent debonding under cyclic loading. 19 mm ($^3/_4$ in.) bolts were used to bolt the steel cover plate. Each bolt was tensioned to 125 kN (28 kips) following the stipulations in AASHTO Table 6.13.2.8-1 (AASHTO, 2013). A 13 mm ($^1/_2$ in.) thick cover plate was chosen because the thickness was sufficient to evenly distribute the force from the tensioned bolts without damaging the CFRP overlays. A very thin steel cover plate could result in an uneven distribution of the bolt force, damaging the CFRP layer and greatly decreasing the effectiveness of the repair. The adhesive bond layer between the steel and CFRP overlay was a 0.6 mm (25-mil) resin layer

Dimensions of both the CFRP overlay and steel cover plate (Figures B.53 and B.54) were chosen as 127 x 267 mm (5.0 x 10.5 in.). A repair system of this size would cover a large portion of the damaged web and the region with the highest stress demand. If for any reason the repair would not perform adequately and allowed crack re-initiation to occur, this type of repair would allow increased fatigue damage to be detected during inspection. A repair of this size was placed on each side of the welded stiffener on the interior face of the web. On the opposite side of the web, the repair system consisted of a single CFRP overlay and cover plate with dimensions of 267 x 283 mm (10.5 x 11.1 in.).
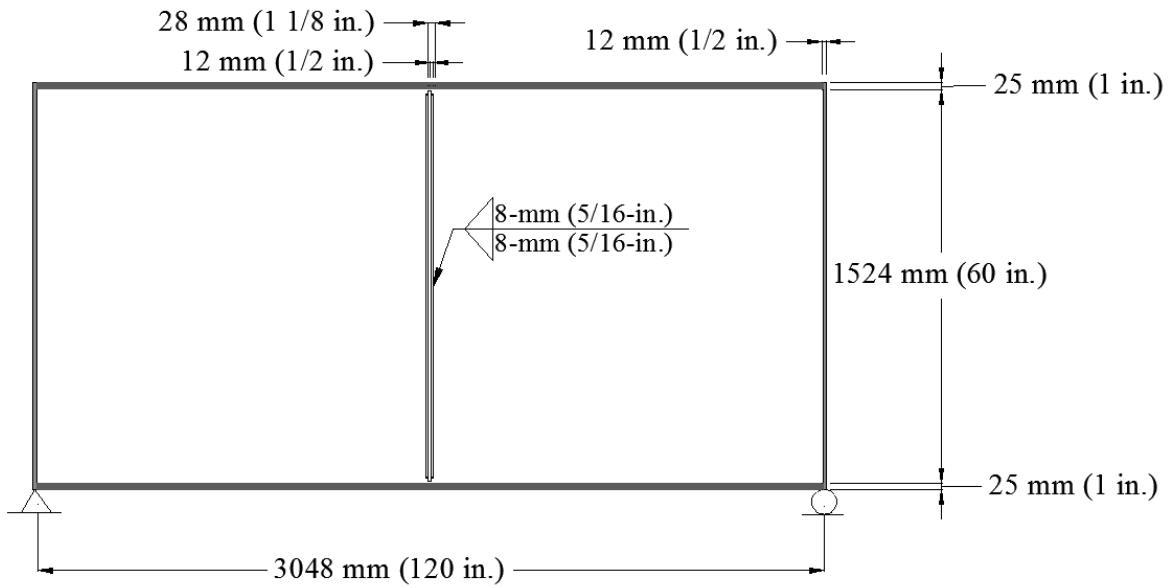
Figure B.52: Circled region shows area of probable fatigue damage and repair
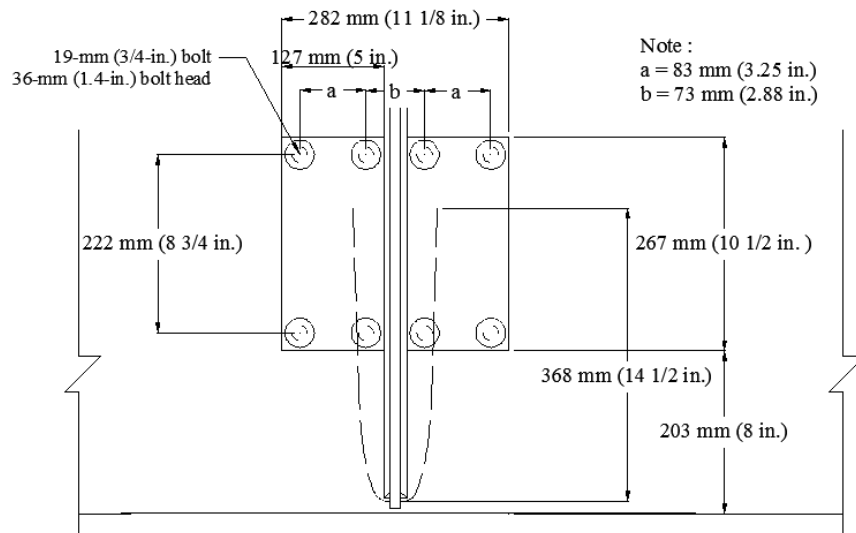
Figure B.53: Repair dimensions for crack length equal to ¼ of the web depth
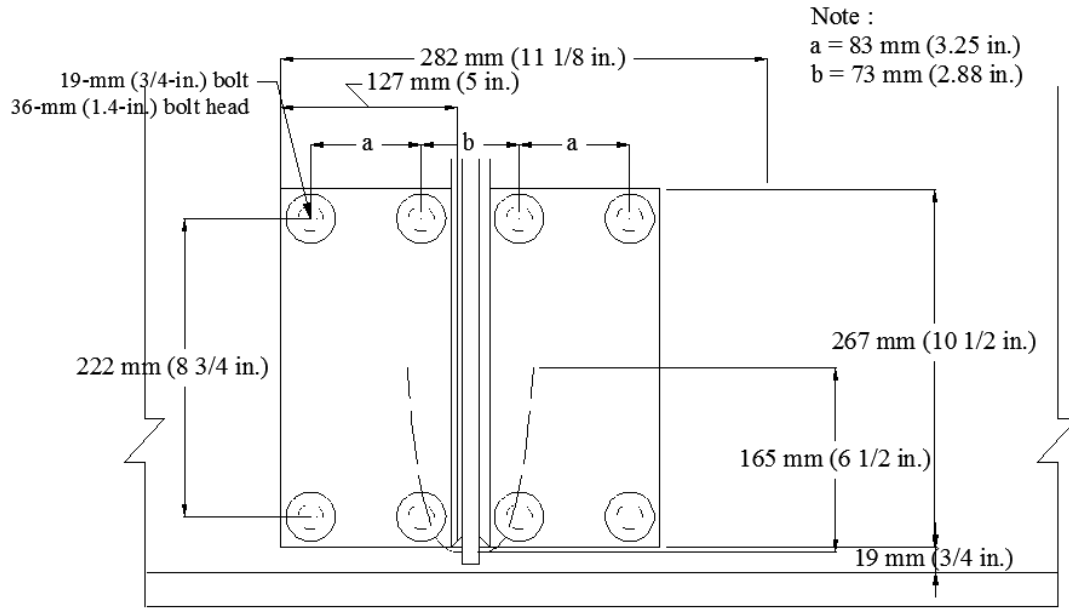
Figure B.54: Repair dimensions for crack length equal to $^1/_8$ of the web depth
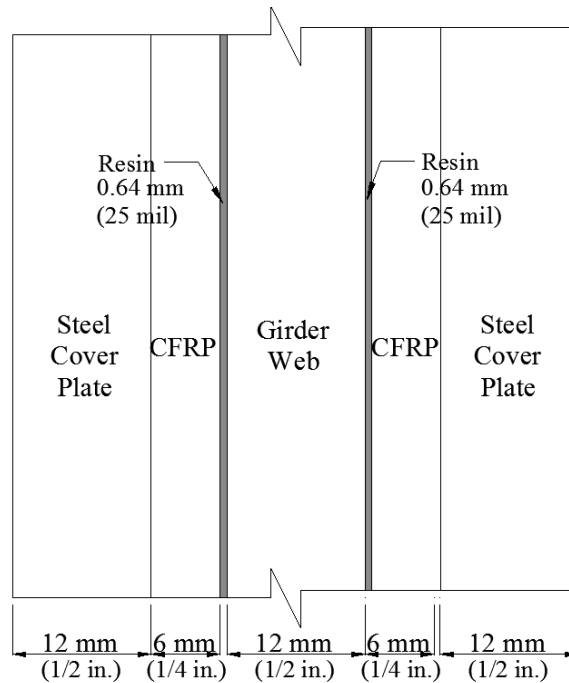
Figure B.55: Cross section of carbon fiber reinforced polymer repair

B.5.5.3 Finite Element Modeling

The Finite Element (FE) models of the segment of bridge girder developed in Abaqus v6.10.2 (SIMULIA 2010) and discussed above were used to evaluate the expected performance of the three repair methods. The model remained linear-elastic and was constructed using three-dimensional elements. Meshes were assembled using 8-node brick elements for the majority of the model, except near regions of fatigue cracking, crack-stop holes, and bolt holes. In these regions a sweep mesh was used to encompass the geometric discontinuities. Each layer of resin, CFRP, and steel cover plate was meshed completely using a sweep mesh. In each model all edges of the girder web were seeded using a uniform size of 6 mm ($^1/_4$ in.). A 25 mm (1 in.) region of tetrahedral meshing was used to transition between sweep and structured meshing in the web. Fatigue cracks were modeled by removing part of the web via cuts and extrudes. The Extended Finite Element Method (XFEM) modeling technique was not used in this part of the study. Instead, fatigue cracks were created by cutting away the web material.

As with previous models, all parts of the girder section that were composed of steel were modeled with a modulus of elasticity of 200 GPa (29,000 ksi) and Poisson's ratio of 0.3. The same material properties were used for both the steel splice and cover plates. Resin layers were modeled with a modulus of elasticity of 207 MPa (300 ksi) and CFRP layers with a modulus of elasticity of 82 GPa (12,000 ksi), each with Poisson's ratios of 0.1. Parts were attached using surface-to-surface tie constraints. Only the weld attaching the connection stiffener to the web was modeled explicitly. A mesh size of 5 mm (0.2 in.) was used for the weld and its material properties matched those of other steel parts. Boundary conditions for these models were consistent with those described previously.

Material characterization tests of CFRP overlays used in the experimental studies showed large scatter in the modulus of elasticity of the CFRP, and a dependency between the modulus of elasticity and the number of plies used in fabricating the CFRP coupons (Alemdar 2011). For this reason, two additional models were produced with modulus of elasticity 25% above and below the modulus of elasticity of CFRP modulus specified above. This produced models with moduli of elasticity of CFRP of 103 GPa (15,000 ksi) and 62 GPa (9,000 ksi).

B.5.5.4 Hot Spot Stress Analysis

The Hot Spot Stress (HSS) method was again used to compare and evaluate the reduction in stress demands associated with each of the three fatigue damage repair methods. However, the Hot Spot Stress paths used in this evaluation were different than those discussed previously. The introduction of a fatigue crack into the girder section created two regions of high stress demand, as will be discussed further in the following sections.

The first region of high stress demand occurred near the tip of the crack or the top outside edge of the crack-stop hole on the web face, where crack re-initiation would be most likely to occur. At this location a horizontal path was defined either 6 mm ($^1/_4$ in.) from the tip of the fatigue crack or 6 mm ($^1/_4$ in.) from the outermost edge of the crack- stop hole, depending on whether the model included a crack-stop hole. The maximum principal stress extracted from this path was designated HSS#3. Reductions in HSS#3 were adopted as an indicator of the effectiveness of the various repair techniques.

The second region of high stress demand occurred in the bottom web gap region at the point of maximum curvature in the horse-shoe shaped crack. This is the location at which crack initiation is expected to occur and where a crack of Type 1 (Figure B.44) would be expected to initiate. A path was defined at a distance of 6 mm ($^1/_4$ in.) from the curved edge of the fatigue crack. The maximum principal stress demand extracted from this path was designated HSS#4. HSS#3 and HSS#4 were determined on both the interior and fascia surfaces of the web.

The extraction of the HSS was complicated by the sweep type mesh used in critical regions. Sweep meshes do not produce a horizontal path at the desired location from which a maximum principal tensile stress could be determined. It was for this reason that HSS#4 (Figure B.56) was extracted from a curved path, because the sweep mesh in this region did produce a fairly uniform curve around the fatigue crack. HSS#3 (Figure B.56) was extracted from points located closest to a horizontal line located at 6 mm ($^1/_4$ in.) from the tip of the crack or edge of the crack-stop hole. Although this resulted in a somewhat uneven path, stress magnitudes in the critical locations of high stress demands were available at the desired distance from either the end of the crack or edge of the crack-stop hole. If no points were available near the intended location of the extraction path, the magnitude of the tensile principal stress was interpolated at

the desired location from two adjacent paths. Results for the reduction in HSS#3 and HSS#4 are reported for all repairs, however, HSS#3 is the most important to this study as it indicates the potential for crack re-initation and further damage.
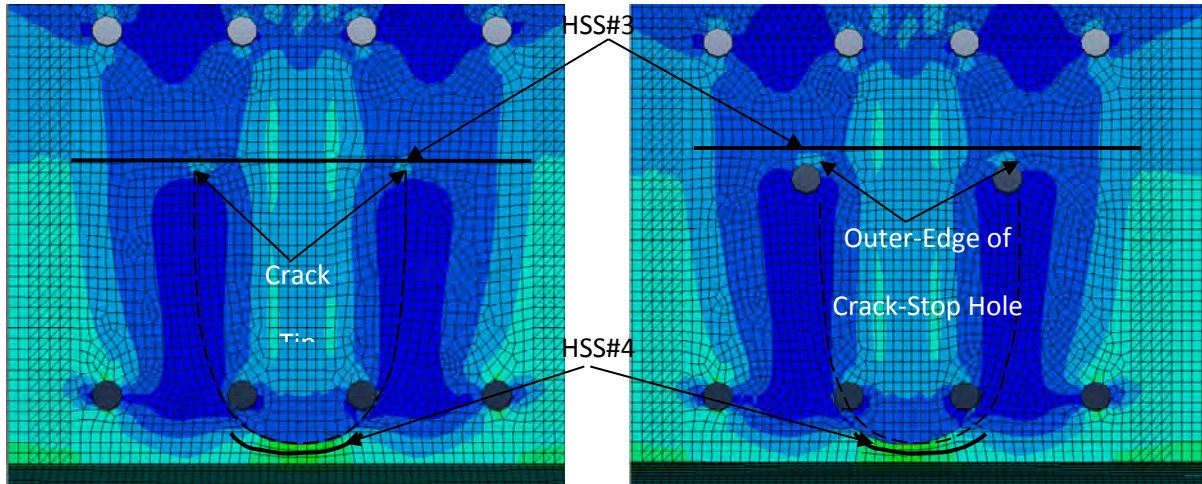
Figure B.56: Hot spot stress paths used to evaluate fatigue damage repair methods

B.5.5.5   Results

B.5.5.5.1   Evaluation of Crack-Stop Holes

In the un-retrofitted base models without crack-stop holes listed in Table B.17, large maximum tensile principal stress demands were observed at four separate locations near the crack. The regions where high maximum stress demands were observed were consistent in all models regardless of crack length. The first region of high stress demands was located in the girder web, at the tips of each end of the crack, on the interior side of the web where the connection stiffener was welded (Figure B.57). High stress demands at this location were expected because of the sharp discontinuity imposed by the tip of the crack (Barsom and Rolfe 1999). On the fascia side of the girder, high stress demands were also found in the web, at each tip of the crack. The main difference between the stress field at the two critical locations was that at the former the high stress demands were localized in the vicinity of the crack tips, and at the latter the high stress demands were not localized and were instead spread along the length of the web, between the two legs of the crack (Figure B.57). The difference in stress distribution between the two faces of the girder can be attributed to the placement of the connection stiffener,

which stiffens the interior face of the web and reduces stress demands in that region. Both of these stress demands were captured by the HSS#3. The third and fourth peak stress locations occurred on both faces of the web in the web gap region, as shown in Figure B.57. The high stress demands at locations 3 and 4 were caused by the combined effects of geometric discontinuities and bending stresses induced in the web gap by the cross frame. These areas of high demand were captured by HSS#4.

While crack-stop holes greatly increase the radius of the crack tip, and should consequently reduce the stress demand at that point (Barsom and Rolfe 1999), the evaluations in this study indicated that in the web gap region the presence of crack-stop holes did not have a significant effect on the maximum stress demands for diameters lower than 51 mm (2.0 in.). The use of a 19 mm ($^3/_4$ in.) crack-stop hole resulted in small reductions in HSS#3 and HSS#4, as shown in Figure, compared to other retrofit techniques. Even for the model with a 51 mm (2.0 in.) crack-stop hole, the only meaningful reduction in stress demand occurred on the interior side of the web, at the crack tips, as shown in Figure B.58(c). The high stress demands at all other critical locations remained unchanged or decreased by a small amount. The introduction of a 51 mm (2.0 in.) crack-stop hole at the tip of the crack with a length equal to $^1/_8$ of the girder depth resulted in reductions in HSS#3 of approximately 17% on the interior face of the web and 12% on fascia side of the web. With the deeper crack, propagating $^1/_4$ of the depth of the web, the 51 mm (2.0 in.) crack-stop hole resulted in higher reductions in peak stress demand (40% and 27% on the interior side and fascia side of the web, respectively). While the magnitude of HSS #3 did in fact decrease with the introduction of a large crack-stop hole, the area of high stress demands on the fascia side of the web increased greatly as the diameter of the crack-stop hole increased [Figure B.58 (b) and (d)]. There was no reduction in HSS#4 observed in models with either crack length.

Models subjected to tensile loading also had large maximum principal stress demands at each tip of the crack. For models with a horse shoe shaped crack, high stress demands were found in the same four regions discussed for models under combined loading. As shown in Figure B.61 the introduction of crack-stop holes did not significantly reduce or alter the stress distribution near the cracked region. High stress demands were still present, even when the

243

crack-stop hole diameter was increased to 102 mm (4.0 in.), a diameter much larger than what could be practically drilled in the field. With this size of crack-stop hole drilled at the tip of the horse shoe shaped crack, HSS#3 decreased by approximately 12% while HSS#4 actually increased by approximately 18%, indicating that drilling large crack-stop holes in the web gap region may have detrimental effects. For a straight crack subjected to pure tension, the condition for which Equation B.7 was intended, the reduction in peak stress demand was approximately 8% for a 102 mm (4.0 in.) crack-stop hole.

Based on the results from all the FE models with crack-stop holes it is concluded that while drilling of crack-stop holes may be effective in reducing the peak demand at the tip of the crack by removing damaged material from the fracture process zone, this type of repair is not effective in mitigating stress demands induced by out-of-plane forces in web gap regions, and should be used in combination with other retrofit measures intended to reduce large stress demands induced by geometric discontinuities in the web gap region. Because the primary benefits of drilling crack-stop holes are the removal of the sharp crack tip and fracture process zone, the drilling of large-diameter crack-stop holes is unjustified, and was shown to be detrimental in some instances.

B.5.5.5.2   Evaluation of full-depth steel splice plates

Repairing the girder web with full depth steel splice plates did provide an alternate load path and reduce HSS#3 demands on both sides of the web, as shown in Figure B.60. Effectiveness of this repair method also increased as the length of the crack increased from $^1/_8$ of the depth of the web to $^1/_4$ of the depth of the web. Reductions in HSS#3 for the model with the shorter crack length were 56% and 78% on the interior and fascia side of the web, respectively. When the crack length was increased to $^1/_4$ of the depth of the web, larger reductions in HSS#3 of 77% and 89% on interior and fascia side of the web, respectively, were observed. Reductions in stress demands of this magnitude are a positive indicator that the potential for crack re-initiation is greatly reduced when this repair method is implemented. Stress reductions in HSS#4 of approximately 30% were found on the interior side of the web for both crack lengths; however, the magnitude of HSS#4 actually increased on fascia side of the girder for both crack lengths.

B.5.5.5.3 Evaluation of CFRP overlay and steel plate retrofit measure

The use of adhesively bonded CFRP overlays in combination with a 19 mm ($^3/_4$ in.) crack-stop hole and bolted steel cover plates showed drastic reductions in stress in the cracked region of the web when compared with simulation results from un-retrofitted models, models repaired with crack-stop holes, and models repaired with full-depth splice plates (Figure B.61).

With a crack length equal to $^1/_8$ of the depth of the web, the introduction of the CFRP steel plate repair measure decreased HSS#3 by 83% and 92% on the interior and fascia sides of the web, respectively. Decreases in HSS#4 were 59% and 23% on the interior and fascia sides of the web, respectively. Of the repair methods evaluated, this was the only one that produced a significant decrease in HSS#4. The use of a resin layer between the steel web and the CFRP layer was shown to be effective in transferring the high stress demands in the web gap to the CFRP and the steel plate. Bonding the CFRP layer had the effect of distributing the stress over the entire area covered by the repair, eliminating the presence of small regions with highly concentrated stress demands. This smoothing effect is the main benefit of this retrofit measure with respect to the others discussed.

The FE model with a crack length $^1/_4$ the depth of the web and the CFRP repair also showed positive results. HSS#3 decreased by 95% and 96% on the interior and fascia side of the web, respectively. The reduction in HSS#4 was not as significant as in the case of the shorter crack configuration because the CFRP overlay and steel plates only covered approximately 50% of the length of the horseshoe-shaped crack. These results suggest that the effective crack length, defined as the length of crack not covered by the retrofit measure, seems to be a driving factor in the magnitude of the reduction in HSS#4. For this reason, an additional CFRP retrofit configuration was evaluated for the model with the longer crack ($^1/_4$ depth) so that the CFRP and steel plates covered the majority of the crack. In this extended configuration, the length of all layers of the retrofit assemblage was increased from 267 mm (10.5 in.) to 444 mm (17.5 in.). The increased dimensions of this retrofit measure made the effective crack length approximately equal for the two crack configurations evaluated. A comparison between the calculated stress demands for the models with a crack length equal to $^1/_4$ of the depth of the girder showed that HSS#4 on the interior side of the web was 43% lower for the configuration with the shorter

overlays and 61% lower for the configuration with the longer overlays. On the fascia of the web, the reductions in HSS#4 were 7% for the model with the shorter overlays and 33% for the model with the longer overlays. These results are consistent with the results from the models with the full-depth splice plate repair in that if the effective crack length was kept approximately constant, the effectiveness of the repair increased as the crack length increased. The decrease in stress demand produced by each retrofit method is shown in Figure B.63.

| (a)   No retrofit – interior | (b) No retrofit – fascia |
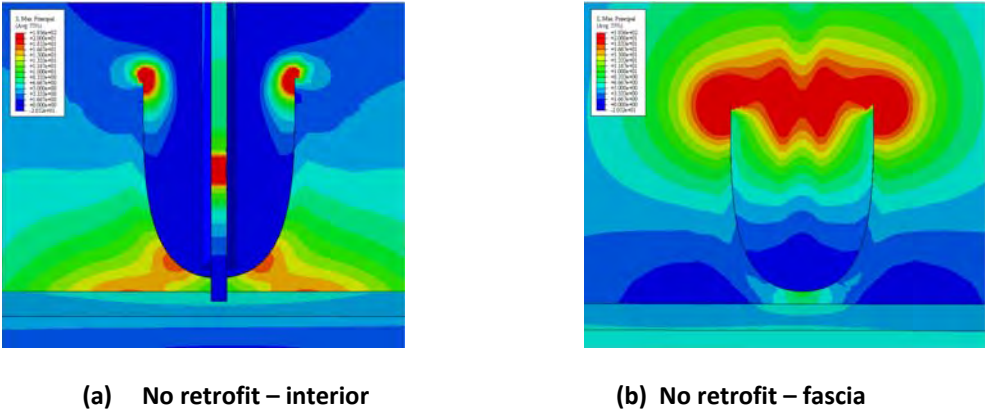
Figure B.57: Maximum principal tension stresses in unrepaired models
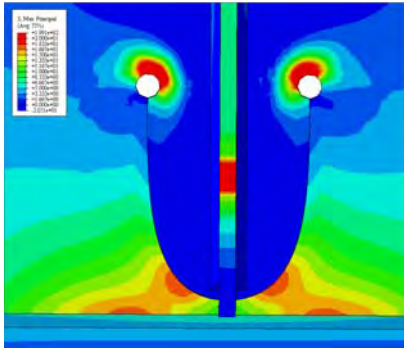
(a) 19 mm (0.75 in.) CSH– interior
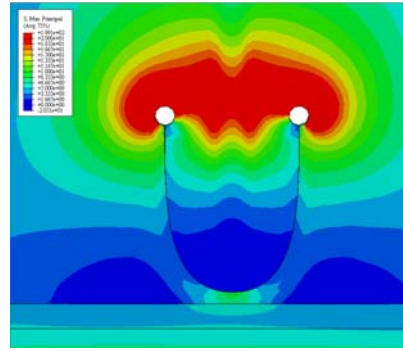
(b) 19 mm (0.75 in.) CSH– fascia
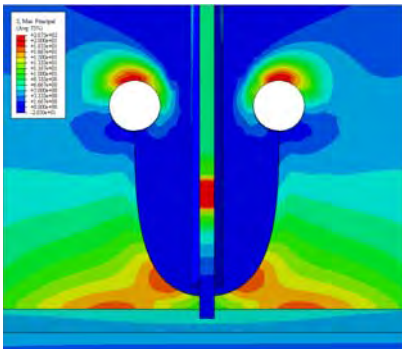
(c) 51 mm (2.0 in.) CSH – interior
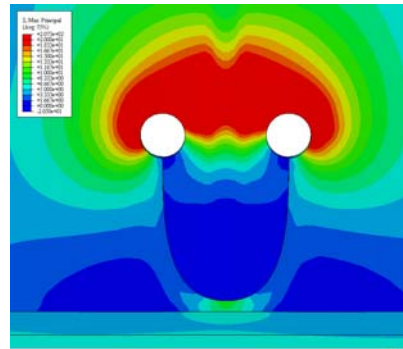
(d) 51 mm (2.0 in.) CSH – fascia

Figure B.58: Maximum principal tension stresses in models repaired with crack-stop holes under combined loading conditions
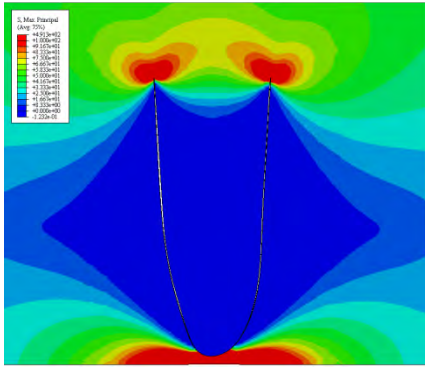
(a) Tension loading – no retrofit
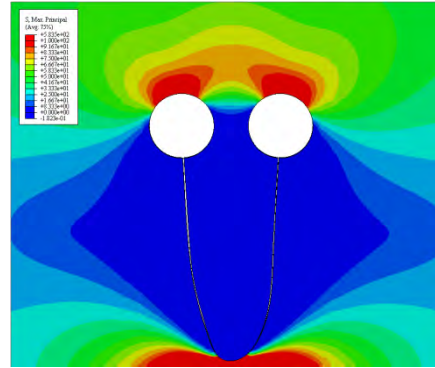
(b) Tension loading – 102 mm (4.0 in.) CSH
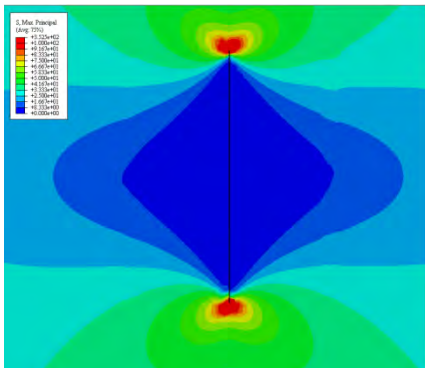
(c) Tension loading – no retrofit
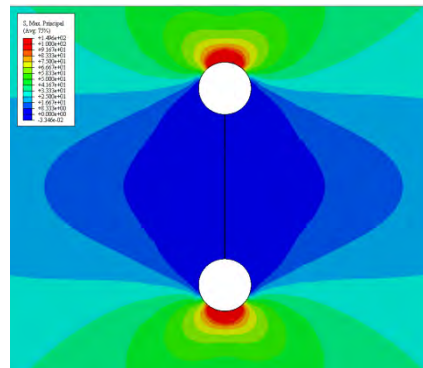
(d) Tension loading – 102 mm (4.0 in.) CSH

Figure 16

Figure B.59: Maximum principal tension stresses in models repaired with crack-stop holes under pure tension loading conditions
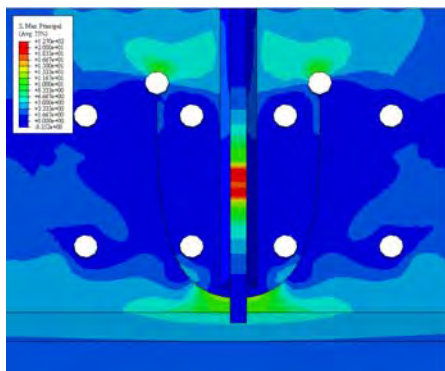
(a) Full-depth splice plate –interior
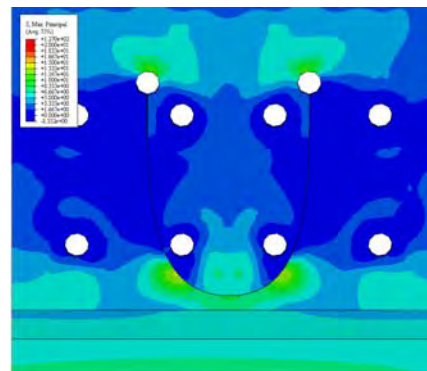
(b) Full-depth splice plate –fascia

Figure B.60: Maximum principal tension stresses in models repaired with full-depth splice plate

248
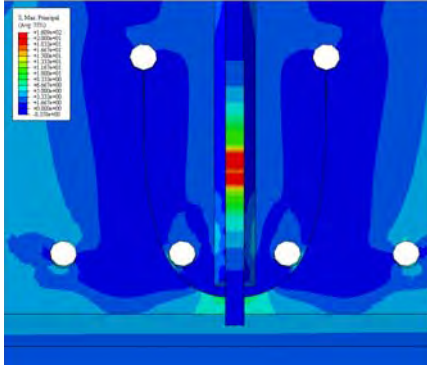
(a) CFRP retrofit system – interior　　　**(b) CFRP retrofit system – fascia**
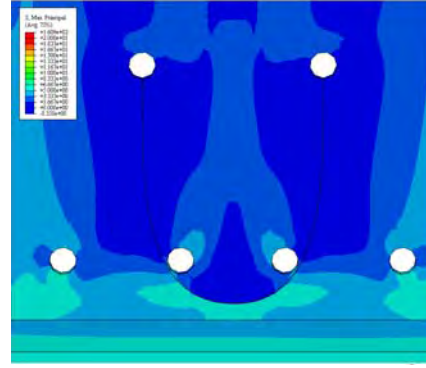
Figure B.61: Maximum principal tension stresses in model repaired with CFRP
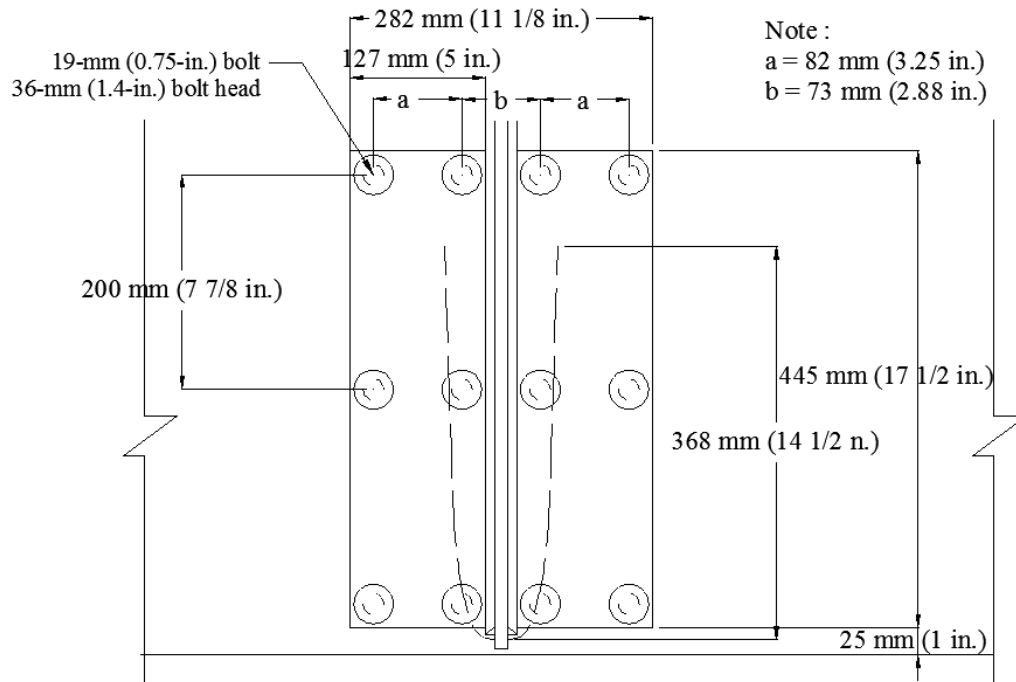
Figure B.62: CFRP repair measure with increased length of repair
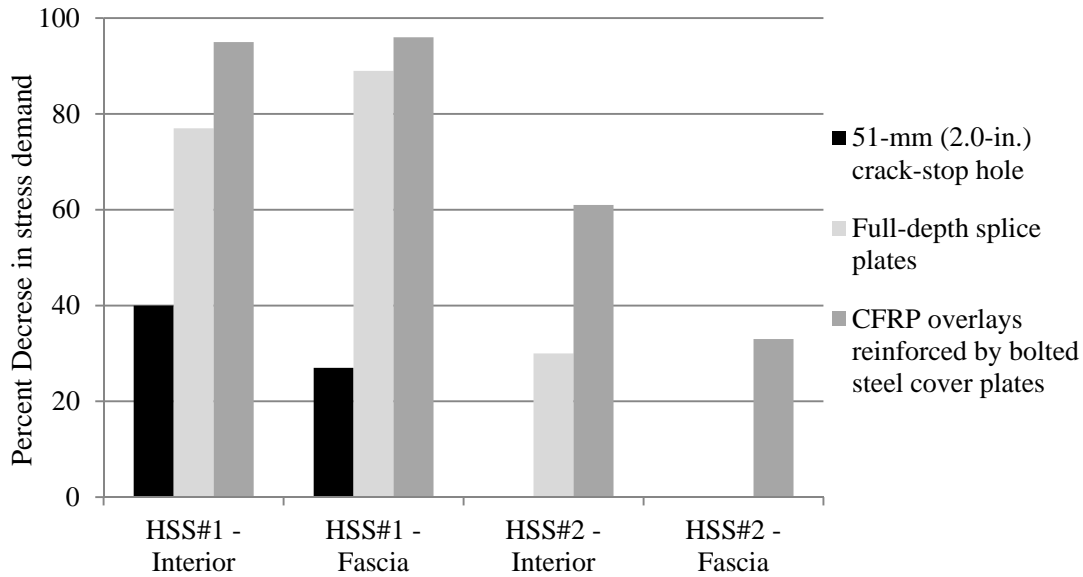
(a)
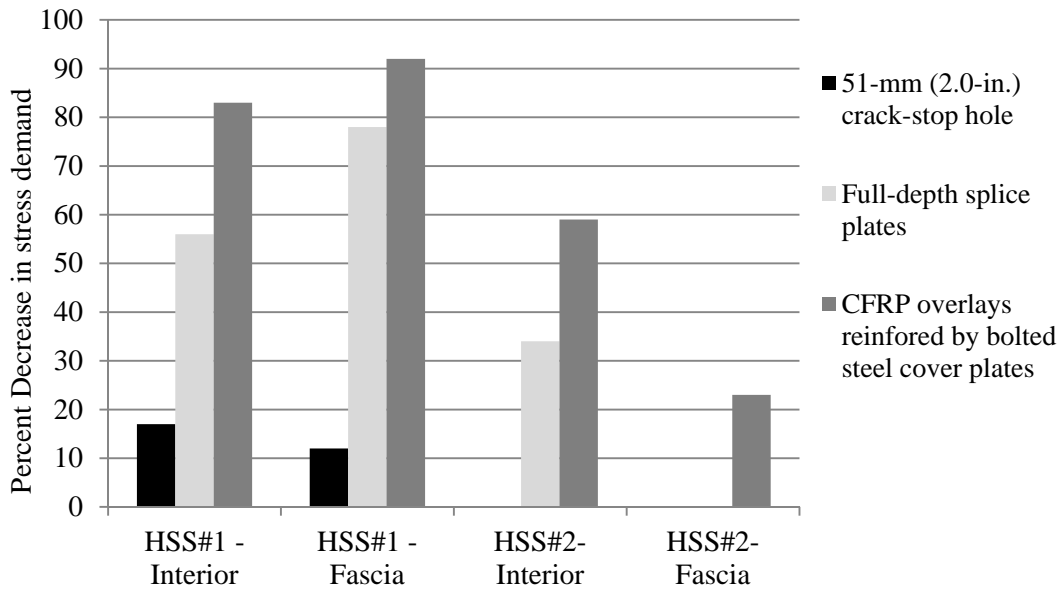
(b)

Figure B.63: Comparison of decrease in stress demand for model with crack length equal to (a) $^1/_4$ the depth of the web and (b) $^1/_8$ the depth of the web

As discussed in the section on finite element modeling, the modulus of elasticity of the CFRP was varied as a parameter because previous research has shown that the stiffness of the

CFRP may have a significant effect on the effectiveness of the repair (Alemdar 2011). For the range of elastic moduli and overlay thickness evaluated in this study it was found that changes in the modulus of elasticity of the CFRP did not have a significant effect on HSS#3 nor HSS#4. This behavior can be attributed to the fact that the layer of CFRP was relatively thin compared with the thickness of the web and the steel cover plates, causing the stiffness of the repair to be dominated by the steel.

The increased effectiveness of the CFRP repair with respect to the bolted splice-plate repair can be attributed to the bond provided by the layer of resin used to attach the CFRP overlay to the web. This layer introduces an alternate load path which allows stresses to transfer between the two sides of the fatigue crack through shear. If bond is lost between the web and the CFRP overlay at localized areas of high peel or shear stress demand the repair is designed to remain effective due to the effect of the tensioned bolts, which are intended to limit the amount of debonding. Although the compression force is likely to keep the overlay in place, it is also possible that the effectiveness of the repair could decrease as a consequence of partial debonding of the overlay. This type of behavior is very difficult to evaluate through computer simulations and should be quantified through physical simulations.

Within the resin layer, the highest shear stress demand in the vertical direction was found to take place at the corner adjacent to the bottom flange and opposite the connection stiffener, where the greatest geometric discontinuity occurs. In the horizontal direction, the largest shear stress demands were found to follow the path of the existing fatigue where the relative motion between the two faces of the fatigue crack is restrained by the repair. Further analytical and physical testing is needed to determine if the shear stress demand at the critical locations in the resin layer is high enough to cause de-bonding of the CFRP. As previously discussed, the compressive stress imposed by the bolts is intended to limit the potential for debonding of the CFRP overlay. Another measure that could reduce the potential for debonding is the fabrication of resin pools extending beyond the edges of the CFRP overlays, which would allow a more gradual transition of stresses by staggering the geometric discontinuities induced by the edge of the overlay and the edge of the resin layer. This technique was shown to drastically increase the number of cycles prior to debonding in three-point bending tests (Kaan et al. 2012).

B.5.6 Conclusions

The effect of in-plane bending and out-of-plane cross-frame forces on the potential for distortion-induced fatigue damage in the web gap region of steel girders was studied, and the following conclusions were drawn:

- As the angle between the cross-frame force and the horizontal increased, the magnitude of maximum principal tensile stress at the connection stiffener-to-web weld and web-to-flange weld (HSS#1 and HSS#2 respectively) decreased. The highest stress demands were found when the cross-frame force was placed parallel to the horizontal.

- As longitudinal bending stress in the top flange increased from 35 MPa to 138 MPa (5 ksi to 20 ksi), magnitudes of HSS#1 and HSS#2 were greatly increased, indicating that in girder segments away from inflection points the potential for fatigue damage is expected to increase as the ratio of live to dead load increases.

- For models in which the gravity load was small relative to the cross-frame load, the highest stress demand was found in the top web gap, on the interior side of the girder. For models in which the stress fluctuations induced by live loads were significant and the cross-frame forces negligible, the highest stress demand was found in the bottom web gap, on fascia side of the web.

- In bridges for which the stress fluctuations due to bending and out-of-plane forces were both significant, the location of maximum stress demand was found to be similar to the case in which the effect of cross-frame forces was negligible, signifying that the potential for fatigue damage was most sensitive to fluctuations in in-plane stress due to live loads that produce bending.

Three different methods to repair severe fatigue damage were evaluated: drilling of crack-stop holes, attaching full-depth steel splice plates, and attaching of CFRP-steel plate assemblages. The effectiveness of the three methods was quantified in terms of the maximum principal stress demands and the following conclusions were made:

- Crack-stop holes implemented as the only repair method were deemed to be ineffective in preventing crack re-initiation regardless of crack length.

- Bolted full-depth splice plates were effective in reducing the magnitude of HSS#3. The maximum stress was reduced by 78% for models with a crack

length of $^1/_8$ the depth of the web and by 89% for models with a crack length of $^1/_4$ of the depth of the web. The change in the magnitude of HSS#4 for either crack length was negligible.

- The CFRP-steel plate retrofit measure resulted in the greatest reductions in stress demand. The magnitude of HSS#3 was reduced by 92% for a crack length of $^1/_8$ of the depth of the web and 96% for a crack length of $^1/_4$ of the depth of the web.

- The CFRP-steel plate repair resulted in the most significant reduction of HSS# 4 with a maximum reduction of 61% was found.

- The effectiveness of the retrofit measure increased with the length of the crack for both the full-depth bolted splice plate and the CFRP-steel plate repairs.

Three methods to repair distortion-induced fatigue damage were evaluated through computer simulations. Of the methods evaluated the most effective was found to be the CFRP-steel plate assemblage. The reduction of stress demands in the web caused by this type of repair is attributed to both the increased stiffness of the strengthened cross section and the transfer of shear stresses through the resin layer. Because the transfer of stresses through the resin layer is of critical importance to the effectiveness of this repair method, more analytical and physical testing is recommended to evaluate the susceptibility this type of repair to debonding. However, the use of CFRP overlays to repair fatigue damage in steel bridge girders has great potential and can be an asset to the field of bridge engineering.

B.5.7 References

AASHTO (2010). AASHTO LRFD Bridge Design Specifications. 5th ed. American Association of State Highway and Transportation Officials, Washington, D.C.

AASHTO (2013). 2013 Interim Revisions to the AASHTO LRFD Bridge Design Specifications. 6th ed. American Association of State Highway and Transportation Officials, Washington, D.C.

Alemdar, F. (2011). Repair of Bridge Steel Girders Damaged by Distortion-Induced Fatigue. (Ph.D. dissertation). University of Kansas, Lawrence, KS.

Barsom, J. M. and Rolfe, S. T. (1999). "Fatigue and Fracture Behavior of Welded Components." Chap. 10 in Fracture and Fatigue Control in Structures: Applications of Fracture Mechanics. 3rd ed. ASTM, West Conshohocken, PA.

Denney, J. J. and Mall, S. (1997). "Characterization of Disbond Effects on Fatigue Crack Growth Behavior in Aluminum Plate with Bonded Composite Patch." Engineering Fracture Mechanics, 57(5), 507-525.

Dexter, R.J. (2004). "Sign, Signal, and Light Support Structures and Manual for Repair of Fatigue Cracks." Third Annual Bridge Workshop: Fatigue and Fracture.

Fisher, J. W. and Mertz, D. R. (1984). "Fatigue and Fracture in Steel Bridges." The Conference on Bridges Official Proceedings, 1st International Bridge Conference, 10-21. Engineers' Society of Western Pennsylvania, Pittsburgh, PA.

Gangel, R. (2012). Use of CFRP Overlays to Repair Fatigue Damage in Steel Bridge Girders and Components. (Master's thesis). University of Kansas, Lawrence, KS.

Hartman, A., Hassel, H., Adams, C., Bennett, C., Matamoros, A., and Rolfe, S. (2010). "Effects of Cross-Frame Placement and Skew on Distortion-Induced Fatigue in Steel Bridges." Transportation Research Record 2200, 62-68. Transportation Research Board, National Research Council, Washington, D.C.

Hassel, H. L. (2011). An Analytical Evaluation of Distortion-Induced Fatigue in Steel Bridges. (Master's thesis). University of Kansas, Lawrence, KS.

Kaan, B. N., Alemdar, F., Bennett, C. R., Matamoros, A., Barrett-Gonzalez, R., and Rolfe, S. (2012). "Fatigue Enhancement of Welded Details in Steel Bridges using CFRP Overlay Elements." Journal of Composites for Construction, 16(2), 138-149.

Khalil, A., Wipf, T.J., Greimann, L., Wood, D.L., and Brakke, B. (1998). "Retrofit Solution for Out-of-Plane Distortion of X-Type Diaphragm Bridges." Transportation Conference Proceedings. Iowa Department of Transportation, 99-102.

Lee, W. Y., and Lee, J. J. (2004)."Successive 3D FE analysis technique for characterization of fatigue crack growth behavior in composite-repaired aluminum plate." Composite Structures, 66(1–4), 513–520.

Liu, H. B., Al-Mahaidi, R., and Zhao, X. L. (2009). "Experimental Study of Fatigue Crack Growth Behaviour in Adhesively Reinforced Steel Structures." Composite Structures, 90(1), 12-20.

Liu, H. B., Xiao, Z. G., Zhao, X. L., and Al-Mahaidi, R. (2009b). "Prediction of fatigue life for CFRP-strengthened steel plates." Thin-Walled Structures, 47(10), 1069–1077.

Mall, S. and Conley, D. S. (2009). "Modeling and Validation of Composite Patch Repair to Cracked Thick and Thin Metallic Panels." Composites Part A: Applied Science and Manufacturing, 40(9), 1331-1339.

Naboulsi, S., andMall, S. (1996). "Modeling of a Cracked Metallic Structure with Bonded Composite Patch Using the Three Layer Technique." Composite Structures, 35(3), 295–308.

Roddis, W. M. K. and Zhao, Y. (2001). "Out-of-Plane Fatigue Cracking in Welded Steel Bridges: Why It Happened and How It Can Be Repaired." Welding Innovation, 18(2), 2-7.

Roddis, W. M. K. and Zhao, Y. (2003). "Finite-Element Analysis of Steel Bridge Distortion-Induced Fatigue." Journal of Bridge Engineering, 8(5), 259-266.

Sabelkin, V., Mall, S., and Avram, J. B. (2006)."Fatigue crack growth analysis of stiffened cracked panel repaired with bonded composite patch."Eng. Fract. Mech., 73(11), 1553–1567

Sabelkin, V., Mall, S., Hansen, M. A., Vandawaker, R. M., and Derriso, M. (2007). "Investigation into Cracked Aluminum Plate Repaired with Bonded Composite Patch." Composite Structures, 79(1), 55-66.

Schubbe, J. J., and Mall, S. (1999)."Investigation of a Cracked Thick Aluminum Panel Repaired with a Bonded Composite Patch." Eng. Fract.Mech., 63(3), 305–323.

SIMULIA. (2010). Abaqus FEA, Version 6.10-2. Providence, RI. http://www.simulia.com.

Umamaheswar, T. V. R. S., and Singh, R. (1999)."Modelling of a patch repair to a thin cracked sheet." Eng. Fract. Mech., 62(2), 267–289.

Zhou, Y., and Biegalski, A. E. (2010) "Investigation of Large Web Fractures of Welded Steel Plate Girder Bridge." Journal of Bridge Engineering, 15(4), 373-383.

B.6: Angles-with-Plate Retrofit Combined with Carbon Fiber Reinforced Polymer for Repairing Distortion-Induced Fatigue Damage at Cross-Frame Connection Plates: Physical Tests

Say Hak Bun[29]

Caroline R. Bennett[30]

Adolfo Matamoros[31]

Ron Barrett-Gonzalez[32]

Stan Rolfe[33]

B.6.1 Abstract

Fatigue cracks in girders' web have been identified in numerous aging bridges throughout the United States that were caused by the secondary stresses induced by the action of distortion-induced fatigue. This paper addresses a retrofit technique that was created through the combined use of carbon fiber reinforced polymer (CFRP) and steel materials with the aim of improving the fatigue life of a 2.8 m (9.3 ft) steel girder segment that was subjected to fatigue cracking at the web gap region. This retrofit consisted of a 1.6 mm ($^{1}/_{16}$-in) thick CFRP overlay, two L6x6x$^{3}/_{4}$ steel angles and a 457x203 mm (18x8-in.) steel plate. To investigate the performance of this technique, a steel girder with existing fatigue cracks was first tested with only steel angles and steel plate (without CFRP) for 1.2 million cycles, and then was tested with the additional presence of CFRP overlays sandwiched between the steel elements and the girder. From the results of the finite element modeling and the physical testing, the retrofit with the presence of CFRP overlays was found to perform better than the retrofit without the CFRP overlays in halting crack propagation.

B.6.2 Introduction and Background

Steel retrofits have been applied extensively as retrofit techniques for distortion-induced fatigue. Fiber reinforced polymer (FRP) materials have been recognized by many researchers to be excellent materials for repairing fatigue cracking. Low strength-to-weight ratios and crack-growth-inhibiting natures of FRPs make them ideal materials to repair and strengthen fatigue-critical details in steel bridges (Meier 1992). FRP materials can have distinct strength advantages over steel when loaded in their optimal orientation, and fiber composite materials such as graphite (carbon)-epoxy and Kevlar-epoxy can outperform steel when subjected to uniform tension (Mallick 1993).

CFRP material was used as a retrofit technique in this research. The superior mechanical and fatigue properties of the CFRP make it a better material for the repair of steel girder bridges subjected to fatigue damage. However, the effectiveness of CFRP retrofit is governed by the quality of the finished CFRP retrofit. Use of CFRP materials as a fatigue enhancement technique has proven challenging in past investigations due to localized delaminating failures experienced at the bond between the steel and composite materials (Colombi et al. 2003). Thus, the application of CFRP on steel must be carefully prepared to achieve the ultimate strength of the fiber.

B.6.3 Objective and Scope

The primary objective of this study was to investigate the effectiveness of using CFRP as a retrofit technique to increase the fatigue life of steel bridge girders loaded in distortion-induced fatigue. The study involved testing two retrofit techniques and comparing the results. One retrofit consisted of steel angles and a back plate, and another retrofit consisted of steel angles, a steel back plate and 1.6 mm ($^1/_{16}$-in) thick CFRP. The retrofits were tested on a 2.8 m (9.3 ft) steel girder that had had fatigue cracks on the girder's web.

B.6.4 Research Approach

B.6.4.1   Experimental Test Set-Up

The physical test setup comprised of a built-up steel girder connected to the concrete floor through a series of C5x9 channels post-tensioned to the 0.9 m (3 ft) thick concrete floor as shown in Figure B.64, and described in detail in Appendix A.1 and A.2. The subassembly was

tested upside-down so that laboratory concrete floor simulated the concrete deck on the bridge. The top flange in the laboratory was restrained from out-of-plane lateral movement by a L3x3x$^3/_8$ angle on each end of the girder. The subassembly was tested with a cyclic tensile force ranged from 2.2 kN (0.5 kip) to 25.4 kN (5.7 kip) applied on a WT section that connected to the cross-frame (Figure B.65).
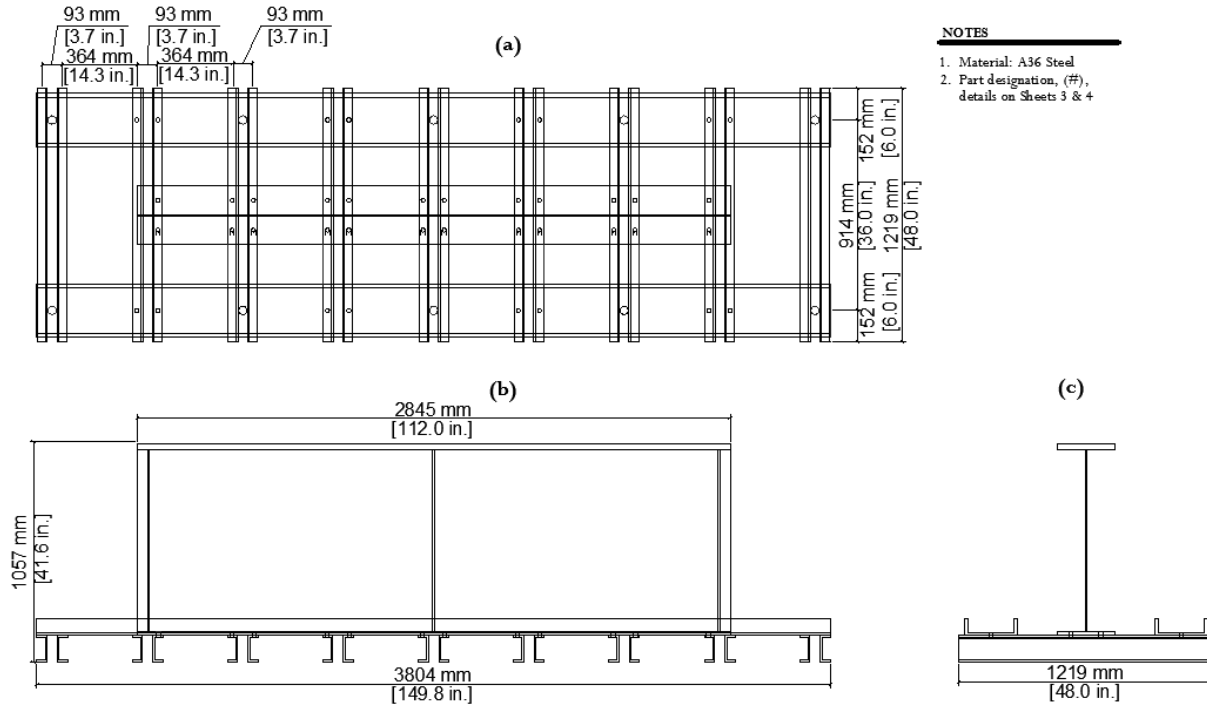
Figure B.64: Girder Specimen
a) Plan view b) Elevation view c) Section view

Figure B.65: Cross-sectional view of the subassembly

B.6.4.2   Specimen Dimensions and Material Properties

The built-up steel girder used in the experimental study was 2.8 m (9.3 ft) long and 918 mm (36 in.) tall. The web had a cross-section dimension of 10 x 876 mm ($^3/_8$ x 34½ in.). The bottom and top flanges had cross-sections of 279 x 16 mm (11 x $^5/_8$ in.) and 279x 25 mm (11 x 1 in.), respectively. The web, bottom flange and top flange all had 345 MPa (50 ksi) yield strength. Full depth stiffeners were provided at the girder ends to prevent from web instability at those regions. At each end of the girder, there were two stiffeners welded to the web and flanges. The four stiffeners were 876 mm ($34^1/_2$ in.) tall and 127 mm (5 in.) wide. There was a connection plate welded to the web at the middle of the girder. The connection plate was 873 mm ($34^3/_8$ in.) tall and 127 mm (5 in.) wide. All stiffeners had a cropped end of 32 mm (1¼ in.), and a thickness of 10 mm ($^3/_8$ in). A cross-frame was used to connect the connection plate and a WT. The cross-frame was made up of three L76 x 76 x 10 mm (L3x3 x $^3/_8$ in.) angles of which two were in an X-configuration, and one was as a horizontal member. This whole assembly had been subjected to fatigue testing of approximately 8 million cycles under a load range from 2.2 kN (0.5 kip) to 25.4 kN (5.7 kip), which had resulted in deep cracks in the girder's web as shown in Figure B.66.

Figure B.66: Existing cracks on exterior face of the girder's web

B.6.4.3 Instrumentation

The girder subassembly was instrumented with three linear variable differential transformers (LVDTs) and nine strain gages (Figure B.67). Two strain gages were placed at the top and bottom web gaps where the cracks commonly initiated. The three LVDTs were used to capture the out-of-plane deflection of the girder at three different locations along the depth of the girder.
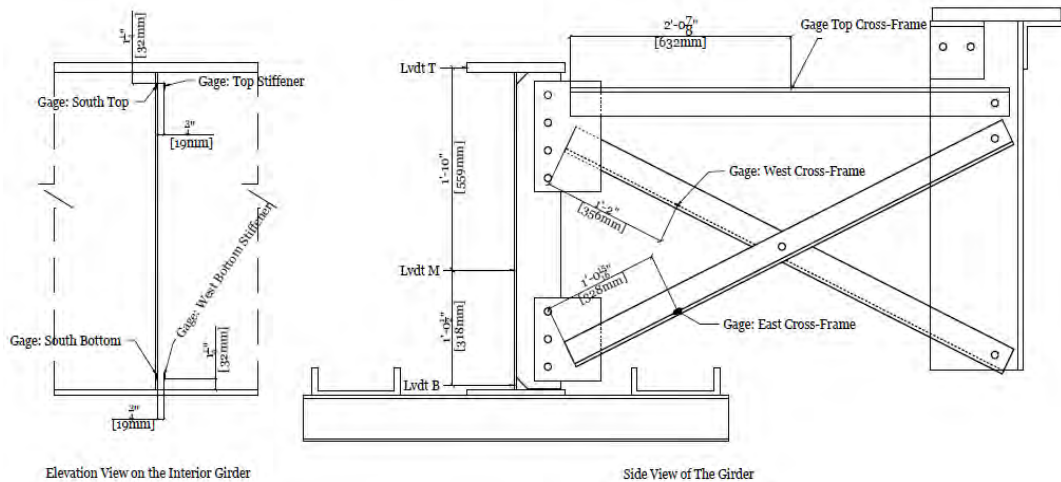
Figure B.67: Instrumentation on the steel girder

B.6.4.4 Experimental Program

The specimen was tested with a cyclic tensile force that ranged from 0.5 kip to 5.7 kips applied on the top of the WT member. The test was divided into two trials: Trial 1 was performed with only the steel retrofit (only angles-with-back-plate retrofit) installed, followed by Trial 2, which included a 1.6 mm ($^1/_{16}$ in.) thick CFRP layer attached to the web and connection plate (Figures B.68 and B.69), and sandwiched between the girder and angles-with-plate repair. In Trial 1, the steel retrofit used was two double angles and a back plate. The angles were 483 mm (19 in.) long, 2L3x3x$^3/_8$ standard angles, and the back plate was 13mm (½ in.) thick with the dimension of 457 mm x 457 mm (18 x 18in.). Each angle was placed on each side of the connection plate and bolted to the girder's web using A325 structural bolts. The back plate was placed on the exterior face of the girder's web where there was no connection plate.

In each trial, the girder subassembly was fatigue cycled to 1.2 million cycles. This targeted cycle number corresponds to the number of cycles on AASHTO S-N curve (AASHTO 2013) for fatigue Category A based on a high stress demand of 193 MPa (28 ksi) at the bottom web gap of an uncracked specimen calculated by Alemdar (2011). The deformation and deflection data were collected continuously throughout the tests. The steel girder was inspected at each end of the trials using UV light and dye penetrant.

Figure B.68: View on the exterior face of the girder's web with a steel back plate

Figure B.69: View on the interior face of the gird's web

B.6.4.5   *Carbon Fiber Reinforced Polymer Preparation Process*

The laminar CFRP materials were made by stacking two layers of graphite fibers and WEST System epoxy. Each layer of the graphite fibers had a thickness of 0.8 mm ($^1/_{32}$ in.) which provided the same thickness as the target thickness. The fabrication process is described as follows.

First, the graphite fiber sheets were cut to dimensions of 457 x 609 mm (18 x 24 in.) and 152 x 483mm (6 x 19 in.). Two layers with the dimensions of 457 x 609 mm (18 x 24 in.) were used on the fascia side of the web where the steel back plate attached to. Four layers of the CFRP having dimensions of 152 x 483 mm (6 x 19 in.) were applied on the interior of the girder on both sides of the connection plate. Second, the steel surfaces were prepared by grinding off the paint, and then degreased using isopropyl alcohol. The steel-to-CFRP bonds were considered to be the most important factors that governed the effectiveness of this retrofit, based upon the studies reported upon in Appendix B.2 and B.3. Third, a two-component epoxy was used for bonding the CFRP laminates to the steel surfaces. The mixing ratio of the epoxy was five parts resin to one part hardener by volume. The epoxy was first applied on the steel surfaces by brushing, then the CFRP sheets were attached to the web and connection plate, one layer at a

time. Finally, the steel angles and back plate were attached to the graphite fibers by pretensioning the bolts (Figures B.70 and B.71). The pressure from the pretension activated the matrix material (epoxy) and caused the matrix to flow entirely around the fibers. For the CFRP to work effectively, high consolidated CFRP must be achieved. High levels of consolidation have higher strength and stiffness characteristics than poorly consolidated composites, and are more resistant to crack propagation (Mallick 1993). The CFRP/steel sandwich composite was left to cure for 48 hours before the test began.
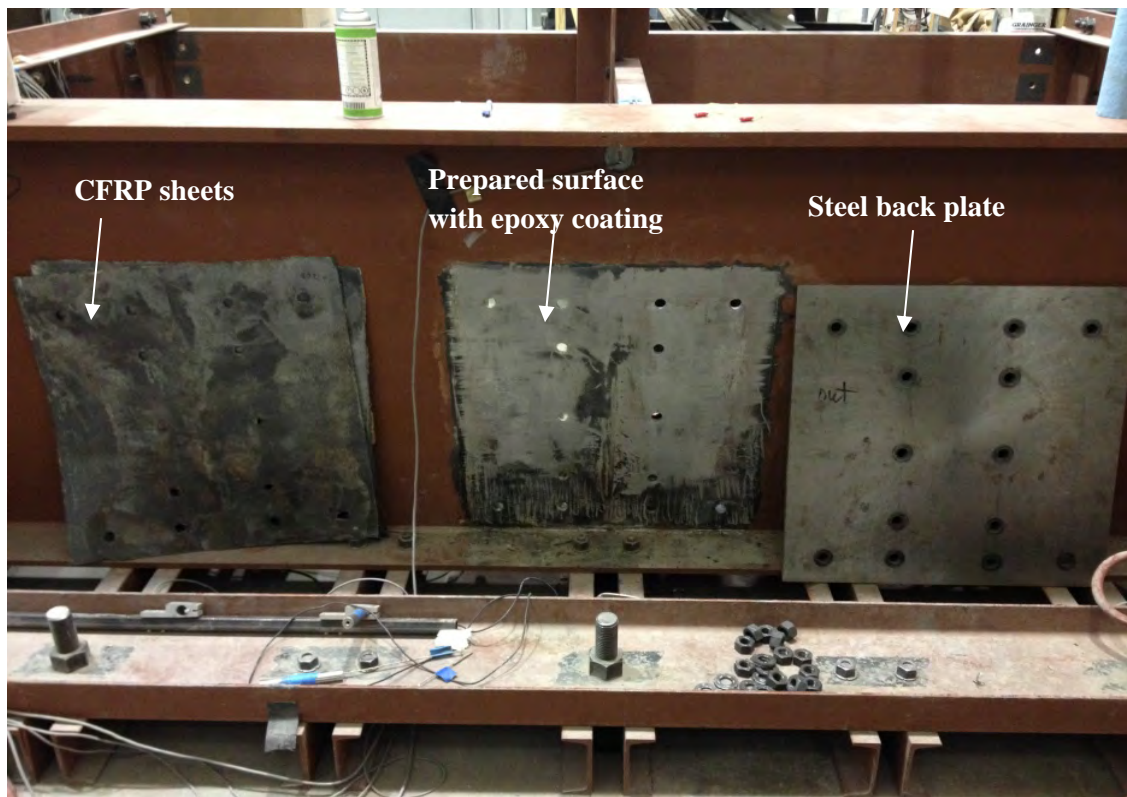
Figure B.70: Trial 2: view of the exterior face of the girder's web

Figure B.71: Trial 2: view of the interior face of the girder's web

B.6.5 Results

From the results of the physical testing, the inspection at the end of both Test Trials 1 and 2 indicated that cracks did not propagate. However, strain data measured at the end of both retrofits indicated that with the presence of the CFRP material, the percentage of stress reduction was greater than the steel-only retrofit by approximately 30% (Table B.19).

Table B.19: One stress and strain data obtained from physical testing

	Steel Retrofit	**Steel / CFRP Sandwich-Type Composite Retrofit**
Strain, μɛ	43	33
Stress, MPa (ksi)	8.96 (1.3)	6.2 (0.9)

B.6.6 Conclusions

From the results of both analytical studies (Appendix B.5) and experimental testing of the two retrofit systems, the steel/CFRP sandwich-type retrofit system performed better than conventional steel retrofit system. Although the FE models were not identical to the version of

the installed retrofit, the results still provided a useful reference by showing greater stress reductions for the steel/CFRP sandwich-type composite than for the steel-only retrofit. The physical testing showed that the steel/CFRP sandwich-type retrofit reduced stresses by approximately 30% more than the steel-only technique. Further testing is recommended by varying the thickness of the CFRP materials in order to reach an optimal thickness.

B.6.7 References

AASHTO (2013). 2013 Interim Revisions to the AASHTO LRFD Bridge Design Specifications. 6th ed. American Association of State Highway and Transportation Officials, Washington, D.C.

Alemdar, F. (2011). Repair of Bridge Steel Girders Damaged by Distortion-Induced Fatigue. (Ph.D. dissertation). University of Kansas, Lawrence, KS.

Colombi, P., Bassetti, A., and Nussbaumer, A. (2003). "Crack Growth Induced Delamination on Steel Members Reinforced by Prestressed Composite Patch." Fatigue & Fracture of Engineering Materials & Structures, 26, 429-437.

Mallick, P. K. (1993). Fiber-Reinforced Composites: Materials, Manufacturing, and Design. 3rd ed. Marcel Dekker, New York, NY.

Meier, U. (1992). "Carbon Fibre-Reinforced Polymers: Modern Materials in Bridge Engineering." Structural Engineering International, 2(1), 7-12.

SIMULIA. (2010). Abaqus FEA, Version 6.10-2. Providence, RI. http://www.simulia.com.

Appendix C and D: Table of Contents

Appendix C and D: List of Tables

Appendix C and D: Table of Figures

Appendix C: Development of PICK Technology

Appendix C is focused on the development and testing of a technique developed for the purpose of treating crack-arrest holes, termed Piezoelectric-Induced Compressive Kinetics (PICK), and includes two parts: C.1 and C.2.

C.1 describes an analytical investigation that demonstrates the feasibility of PICK treatment for fatigue life enhancement in steel structures.

C.2 describes the development of the PICK technology and its physical testing, which included: fatigue testing, metallurgical examination, hardness testing, measurement of retained expansion, and neutron diffraction measurements taken at Oak Ridge National Laboratories.

C.1: Development of a Technique to Improve Fatigue Lives of Crack-Stop Holes in Steel Bridges

Josh S. Crain[1]

Gary G. Simmons[2]

Caroline R. Bennett[3]

Ron Barrett-Gonzalez[4]

Adolfo B. Matamoros[5]

Stanley T. Rolfe[6]

C.1.1 Abstract

A common technique used to prevent the propagation of fatigue cracks in bridge girders is the drilling of crack-stop holes at crack tips. By doing so, stress concentrations at the crack tips are reduced and fatigue life of the bridge is extended. The size of the crack-stop hole needed to prevent any further crack growth is determined by utilizing known material properties and relationships developed through experimentation. However, these equations often result in a crack-stop hole diameter larger than can be practically drilled; physical limitations force crack-stop holes to be undersized in the field. To improve effectiveness of undersized holes to that of full-sized holes, a method is needed to strengthen undersized crack-stop holes.

The purpose of this study was to investigate the potential of a new technique to improve the fatigue life of undersized, crack-stop holes. The technique uses piezoelectric actuators operated at ultrasonic frequencies to convert electrical signals into mechanical work. This technique produced residual compressive stresses of the same order of magnitude as those produced by static cold expansion. A suite of finite element models was created to quantify and

---

[1] Josh S. Crain, M.S., PE, Structural Engineer, Genesis Structures, Kansas City, MO

[2] Gary G. Simmons, PhD, PE, University of Kansas, 1530 W. 15th St., Lawrence, KS 66045

[3] Caroline R. Bennett, PhD, PE, Associate Professor, University of Kansas, 1530 W. 15th St., Lawrence, KS 66045

[4] Ron Barrett-Gonzalez, PhD, Associate Professor, University of Kansas, 1530 W. 15th St., Lawrence, KS 66045

[5] Adolfo B. Matamoros, PhD, Professor, University of Kansas, 1530 W. 15th St., Lawrence, KS 66045

[6] Stanley T. Rolfe, PhD, PE, A.P. Learned Distinguished Professor, University of Kansas, 1530 W. 15th St., Lawrence, KS 66045

characterize the residual stresses surrounding the cold-expanded, undersized, crack-stop holes. Results were compared with analyses found in past literature.

C.1.2 Introduction

As a result of the relatively long propagation life between initiation of a fatigue crack and eventual failure, measures can be taken to retrofit and preserve existing cracked bridge members if fatigue cracks are detected early. There are several existing methods that can retard or stop the propagation of fatigue cracks. These methods include: repair welding or grinding of shallow cracks; metal reinforcements; adhesive CRFP patching; altering connection details; and drilling stop holes at crack tips (Domazet 1996; Vulic et al. 1997; Roddis and Zhao 2003; Zhao and Roddis 2007; Hu et al. 2005). These methods are attractive considering that the alternatives are either complete replacement of the cracked structural member or reducing external loads coupled with careful monitoring.

The technique of drilling a hole at a crack tip is a well-known procedure used in everyday practice to enhance fatigue life of steel structures (Vulic et al. 1997). The primary challenges associated with correctly applying this technique are that the theoretical size of the crack-stop hole is often too large for practical implementation in the field or the location is blocked by other members. To overcome these issues, crack-stop holes are often drilled undersized and left unreinforced. While undersized holes do improve fatigue life of a cracked structural member, it has been shown that varying levels of cold expansion can increase fatigue life of an unreinforced crack-stop hole by an order of magnitude (Amrouche et al. 2000; de Matos et al. 2007; Forgues et al. 1993; Herman and Ozdemir 1999; Landry et al. 1986; Pavier et al. 1999; Shin et al. 1996; Zhang et al. 2005; Ball and Lowry 1998). The increase in fatigue life provided by cold expansion is a result of the three principal residual stresses induced by cold expansion: tangential, radial and transverse. Among these, compressive tangential stresses (also referred to as hoop or circumferential stress) is the major contributor to significant gains in fatigue life (Domazet 1996).

Several techniques have been developed to cold expand holes in metal structures, each having the common feature of inducing a layer of residual compressive stress around the outside of the hole. These compressive residual stresses are the direct result of forced, inelastic

deformation of material around the circumference of a crack- stop hole. As a crack-stop hole is forced to expand through a mechanical process, yielding will first initiate along the edges of the hole where stresses are highest. As further expansion is mechanically induced, the zone of plasticity spreads further outward from the hole. Material that lies beyond this plastically-deformed region will deform elastically under applied stress. After the mechanically-applied pressure or displacement is removed from the system, residual compressive stresses around the hole are created from the elastic rebounding, or "springback," of the unyielded material surrounding the permanently-deformed plastic zone (Poolsuk 1977). Figure C.1 shows the level of residual tangential compressive stress that can be expected to develop around a mechanically expanded hole.
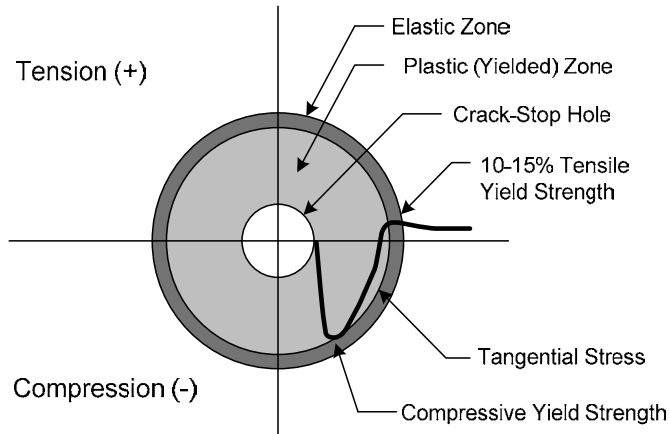
Figure C.1: Residual tangential (i.e., circumferential or hoop) stress surrounding cold-expanded hole

A different technique, examined by Reemsnyder (1975), involved the installation of high-strength bolts in crack-stop holes used to enhance fatigue performance. While the main focus of the study by Reemsnyder (1975) was the potential fatigue life improvement of previously cracked holes in riveted bridge connections, the study mentioned that high-strength bolts were installed in drilled crack-stop holes located a predetermined distance away from the riveted connections. Cracks did not reinitiate from the crack-stop holes with the installed high-strength bolts; however, because fatigue life improvement of crack-stop holes was not the main focus of the study, no quantified fatigue life improvement was provided.

273

In separate studies performed by Huhn and Valtinat (2004) and Brown et. al. (2007), the influence of fully-tensioned high-strength bolts on the fatigue life of bolt holes in slip critical connections was examined. According to both studies, tensioned high-strength bolts significantly increased fatigue life of the bolt hole plate. According the authors, "this was due to the high pressure under the washers of the bolts. This high pressure gives a certain protection of the area around the hole, so that the stress distribution in the net section became much more favorable, even after the slip of the connections." (Huhn and Valtinat 2004)

The method of installing high-strength bolts does not appear to improve fatigue performance as a result of cold working. No study (Reemsnyder 1975; Huhn and Valtinat 2004; Brown et al. 2007) reported mechanical expansion occurring at the edges of the holes as a result of tensioning the high-strength bolts. Installing tensioned high-strength bolts is a separate technique and is one that could potentially be coupled with cold working to produce even larger improvements in fatigue life.

The technique described in this article used piezoelectric actuators to dynamically work and cold-expand the volume of steel plate surrounding the inner surface of a crack-stop hole. Dynamically working steel through impact at high frequencies is a proven method for refining coarse grained steel into finer grained material (Statnikov 2004), which can translate into improved fatigue performance. Plastic strains induced by the cold-expansion from the piezoelectric transducers were intended to create a residual compressive stress field similar to that achieved through existing techniques. The technique discussed in this paper has been termed Piezoelectric Impact Compressive Kinetics (PICK).

C.1.3 Background

C.1.3.1 Existing Cold Working Techniques

While development of the PICK technique has focused solely on improving the fatigue performance of steel bridges, similar challenges are commonly encountered in the aerospace industry. Fastener holes in aircraft structures are sources of large stress concentrations and, as a result, are potential sites for cracks to initiate and propagate. It is common practice in the aerospace industry to cold-expand fastener holes, often resulting in a fatigue life improvement of three to ten times that of an untreated hole (Pavier 1999). Most of the development of cold

274

expansion has been performed within the aerospace field. As a result, the majority of existing studies involve numerical modeling and testing with various grades of aluminum, titanium, and high strength steel (Phillips 1974). Benefits obtained from cold expansion of mild grade steel are expected to be similar to those found in aerospace-industry materials as a result of the similarity in the stress-strain relationship of the two types of materials when stressed beyond yield.

The most common technique currently used to cold-work fastener holes in aerospace applications is the split sleeve mandrel process. While a thorough review of literature on this topic did not expose any application of this technique to bridges, it has been used extensively in other structural applications. The process utilizes a solid, tapered mandrel and an internally lubricated steel split sleeve. Application of this technique begins by positioning the sleeve over the mandrel and inserting the mandrel into the hole. The hole is then expanded as the mandrel is drawn back through the sleeve. The expanded sleeve remains in the hole and can be discarded. It should be noted that it is common practice to remove existing damage by reaming and/or drilling the inside of the fastener hole (Leon 1998).

C.1.3.2   Crack-Stop Holes

Current methods used to determine the size of crack-stop holes needed to prevent crack reinitiation are based on linear-elastic fracture-mechanic theory (Barsom and Rolfe 1999). Analytical methods involving linear-elastic fracture mechanics are based on the procedure that relates magnitude of the stress-field near the tip of a crack to nominal applied stress, as described by Equation C.1

$$\sigma_{max} = k_t \sigma_{nom} \hspace{3cm} \textbf{Equation C.1}$$

Parameters that affect the magnitude of the stress amplification factor, k_t, are: size, shape, and orientation of the crack or crack-like imperfections. The elastic-stress field at the edge of an imperfection, as described in Equation C.2, is derived under the assumption that the shape of the imperfection is either elliptical or hyperbolic (see Figure C.2) and the nominal applied stress is normal to the plane of the imperfection.
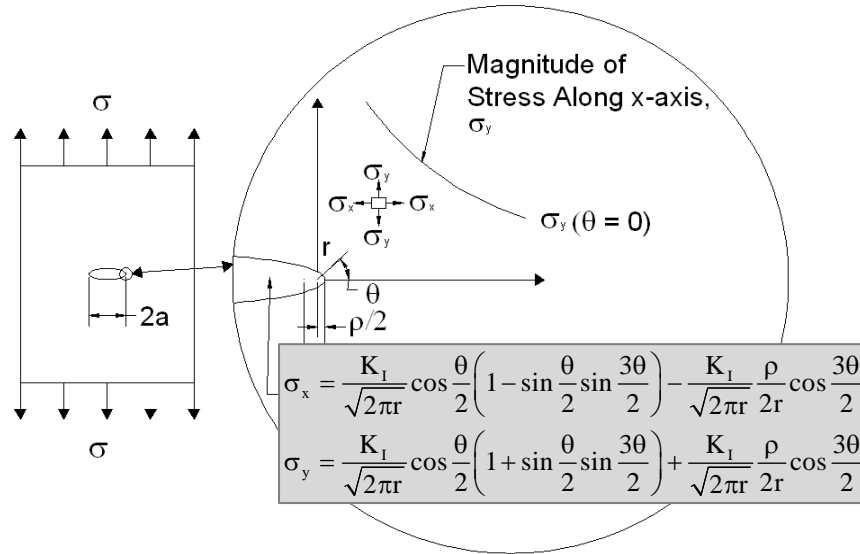
Figure C.2: Schematic representation of elastic-stress field distribution near the tip of an elliptical crack

$$\Delta\sigma_{max} = \frac{2\Delta K_I}{\sqrt{\pi\rho}}$$
<div align="right">**Equation C.2**</div>

In Equation C.2, the stress intensity factor, ΔK_I, is determined assuming a zero radius crack tip and an initial crack length, $a = a_o + \rho$, where ρ is the radius of the hole.

From Equation C.2, it is observed that both ΔK_I and the square root of the radius of the notch tip, $\sqrt{\rho}$, have an effect on the magnitude of maximum stress at the edge of the notch. Equation C.2, which is valid for relatively sharp notches, is only exact when the notch tip radius is equal to zero. However, finite element analyses have shown that Equation C.2 provides a fairly accurate relationship for imperfections with notch tip radii small compared with the crack length, $2a$ (Creager 1966). The theoretical relationship between terms $(\Delta K_I/\sqrt{\rho})$ and maximum stress, $\Delta\sigma_{max}$, led to further laboratory investigation to study its significance to fatigue crack initiation life. Thus, through basic fracture mechanic theory and extensive laboratory testing, Equation C.3 was derived in (Barsom and Rolfe 1999), and can be used for determining the minimum crack-stop hole radii needed to prevent crack reinitiation in steel bridges:

$$\rho = \left(\frac{\Delta K_{total}}{10\sqrt{\sigma_{ys}}} \right)^2 \qquad \text{Equation C.3}$$

As an illustrative example of how Equation C.3 may be used in a practical application is presented in the following. A fatigue crack is found during an inspection in the web of a bridge girder, near the top flange. The crack runs longitudinal to the girder, as shown in Figure C.3, and is 216 mm (8.50 in.) long, offset 12.7 mm (0.50 in.) from the top flange. Therefore, there is sufficient space for a crack-stop hole with an approximate diameter of 25.4 mm (1.0 in).
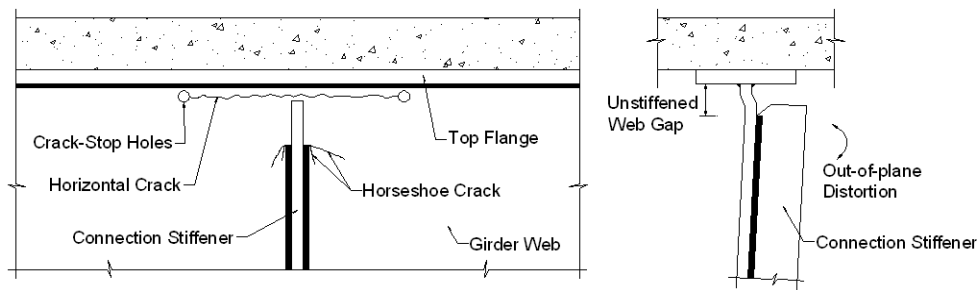
Figure C.3: Fatigue crack caused with drilled crack stop holes in steel bridge girder

For the fatigue crack scenario presented, the steel in the girder web is Gr. A36 with a yield strength under static loading, $\sigma_{ys} = 248$ MPa (36.0 ksi). For the 216 mm (8.50 in.) length crack, the stress intensity factor, ΔK_{total}, can be determined as follows (note that the following calculations are provided in US standard units as Equation C.3 is not dimensionally independent):

$$\Delta K_{total} = \Delta\sigma\sqrt{\pi\alpha} \qquad \text{Equation C.4}$$

$$\Delta K_{total} = \left(26.0^{ksi}\right)\sqrt{\left(\pi\right)\left(\frac{8.50^{in.}}{2}\right)} = 95.0 ksi\sqrt{in.}$$

The value of 179 MPa (26.0 ksi) assumed for the nominally applied stress was taken from previous finite element studies (Roddis and Zhao 2003; Zhao and Roddis 2007) which quantified the nominal stress demand at web gaps of details similar to that shown in Figure C.3. The

required radius to prevent further crack propagation can then be directly solved for from Equation C.3:

$$\rho = \left(\frac{95.0^{ksi\sqrt{in.}}}{10\sqrt{36.0^{ksi}}} \right)^2 = 2.51in.$$

Therefore, the required crack-stop hole diameter for the 216 mm (8.50 in.) long crack is approximately 127 mm (5.00 in). For this crack length, there is not enough space to install a properly-sized crack-stop hole, and even if there was, the 127 mm (5.00 in.) diameter seems excessive. Given the dimensional constraints the hole would have to be undersized. The 25.4 mm (1.00 in.) diameter hole could serve as a temporary aid to retard the crack from propagating. However, eventually the fatigue crack would reinitiate and propagate away from the edge of the undersized hole until eventual failure of the structural member or additional repair. This situation is often typical for crack-stop hole design scenarios, where the hole diameter needed to completely prevent crack reinitiation is simply too large to be practically implemented.

C.1.4 Objective

The objective of this study was to explore the potential for inducing residual compressive stresses in undersized, drilled crack stop holes to extend the fatigue life of steel bridges. The residual stresses are induced through use of a PICK tool. A significant body of work with cold expansion has been developed in the aerospace field over the past three decades, and one of the goals of this paper was to provide a meaningful link between existing technologies developed for application in the aerospace industry and practical needs within the steel bridge industry.

C.1.5 Development of Pick Tool

A proof-of-concept prototype tool was developed for the laboratory, which utilized ultrasonic piezoelectric actuators. The PICK tool was used to treat Gr. A36 steel fatigue specimens, which consisted of a 3.18 mm (0.125 in.) thick x 760 mm (30.0in.) long plate fabricated with varying width. The minimum width of the cross section was 31.7 mm (1.25 in.), at the center of the plate. A 3.18 mm (0.125 in.) diameter hole was precisely drilled at the center of the specimen and an aluminum plug pressed into the hole. The PICK tool utilizes piezoelectric

actuators, which deform proportionally to a harmonic electric signal, inducing a harmonic load large enough to plastically deform the aluminum plug inside the hole, causing the hole to expand. After the hole was plastically expanded, the plug was carefully removed from the hole exploiting the thermal mismatch between steel and aluminum.

The PICK device was powered by a signal generator supplying a sine wave and an amplifier circuit. A strip of piezoelectric material was attached to the rear of the tool to measure the acceleration response of the tool. A strain gage was attached to the inside surface of the vertical element of the PICK tool to measure the strain induced by tightening the bolt and from the sine wave excitation. A calibration curve was developed to establish a relationship between the load applied to the aluminum plug and the strain measured on the PICK tool. This allowed the load imparted from the transducers during application to be directly evaluated. Figure C.4 shows the PICK tool and a steel specimen being treated.
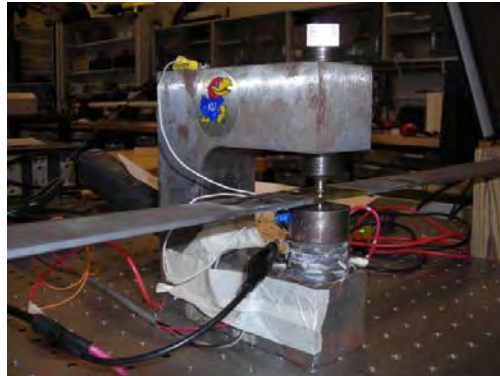
Figure C.4: Photograph showing PICK tool being used to treat a crack stop hole in a steel fatigue specimen

The aluminum plug used as expansion media within the crack-stop hole was 3.18 mm (0.125 in.) tall x 3.18 mm (0.125 in.) diameter 6061-T6 aluminum with 276 MPa (40.0 ksi) nominal yield strength. In operation, the plug was pressed into the specimen and the integral bolt tightened on the PICK device until the load was large enough to cause yielding of the aluminum plug. Because the amount of strain energy in the steel is proportional to the strain, a frequency sweep was performed until the measured strain was maximized, at a frequency corresponding to a natural frequency of the PICK device. Operating the tool at this frequency maximizes the distortional energy applied to the steel specimen being treated. Typically, the frequency ranged

between 30 – 34 kHz (outside the audible range) and the strain ranged between approximately 220 με and 320 με. The strain values corresponded to loads of 9.56 kN (2.15) kips and 13.9 kN (3.12 kips) on the aluminum plug.

The effect of the deformation on the inside of the hole was evaluated analytically, and compared with results from 2-D and 3-D finite element analyses that examined the performance of uniformly-expanded crack stop holes. The 2-D and 3-D uniform expansion finite element analyses were validated through comparison with similar uniform expansion models performed on aluminum plates, reported in aerospace engineering literature and replicated in this study to serve as a basis for comparison. It should be noted that an ongoing experimental thrust aimed at evaluating the fatigue performance of PICK-treated crack-stop holes is not described in this article. This article has focused instead on the feasibility of achieving sufficient residual stresses and the characteristics of the necessary expansion to have a beneficial effect on fatigue life of steel bridges.

C.1.6 Methodology

C.1.6.1 Analytical Approach

C.1.6.1.1 Closed-Form Solutions

Previous analytical investigations of cold expansion (Roddis and Zhao 2003; Zhao and Roddis 2007; Pavier et al. 1999; Zhang et al. 2005; Leon 1998) have been based largely on two-dimensional approximations. These closed-formed solutions have been applied to both the plain-strain condition of the thick-walled cylinder and the plain-stress condition of holes in infinitely wide plates. These analytical simplifications used both Tresca and von Mises yield criterion with assumptions of either elastic-perfectly-plastic or strain-hardening material properties. An extensive review of these closed-form solution techniques has been performed (Ball and Lowry 1998).

Each method reported attempted to quantify and characterize the level of residual stress that could be achieved through cold expansion. Each method of analysis was consistent in showing that a level of residual compressive stress approximately equal to the yield strength of the material could be achieved in the tangential direction near the edge of a hole. These methods have also shown that the residual compressive stresses decay rapidly in the radial direction and

ultimately change to tensile stresses at a point referred to as the elastic-plastic boundary, r_p. From these studies, the maximum r_p is shown to occur at approximately one hole diameter away from the hole edge and has been shown to be a function of the varying levels of expansion.

C.1.6.1.2 Uniform Expansion of Crack-Stop Holes

A significant body of literature exists describing numerical simulation studies that have been performed with the intent of comparing uniform levels of expansion with existing cold expansion techniques. Most of these studies have simulated the process of split sleeve mandrel cold expansion in aluminum plates, a common application in the aerospace field. For the study described in this article, a similar analysis approach was used to compare uniform expansion of mild steel with expansion created using the PICK tool technique.

The material properties of the aluminum and mild steel uniform expansion models are shown in Table C.1. Values reported for the mild steel are from tensile tests performed as part of this study, while the values used for aluminum are from the existing body of literature.

Table C.1: Material Properties Used for Models Simulating Uniform Expansion

Material	Modulus of Elasticity, MPa (ksi)	Yield Strength, MPa (ksi)	Ultimate Strength, MPa (ksi)	Poisson's Ratio
Aluminum	77,220 (11,200)	312 (45.2)	440 (63.8)	0.35
Mild Steel	200,000 (29,000)	319 (46.3)	463 (67.2)	0.30

Abaqus, a general-purpose finite element program capable of nonlinear, large-deflection, plastic analysis, was used as the analytical engine. The first task was to create a 2-D model in Abaqus with aluminum material properties, with the purpose of corroborating results with those from published studies. After results from the 2-D aluminum model were confirmed, a similar 2-D model was created using material properties for mild steel as determined from standard tension tests.

Previous research has shown that an optimum level of cold expansion of a fastener hole using presently-accepted cold expansion techniques is approximately 4% larger than the original hole size (Herman and Ozdemir 1999; Poussard et al. 1995; Ozelton and Coyle 1986). The general equation governing the degree of expansion, i, is:

$$i = \frac{D_E - D_0}{D_0} \times 100\%$$
<div align="right">**Equation C.5**</div>

where D_e is equal to the hole diameter after expansion has occurred, and D_0 is hole diameter prior to expansion. This optimum level of expansion, 4%, is the level at which minimal additional benefit is gained with increased levels of expansion. 2-D mild steel and aluminum models created for this study examined four uniform levels of expansion: 3%, 4%, 5% and 6%.

The uniform expansion Abaqus models were created using a two-step process. To obtain the desired level of uniform expansion in each of the four 2D models, an outward displacement was induced and the inside of the hole was expanded to the levels described previously. Then, the uniform displacement was removed, and a permanently deformed surface with residual stresses remained.

After general behavior was confirmed for the 2-D models, four 3-D models were created to analyze the change in residual stress through the thickness of the specimens under uniform expansion using the same levels of expansion as studied in the 2-D models. The 3-D models were created to have the exact same dimensions and thickness of the 3.18 mm (0.125 in.) thick mild steel fatigue specimens used in axial fatigue tests. Figure C.5 (a) shows the mesh geometry in the 3D models, as well the residual stress field around a hole in mild steel plate after 6% uniform expansion.

C.1.6.1.3   Plug-Plate-Tool Interaction Model

A 3-D finite element (FE) model was created to examine the plug-plate-tool interaction behavior specific to the PICK method of treatment. The model required the large-displacement, nonlinear, plastic-material capabilities of Abaqus to perform the analysis and included the aluminum plug and a 50.8 mm (2.00 in) length of the plate. Material properties used were from tension tests of the Gr. A36 plate and from published typical curves (Boyer 1987). Load was applied as a non-following surface traction to the top and bottom of the plug, and the plate was simply constrained in all directions at discrete locations along the edges. Eight-node, 3-D, hybrid continuum elements with incompatible modes were used in all plug and plate parts. The surfaces

between the plug and the plate were modeled as frictionless contact surfaces. To achieve convergence of the highly nonlinear analysis, automatic stabilization was included in all steps by specifying a dissipated energy fraction of 0.004.

The analysis was performed through a series of steps, first loading the plug on its exposed surfaces so that it expanded inside the plate. The restart feature in Abaqus allowed the converged configuration to become the new base model for the step to remove the plug. In this step, the plug was removed by specifying a linear displacement of both top and bottom surfaces of the plug. After the plug was removed, residual stresses were examined. Figure C.5 (b) shows the permanently deformed shapes of the crack-stop hole and plug.

(a)   (b)
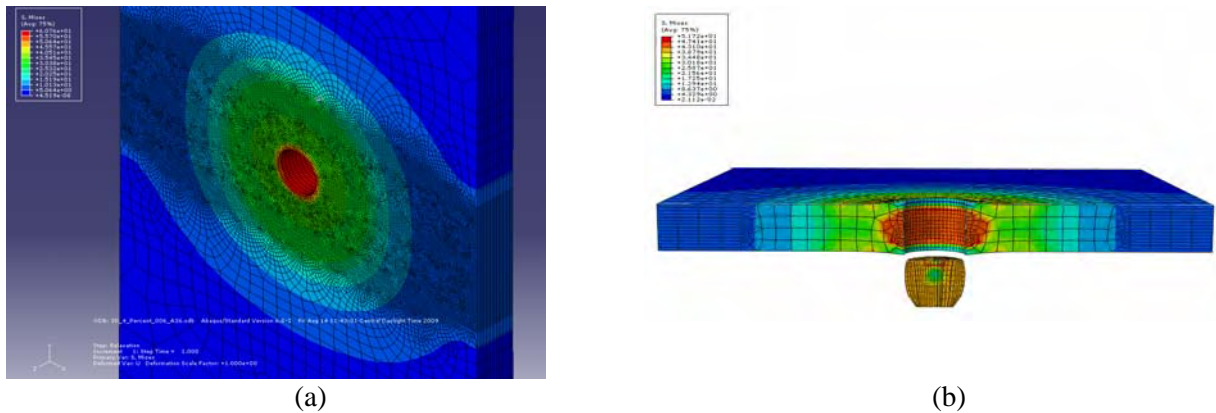
Figure C.5: Screenshots
From (a) 3D modeling of uniform expansion and resulting residual stresses in a crack-stop hole; (b) Cross-section view of plug-plate-tool interaction model showing residual stresses after the plug was loaded and removed

C.1.7 Results and Discussion

C.1.7.1   Finite Element Modeling Results

C.1.7.1.1   Uniform Expansion of Crack-Stop Holes

The results for the 2-D aluminum models were comparable in both shape and magnitude with previously published finite element studies (Herman and Ozdemir 1999; de Matos et al. 2005). The level of tangential residual stress was shown to be approximately equal to the yield strength of the material and the transition between compressive to tensile stresses was shown to occur at approximately the diameter of the hole away from the edge of the hole.

There was a slight difference between the 2-D mild steel and aluminum model results in the shape of the residual tangential stress fields, as highlighted in Figure C.6. Results for the 2-D mild steel model showed a slight discontinuity in the curve after the level of residual stress reached a value approximately equal to the yield strength, which was not observed with the aluminum models. This difference is thought mostly to be a result of the yield plateau implemented in the mild steel model. Tangential residual stresses induced by 3%, 4%, 5%, and 6% expansion in the 3-D mild steel model are presented in Figure C.7.

------ Aluminum 2-D Model   — — Mild Steel 2-D Model
——— Mild Steel 3-D Model (mid-thickness)
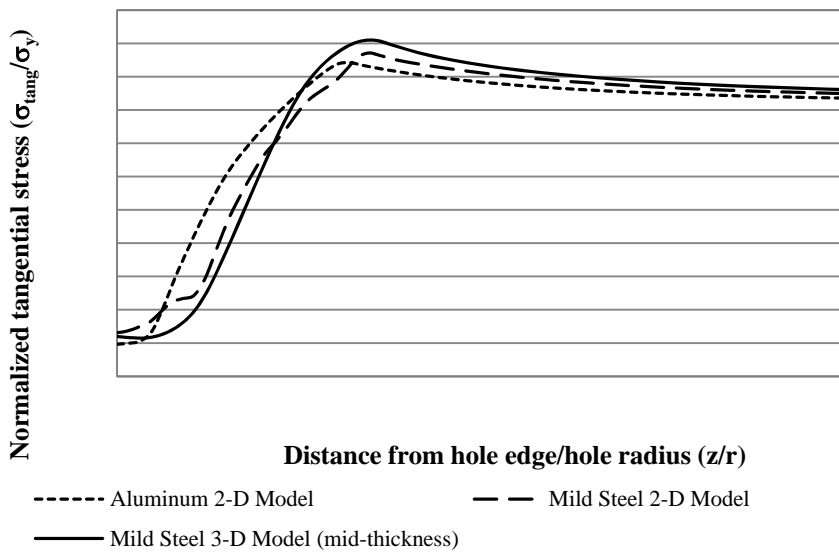
Figure C.6: Tangential residual stress normalized with respect to material yield strength comparing model results for aluminum and mild steel at 4% uniform expansion
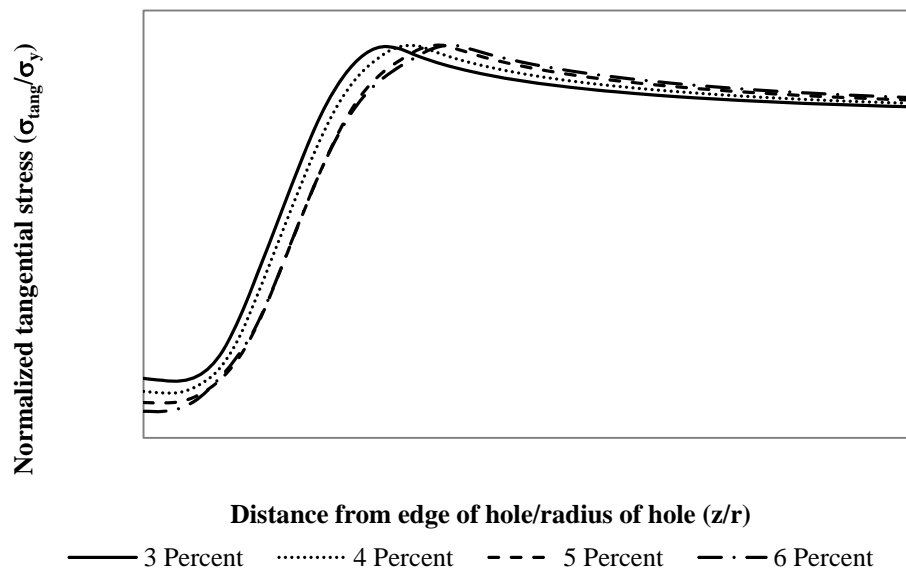
Figure C.7: Tangential residual compressive stress fields resulting from uniform expansion mild steel 3-D models

The 3-D model for a uniform 4% expansion in a 3.18 mm (0.125 in.) thick mild steel plate displayed similar results to the 2-D mild steel models at mid-thickness of the plate, as can be noted in Figure C.8. However, the level of tangential residual stress achieved at mid-thickness, -437 MPa (-63.4 ksi), was greater than that found at the edges of the plate, -370 MPa (-53.7 ksi). This finding was consistent with results from previous studies (Herman and Ozdemir 1999; de Matos et al. 2005). The higher level of tangential stress found at mid-thickness was thought to be a result of the constraint provided by the thickness of the plate.

C.1.7.1.2   Plug-Plate-Tool Interaction Model

FE analyses of the plug-plate-tool model showed that the PICK device deformed the aluminum plug well into the plastic range causing the plug to develop a barrel shape. As the top and bottom of the plug were compressed, the top and bottom surfaces of the plug deformed inside the corresponding surfaces of the plate, losing contact with the edges of the hole. This resulted in non-uniform expansion of the inner surface of the crack-stop hole. In addition, the analyses also showed that the inside of the hole was expanded well into the plastic range, although not uniformly.

Residual tangential stresses on the inside of the hole in the uniform expansion model were found to vary uniformly through the plate thickness, however, the 3-D plug-plate-tool

285

model showed that the residual tangential stresses were in tension at the surfaces (90 MPa [13 ksi]) and compressive (-270 MPa to -349 MPa [-41.0 ksi to -53.0 ksi]) through the center as a result of the deflected shape of the plug, as detailed in Figure C.9.
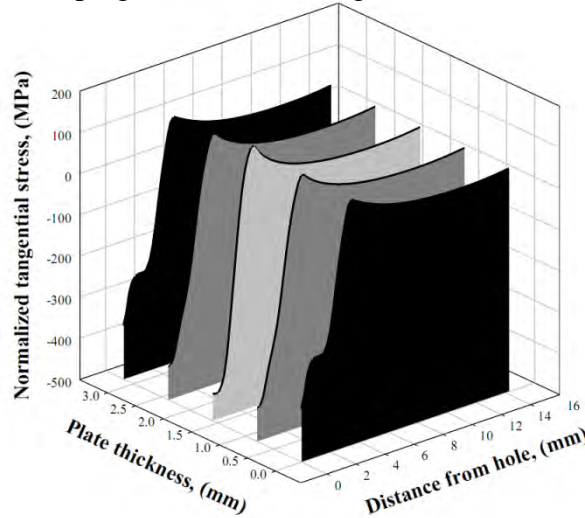
Figure C.8: Through-thickness residual stress distribution 3-D model with uniform 4% expansion
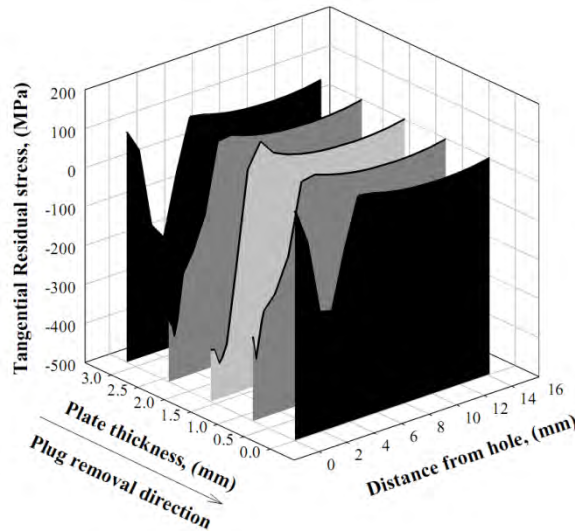
Figure C.9: Through-thickness residual stress distribution 3-D plug-plate-tool interaction model

The expansion from the 3-D plug-plate-tool model analyses was found to be in agreement with the measured expansion for the treated specimen; in the center of the hole, the model and physical measurements both showed approximately 7% expansion. The analyses showed that the maximum expansion was similar to that required to obtain maximum benefit for an undersized

hole. However, the analyses also highlighted that the expansion at the plate surfaces was less than that at the center. The measured expansion at the plate surfaces was found to be much less than that needed to significantly improve the fatigue performance of an undersized hole. The difference between the analyses and the measured expansion was likely due to difficulties in perfectly aligning the tool with the plug, and indicates that further refinement of the tool geometry is necessary. Figure C.10 presents the amount of expansion determined numerically through the thickness of the plug, as well as measured expansion amounts at top, mid-thickness, and bottom of a treated crack stop hole.
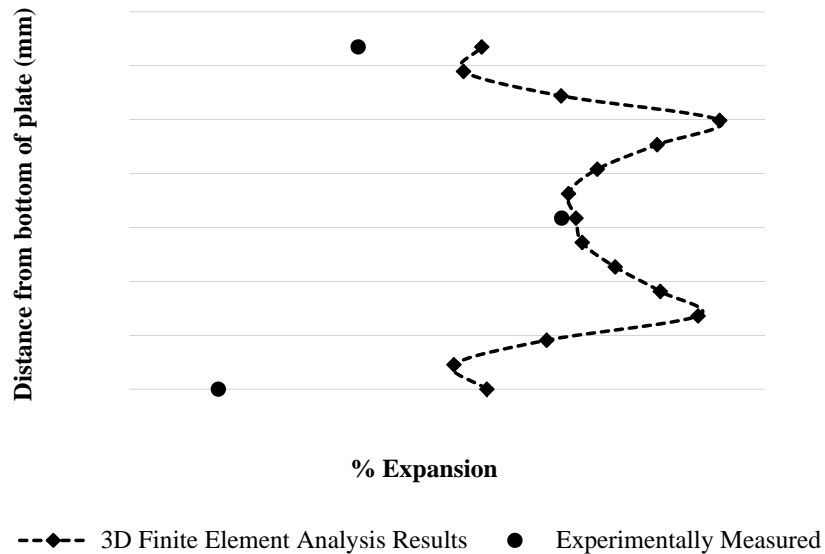
Figure C.10: Percent expansion from finite element analysis compared to measured expansion at top, bottom, and mid-depth of treated crack-stop hole

C.1.8 Conclusions

The results of a study exploring the potential of inducing compressive residual stresses in drilled crack stop holes using an ultrasonic piezoelectric transducer has led to the following conclusions:

- A 4% expansion of crack stop holes in steel plates was found to have a very similar effect to that observed in aluminum plates. This conclusion is based on the similarity of normalized tangential residual stress for both materials. This was an important finding, because it helps to provide a meaningful link between existing research performed in the aerospace

287

engineering literature and current needs within the field of bridge engineering. Results from the 2-D and 3-D uniform expansion modeling can be interpreted to be independent from the particular technique chosen to cold-expand undersized crack stop holes, and can be used in future studies to corroborate detailed finite element analyses and experimental findings for specific techniques applicable to steel bridges.

- It has previously been shown that the levels of residual stress corresponding to 4% expansion of crack stop holes in aluminum have been sufficient to improve the fatigue performance of fatigue specimens by an order of magnitude. Because of the general overall similarity in behavior of metals subjected to fatigue loading, it is expected that steel specimens will respond similarly to aluminum when crack-stop holes are treated with 4% or more expansion. Therefore, based on the results of this study, it is concluded that significant gains in fatigue capacity may be realized in mild steel when expansion on the order of 4% or more is achieved in crack stop holes.

- Finite element analyses and physical measurements of treated specimens showed that the prototype PICK device was capable of expanding an undersized, 3.18 mm (0.125 in.) diameter crack stop hole in 3.18 mm (0.125 in.) thick plate between 5% and 9% at the interior of the hole. These levels of expansion in the steel plates modeled are similar to or greater than levels of expansion noted in identical models performed on aluminum plates.

- Detailed 3D Plug-Plate-Tool interaction numerical analyses showed that tensile residual stresses were imparted in the treated crack stop hole at the outer faces of the hole. This was an important finding, because it represents a need to refine the treatment process such that more uniform compressive residual stresses result from treatment. It is also important because great care was taken in the physical development of this technique to produce uniform compressive stresses in the crack-stop hole; therefore, detailed analyses should be performed on all new techniques that may be developed in the future to perform a similar task to ensure that undesirable consequences are not being realized.

- Although the crack-stop hole examined was "bench-sized," results of this study lend confidence to the ability of the device to be scaled up to treat

288

thicker plate material and larger diameter crack-stop holes, and lend credence to the plug-plate interaction treatment approach chosen.

The technique of cold expansion of holes in metallic structures has already been proven as a highly effective retrofitting technique in the aerospace industry. A suite of 2D and 3D uniform expansion and detailed 3D Plug-Plate-Tool interaction numerical analyses have shown that a new treatment technique was capable of inducing normalized compressive residual stresses of the same order of magnitude in steel structures as those achievable with current techniques used on aluminum structures. Additionally, 2D and 3D uniform expansion models performed as part of this study may be useful to future researchers attempting to achieve compressive residual stresses in steel crack-stop holes using new treatment techniques. Given the success of this technique in the aerospace industry, the potential benefits of using a similar process to improve the fatigue life of existing steel bridges with fatigue cracks are very significant.

C.1.9 References

Ball, D. and Lowry, D. R. (1998). "Experimental Investigation on the Effects of Cold Expansion of Fastener Holes." Fatigue & Fracture of Engineering Materials & Structures, 21(1), 17-34.

Barsom, J. M. and Rolfe, S. T. (1999). Fracture and Fatigue Control in Structures: Applications of Fracture Mechanics. 3rd ed. ASTM, West Conshohocken, PA.

Boyer, H. E. (1987). Atlas of Stress-Strain Curves. ASM International, Metals Park, OH.

Brown, J. D., Lubitz, D. J., Cekov, Y. C., Frank, K. H., and Keating, P. B. (2007). Evaluation of Influence of Hole Making Upon the Performance of Structural Steel Plates and Connections. CTR Technical Report 0-4624-1. Center for Transportation Research, University of Texas at Austin.

Creager, M. (1966). The Elastic Stress Field Near the Tip of a Blunt Crack. (Master's thesis). Lehigh University, Bethlehem, PA.

de Matos, P. F. P., McEvily, A. J., Moreira, P. M. G. P., and de Castro, P. M. S. T. (2007). "Analysis of the Effect of Cold-Working of Rivet Holes on the Fatigue Life of an Aluminum Alloy." International Journal of Fatigue, 29(3), 575-586.

de Matos, P. F. P., Moreira, P. M. G. P., Camanho, P. P., and de Castro, P. M. S. T. (2005). "Numerical Simulation of Cold Working of Rivet Holes." Finite Elements in Analysis and Design, 41(9-10), 989-1007.

Domazet, Z. (1996). "Comparison of Fatigue Crack Retardation Methods." Engineering Failure Analysis, 3(2), 137-147.

Forgues, S. A., Bernard, M. and Bui-Quoc, T. (1993). "3-d Axisymmetric Numerical Analysis and Experimental Study of the Fastener Hole Coldworking Process." In C. A. Brebbia and M. H. Aliabadi (Eds.), Computer Methods and Experimental Measurements for

Surface Treatment Effects Engineering Sciences. 61-70. Computational Mechanics Publications, Southampton, England.

Ghfiri, R., Amrouche, A., Imad, A., and Mesmacque, G. (2000). "Fatigue Life Estimation After Crack Repair in 6005 A-T6 Aluminum Alloy Using the Cold Expansion Hole Technique." Fatigue & Fracture of Engineering Materials & Structures, 23(11), 911-916.

Herman, R. and Ozdemir, A. T. (1999). "Effect of Expansion Techniques and Plate Thickness on Near-Hole Residual Stresses and Fatigue Life of Cold Expanded Holes." Journal of Material Science, 34, 1243-1252.

Hu, Y., Shield, C. K. and Dexter, R. J. (2005). "Use of Adhesives to Retrofit Out-of-Plane Distortion at Connection Plates." 6th International Bridge Engineering Conference, Transportation Research Record CD 11-S, 419-427. Transportation Research Board, National Research Council, Washington, D.C.

Huhn, H. and Valtinat, G. (2004). "Bolted Connections with Hot Dipped Galvanized Steel Members with Punched Holes." Proceedings of the ECCS/AISC Workshop, Connections in Steel Structures V: Innovative Steel Connections, June 3-5, 2004, Amsterdam. European Convention for Construction Steelwork and American Institute of Steel Construction.

Landy, M. A., Armen, H., Jr., and Eidinoff, H. L. (1986). "Enhanced Stop-Drill Repair Procedure for Cracked Structures." In J. M. Potter (Ed.), Fatigue in Mechanically Fastened Composite and Metallic Joints, ASTM Special Technical Publication 927, 190-220. ASTM, Philadelphia, PA.

Leon, A. (1998). "Benefits of Split Mandrel Coldworking." International Journal of Fatigue, 20(1), 1-8.

Ozelton, M. W. and Coyle, T. G. (1986). "Fatigue Life Improvement by Cold Working Fastener Holes in 7050 Aluminum." In J. M. Potter (Ed.), Fatigue in Mechanically Fastened Composite and Metallic Joints, ASTM Special Technical Publication 927, 53-71. ASTM, Philadelphia, PA.

Pavier, M. J., Poussard, C. G. C., and Smith, D. J. (1999). "Effect of Residual Stress Around Cold Worked Holes on Fracture Under Superimposed Mechanical Load." Engineering Fracture Mechanics, 63(6), 751-773.

Phillips, J. L. (1974). Sleeve Cold Working Fastener Holes, Vol. 1. AFML-TR-74-10. Air Force Materials Laboratory, Wright-Patterson AFB, OH.

Poolsuk, Saravut. (1977). Measurement of the Elastic-Plastic Boundary Around Coldworked Fastener Holes. (Ph.D. dissertation). Michigan State University, East Lansing, MI.

Poussard, C., Pavier, M. J. and Smith, D. J. (1995). "Analytical and Finite Element Predictions of Residual Stresses in Cold Worked Fastener Holes." Journal of Strain Analysis for Engineering Design, 30(4), 291-304.

Poussard, C. G. C., Pavier, M. J. and Smith, D. J. (1994). "Prediction of Residual Stresses in Cold Worked Fastener Holes Using the Finite Element Method." Proceedings of the 2nd

Biennial European Joint Conference on Engineering Systems Design and Analysis, 8(A), 47-53. ASME, New York, NY.

Reemsnyder, H. S. (1975). "Fatigue Life Extension of Riveted Connections." Journal of the Structural Division, 101(12), 2591-2608. American Society of Civil Engineers, New York, NY.

Roddis, W. M. K. and Zhao, Y. (2003). "Finite-Element Analysis of Steel Bridge Distortion-Induced Fatigue." Journal of Bridge Engineering, 8(5), 259-266.

Shin, C. S., Song, P. S., and Wang, C. M. (1996). "Fatigue Damage Repair: a Comparison of Some Possible Methods." International Journal of Fatigue, 18(8), 535-546.

Statnikov, E. S. (2004). "Physics and Mechanism of Ultrasonic Impact Treatment." IIW Document XIII-2004-04. International Institute of Welding, Paris, France.

Vulić, N., Jecić, S., and Grubišić, V. (1997). "Validation of Crack Arrest Technique by Numerical Modeling." International Journal of Fatigue, 19(4), 283-291.

Zhang, Y., Fitzpatrick, M. E., and Edwards, L. (2005). "Analysis of the Residual Stress Around a Cold-Expanded Fastener Hole in a Finite Plate." Strain, 41(2), 59-70.

Zhao, Y. and Roddis, W. M. K. (2007). "Fatigue Behavior and Retrofit Investigation of Distortion-Induced Web Gap Cracking." Journal of Bridge Engineering, 12(6), 737-745.

C.2: Improving the Fatigue Performance of Drilled Holes in Steel Bridges through Use of Mechanical Treatments

G. G. Simmons[7]

Caroline R. Bennett[8]

Adolfo B. Matamoros[9]

Ron Barrett-Gonzalez[10]

Stanley T. Rolfe[11]

C.2.1 Abstract

A proof-of-concept study was performed to determine the effectiveness of two mechanical techniques for improving fatigue life of drilled holes in steel bridges. The treatments studied were cold-expansion of drilled holes and a newly-developed technique termed "Piezoelectric Impact Compressive Kinetics," or PICK treatment. The study involved testing 15 fatigue specimens, examining levels of retained expansion in 16 specimens, a metallurgical investigation to compare grain sizes in treated and untreated specimens, and neutron diffraction measurements of residual strain.

It was found that both cold-expansion and PICK-treatment of drilled holes were effective in extending fatigue initiation life beyond that measured for untreated specimens. Deformation measurements showed that both techniques were capable of producing enough permanent retained expansion (*RE*) to improve fatigue life. PICK-treated specimens exhibited greater fatigue lives and higher *RE* values than specimens subjected to cold-expansion only.

---

[7] Gary G. Simmons, PhD, PE, University of Kansas, 1530 W. 15th St., Lawrence, KS 66045

[8] Caroline R. Bennett, PhD, PE, Associate Professor, University of Kansas, 1530 W. 15th St., Lawrence, KS 66045

[9] Adolfo B. Matamoros, PhD, Professor, University of Kansas, 1530 W. 15th St., Lawrence, KS 66045

[10] Ron Barrett-Gonzalez, PhD, Associate Professor, University of Kansas, 1530 W. 15th St., Lawrence, KS 66045

[11] Stanley T. Rolfe, PhD, PE, A.P. Learned Distinguished Professor, University of Kansas, 1530 W. 15th St., Lawrence, KS 66045

C.2.2 Introduction

There are approximately 120,000 steel bridges in the highway bridge inventory in the United States, many of which are susceptible to high-cycle fatigue damage caused by truck traffic. Due to the potential hazard this type of damage presents to the driving public, it is a major driver of expenses related to inspection, maintenance, and repair of steel bridges. High-cycle fatigue cracks usually form in steel bridge connections, in areas of high stress demand caused by geometric discontinuities. The driving force causing the cracks may be either in-plane or out-of-plane with respect to the main axis of the structural member.

The high-cycle fatigue problem is approached from very different perspectives depending on whether the potential for damage is in a new or an existing bridge structure. Current design specifications (AASHTO 2013) are intended to prevent fatigue damage under present-day truck loads for a 75-year design life. Although there are well-known connection details that can be used to achieve that design goal, identifying new methods for improving the fatigue performance of structural connections in new bridges is still a desirable goal if those methods are more economical or can be used to extend the design life beyond the 75-year design objective. Service loads continue to increase across the national highway network, and there is great interest amongst bridge owners of achieving service lives of 100 years and beyond. Satisfactory performance of bridges under these larger demands is not a guarantee under the current design specifications for fatigue.

One of the most commonly used details in steel bridge girders is a drilled or punched hole. Holes are ubiquitous due to the common use of bolted connections in bridge structures. Admittedly, drilled holes are not highly susceptible to in-plane fatigue loading, and are generally classified as AASHTO Category B details. Punched holes are assigned a lesser fatigue category to reflect greater imperfections around the hole surface.

Mitigating fatigue damage in existing structures is a much more complex problem because engineers are constrained by the configuration of the bridge. The threat that fatigue cracks pose to the structural integrity of the bridge make this an immediate and pressing problem for bridge owners. Fatigue cracks detected in bridge structures must be closely monitored or repaired. The most common course of action after crack detection is to blunt the crack by drilling

crack-arrest holes at the tips of the crack. This common procedure has the effect of increasing the radius of the crack tip from infinitely small to equaling the radius of the hole, and can greatly reduce the propensity of the crack for propagation. Unfortunately, crack-arrest holes have several limitations as a method to mitigate fatigue damage. The conceptual framework for determining the radius of crack-arrest holes was developed primarily based on cracks in uniaxial tension stress fields in steel plates, and not in the complex multiaxial stress fields associated with connections in steel bridges. Due to these differences there is no well-established method for determining the optimal diameter of crack-arrest holes near steel connections and the potential for crack re-initiation is high. Additionally, if a crack-arrest hole is used as a secondary retrofit measure, and the primary retrofit measure is ineffective in mitigating the fatigue damage, the crack-arrest hole may be insufficient to resist crack initiation on its own. For these stated reasons developing a method to improve the fatigue performance of crack-arrest holes is a useful endeavor.

C.2.2.1 Objective and Scope

The objective of this research was to explore the potential of two different mechanical techniques for improving the fatigue performance of drilled holes in bridge girders. The first treatment technique considered consisted of cold-expansion of the hole, and the second utilized a new technology termed Piezoelectric Induced Compressive Kinetics (PICK). Given the novel nature of the tool developed for implementation of the second technique, the evaluation was carried out through a proof-of-concept experimental investigation. It was hypothesized that both the cold expansion procedure and the PICK technology would result in greater fatigue resistance of holes than the fatigue resistance of untreated holes.

The scope of this study included 15 fatigue tests, in which the fatigue performance of steel specimens with untreated holes, holes treated with cold expansion, and holes treated with the PICK treatment was investigated. This study also included determining levels of retained expansion (*RE*) in 16 fatigue and plate specimens, as well as a metallurgical study to examine the microstructure of treated and untreated fatigue specimens.

The technique developed and investigated to expand and treat the undersized hole has been termed Piezoelectric Induced Compressive Kinetics (referred to as PICK) and, in general, consists of the following steps in the laboratory:

1) Drilling a hole in a fatigue specimen made from steel plate,

2) Driving an oversized aluminum plug into the hole,

3) Compressively loading the aluminum plug to develop plastic deformations in the aluminum plug and in the adjacent steel specimen,

4) Using piezoelectric elements to induce ultrasonic vibrations on the aluminum plug and steel around the hole. This is accomplished by exciting the piezoelectric elements with a high-frequency oscillating voltage, and

5) Removing the aluminum plug from the steel specimen when treatment is completed.

It was hypothesized that this process would produce three separate results which would contribute to prevention of crack reinitiation and propagation. First, the compressive force on the plug during cold-expansion would induce tensile stresses in the circumferential direction around the hole; these tensile stresses would become compressive residual stresses after the plug was removed. Second, computer simulations showed that the cold-expansion would cause work hardening, which would increase both the yield and ultimate strength of the steel. Third, it was anticipated that energy input in the form of ultrasonic vibration from the piezoelectric elements would produce ultrasonic hardening of the steel. This paper focuses on the design, fabrication, and operation of the PICK tool. A description of the PICK treatment process is provided, and the effectiveness of the PICK tool was assessed by examining results from fatigue tests, measured retained expansion, hardness testing, and metallurgical examination.

Experimental research reported upon in this paper is a follow-up to research reported upon in Appendix C.1, which was an analytical proof-of-concept investigation focused entirely on holes which had been cold-expanded.

C.2.3 Background

Mechanical treatment techniques aimed at improving the fatigue performance of holes through cold expansion have been widely-used in the aerospace industry. Two applications of this concept are the use of a split-sleeve mandrel (Fatigue Tech) and the installation of interference fit fasteners (Lanciotti and Polese 2005). These two techniques are discussed separately in the next two paragraphs. Research by Crain et al. (2010) is discussed at the end of this section because it represents a link between applications in the aerospace and civil infrastructure industries.

Mechanical expansion delivered through a split-sleeve mandrel is an accepted technique to reinforce bolt and/or rivet holes in aluminum aircraft members during both manufacturing and maintenance. This technique is used to prevent fatigue cracks from developing or to extend fatigue life in the presence of existing cracks. A literature review did not produce any documented examples in which this technique has been used outside the aircraft industry but, from a personal conversation with L. Reid of Fatigue Technology, mechanical expansion has recently been used on railroad tracks and bridges. This technique is being used by railroads to improve the fatigue performance of the bolt holes in connections joining rail sections and it has been used on one bridge structure, an elevated section of a highway in California. The Fatigue Technology mechanical expansion process utilizes a split-sleeve mandrel system that consists of a solid, tapered mandrel and an internally lubricated split sleeve. The split sleeve is placed on the small end of the tapered mandrel and the mandrel split-sleeve placed in the hole with the large end of the mandrel going in first. An external force is then applied to the small end of the mandrel and the large end of the mandrel is pulled through the split-sleeve, causing the sleeve and hole to expand and plastically deform the inside of the hole in both the radial and tangential directions. The sleeve is then withdrawn. This results in cold-working the inside diameter of the hole and induces residual compressive stresses tangentially and radially around the hole. Both the cold-working and the residual compressive stresses act to retard crack initiation and propagation.

Use of interference fit fasteners is also limited to the aircraft industry, where this type of fastener is applied to improve fatigue performance of drilled holes; their use has not translated to

bridges or other civil structures (Bontillo 2011). Interference fit fasteners consist of a tapered bolt and an internally tapered and flanged outer-sleeve, which is ground straight externally for use in a straight-sided hole. The interference fit is achieved by tightening the bolt, forcing the taper of the bolt to work against the taper of the sleeve. Fatigue tests have shown an increase in fatigue life by a factor of 10 ($1x10^5$ cycles to $1x10^6$ cycles) associated with the use of interference fit fasteners (Lanciotti and Polese 2005).

Given that most investigations involving the fatigue performance of cold-expanded holes fall within the realm of aerospace engineering, Crain et al. (2010) performed a study to investigate the use of these technologies in the steel bridge industry. Crain et al. performed an analytical study comprised of a suite of two-dimensional and three-dimensional nonlinear finite element simulations using the commercially-available software Abaqus. Because most of the pertinent aerospace literature has focused on cold-expansion in aluminum materials, work performed by Crain et al. included a series of simulations utilizing material properties for aluminum. Results from these models were compared with results from similar studies performed on aluminum and reported upon in the aerospace literature. After close agreement was found, Crain et al. performed a suite of similar simulations utilizing material properties for Gr. A36 steel. It was found that a 4% retained expansion of holes in steel plates produced a similar effect to that observed in aluminum under the same level of retained expansion. The authors noted that because it has previously been shown that a 4% retained expansion in holes drilled in aluminum was sufficient to produce an order-of-magnitude increase in fatigue performance, there was sufficient reason to believe that similar retained expansion values would result in similar fatigue performance increases for holes drilled in steel. Crain et al. also demonstrated that PICK technology had the potential to result in retained expansion levels of 5-9% at mid-thickness. It should be noted that the analytical investigation performed by Crain et al. did not account for dynamic effects (work-hardening), only cold-expansion effects.

The research described in the following sections follows the analytical research performed by Crain et al. (2010) with a proof-of-concept experimental investigation examining the performance of two mechanical treatment techniques for drilled holes. The tests were performed on structural steel specimens, further validating the implementation of aerospace

297

technology to civil infrastructure. Additionally, one of the two techniques (PICK technology) utilized dynamic effects in addition to creating a residual stress field induced by cold expansion, a combination that has only been recently developed.

C.2.4 Development of the PICK Tool

C.2.4.1 Experimental Setup

This paper describes a proof-of-concept study that used a reduced-scale, laboratory-compatible PICK tool and fatigue specimens to determine viability of the technique. The PICK tool, specimens, and instrumentation setup are described in the following.

C.2.4.1.1 PICK Tool

The PICK tool was designed to apply a compressive force to an aluminum plug pressed into a drilled hole in a steel specimen. Poisson's effect causes the aluminum plug to expand in the radial direction, expanding the diameter of the hole in the specimen and focusing ultrasonic vibration into the steel specimen. The PICK tool was bench-mounted with its major components being a C-shaped base, a threaded bolt, piezoelectric elements, and a round load-transfer plate. The tool was machined from 4140 annealed steel with yield strength of 412 MPa (60 ksi). The end of the bolt was machined to form a 3.2 mm ($^1/_8$ in.) diameter tip; force was applied to the plug by tightening the bolt at the top of the tool, thereby pressing the tip into the aluminum plug. Underneath the fatigue specimen was a round, load-transfer plate, which was machined to fit on top of a nylon rod and fit tight with the top of the piezoelectric stack beneath it. A hardened steel rod with a tip also machined to a 3.2 mm ($^1/_8$ in.) diameter was pressed into the top of the round load-transfer plate and completed the load path through the aluminum plug. A Micro-Measurements strain gage (EA-06-062AQ-350) and a small strip of piezoelectric material (7.5-mil thick strip of PZT-5A from Piezo Systems) were attached to the PICK tool.

The piezoelectric elements were obtained by disassembling a commercial ultrasonic cleaner; these were assumed to be PZT-4 material, which is the commonly used piezoelectric element in these cleaners. The properties for PZT-4 are shown in Table C.2. Piezoelectric elements have positive and a negative faces. After the positive and negative faces were identified, the four piezoelectric elements were assembled such that direction of current was the same across each element. With the piezoelectric elements stacked in this manner, expansion and

contraction deformations obtained by applying an electric field across the elements were additive in all the elements.

Table C.2: Assumed Properties for Piezoelectric Elements

Electromechanical coupling coefficient - κ	Piezoelectric transfer efficiency - ζ	Activation constant for strain in the 3-direction for current in the 3-direction - d_{33}	Short circuit Young's modulus of piezoelectric material - Y^E_{33}
0.70	0.84	285×10^{-12} m/volt (1.1×10^{-8} in/volt)	6.6×10^{10} N/m^2 (9.6×10^6 psi)

Electronics powering the PICK tool consisted of a sine wave generator and an amplifier. The sine wave generator was a Hewlett Packard 3300A Function Generator with a variable-sweep-frequency capability and adjustable voltage output. The amplifier was a Piezo Systems Inc. Linear Amplifier Model EPA-104 with adjustable gain.

Figure C.11: PICK tool schematic

C.2.5 Test Methodology

C.2.5.1 Fatigue Test Specimens

The testing program consisted of fifteen tensile fatigue specimens fabricated using Gr. A36 steel. The specimens were manufactured using 3.2 mm ($^1/_8$ in.) thick steel bar with a

reduced cross-section at the center, as shown in Figure C.12. A hole with a diameter of 3.2 mm ($^1/_8$ in.) was drilled and reamed at the center of each specimen, at the point of minimum width. The expectation was that cracking would initiate at the location of the hole, and would propagate in a direction perpendicular to the longitudinal axis of the specimen. The ends of the specimen were reinforced to prevent a localized failure in the region where the specimen interfaced with the grips of the testing machine.

The pressure-only and PICK treatments were applied to the specimens through an aluminum plug inserted into the 3.2 mm ($^1/_8$ in.) diameter hole. The aluminum plugs were fabricated from 6061-T6 aluminum dowel stock having a slightly larger diameter than the hole drilled in the steel specimens. Each plug was also cut such that it was slightly longer than the thickness of the steel specimens.

Material properties for the Gr. A36 steel were determined following standard tension testing requirements for flat bars (ASTM E8-04). The Gr. A36 steel exhibited a yield strength of 46.3 ksi (3119 MPa), tensile strength of 67.2 ksi (463 MPa), and a modulus of elasticity approximately equal to 29,000 ksi. Material properties for the 60601-T6 aluminum plug used in computer simulations were adopted from the literature (Boyer 1987). The 6061-T6 Aluminum was assumed to have typical properties for yield strength of 45 ksi (312 MPa), tensile strength of 63.8 ksi (440 MPa), modulus of elasticity of 11,200 ksi (77,220 MPa), and Poisson's ratio of 0.35.
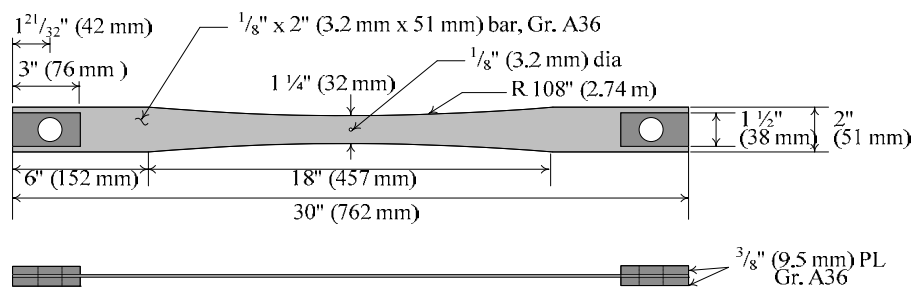
Figure C.12: Fatigue specimen dimensions

C.2.5.2   Specimen Treatment

Two different types of treatment were applied to the specimens used in this study: (1) pressure-only treatment and (2) PICK treatment. In this study, both types of treatment were applied using the PICK tool developed at the University of Kansas, however, it is expected that other techniques could be used to achieve the pressure-only treatment. A description of the PICK tool and the procedures use to apply the pressure-only and PICK treatments to the specimens follows.

The PICK tool was designed to compress the aluminum plug after it was inserted into a pre-drilled hole in the plate, to hold the compressive force on the plug, and to provide a stiff reaction platform to focus ultrasonic vibration into the aluminum plug and steel specimen. The PICK tool was proportioned have a large stiffness to ensure that most of the energy generated during ultrasonic vibration entered the specimen and plug, and was not absorbed by the tool itself. Ultrasonic vibration was induced by a stack of four piezoelectric transducer elements. The PICK tool was bench mounted with its major features being a C-shaped solid steel base, threaded bolt, four piezoelectric elements, and round load-transfer plate. The base and other steel components were machined from 4140 annealed steel with a yield strength of 60 ksi (412 MPa), and are shown in Figure C.13. The PICK tool was designed to accept plate material above the load transfer plate and piezoelectric element stack, and below the tip of the bolt. The hardened steel bolt tip was machined to have a truncated cone shape, with the smaller end matching the surface of the 3.2 mm ($^1/_8$ in.) diameter aluminum plug. Underneath the fatigue specimen there was a round load-transfer plate, which was machined to fit on top of a nylon rod and fit tight with the top of the stack of piezoelectric elements beneath it; the nylon rod also held the piezoelectric elements in place. A hardened steel rod with a tip also machined to a dimension of 3.2 mm ($^1/_8$ in.) was pressed into the top of the round load-transfer plate and completed the load path through the aluminum plug. Forces generated when the piezoelectric elements were powered with an amplified sine wave were transferred through the round load-transfer plate and into the aluminum plug. Further details regarding the design and functionality of the PICK tool are reported by Simmons (2013) and Simmons et al. (2013).

Figure C.13: PICK tool being used to treat a steel tensile fatigue specimen

Before using the PICK tool to treat fatigue specimens, a strain gage was attached to the surface of the PICK tool and calibrated with a load cell to establish a load versus strain relationship (Simmons 2013); this calibration provided a relationship to calculate the load applied to the aluminum plug based on strain measurements on the PICK tool itself.

In preparing fatigue specimens for treatment, an area approximately 51 mm (2 in.) long and centered on the fatigue specimen was cleaned of mill scale. Next, dimensional measurements were taken for the specimen using digital calipers, including the width and thickness at the center of the hole as well as the hole diameter. The alignment of the PICK tool was adjusted such that the tips of the bolt and the round load-transfer plate were aligned with the hole in the fatigue specimen. Next, the aluminum plug was pressed into the hole.

For specimens that were treated with pressure-only, the following procedure was used. (1) The specimen was placed in the PICK tool, the alignment was checked, and the bolt was tightened carefully to ensure the tips aligned with the plug. (2) After suitable alignment was achieved, the bolt was tightened until a value of 224 microstrain was measured with the strain gage. According to the calibration curve, this equated to a force of 2.1 kips (9.2 kN), which was large enough to deform the aluminum plug beyond the elastic range. (3) The force on the aluminum plug was maintained for a duration of 114.5 hours without readjustment to the bolt. This arbitrary duration was adopted and used consistently throughout the testing program to maintain an objective basis for comparing results.(4) Next, the aluminum plug was gently pressed out of the specimen. After treatment was completed, the dimensions of the hole were measured along 10 different diametric locations using a caliper.

Specimens that were treated with the PICK technology also followed steps (1) and (2) as described for the pressure-only treatment. The following additional steps were taken for specimens treated with the PICK technology. (3) After the bolt was tightened to the pre-defined force of 2.1 kips (9.2 kN), a sinusoidal voltage excitation was applied to the piezoelectric wafers of the PICK tool. The dynamic excitation was applied in a sequence of two steps. (4) First, the frequency of the excitation wave was varied to perform a sweep with the goal of identifying the resonant frequency of the tool. This was accomplished by monitoring the amplitude of the response measured with a piezoelectric strip attached to the back of the PICK tool. (5) After the resonant frequency was determined, the bolt on the PICK tool was readjusted until the 224-microstrain reference strain was re-established. The ultrasonic treatment was continued for 114.5 hours. (6) After that duration was reached, the specimen was taken out of the tool, photographed, measured in the same manner used for the pressure-only treated specimens, and the plug was pressed out.

During the course of both types of treatment on fatigue specimens (pressure-only and PICK), the load in the bolt was observed to decay with respect to time. When no adjustment was made to the bolt force over the course of the 114.5-hour treatment, the load applied through the PICK tool onto the aluminum plug decreased from an initial magnitude of approximately 2.2 kips (9.2 kN) to a value that ranged between 1.6 kips to 1.9 kips. This behavior was observed to be consistent between specimens, regardless of whether the treatment applied was pressure-only or PICK-treatment (the latter of which included a periodic variation of the force in the ultrasonic range). The load decay phenomenon is believed to have occurred due to inelastic deformations occurring in the aluminum plug and the hole expansion in the steel fatigue specimen during treatment.

C.2.5.3   Testing Protocol for Fatigue Tests

After treatment, all fatigue specimens were tested under tensile cyclic loading using an MTS universal testing machine. The frequency of the cyclic load was approximately 2 Hz, and the stress range was 32 ksi (221 MPa), with 2 ksi (14 MPa) being the lower limit and 34 ksi (234 MPa) being the upper limit.

The first step of the test protocol was to establish the displacement range of the uncracked specimen for the applied load range. After this range was recorded, a crack-initiation indicator was established by setting up a detection limit in the testing machine corresponding to several thousandths of an inch larger than the largest displacement of the uncracked specimen. After this limit was reached, the test was immediately halted and the specimen inspected to determine if a fatigue crack had actually initiated. Dye penetrant was applied and fatigue testing restarted. The use of dye penetrant in specimens subjected to cyclic loading facilitated the detection of small fatigue cracks due to the pulsating motion of the dye penetrant fluid. If the inspection resulted in the detection of a fatigue crack, the number of cycles was recorded as the number of cycles to failure of the corresponding specimen. If not, the test was resumed with slightly larger displacement limits and the process was repeated until a fatigue crack was detected.

Despite specimen fabrication with close tolerances and careful alignment of the UTS grips, some bending was induced in the tensile fatigue specimens during testing. These small eccentricities were found to have a noticeable effect on the stresses recorded at the center of the slender fatigue specimens. To eliminate or minimize this bending effect, cable ferrules were pressed on the ends of two small wire cables and one end of each cable threaded through the hole of the fatigue specimen. The other ends of the cables were attached to turnbuckles which were in turn attached through cables to the columns of the MTS testing machine. To minimize the induced bending strain, tension in the cables was adjusted using the turnbuckles so that the center of the fatigue specimen was held in an aligned position. Measurements from the two strain gages attached to the fatigue specimen were collected and processed with LabView to separate bending and tension strains. Tension in the wire cables connected to the center of the fatigue specimens was adjusted to minimize bending strain. In accordance with the requirements in ASTM E466-07 (ASTM 2007) specimens in which the bending strains exceeded 5% of the tensile strains were excluded from the data set.

C.2.5.4　Retained Expansion

Retained expansion (*RE*) is an important parameter that, as discussed in the Background section, has been commonly used in prior research to measure the effectiveness of cold-expansion. Retained expansion is defined as the change in radius of an expanded hole, expressed as a percentage of the initial radius (Equation C.4).

$$RE = \left(\frac{R_{final} - R_{initial}}{R_{initial}} \times 100 \right)\%$$

Equation C.4

In Equation C.4, R_{final} is the final radius of the hole, and $R_{initial}$ is the initial radius before cold expansion.

In this study, *RE* values were determined by using a digital caliper to measure the hole diameter before and after expansion. The average hole diameter was determined by taking 10 measurements around the hole on each side of the specimen, for a total of 20 hole diameter measurements for each specimen configuration. These 20 measurements were subsequently averaged to obtain a single value of hole diameter for the specimen.

A total of four small plates were fabricated from fatigue tension specimens to study the effect of PICK treatment protocol on Retained expansion (*RE*).These plate specimens were treated for the express purpose of measuring *RE* values when a different treatment protocol was followed and were not tested under cyclic loading. The treatment protocol used in these four plates differed from the one previously described for the fatigue tension specimens in that the tension of the bolt in the PICK tool was adjusted periodically to prevent load decay in the aluminum plug over time. These plates were fabricated from sections of the specimens shown in Figure C.14; for plates manufactured from the section of the specimen without a hole, the new hole was fabricated in the same manner as the hole in the original fatigue specimens.
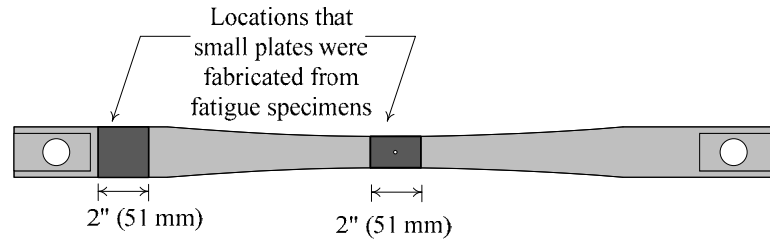
Figure C.14: Locations from which plates were cut from the fatigue specimens to study the effect of treatment protocol on *RE*

C.2.6 Results and Discussion

C.2.6.1　　Fatigue Testing Results

Experimental results from five control specimens (designated with a prefix of "Ctrl"), four pressure-only treated specimens (designated with a prefix of "PO"), and six PICK-treated specimens (designated with a prefix of "PICK") are presented in Table C.3. Results presented in Table C.3 are indicative of all specimens in which bending strains were controlled to levels admissible according to ASTM E466-07. The results in Table C.3 show that the difference in average fatigue life between the three groups of specimens tested was significant.

Table C.3: Fatigue Test Results

Specimen	Cycles to Crack Initiation	Average No. of Cycles to Crack Initiation	Standard Deviation (cycles)	Coeff. Of Variation	95% Confidence Level (cycles)
Ctrl9	234,824	194,164	25,335	13%	170,000
Ctrl10	177,106				
Ctrl11	169,222				
Ctrl12	195,220				
Ctrl13	194,449				
PO6	426,302	387,485 (538,641*)	44,738 (304,511*)	12% (57%*)	312,000 (180,328*)
PO7	397,595				
PO8	338,557				
PO9[†]	992,108				
PICK3	818,635	600,380	195,715	33%	439,000
PICK4	743,725				
PICK10	532,310				
PICK11	744,767				
PICK12	350,026				
PICK13	412,814				

*Results are provided for cases in which PO9 is included and excluded from the data set; values reported with an asterisk (*) indicate that specimen PO9 was *included* in the calculation.

Specimen PO9 exhibited a fatigue life significantly greater than the other three specimens treated with pressure-only. Due to the limited size of the data set, it was unclear whether this test should be treated as an outlier; for this reason, results in Table C.3 are shown for pressure-only data sets that include and exclude specimen PO9.

A 95% confidence level was established using Student's t-distribution for each of the three sub sets of specimens. The calculated confidence level provides a statistical estimate of the number of cycles to crack initiation that will be exceeded by 95% of specimens within the data set; only 5% of the fatigue specimens will have fatigue life for crack initiate below this number of cycles-to-failure. The 95% confidence limit for control specimens occurred at 170,000 cycles. Calculating the 95% confidence limit for pressure-only treated specimens with and without consideration of specimen PO9 resulted in limits of 180,000 (6% increase over the 95% confidence limit for control specimens) and 312,000 cycles (84% increase over the 95% confidence limit for control specimens), respectively. Comparing the 95% confidence levels of fatigue life between specimens with no treatment and those fully treated with the PICK tool (440,000 cycles) showed an increase of 160%.

Data for the three groups of specimens have also been plotted on the AASHTO (2013) S-N Diagrams in Figure C.15. The figure shows that the three groups of data formed separate data clusters. The 95% confidence levels were plotted on the S-N diagram for reference.
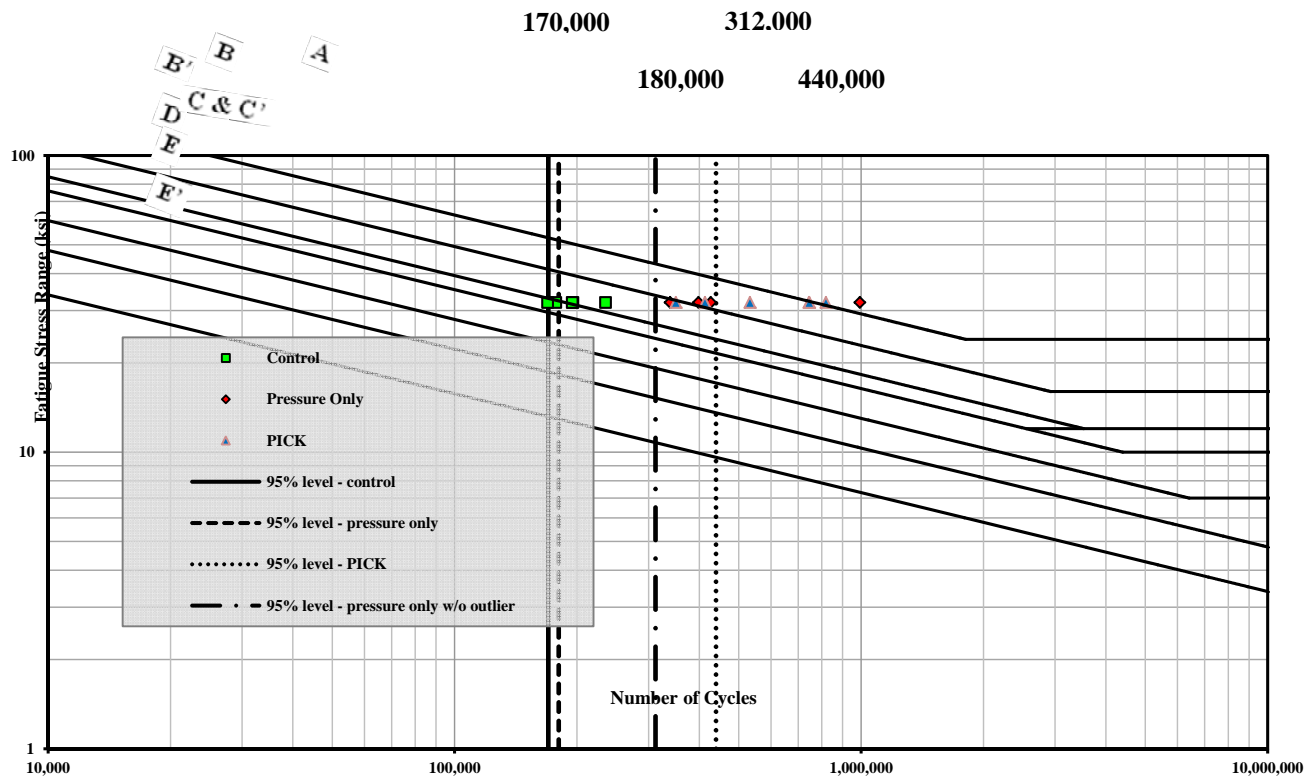
Figure C.15: Fatigue test results plotted on S-N diagram

Control specimens exhibited an average fatigue life (to first visually-observable crack initiation) of approximately 190,000 cycles, which corresponds to AASHTO fatigue Categories C and B'.

Specimens treated with pressure-only exhibited performance consistent with AASHTO B' and B Categories (except PO9, which performed at the Category A level). This level of performance was approximately one AASHTO fatigue category better than observed for the control specimens.

Specimens treated with PICK technology performed at the level of AASHTO Categories B and A, exhibiting a one-category increase in performance beyond the pressure-only treated specimens. Based on this comparison, it is reasonable to conclude that treating the specimens with the pressure-only protocol resulted in an improvement in fatigue performance over that of

the control specimens, and that treating the specimens with the PICK treatment protocol resulted in a further increase in fatigue performance.

C.2.6.2 Retained Expansion (RE)

The hole diameter at the center of each test specimen was measured before and after treatment, for the purpose of calculating retained expansion (*RE*) in each specimen. Levels of measured retained expansion for the pressure-only and PICK-treated fatigue and plate specimens are reported in Figure C.16.

.

Retained Expansion (%)
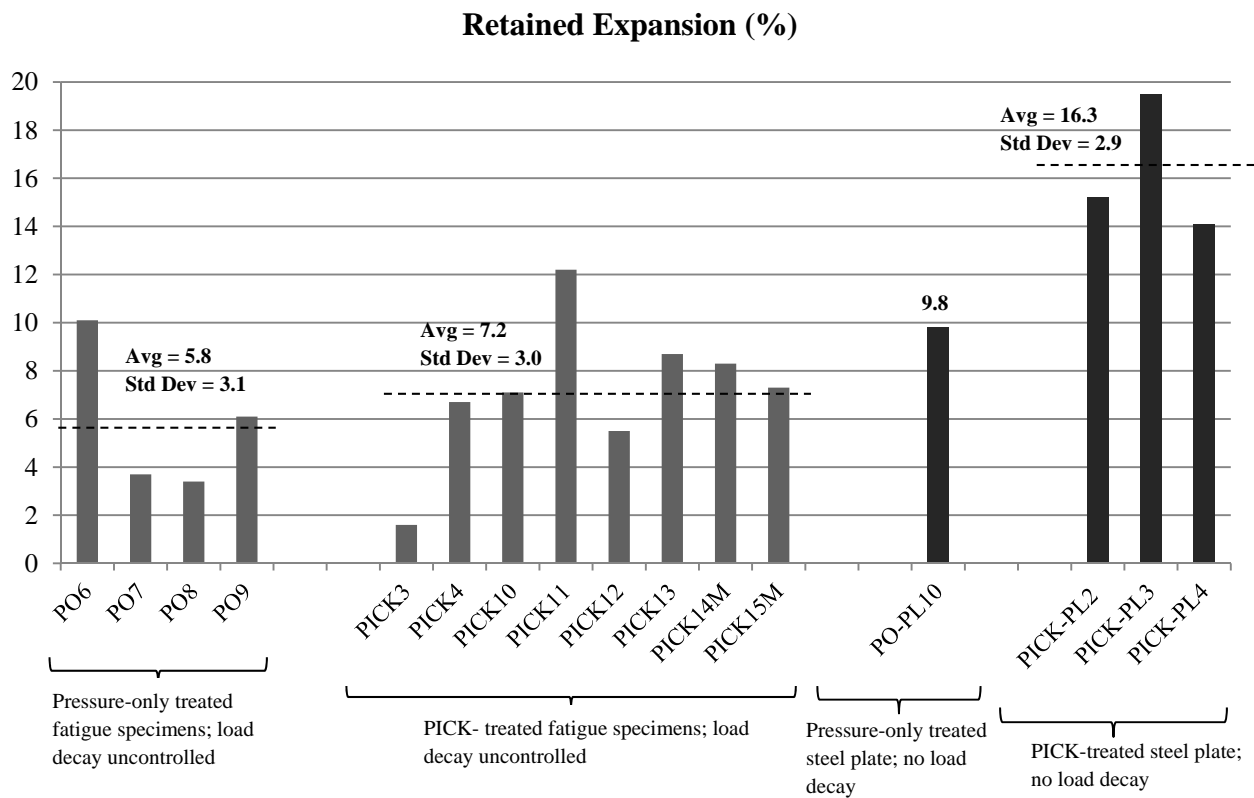
Figure C.16: Retained expansion (%) for holes treated with pressure-only and PICK.

The results shown in Figure C.16 have been clustered for specimens treated with pressure-only and with PICK treatment. Additionally, results for the two treatment types have been separated out to reflect the type of specimen the treatment was applied to (fatigue specimens shown in gray or plate specimens shown in black). A comparison of measured *RE*

309

values for the various data groups shows several important trends. First, the overall data spread, including results from both treatment types and both specimen types, resulted in an average value for retained expansion of 8.7% with a standard deviation of 4.7%. This average value was significantly greater than the *RE* value of 4% that has been shown to be an effective level of hole expansion (Crain et al.). The *RE* value corresponding to one standard deviation below the mean was approximately 4%.

The average *RE* measured in pressure-only treated fatigue specimens (5.8%) was lower than the average *RE* measured for the PICK-treated specimens (7.2%). Given that the standard deviation for both of these data sets was similar, the higher *RE* values observed in the PICK-treated specimens is attributed to a combination of cold-expansion and work-hardening induced by the PICK treatment.

Although the data set for plate specimens is more limited, a similar trend was observed when comparing *RE* values from pressure-only and PICK-treated specimens (9.8% and 16.3%, respectively). These measurements corroborate the findings from the fatigue tests, in which the PICK-treated specimens outperformed the pressure-only treated specimens in terms of fatigue life. The correlation between measured *RE* values and observed fatigue life indicates that *RE* was an indicator of fatigue life extension.

Another important finding was that *RE* values for plate specimens were determined to be approximately twice as large as the corresponding *RE* values for fatigue specimens, the latter of which were not controlled for load decay. These results show that preventing load decay further increases the level of retained expansion for both types of treatment. It should be noted that prior research (Crain et al. 2010; Crain 2010) has shown that *RE* values greater than 4% obtained through cold expansion result in greatly diminishing levels of fatigue improvement. Therefore, it is hypothesized that the additional level of *RE* obtained by maintaining constant pressure on the aluminum plug throughout treatment would not result in significant increases in fatigue life. Additional fatigue testing should be performed in the future to evaluate this hypothesis.

C.2.6.3   Metallurgical Findings

A metallurgical investigation was performed to analyze grain size using an optical microscope. For untreated specimens it was found that grain sizes were mixed, averaging between 0.0133 mm and 0.0159 mm (.000524 in. and 0.000626 in.). The untreated (control) specimens were only subjected to drilling and reaming of the hole, and the optical microscope revealed shallow grain deformation of the grains at the surface of the hole [Figure C.17(a)]. The observed deformations were limited to those grains located immediately surrounding the hole surface.

For the pressure-only treated specimen, a layer around the surface of the hole exhibited grain deformations to a depth of approximately 0.008 to 0.009 mm (0.0003 to 0.0035 in.), as shown in [Figure C.17(b)].

For the PICK-treated specimen, a layer of grain deformation was noted as occurring up to a depth of 0.001 mm (0.0040 in.) from the surface of the hole [Figure C.17(c)]. One sample displayed semi-circular regions immediately adjacent to the edge of the hole where grain deformations extended to a distance of 0.038 mm (0.0015 in.). Within these regions, the grains appeared to be flattened and highly elongated.

(a) Control specimen (500x)   (b) Pressure-only treated specimen (500x)   (c) PICK-treated specimen (500x)
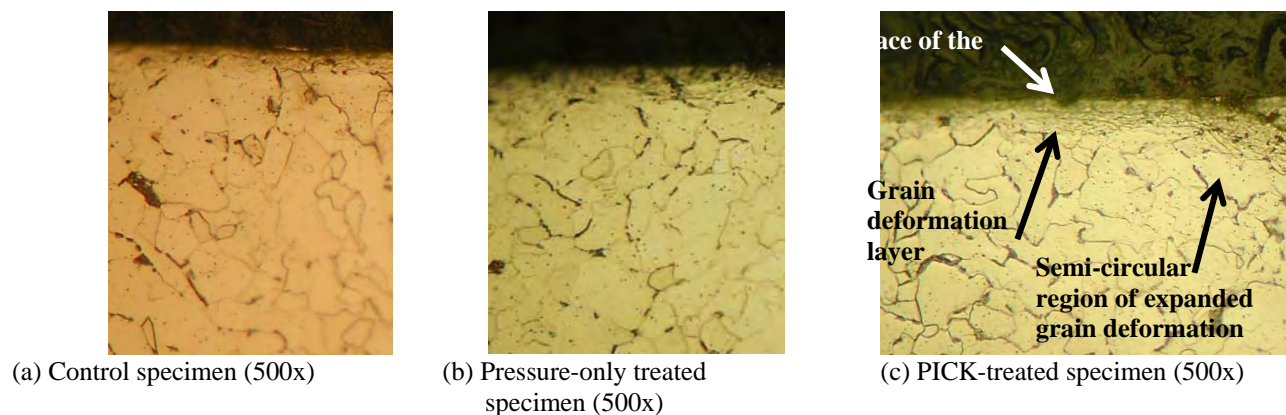
Figure C.17: Comparison of control, pressure-only, and PICK-treated microstructures at the hole surface

Findings of the metallurgical investigation are important when analyzed in the context of the fatigue tests and RE measurements. The fact that the grain deformations were measurably

different between control, pressure-only, and PICK-treated specimens lends additional weight to the fatigue test results, which showed measurable differences in fatigue performance between those three groups. Additionally, the marked difference in grain deformations between the pressure-only and the PICK-treated specimens supports the observed increase in retained expansion from the pressure-only specimens to the PICK-treated specimens.

C.2.6.4   Neutron Diffraction Measurements

The tangential, radial, and normal strains measured by neutron diffraction are plotted in Figure 4.16. For the tangential residual strain, the minimum strain is $-1553\mu\varepsilon$, the maximum is $396\mu\varepsilon$, while the elastic-plastic boundary is about $r/r_i = 5.6$. Note that the tangential strain near the hole edge ($r/r_i = 1$) appears to showed yielding in compression.
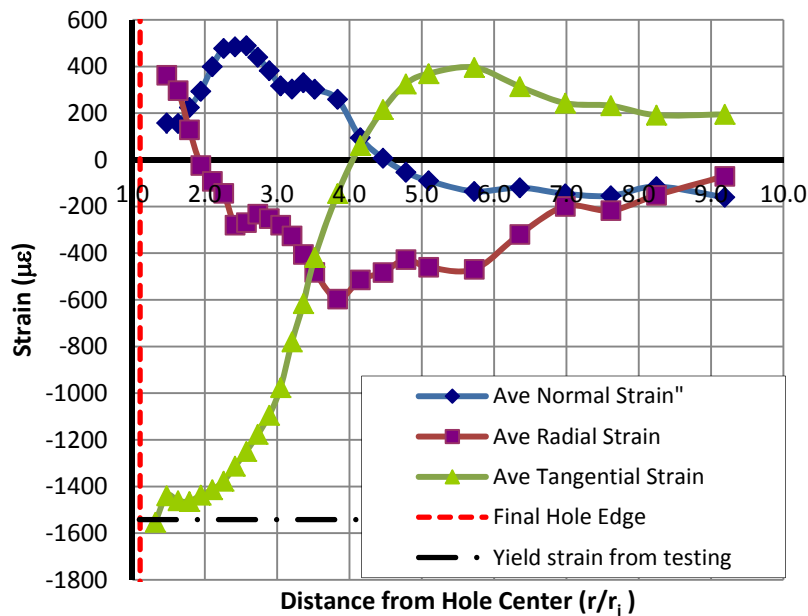
Figure C.18: Strains in PICK-treated specimen from neutron diffraction (ND) measurements taken at ORNL

The shapes of the radial and tangential residual strain, in general, matched the curves of stress calculated from the classic closed-form procedures presented in Nadai (1943) and Ball (1995) for this problem.

C.2.6.5   Hardness Testing

Microhardness readings were taken along several paths on different cut surfaces of the samples sent to the metallurgical laboratory. One cut with a slow-speed diamond saw was made well away from the hole and the area affected by the PICK treatment around the hole to provide a surface which had not been affected by any treatment. Microhardness readings were taken along the centerline of this surface and used to establish a baseline hardness for untreated steel. On one fully treated PICK specimen, one set of readings was taken along a line at mid-plane and the other was taken along a line near the surface, both along a diametric line through the center of the hole. The other three specimens (untreated, mechanically expanded only, and fully PICK-treated) had microhardness readings taken only along the midplane of the cuts, which was through the specimen, along a diametric line through the center of the hole. The microhardness readings were converted from the Vicker's hardness scale to the Rockwell hardness B scale using tables in ASTM E140. The metallurgical report is presented in Simmons (2013). The hardness values were further converted from Rockwell hardness B to ultimate tensile strength using a conversion table in Moniz (1994).

Results of the hardness testing are presented in Figure C.19. All the trend lines for both the mechanically expanded and the fully PICK-treated data showed an increase in hardness and ultimate strength over the control specimen. The trend line for the near-surface traverse showed an approximate linear reduction in hardness and ultimate tensile strength with distance from the hole.
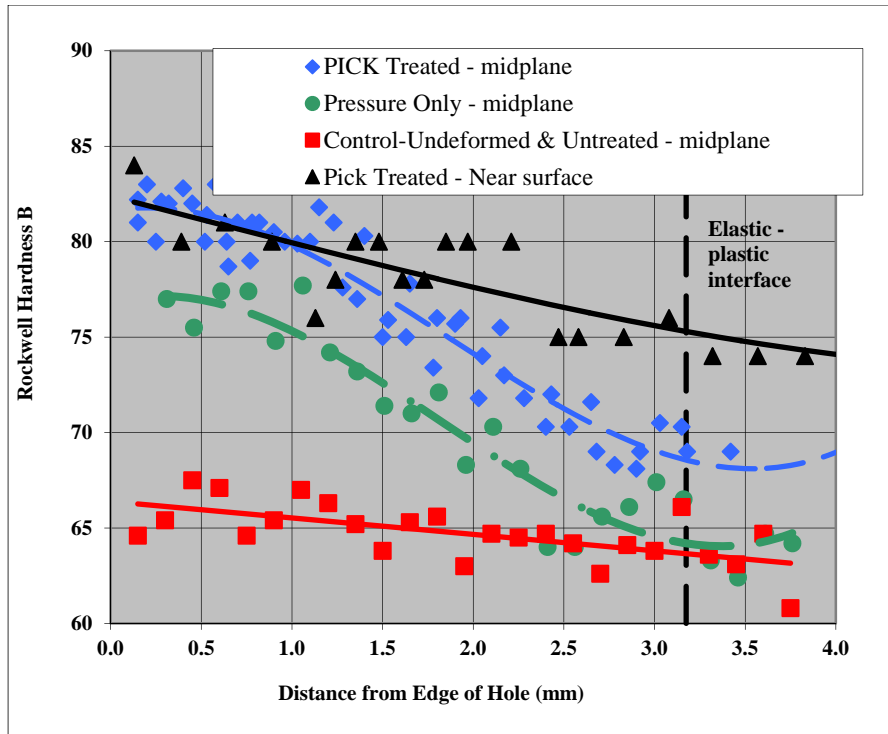
Figure C.19: Increase in hardness and ultimate strength with different cold-expansion treatments

C.2.7 Conclusions

A study focused on determining the performance of drilled holes in steel bridges treated with two mechanical techniques, pressure-only and PICK, resulted in the following conclusions:

- The performance of untreated control specimens tested in fatigue corresponded to AASHTO fatigue categories of C and B'.
- Treating specimens with pressure-only (simple expansion of the drilled hole) was found to increase the fatigue performance of specimens with drilled holes beyond that of untreated specimens. Pressure-only specimens exhibited performance consistent with AASHTO fatigue categories B' and B.
- Treating specimens with PICK technology further increased the fatigue performance of specimens with drilled holes beyond that of the pressure-only treated specimens. PICK-treated specimens performed at a level consistent with AASHTO fatigue categories B and A, indicating a performance increase of approximately two categories beyond that of untreated specimens.
- The average *RE* measurements for both treatment techniques examined indicate that *RE* values were well above the 4% threshold shown to be effective in improving the fatigue life of drilled holes.

314

- The *RE* values measured for PICK-treated drilled holes were higher, on average, than pressure-treated drilled holes. Further study is necessary to develop a better understanding of this phenomenon.
- *RE* values for both pressure-only and PICK-treated specimens were significantly greater (approximately 2 times) when the load applied to the aluminum plug was monitored at regular intervals to maintain it nearly constant, instead of being allowed to decay with time. It should be noted that the *RE* values determined when the load on the aluminum plug was maintained nearly constant were significantly higher than the optimal value of 4% commonly accepted as needed to achieve a significant increase in fatigue life.
- The retained expansion values were in good agreement with the fatigue test results. PICK-treated specimens out-performed pressure-only treated specimens in terms of fatigue life and had higher levels of *RE*.
- The metallurgical investigation showed increasing levels of grain deformations between the pressure-only and PICK-treated specimens, which supports the conclusions from the fatigue tests and the *RE* measurements.

This proof-of-concept study has shown the merit of pressure-treating drilled holes in bridges to increase the fatigue performance, providing the fundamental groundwork for additional research to be performed on larger scale specimens. Additionally, this research has shown that ultrasonic treatment using PICK technology can be used to further improve the fatigue performance of drilled holes in bridges through a combination of cold expansion and cold-working. Solutions such as these can be used for new bridge construction (bolted connections) and for existing steel bridges susceptible to fatigue cracking (drilled crack-arrest holes) to extend the useful life of the nation's infrastructure. Future work in this area is recommended to examine whether similar results could be expected to be achieved in punched holes, to experimentally examine pressure-only treatment in thicker steel plates, as well as to expand the line of study beyond a proof-of-concept PICK tool to a field-ready tool that is capable of treating thicker steel plate material.

C.2.8 References

AASHTO (2013). 2013 Interim Revisions to the AASHTO LRFD Bridge Design Specifications. 6th ed. American Association of State Highway and Transportation Officials, Washington, D.C.

ASTM E466-07 (2007). Standard Practice for Conducting Force Controlled Constant Amplitude Axial Fatigue Tests of Metallic Materials. ASTM International, West Conshohocken, PA.

Ball, D.L. (1995). Elastic-Plastic Stress Analysis of Cold Expanded Fastener Holes. Fatigue and Fracture of Engineering Materials and Structures, Vol. 18, Issue 1.

Bontillo, R. (2011). PBFasteners, personal communications.

Crain, J. (2010). Fatigue Enhancement of Undersized, Drilled Crack-Stop Holes. (Master's thesis). University of Kansas, Lawrence, KS.

Crain, J., Simmons, G., Bennett, C., Barrett-Gonzalez, R., Matamoros, A., and Rolfe, S. (2010). "Development of a Technique to Improve Fatigue Lives of Crack-Stop Holes in Steel Bridges." Transportation Research Record 2200, 69-77. Transportation Research Board, National Research Council, Washington, D.C.

Fatigue Tech Inc. http://www.fatiguetech.com/

Lanciotti, A. and Polese, C. (2005). "The Effect of Interference-Fit Fasteners on the Fatigue Life of Central Hole Specimens." Fatigue & Fracture of Engineering Materials & Structures, 28, 587-597.

Moniz, B. J. (1994). Metallurgy. 2nd ed. American Technical Publishers, Inc., Homewood, IL.

Nadai, A. (1943). Theory of Expanding of Boiler and Condenser Tube Joints through Rolling. Transaction of the American Society of Mechanical Engineers, Vol.65, Issue 8.

Reid, L. (2011). Fatigue Technology, Inc., personal communications.

Simmons, G. (2013a). Fatigue Enhancement of Undersized, Drilled Crack-Arrest Holes. (Ph.D. dissertation). University of Kansas, Lawrence, KS.

Simmons, G., Bennett, C., Barrett-Gonzalez, R., Matamoros, A., and Rolfe, S. (2013). "Design, Modeling, and Testing of a Piezoelectric Impact Compressive Kinetic (PICK) Tool for Crack-Stop Hole Treatment." Proceedings SPIE 8692, Sensors and Smart Structures Technologies for Civil, Mechanical, and Aerospace Systems 2013. SPIE, Bellingham, WA.

Appendix D: Skewed Bridge Analytical Investigation

Appendix D is are focused on improving the understanding of distortion-induced fatigue in skewed bridges.

Appendix D.1 focuses on a sophisticated parametric analysis, in which over 1,000 highly-detailed 3D finite element models were used to examine the effects of skew angle, cross-frame spacing, cross-frame layout, cross-frame stiffness, and load placement on the potential for distortion-induced fatigue in steel bridges.

Appendix D.2 also utilizes an analytical parametric analysis approach to examine the effects of lateral bracing placement in skewed steel bridges.

D.1: Parametric Analysis of Cross-Frame Layout on Distortion-Induced Fatigue in Skewed Steel Bridges

H. L. Hassel[12]

Caroline Bennett[13]

Adolfo Matamoros[14]

Stan Rolfe[15]

D.1.1 Abstract

The effects of skew angle, cross-frame spacing, cross-frame layout, cross-frame stiffness, and load placement on the potential for distortion-induced fatigue damage in steel bridges was investigated by performing a suite of more than 1,000 analysis jobs of high-resolution 3D finite element models. Susceptibility to fatigue damage was quantified in terms of computed stress demand in the web gap region of the girders. Bridge configurations with three different cross-frame layouts were evaluated, including configurations with cross-frames placed parallel to skew angle (skewed-parallel) and perpendicular to the girder line, both staggered (skewed-staggered) and unstaggered (skewed-unstaggered). Skew angles of configurations evaluated ranged between 0° and 50°, and cross-frame spacing ranged from 2.29 to 9.14 m (7.50 to 30.0 ft).

Influence and envelope surfaces were constructed to show the relationship between load placement, location of the maximum web gap stress, and the magnitude of the maximum web gap stress. It was found that maximum web gap stress always occurred when loads were positioned directly above the intersection of a cross-frame and girder web. The parametric study showed that cross-frame stiffness and spacing had a significant effect on the susceptibility to distortion-induced fatigue damage; greater cross-frame stiffness resulted in higher web gap stresses, and increased cross-frame spacing resulted in increased web gap stresses. It was also found that the bridge configuration was key to determining the location of the web gaps where

---

[12] Heidi L. Hassel, M.S., Burns and McDonnell, 9400 Ward Parkway, Kansas City, MO, 64114.

[13] Caroline Bennett, PhD, PE, Associate Professor, University of Kansas, 1530 W. 15th St., Lawrence, KS 66045.

[14] Adolfo B. Matamoros, PhD, Professor, University of Kansas, 1530 W. 15th St., Lawrence, KS 66045.

[15] Stanley T. Rolfe, PhD, PE, A.P. Learned Distinguished Professor, University of Kansas, 1530 W. 15th St., Lawrence, KS 66045

damage is most likely to occur. In skewed-parallel and skewed-unstaggered layouts, maximum web gap stresses were identified in top web gaps, while in skewed-staggered configurations maximum stresses occurred in bottom web gaps. It was found that in configurations with staggered cross-frames, maximum web gap stresses tended to occur in regions of support, where cross-frames are often placed back-to-back along the skewed alignment.

D.1.2 Introduction

Distortion-induced fatigue is a significant problem facing State Departments of Transportation (DOTs) tasked with the duty of inspecting and repairing steel bridges susceptible to fatigue damage currently in their highway inventory. Many steel bridges designed prior to the mid-1980s were constructed with connection details that, although considered to be in accordance with best detailing practices at the time, are now recognized to be fragile under the action of cyclic secondary stresses. One such common detail is known as a *web gap*, a short length of unsupported web between the extreme edge of a transverse connection stiffener and adjacent flange not attached to the stiffener. The transverse connection stiffener is part of a mechanism to connect cross-frames or diaphragms to girder webs, and as such, imposes lateral forces on the web as live loads are distributed through the bridge system. When older bridges were designed, it was often assumed that these lateral forces produced stresses much lower in magnitude than those induced by the flexural demand on the girders. Contrary to this assumption, commonly-used connection details in the web gap region give rise to high stress-concentration factors due to abrupt changes in geometry; this magnifies the out-of-plane stress demands on the web gap region, and leads to initiation and propagation of fatigue cracks. Fatigue damage caused by these out-of-plane stresses is often referred to as distortion-induced fatigue. Approximately 90% of fatigue cracking is thought to be caused by secondary stresses at fatigue-sensitive details (Connor and Fisher 2006).

Distortion-induced fatigue is considered to be more problematic in bridges with skewed supports than in non-skewed bridges (Fisher and Mertz 1984). Differential deflection between girders is magnified in skewed bridges, as adjacent girders at equal stations along a skewed bridge are at different span points and deflect unevenly (Berglund and Schultz 2006). Although much research has been performed on mitigating the effects of distortion-induced fatigue

319

(Roddis and Zhao 2001; Khalil et al. 1998; Connor and Fisher 2006), the relationship between skew angle, cross-frame layout and stiffness, load placement, and distortion-induced fatigue susceptibility is not well understood. A better understanding of this relationship is critical so that characteristics of skewed steel bridges that increase susceptibility to distortion-induced fatigue damage may be identified, enabling bridge engineers to maintain the existing bridge inventory in a more efficient manner. This knowledge is also important to ensure that new bridges are designed with an understanding of distortion-induced fatigue demands associated with each particular bridge configuration. This paper describes a research program aimed at investigating the effects of skew angle, cross-frame layout, cross-frame stiffness, and load placement on the potential for distortion-induced fatigue damage in steel bridges.

D.1.3 Background

Three bracing layouts commonly used in skewed bridges are shown in Figure D.1. For the purpose of this paper, the terms *brace* and *bracing* will be used to denote instances in which either cross-frames or diaphragms may be used, and always refers to upright bracing, as opposed to lateral (floor) bracing. Bracing may be placed parallel to the skew angle or perpendicular to the girder line in either a staggered or unstaggered layout. These layouts will be referred to throughout this paper as skewed-parallel, skewed-staggered, and skewed-unstaggered, respectively. Skewed-parallel layouts are generally considered the least susceptible to distortion-induced fatigue, because both ends of a cross-frame are attached at the same span point along adjacent girders. Provisions in the AASHTO LRFD Bridge Design Specifications (AASHTO 2013) require that bracing be placed perpendicular to the girder line in bridges with skew angles larger than 20°, due to concerns about increased cross-frame flexibility and reduced effectiveness in distributing live loads. Contrary to the provisions in the AASHTO LRFD Bridge Specifications (AASHTO 2013), design provisions in some states allow the use of the skewed-parallel layout beyond this limit; this is done to accommodate connections between cambered girders at different points in their respective spans. This practice is also thought to reduce differential deflections between girders and consequently decrease vulnerability to distortion-induced fatigue (KDOT 2010).
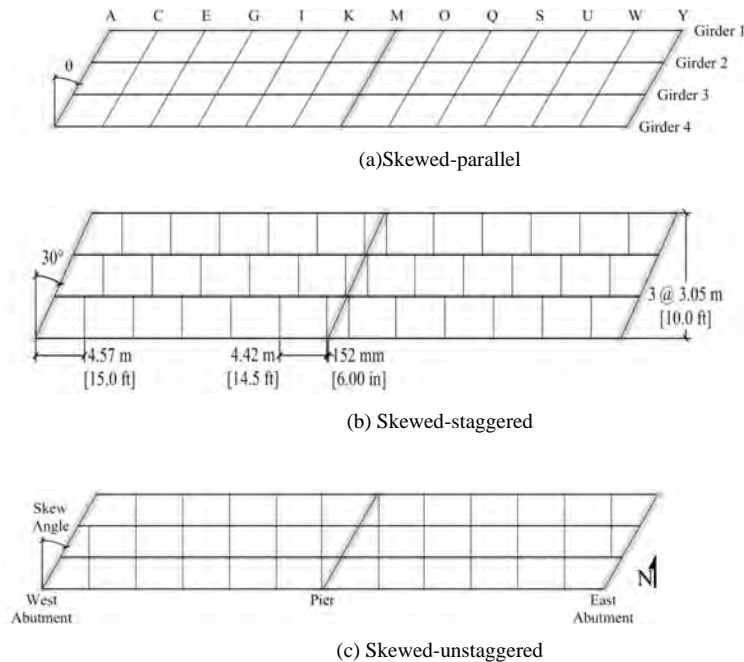
Figure D.1: Bridge layouts (30° Skew with 4.57 m (15.0 ft) cross-frame spacing)

For bridges with braces placed perpendicular to the girder line (skewed-staggered and skewed-unstaggered), previous research is not conclusive as to which layout performs better with respect to distortion-induced fatigue. Some studies have concluded that large out-of-plane girder deflections in bridge configurations with skewed-staggered bracing makes them less effective at distributing gravity loads through cross-frames (Fraser et al. 2000; Barth and Bowman 2001; Hartman et al. 2010). Laboratory testing of both perpendicular brace layouts showed that cracks were more common in the unstaggered layout because back-to-back braces (diaphragms, in this case) were less flexible, tending to act as one continuous member (Barth and Bowman 2001). Therefore, damage may be less likely in skewed-staggered bridges due to reduced load transfer, but reduced load sharing between girders may not necessarily be a desirable characteristic for a bridge system.

Conclusions from previous studies illustrate the difficulty in making generalizations about the locations within bridge structures where distortion-induced fatigue might occur; in fact, some of the existing literature on this subject is contradictory. While studies by Zhao and Roddis (Roddis and Zhao 2001; Zhao and Roddis 2003) found that cracks were likely to occur in regions of positive bending of continuous-span girders, other researchers noted cracking in regions of

321

negative bending (Jajich and Schultz 2003; Khalil et al. 1998). Likewise, cracks have been noted in web gaps adjacent to both the top and bottom girder flanges. Overall bridge layout has been observed to have an impact on the location of fatigue cracks; for example, Fisher et al. (1990) noted that cracks occurred only in top web gaps unless staggered diaphragms were used.

Because the stiffness of bracing and connecting elements controls the ability of each brace to attract and distribute load, brace stiffness is hypothesized to be an essential parameter affecting bridge susceptibility to distortion-induced fatigue. No previous research was found that directly investigated the effect of bracing stiffness on distortion-induced fatigue, although some studies have considered similar parameters (Fisher et al. 1980; Li and Schultz 2005). It is apparent that bracing and connecting element stiffnesses can be significantly reduced when bracing is not placed perpendicular to the girder line. In addition to a reduction in stiffness that occurs due to increased length, brace element stiffness (β_{br}) is multiplied by a $cos^2\theta$ term to determine the stiffness of skewed bracing, making overall brace stiffness a function of $cos^3\theta$ (Wang and Helwig 2008), where θ is the skew angle (degree):

$$\beta_{br,skew}=\beta_{br}cos^2\theta \qquad\qquad \text{Equation D.1}$$

Research has also shown that brace stiffness (β_b) is dependent on stiffness of both the brace elements and connection stiffeners (β_{conn}) (Yura et al. 1992; Yura 2001). This relationship has been described as (AISC 2005):

$$1/\beta_b = 1/\beta_{br} + 1/\beta_{conn} \qquad\qquad \text{Equation D.2}$$

The sensitivity of brace and connecting element stiffness to skew angle, and the importance of overall brace stiffness on the susceptibility of bridges to distortion-induced fatigue damage, underscores the importance of evaluating the effect of these parameters on distortion-induced fatigue.

D.1.4 Objectives and Scope

The objective of this study was to evaluate the effects of skew angle, cross-frame spacing, cross-frame layout, and cross-frame stiffness on the likelihood of distortion-induced

fatigue damage in web gap regions of steel bridges. It was also a goal of this study to evaluate the relationship between load placement and web gap stresses, which was used to quantify the potential for damage due to distortion-induced fatigue. The parameters investigated were selected because there is very little information in the literature about their effect on distortion-induced fatigue damage.

Other parameters such as web gap size, concrete deck thickness, span length, and girder depth are expected to be independent from the parameters studied in this investigation (i.e., web gap length and deck thickness are expected to have little to no correlation to cross-frame layout), and therefore were not within the scope of research described within this paper. Some of these parameters such as web gap size and deck thickness were chosen to be representative of bridges in the state of Kansas, where large variations in the dimensions of these parameters are not common. Span length and girder depth affect the magnitude of the bending stress on the girder and the angle of inclination of the cross-frame elements. The effect of both of these parameters was studied in simulations by Gangel (2012) and are described in detail in a separate study. Curved and skewed-curved bridges were not considered within the scope of this investigation.

D.1.5 Research Methods

The effects of (1) skew angle, (2) cross-frame spacing, (3) cross-frame layout, (4) cross-frame stiffness, and (5) load placement on the potential for distortion-induced fatigue were investigated by performing a suite of computer simulations using the commercially-available finite element analysis (FEA) software Abaqus v6.8.2. Maximum principal tensile Hot Spot Stresses (HSS) at web gaps were used to quantify and compare bridge susceptibility to distortion-induced fatigue damage.

Experimental and computer simulations performed by the authors on 914 mm (36 in.) deep girder sub-assemblies subjected to distortion-induced fatigue showed that maximum principal hot spot stresses calculated using high resolution linear-elastic finite element models provided excellent prediction of crack initiation location and crack propagation paths (Appendix A.1 and A.2). The girder specimens reported upon in Appendix A.1 and A.2 analytically and experimentally were very comparable in dimension and connection detail to the bridge details in the current investigation. Multiple quantities calculated with the finite element models were

323

evaluated as predictors for crack initiation sites and propagation paths, including the J-Integral and the Hot Spot Stress technique. When the numerical calculations were compared directly with the physical testing, it was repeatedly found that maximum principal HSS was an excellent indicator of crack initiation location and propagation path. It is for this reason that maximum principal HSS were adopted as an indicator for crack propensity in this study and for the purpose of comparing stress demands at web gaps of different bridge configurations. HSS were used instead of the maximum computed nominal stresses because HSS have been shown to be less sensitive to variations in mesh size (Adams 2009).

Various definitions of HSS exist in the literature. Adams (2009) evaluated several definitions of HSS in the context of distortion-induced web gap stresses in girders. Following the recommendation by Adams (2009), a simple one-point procedure was used in this study, in which stress 5 mm (0.2 in) away from the weld toe (approximately half the web thickness) was extracted and used to represent the stress demand at the connection.

The baseline bridge configuration used for the parametric analysis was adapted from American Iron and Steel Institute's (AISI) Design Example 2 (1997). The configuration of this bridge can be considered typical of a multi-girder highway overpass, and has been used in other scholarly literature to demonstrate different bridge engineering concepts (Barth et al. 2004). The bridge is comprised of two 27.40 m (90.0 ft) continuous spans, with four girders spaced at 3.05 m (10.0 ft). The composite concrete deck is 203 mm (8.0 in.) thick, with a 1.07 m (3.50 ft) overhang on each side. Separate built-up cross sections were used in regions of positive and negative bending. Each girder was supported by a pin at the central pier and roller supports at both ends. Dimensions are provided in Figure D.2.

(a) Positive cross section   (b) Negative cross section
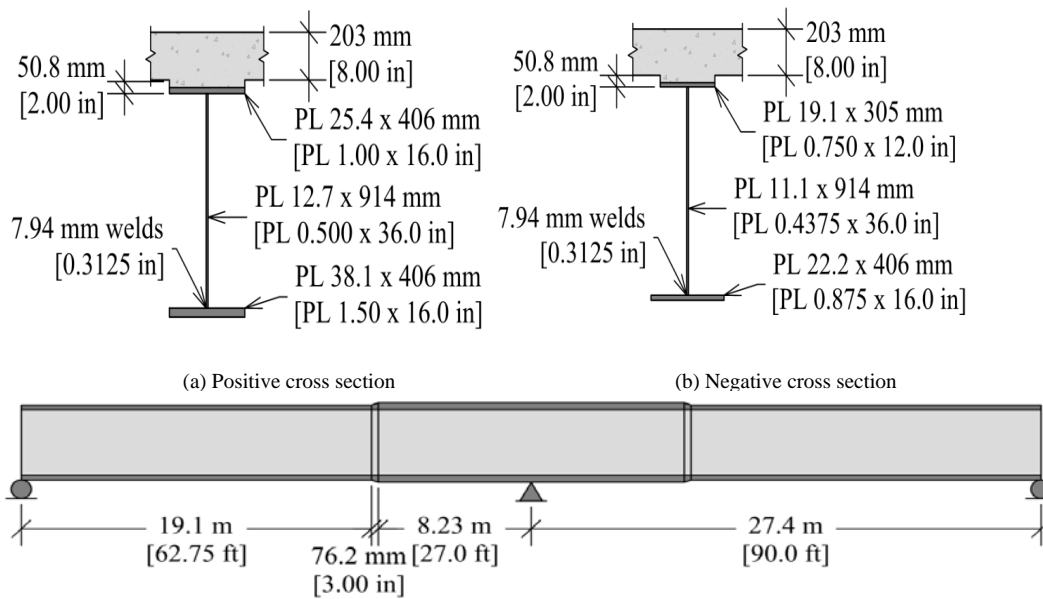
(a)   Overview of girder

Figure D.2: Bridge geometry used in the study

Table D.1 shows a matrix of the 60 different bridge configurations considered in the parametric analysis. Cross-frame layouts are illustrated in Figure D.1. The skewed-parallel cross-frame layout was modeled only for skew angles up to 40° to account for the limited use of this layout allowed by state DOTs (KDOT 2010).

Table D.1: Parameters Considered

| Skew Angle | Cross-frame Spacing, m (ft) | | | | | | | | | | | |
	2.29 (7.50)			4.57 (15.0)			6.86 (22.5)			9.14 (30.0)		
0		N*			N			N			N	
10	P	S	U	P	S	U	P	S	U	P	S	U
20	P	S	U	P	S	U	P	S	U	P	S	U
30	P	S	U	P	S	U	P	S	U	P	S	U
40	P	S	U	P	S	U	P	S	U	P	S	U
50		S	U		S	U		S	U		S	U

*N = Non-skewed, P = skewed-Parallel, S=skewed-Staggered, and U=skewed-Unstaggered

325

Cross-frames used in all bridge configurations studied consisted of three equal-leg angle sections, oriented as shown in Figure D.3. In skewed-parallel configurations, cross-frame length increased with skew angle and bent plate connection stiffeners were modeled taking into account construction considerations, making both cross-frame element and connection stiffness important parameters. A secondary study was conducted to ensure cross-frame element/connection stiffener (angle/stiffener) combinations were selected to have approximately constant stiffness, such that the effects of skew angle, cross-frame layout, cross-frame spacing, and load placement could be evaluated independently from the effect of cross-frame stiffness.
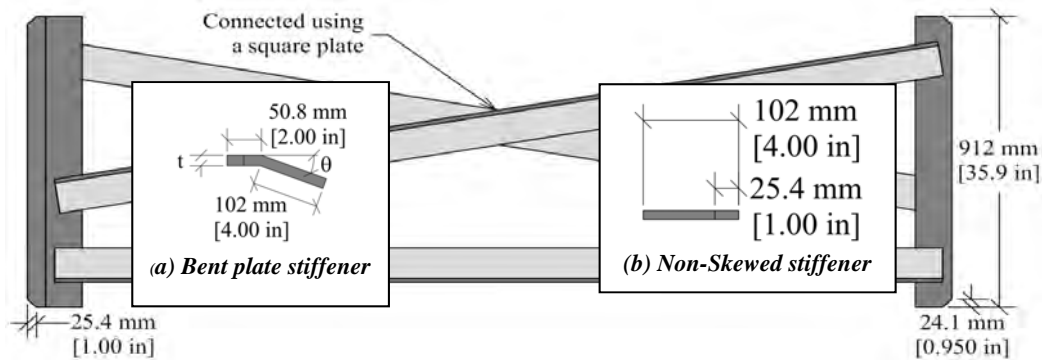
Figure D.3: Connection stiffener geometries used in (a) Skewed bridge geometries and (b) Non-skewed bridge geometries

Equal-leg angle cross-frame elements were selected for skewed bridges on the basis of both slenderness ratio and stiffness. Cross-sections not included in the American Institute of Steel Construction Steel Construction Manual (AISC 2005) were used in proportioning the cross-frames with the intent of maintaining cross-frame stiffness nearly constant for all skew angles. An L108x108x13 mm (L4$^1/_4$ x 4$^1/_4$ x $^1/_2$ in.) section was selected for the non-skewed bridge based on a maximum slenderness ratio (L/r) of 140 (AASHTO 2013); slenderness ratios for single angles were computed using the provisions in AISC, Section E5 (2005). For the purpose of comparison, cross-frame member stiffness was quantified in terms of the approximate relative stiffness, defined as $A \cos^3 \theta$, where A is the cross-sectional area of a single angle (mm^2 [in^2]) and θ is the skew angle (degree) (Yura 2001; Wang and Helwig 2008). Equal-leg angles for skewed cross-frames were selected to have a slenderness ratio less than 140 and a relative stiffness term

($A\ cos^3\theta$) closest to that used in the non-skewed bridge configuration, and were chosen to the nearest 3 mm ($^1/_8$ in.) increment.

For each skew angle, the connection stiffener thickness that would result in cross-frame forces similar to those produced in the non-skewed layout was determined by performing simulations of sub-models using Abaqus v6.8.2 (SIMULIA 2008). Sub-models consisted of three 9.14 m (30.0 ft) long sections of girder connected by cross-frames spaced every 4.57 m (15.0 ft) with a concentrated load applied to the center girder at mid-span. Sub-models with varied skew angle and bent plate stiffener thickness were evaluated; lateral forces computed in cross-frame members were used to match the cross-frame stiffness of skewed sub-models to that of the non-skewed sub-model. Angle sizes and connection stiffener thickness for each skew angle determined in this manner are provided in Table D.2. An exception to this procedure was made for bridges with 40° and 50° skew angles because the required connection stiffener thickness to match the forces in the non-skewed sub-model exceeded 38 mm ($1^1/_2$ in.), which was considered to be unrealistic. A larger equal-leg angle was selected for the cross-frame elements in those bridge layouts so that a maximum stiffener thickness of 25 mm (1 in.) would be sufficient to match the lateral forces computed in the non-skewed submodel. As a result, skewed cross-frames in 50° skewed bridges had the same equal-leg angle/stiffener combination as used in 40° skewed bridges, and the cross-frame stiffness was different due to the unrealistic plate size that would be needed to maintain the cross-frame forces nearly equal. While it is recognized that the use of a 25 mm (1 in.) thick stiffener is also questionable in terms of constructability, adopting such a large dimension was unavoidable due to the large effect that the stiffener properties have on cross-frame forces in bridges with large skew angles.

Detailed three-dimensional finite element (FE) models of the entire bridge superstructure were created using Abaqus v.6.8-2 (SIMULIA 2008). All materials were modeled as linear-elastic. Girders were defined as having a steel material model with a modulus of elasticity of 200,000 MPa (29,000 ksi) and Poisson's ratio of 0.30. The concrete deck was modeled with a modulus of elasticity of 24,850 MPa (3,605 ksi) and Poisson's ratio of 0.15. The mesh was highly refined in the web gap regions (Figure D.4), while a maximum mesh size of 50.8 mm (2.0 in.) was used for other steel parts; all elements were solid type, the majority being 8-node

brick elements. A mesh sensitivity analysis was performed before selecting a 152.4 mm (6.0 in.) mesh size for the concrete deck solid elements, making the bridge deck two elements thick. Surface-to-surface tie constraints were used to attach parts, and welds (modeled with solid elements and attached to the joined surfaces with tie constraints) were used to connect the web to the top and bottom flanges, connection stiffeners to the webs, and cross-frames to connection stiffeners. Interaction between connection stiffeners and girder flanges was defined using hard contact, which caused the connection stiffeners to bear on girder flanges when flange rotation was significant. The models each contained approximately 4 million elements and 27 million degrees of freedom. In most of the bridge models the supports were modeled by applying a translational restraint over a narrow, 50.8 mm (2.0 in.) strip of the bottom flanges. In a few models, behavior at supports was investigated in more detail by creating highly-refined renditions of the supports, as later discussed.

Table D.2: Cross-Frame Dimensions

Skew, degree	Angle, mm (in.)	Connection Stiffener Thickness, mm (in.)
0	L108x108x12.7 (L4.25x4.25x0.500)	9.53 (0.375)
10	L114x114x12.7 (L4.50x4.50x0.500)	9.53 (0.375)
20	L121x121x19.1 (L4.75x4.75x0.500)	19.1 (0.750)
30	L133x133x19.1 (L5.25x5.25x0.750)	22.2 (0.875)
40	L152x152x25.4 (L7.00x7.00x1.00)	25.4 (1.00)
50	L152x152x25.4 (L7.00x7.00x1.00)	25.4 (1.00)
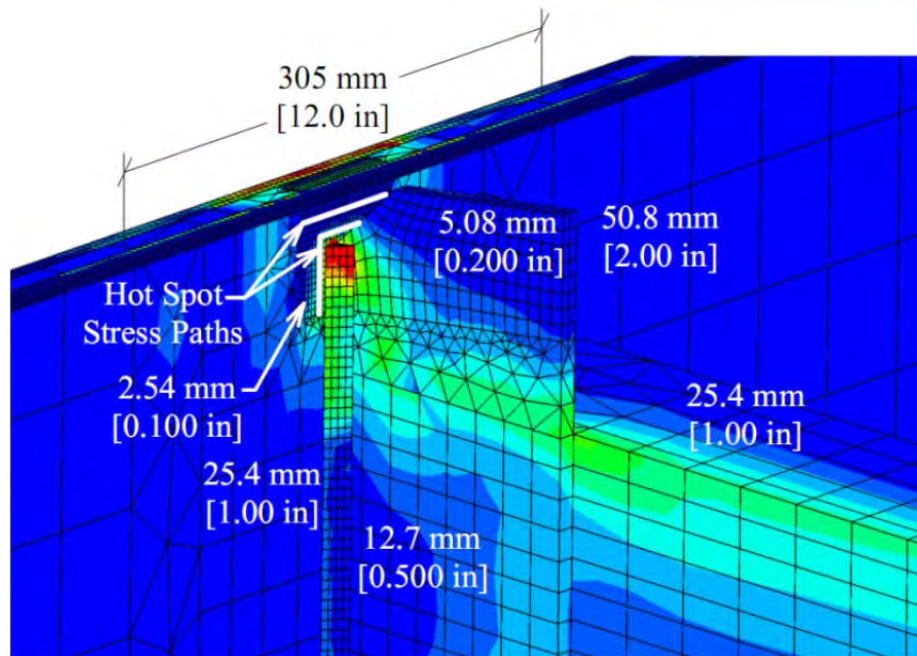
Figure D.4: Hot Spot Stress analysis and mesh sizes
Dimensions provided are element sizes

Loads applied to the bridge models consisted of the AASHTO (2013) fatigue truck load pattern placed at optimal locations chosen to induce the maximum principal stress demand at the web gap. Previous studies based on simpler computer models have focused on placing loads to maximize the differential deflection between adjacent girders (Berglund and Schultz 2006). An advantage of the high-resolution models employed in this study is that optimal load placement could be determined on the basis of the web gap stress demand, which provides a more direct measure of the potential for fatigue damage than the differential deflection. Additionally, prior research has demonstrated that the location of the truck load pattern that causes the maximum differential deflection between girders does not always coincide with the location that causes the maximum hot spot stress (HSS) in the web gap (Hartman et al. 2010).

The AASHTO fatigue truck load pattern (AASHTO 2013) was used because it is a commonly-accepted fatigue loading pattern that is easily repeatable between studies. The AASHTO fatigue truck design load was originally developed not to represent any particular vehicle type, but to capture the envelope of fatigue effects that could be expected by a multitude of service vehicles. More specifically, the AASHTO fatigue truck load pattern is expected to

329

produce a live-load stress approximately one-half that of the heaviest truck expected in 75 years. For this reason, the AASHTO fatigue truck load pattern is believed to be the most appropriate loading pattern for this study.

Optimal load placement was determined by analyzing FE models in which the load placement was varied systematically, using computed stress demands to develop influence and envelope surfaces showing the maximum principal HSS at the web gap. Three different bridge configurations were analyzed using the bridge geometry and modeling techniques previously described. All three bridge configurations had cross-frames spaced at 4.57 m (15.0 ft), with the cross-frame layout varied as follows: (1) non-skewed, (2) 40° skewed-parallel, and (3) 40° skewed-staggered. In each of the three layouts, the bridge deck was divided into a grid of 305 m (1.0 ft) squares for the purpose of defining the load placement. A series of 4.45 kN (1.0 kip) loads, each acting over an area of 645 mm^2 (1.0 ft^2), were applied, and maximum principal HSSs were extracted from each web gap in each model. The number of analysis jobs was reduced by analyzing models with loads densely populated for one half of the bridge and using a smaller number of jobs to verify symmetry when loads were placed on the other half of the bridge. A total of 400, 258, and 350 analysis jobs with different load placement were performed for the non-skewed, skewed-parallel, and skewed-staggered bridge layouts, respectively, for a total of 1,008 different job executions.

After influence and envelope surface analyses were completed, a second iteration of cross-frame stiffness optimization was carried out to refine the accuracy of the models. Stress demands computed using models with updated cross-frame dimensions were compared with companion models used to generate the influence surfaces and it was found that differences in the computed values of HSS were negligible.

D.1.6 Results

Results from (1) the influence/envelope surface analysis and (2) the parametric analysis are described in the following. Two separate paths were used to evaluate the potential for fatigue damage (Figure D.4) following the recommendation by Fisher et al. (1990). Maximum principal tensile stress magnitudes were extracted along each path, from both sides of the web, even when cross-frames were not placed back-to-back. The maximum principal tensile stress along each

path was adopted as the controlling HSS for that stress path. HSS1 and HSS2 are used herein to designate the maximum stress demands in the web near (1) the connection stiffener-to-web weld, and (2) the flange-to-web weld, respectively. HSS1 was evaluated separately from HSS2 at every cross-frame location because the relative importance of the two may be heavily affected by bridge geometry and weld quality.

D.1.6.1   Influence and Envelope Surface Results

Web gap stresses computed for each unit load placement were used to develop influence and envelope surfaces. An *envelope surface* is defined herein as a plot presenting the maximum HSS magnitude (occurring at any web gap in the bridge) for each load placement analyzed, with the magnitude of the maximum HSS plotted at the location corresponding to the load placement. Therefore, an envelope surface (Figure D.5) shows the load placement that produces the highest web gap stresses, although it does not offer any indication of where the maximum web gap stress takes place in the bridge, as an influence surface does.

Analysis results showed high HSS magnitudes with atypical stress distributions at web gaps near support locations. To investigate whether these stresses were meaningful values or artifacts caused by the simplified approach used to model the supports, several additional models were created having highly refined models of the bridge supports (Hassel 2011). For each different bridge layout, unit loads were placed at locations that induced high stress demands in the web gaps near the supports. A comparison of stress demands computed with refined and simplified support models showed that stress demands in the top and bottom web gaps at the supports were sensitive to the manner in which the supports were modeled, and that in models with simplified support constraints the computed demands at the web gaps were artificially inflated due to the boundary conditions. In addition, maximum HSS values computed at the supports of refined models were not as high as HSS values computed in other regions of the bridge. Therefore, for the remainder of the study analyses were performed with simplified support constraints and the HSS demands computed at the supports were neglected. While refined support simulations performed in this study showed that the web gap stresses at support locations were smaller than at other locations of the bridge, the authors caution that this may not be the case for bridge configurations different from those used in this study.

(a)HSS1

(b)HSS2
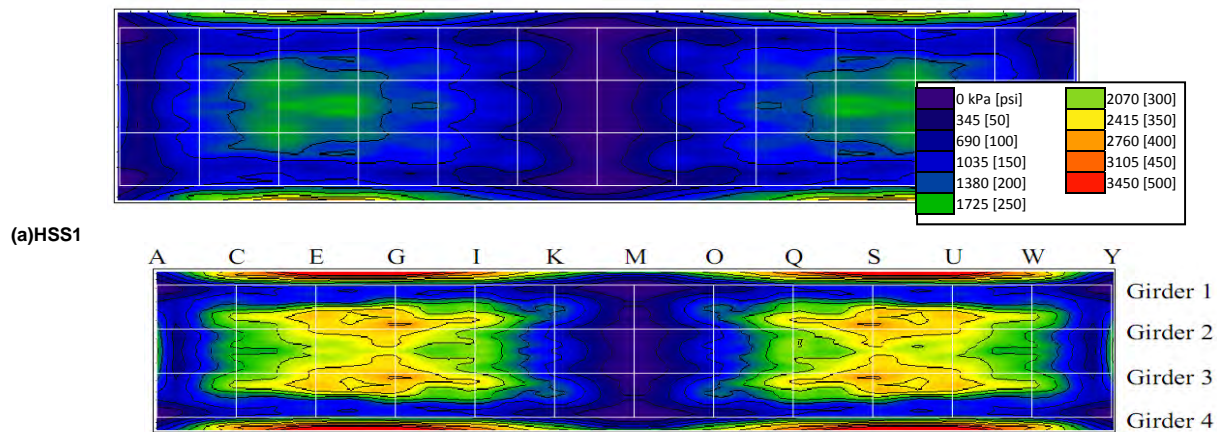
Figure D.5: Envelope surfaces for the non-skew bridge

Values of HSS1 and HSS2 in the non-skewed bridge are presented in Figure D.5 in the form of envelope surfaces. Results have been mirrored from load placements at the northwest (top left) quadrant of the bridge, which corresponded to the largest number of analysis jobs. Figure D.5 shows that HSS2 magnitudes were significantly higher than HSS1 in the non-skewed bridge configuration, and that loads placed near mid-span induced the greatest HSS. Critical load placements were determined from the envelope surfaces, which included loads placed at the deck overhang and the interior girders near mid-span for both HSS1 and HSS2. It is unlikely that fatigue loading would occur on the 1.07 m (3.5 ft) overhang of the bridge configurations analyzed in this study because that space would be occupied by the traffic barrier and roadway shoulder. Stresses computed with loads placed on the overhang are presented in Figure D.5 because they may be important for other bridge configurations, but are neglected in the remainder of this paper.

Maximum HSS2 magnitudes in the non-skewed bridge configuration occurred near mid-span, on the fascia side of the top web gap of exterior girders, and were caused by loads placed near the interior girders. The largest HSS1 magnitudes were produced by loads placed near an interior girder, near mid-span. As illustrated by the influences surface shown in Figure D.6, HSS1 was greatest near mid-span at the top web gap, on the interior side of exterior girders. The cross-frame-to-web intersection containing the web gap for which stresses are described in the influence surface is circled in Figure D.6. An important finding was that maximum HSS always

occurred when loads were placed on the bridge deck above the intersection of a cross-frame and girder web.
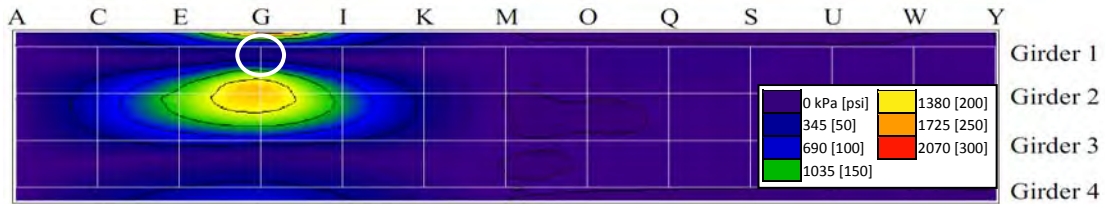
Figure D.6: HSS1 influence surface of the non-skewed bridge for the top web gap on the interior side of the north exterior girder in cross-frame row G

Analysis of the 40° skewed-parallel bridge showed a similar relationship between load placement and the location of the highest web gap stresses as the non-skewed bridge. This was expected, because the overall cross-frame layouts were similar, with cross-frames placed back-to-back in both cases. Maximum stresses occurred in the same web gaps as in the non-skewed bridge configuration: top web gaps within the positive moment region due to loads also placed in the positive moment region.

An influence surface is presented in Figure D.7(a) for the web gap in the skewed-parallel configuration that experienced the highest HSS1 magnitude. The maximum HSS1 magnitude was approximately 30% (6895 kPa [100 psi]) higher than the maximum HSS1 magnitude in the non-skewed bridge configuration. Maximum HSS2 was approximately 10% (345 kPa [50 psi]) lower than in the case of the non-skewed bridge configuration.

In the 40° skewed-staggered bridge configuration, maximum HSS occurred in the positive moment regions and were caused by loads placed in the positive moment region, similar to the other two bridge configurations. Other results for the 40° skewed-staggered bridge were notably different from those of the non-skewed and skewed-parallel bridge configurations. The magnitude of the largest HSS1 was between those computed for the non-skewed and 40° skewed-parallel bridge configurations. HSS1 was greatest in the bottom web gap of the loaded, interior girder, which caused HSS2 magnitudes to be significantly lower than those computed for the non-skewed and skewed-parallel bridge configurations. The transverse forces that the cross-frames exerted on the top web gap were lower than when maximum HSS1 occurred in the top

web gap, leading to lower web rotations and stress demands at the flange-to-web weld (HSS2) in the skewed-staggered configuration.

(a)Skewed-parallel bridge

(b)Skewed-staggered bridge
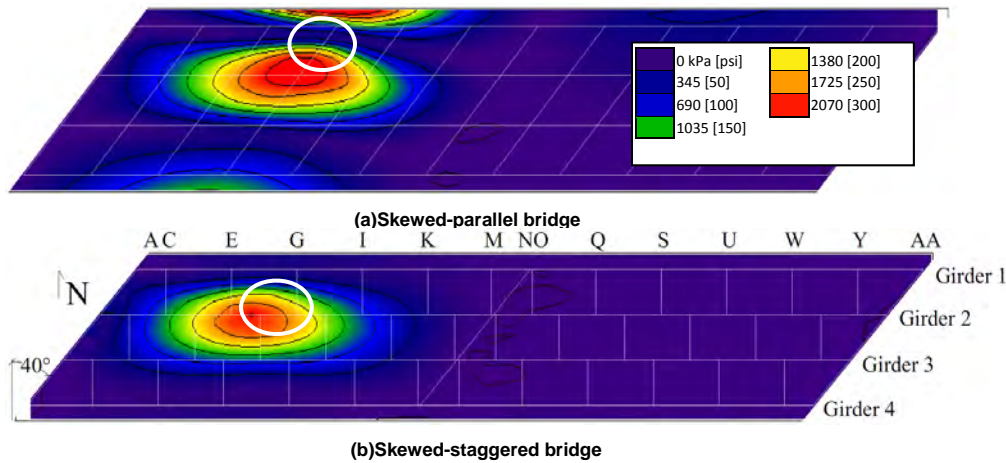
Figure D.7: HSS1 influence surfaces for cross-frame row G on the (a) Top web gap on the interior side of the north exterior girder and (b) Bottom web gap on the exterior side of the north interior girder

Based on the envelope and influence surface analysis of the three bridge configurations, it was determined that to produce maximum web gap stresses the fatigue truck loading pattern should be centered over an interior girder in the positive moment region. Girder 2 (in the west span) was selected as the loaded girder. Influence surfaces showed that the greatest stresses occurred due to loads placed on the bridge deck near a cross-frame-to-girder connection. Because cross-frame position varied significantly throughout this study, a consistent truck load placement routine was defined as follows. In all bridge configurations evaluated, the point of maximum positive moment along the loaded girder [11.0 m (36.0 ft) from either end of the bridge] was between the two rows of cross-frames that produced maximum HSS magnitudes. Accordingly, two different placements for the truck loading pattern were considered in subsequent parametric analyses for each bridge configuration, with each truck load placement centered over a row of cross-frames on either side of the point of maximum moment on Girder 2 (Figure D.1). The fatigue truck loading pattern was oriented with the front 142 kN (32.0 kip) axle over the cross-frame row of interest; directional orientation of the truck loading pattern (west-facing or east-facing) was chosen in each case to induce the maximum effect. Only results from the truck load placement which produced the highest stress demands are presented.

D.1.6.2 Parametric Analysis Results

A total of 60 different bridge configurations were evaluated for each of the two truck load placements defined in the loading procedure. In addition, skewed-parallel bridges were modeled with varied cross-frame stiffness, for a total of 130 FE models included in the parametric analysis. Results for HSS#1 and HSS#2 presented in Figures D.8 to D.11, and have been normalized to present the data in a form that may be most useful to designers. Data in Figures D.8 to D.10 have been normalized to a cross-frame spacing of 4.57 m (15.0 ft) and the non-skewed configuration, and data in Figure D.11 have been normalized to the non-skewed configuration.

(a)   (b)
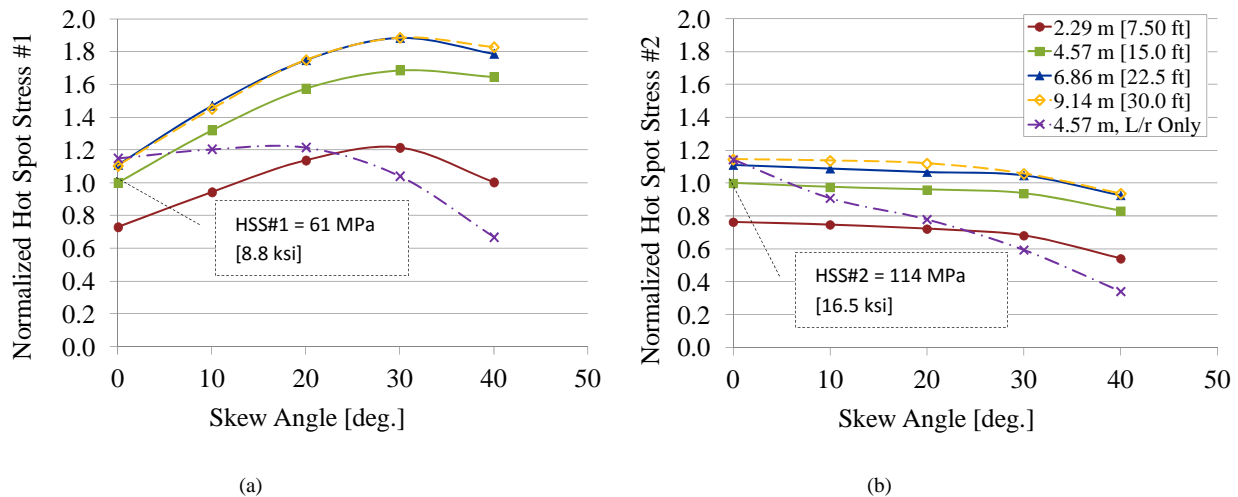
Figure D.8: HSS versus skew angle for skewed-parallel bridge layouts for each cross-frame spacing evaluated. Results have been normalized to a 4.57 m (15.0 ft) spacing and the non-skew configuration

335
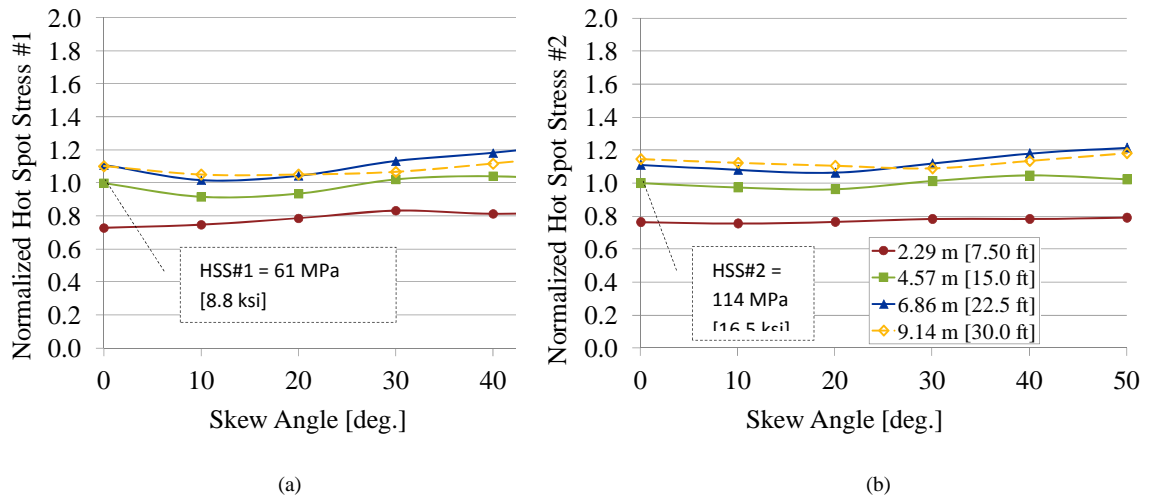
Figure D.9: HSS versus skew angle for skewed-unstaggered bridge layouts for each cross-frame spacing evaluated. Results have been normalized to a 4.57 m (15.0 ft) spacing and the non-skew configuration.
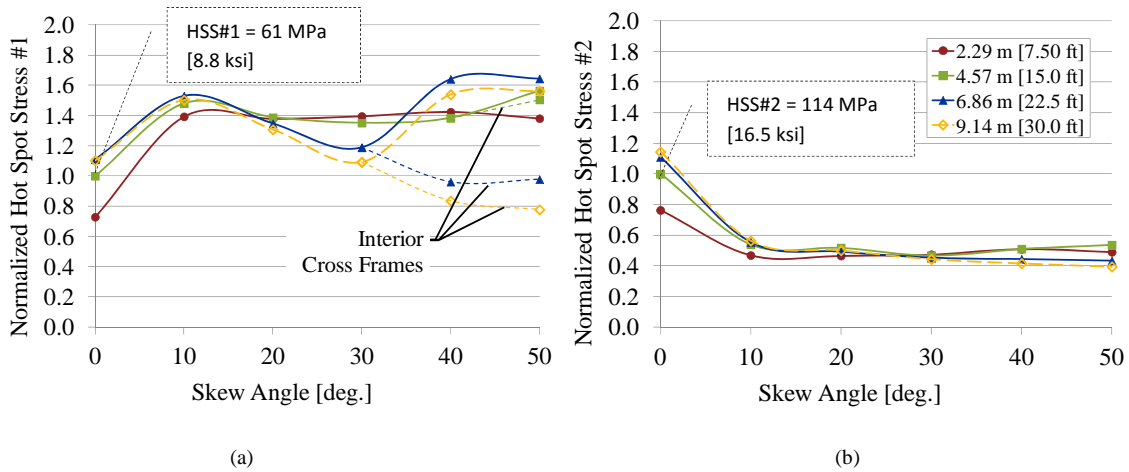
Figure D.10: HSS versus skew angle for skewed-staggered bridge layouts for each cross-frame spacing evaluated. Results have been normalized to a 4.57 m (15.0 ft) spacing and the non-skew configuration.

336
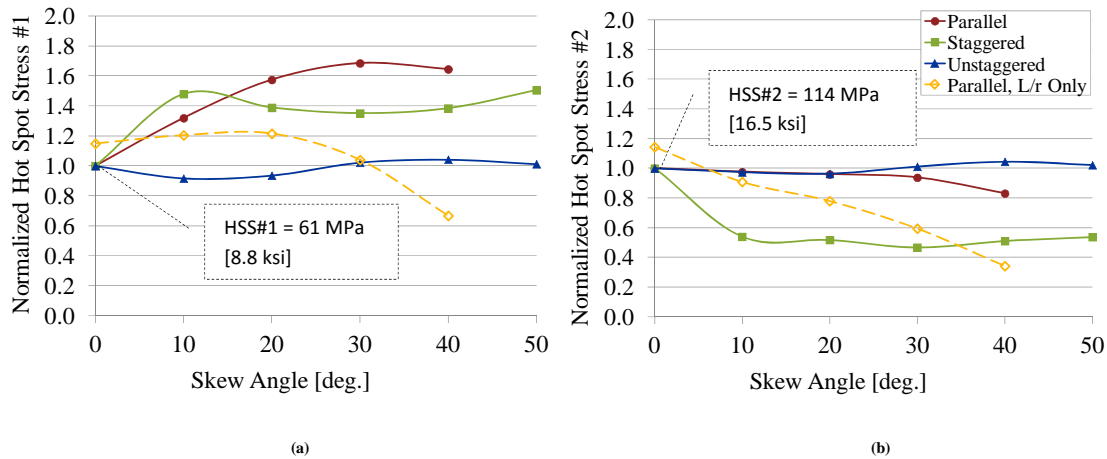
Figure D.11: HSS versus skew angle for layouts with a 4.57 m (15.0 ft) spacing Results have been normalized to the non-skew configuration

D.1.6.3   *Skewed-Parallel Bridge Configurations*

Results for skewed-parallel bridge configurations are presented in Figure D.8 and show the effect of skew angle, cross-frame spacing, and cross-frame stiffness on HSS1 [Figure D.8(a)] and HSS2 [Figure D.8(b)]. As skew angle increased, HSS1 generally increased and HSS2 decreased. However, HSS1 decreased between 30° and 40° skew angles. Cross-frame stiffness of the angle/stiffener combination used in 30° skewed models was slightly higher than that used in the 40° skewed models, because stiffener thickness was varied in 3.2 mm ($^1/_8$ in.) increments. The decrease in HSS1 from the 30° skew to the 40° skew is attributed to the sensitivity of the models to cross-frame assembly stiffness, which illustrates the importance of this parameter on computed web gap stresses.

Skewed-parallel cross-frames were proportioned to maintain lateral forces similar to other cross-frame layouts. In addition to a lateral force component, skewed cross-frames also carry a force component that is parallel to the girder line. Therefore, the axial force in the cross-frames increases with skew angle, which in turn magnifies the resultant force exerted on the web gaps and increases HSS1; this finding is consistent with results of previous research (Fisher and Mertz 1984).

Both HSS1 and HSS2 magnitudes were greater for bridges with large cross-frame spacing, as illustrated in Figure D.8. As cross-frame spacing increased, the number of cross-

337

frames decreased and the remaining cross-frames distributed a greater percentage of the load, increasing force (and HSS) in the remaining cross-frames. However, the change in stress was not consistent with each increase in spacing. Change in HSS was most significant when spacing increased from 2.29 to 4.57 m (7.50 to 15.0 ft), but was almost negligible when spacing increased from 6.86 to 9.14 m (22.5 to 30.0 ft). These results suggest that there is limit to the effectiveness of the cross-frames to distribute lateral loads as cross-frame spacing increases, and that for the bridges analyzed in this study that limit was reached when the cross-frame spacing reached 6.86 m (22.5 ft).

Provisions in previous versions of the AASHTO-LRFD Bridge Design Specification established an upper limit to cross-frame spacing of 7.62 m (25.0 ft) (AASHTO 2004), but in more recent versions of the LRFD Bridge Design Specification this limit has been removed in lieu of performing a rational analysis (AASHTO 2013). Many state DOTs still adhere to the limit established in the 2004 AASHTO Bridge Design Specification (IlDOT 2009, IoDOT 2010, KDOT 2010, and WDOT 2002). Results from models evaluated in this study suggest that in the bridge system examined, 7.62 m (25.0 ft) may be a reasonable upper limit for cross-frame spacing based on the live load distribution, as similar HSS magnitudes were found in bridges with 6.86 and 9.14 m (22.5 and 30.0 ft) cross-frame spacing. Results of the parametric analysis highlight that cross-frame spacing should be carefully selected; while large cross-frame spacing minimizes the number of fatigue prone details, it may increase susceptibility of each detail to distortion-induced fatigue and reduce the level of redundancy. This should also be carefully considered when cross-frames are removed as a retrofit procedure.

In addition to skew angle and cross-frame spacing, the effect of cross-frame stiffness on stress demand was also investigated in this parametric study. As discussed, cross-frame member/stiffener combinations were selected to have approximately equal stiffness on the basis of the lateral load imposed on the girders. It is acknowledged that the cross-frame member/stiffener combinations used herein are much larger those found in existing bridges; this was corroborated through a review of state DOT bridge design manuals and standard details (Colorado DOT 2009; Iowa DOT 2010; Kansas DOT 2010; Texas DOT 2009; and Wisconsin DOT 2002). The aforementioned State DOT bridge design provisions advise that angle sizes

should be selected based primarily or solely on slenderness considerations, and many do not address the effect of skew angle beyond its contribution to increased cross-frame length. Furthermore, provisions generally do not address the effects of the flexibility of the connection between the cross-frame and the web on the stiffness of the cross-frame assembly, which as previous research has shown, can be very significant (Yura 2001).

To address this concern, an additional set of cross-frame member/stiffener combinations representative of standard bridge construction practice were also analyzed for skewed-parallel bridges with 4.57 m (15.0 ft) cross-frame spacing. Cross-frames were proportioned based on L/r requirements only. L127x127x7.94 mm (L5x5x$^5/_{16}$ in.) angles were used for the 0° to 30° skewed-parallel bridge layouts and L152x152x9.53 mm (L6x6x$^3/_8$ in.) angles were used in the 40° skewed-parallel bridge. Stiffeners were sized to meet projecting width and moment of inertia limitations only, as is commonly performed in practice. A 9.52 x 127 mm ($^3/_8$ x 5.0 in.) stiffener was used in the non-skewed bridge and was lengthened to 152 mm (6.0 in) when the bent plate stiffener was used in skewed layouts.

Models with "L/r only" cross-frames used the same cross-frame member/stiffener combination throughout the bridge to maintain consistency between all models, although in practice connection stiffeners used at points of support would likely be larger than intermediate stiffeners because these stiffeners would be designed to accommodate large bearing load demands on the web at these points.

The significant effect of cross-frame stiffness on web gaps stress demand is illustrated in Figure D.8. Results show that cross-frame stiffness is an important parameter, having an equally significant effect on HSS as the other parameters investigated. In fact, in skewed-parallel bridges with "L/r only" cross-frames, HSS did not increase with skew. Instead, as skew angle increased, bracing became significantly more flexible and less effective in load transfer, and susceptibility to distortion induced fatigue was decreased.

While neglecting to properly account for cross-frame stiffness has important implications in terms of distortion-induced fatigue, there are broader implications that must be considered as well. Previous research by Yura (2001) and Wang and Helwig (2008) has shown the importance of properly quantifying brace and connection stiffness from a stability standpoint. Brace stiffness

339

should be selected with care to ensure that brace sizes are sufficiently large to stabilize girders during the erection sequence and adequately distribute lateral loads during operation of the bridge, as discussed by Yura (2001) and Wang and Helwig (2008). However, excessively large brace sizes when there is no connectivity between the brace and the flange increases the potential for damage due to distortion-induced fatigue.

D.1.6.4 *Skewed-Unstaggered Bridge Layouts*

Results from skewed-unstaggered bridge configurations are presented in Figure D.9. HSS2 magnitudes were over two times larger than HSS#1 magnitudes. Although these results suggest that for this bridge configuration fatigue cracking is more likely to occur at the flange-to-web intersection (HSS2) than at the web-to-stiffener weld due to the higher stress demand, it should be recognized that localized weld quality for individual details may be more of a critical parameter than stress demand alone. For example, in an experimental study performed by Fisher et al. (1990), very low occurrence of web-to-flange cracking was noted, and this was attributed to the unusually high weld quality of that detail in the specimens tested.

Both HSS1 and HSS2 remained approximately constant for all skew angles evaluated. Increasing cross-frame spacing amplified HSS; however magnitudes were similar for cross-frames spaced at 6.86 m (22.5 ft) and 9.14 m (30.0 ft).

D.1.6.5 *Skewed-Staggered Bridge Layouts*

Unlike all other bridge configurations evaluated, both skew angle and cross-frame spacing had a very significant effect on the out-of-plane girder deflection for skewed-staggered bridge configurations. Results are presented in Figure D.10. Out-of-plane deflections of the bottom flange of the girder were sensitive to the magnitude of the differential deflection, the stiffness of the cross-frames, and the spacing of the cross-frames. Because in this layout cross-frames were not oriented back-to-back, lateral forces imposed by adjacent cross-frames were transferred from one cross-frame to the next through weak-axis bending of the girder and torsion about the longitudinal axis of the girder (Fraser et al. 2000; Hartman et al. 2010). Previous studies have shown that live loads are not distributed efficiently through interior cross-frames in bridge systems in which the girders sustain large out-of-plane deflections (Barth and Bowman 2001).

340

Skew angle and cross-frame spacing influenced out-of-plane girder response in the following ways: (1) Increases in cross-frame spacing led to layouts with fewer cross-frames and higher cross-frame forces, which caused the torsion and bending moment of the girders about the weak-axis to increase; (2) Increased skew angle led to greater disparities in the distance between the cross-frame-to-web connection and the support of adjacent girders, causing the differential deflection to increase; and (3) Increasing the skew angle caused an increase in the degree of stagger and the distance between cross-frames, which increased the flexibility of the girder with respect to weak axis bending and torsion.

The relatively large out-of-plane girder deflections found in the skewed-staggered bridge configurations led to a shift in the location of maximum HSS1. The maximum HSS in the bottom web gap of the loaded girder, at the abutment, and the HSS1 at interior cross-frames are shown in Figure D.10. Intermediate cross-frames were not very effective in the distribution of live loads for bridge configurations with large skew angle and large cross-frame spacing because the relatively large distance between cross-frames significantly increased the flexibility of the girders with respect to bending about the weak axis. The maximum HSS1 for this type of configuration was found at the supports, where cross-frames were placed back-to-back. HSS1 magnitudes were relatively high in these cases due to the large difference in the vertical flexibility at the cross-frame-to-web connections of adjacent girders. Unlike interior spans, both flanges of the girder are restrained at the support and there is a significant difference in the distance between the cross-frame-to-web connection and the support of adjacent girders. Both of these factors contributed to a much larger percentage of the live load being transmitted through the cross frame than at intermediate cross-frames. Additional models with refined boundary conditions were used to verify that the computed HSS magnitudes were not a numerical artifact caused by inadequate modeling of the boundary conditions (Hassel 2011).

D.1.6.6   Comparison of Bridge Layouts

Figure D.11 presents results for all bridge configurations with cross-frames spaced at 4.57 m (15.0 ft). Skewed-unstaggered configurations exhibited the lowest HSS1 magnitudes (excluding the skewed-parallel models with (L/r)-based cross-frame stiffness). However, HSS2

was highest in skewed-unstaggered configurations, highlighting the importance of considering both potential crack locations when evaluating risk of distortion-induced fatigue.

In bridge configurations with 4.57 m (15.0 ft) cross-frame spacing, HSS was higher in skewed-parallel than in skewed-staggered bridge configurations, which suggests that skewed-staggered bridges may be less susceptible to distortion-induced fatigue than skewed-parallel bridges. This is contrary to the common perception that skewed-parallel bridge configurations are less susceptible to distortion-induced fatigue. Because the cross-frame stiffness was maintained nearly constant between models regardless of cross-frame layout, it is important to note that design provisions adopted by most DOTs would lead to cross-frames with different lateral stiffness for the skewed and non-skewed bridge configurations, and that models with skewed-parallel configurations and "L/r-only" cross-frame sizes exhibited lower HSS#1 magnitudes than either the skewed-staggered or skewed-parallel layouts with matched cross frame stiffnesses. Although this finding supports the practice of using skewed-parallel layouts for bridge configurations with skew angles greater than 20 degrees when the cross-frames are proportioned on the basis of the slenderness ratio (L/r) and commonly-used connection plate dimensions are utilized, caution must be exercised to ensure that the increased flexibility of the cross-frames is sufficient to provide lateral stability to the girders during the construction phase of bridge. In these instances it is also important to verify that the reduced ability to distribute live loads through the cross-frames is properly factored in the design of the girders.

Relative HSS2 magnitudes were similar for all cross-frame spacings evaluated, with skewed-staggered bridge configurations producing the lowest stresses. HSS1 also had similar maxima for all cross-frame spacings except 2.29 m (7.50 ft). Skewed-staggered bridge configurations had higher HSS#1 than skewed-parallel bridge configurations for models with cross-frames spaced at 2.29 m (7.50 ft).

D.1.7 Conclusions

The effects of skew angle, cross-frame spacing, bracing layout, cross-frame stiffness, and load placement on bridge susceptibility to distortion-induced fatigue were evaluated by performing more than 1,000 analysis jobs of high-resolution 3D finite element models. The following conclusions were drawn by analyzing the results of the computer simulations:

- Two distinct locations prone to the initiation of fatigue cracks were identified in the web gap region; one at the connection stiffener-to-web weld (HSS1) and another at the flange-to-web weld (HSS2). Both are important in assessing the vulnerability to fatigue damage and should be examined independently.
- Maximum HSS magnitudes occurred in top web gaps of girders in regions of positive bending when cross-frames were placed back-to-back, but occurred in bottom web gaps of skewed-staggered bridge configurations. Maximum HSS was always produced when loads were placed on the bridge deck above the intersection of a cross-frame and girder web.
- In skewed-parallel bridge configurations, the stress demand at the web-to-stiffener weld (HSS1) increased with skew angle, while the stress demand at the web-to-flange weld (HSS2) decreased with skew angle. Skew angle did not have a significant effect on HSS in skewed-unstaggered bridge configurations.
- Increases in cross-frame spacing in non-skewed, skewed-parallel, and skewed-unstaggered bridge configurations led to increased HSS at both weld locations (HSS1 and HSS2). For the bridge configurations analyzed in this study it was found that this effect became negligible when the cross-frame spacing exceeded 6.86 m (22.5 ft) as evidenced by the fact that HSS magnitudes were similar for bridges with cross-frames spaced at 6.86 m (22.5 ft) and 9.14 m (30.0 ft).
- Out-of-plane girder deflections had a very significant effect on the location and magnitude of the HSS in skewed-staggered bridge configurations. The out-of-plane girder deflections were proportional to the flexibility of the girder with respect to bending about the weak axis and torsion, which were related to cross-frame spacing or the skew angle.
- Stiffness of both cross-frame elements and connection stiffeners had a significant impact on the susceptibility to distortion-induced fatigue and was found to be as important as other evaluated parameters, including skew angle and cross-frame spacing. Larger cross-frame and connection plate sizes corresponded with increased web gap HSS.
- In skewed-parallel bridges with "L/r only" cross-frames spaced at 4.57 m (15.0 ft), HSS did not increase with skew angle. Instead, bracing became more flexible with the increased skew angle, and was less effective in load transfer. Subsequently, distortion-induced fatigue susceptibility was

343

lessened; however, the reader is cautioned that skewed bracing should also be designed considering lateral stability demands of the girders.

- Given the relationship that was found between cross-frame stiffness and web gap HSS, the relative stiffnesses of the cross-frames within a bridge may control the region of the bridge most susceptible to distortion-induced fatigue cracking. This may be one reason previous literature presents conflicting conclusions regarding the region of the bridge most vulnerable to distortion-induced fatigue.

It is of great importance for public safety and efficient bridge maintenance to identify parameters that affect the potential for damage due to distortion-induced fatigue in steel bridges. This study evaluated the effect of skew angle, cross-frame spacing, cross-frame layout, and cross-frame stiffness on HSS, which was used to quantify the potential for fatigue crack initiation.

It should be noted that other parameters such as geometric properties of the bridge and the characteristics of the slab also may have a significant effect on distortion-induced fatigue damage and that the findings of this study are not intended to imply otherwise. Future research should carefully examine other bridge parameters to determine their effects upon distortion-induced susceptibility. Additionally, research is needed in the area of curved and skewed-curved bridges to determine susceptibility of such systems to distortion-induced fatigue. Finally, the authors would like to stress the importance of field observation to follow the analytical study described in this paper.

D.1.8 References

AASHTO (2004). AASHTO LRFD Bridge Design Specifications. 3rd ed. American Association of State Highway and Transportation Officials, Washington, D.C.

AASHTO (2013). 2013 Interim Revisions to the AASHTO LRFD Bridge Design Specifications. 6th ed. American Association of State Highway and Transportation Officials, Washington, D.C.

Adams, C. (2009). Finite Element Study of Bridge Details Susceptible to Distortion-Induced Fatigue. (Master's thesis). University of Kansas, Lawrence, KS.

AISC (2005). Steel Construction Manual. 13th ed. American Institute of Steel Construction, Chicago, IL.

AISI Example 2: Two-Span Continuous Composite I Girder (1997). American Iron and Steel Institute, Washington, D.C.

Alemdar, F. (2011). Repair of Bridge Steel Girders Damaged by Distortion-Induced Fatigue. (Ph.D. dissertation). University of Kansas, Lawrence, KS.

Barth, A. S. and Bowman, M. D. (2001). "Fatigue Behavior of Welded Diaphragm-to-Beam Connections." Journal of Structural Engineering, 127(10), 1145-1152.

Barth, K. E., Hartnagel, B. A., White, D. W., and Barker, M. G. (2004). "Recommended Procedures for Simplified Inelastic Design of Steel I-Girder Bridges." Journal of Bridge Engineering, 9(3), 230-242.

Berglund, E. and Schultz, A. (2006). "Girder Differential Deflection and Distortion-Induced Fatigue in Skewed Steel Bridges." Journal of Bridge Engineering, 11(2), 169-177.

Colorado Department of Transportation (2009). Bridge Design Manual. Colorado Department of Transportation, Denver, CO.

Connor, R. J. and Fisher, J. W. (2006). "Identifying Effective and Ineffective Retrofits for Distortion Fatigue Cracking in Steel Bridges Using Field Instrumentation." Journal of Bridge Engineering, 11(6), 745-752.

Fisher, J. W., Barthelemy, B. M., Mertz, D. R., and Edinger, J. A. (1980). Fatigue Behavior of Full-Scale Welded Bridge Attachments. NCHRP Report 227. Transportation Research Board, National Research Council, Washington, D.C.

Fisher, J. W., Jian, J., Wagner, D. C., and Yen, B. T. (1990). Distortion-Induced Fatigue Cracking in Steel Bridges. NCHRP Report 336. Transportation Research Board, National Research Council, Washington, D.C.

Fisher, J. W. and Mertz, D. R. (1984). "Fatigue and Fracture in Steel Bridges." The Conference on Bridges Official Proceedings, 1st International Bridge Conference, 10-21. Engineers' Society of Western Pennsylvania, Pittsburgh, PA.

Fraser, R. E. K., Grondin, G. Y., and Kulak, G. L. (2000). Behaviour of Distortion-Induced Fatigue Cracks in Bridge Girders. Structural Engineering Report no. 235. University of Alberta, Edmonton, Canada.

Gangel, R. E. (2012). Use of CFRP Overlays to Repair Fatigue Damage in Steel Bridge Girders and Components. (Master's thesis). University of Kansas, Lawrence, KS.

Hartman, A., Hassel, H., Adams, C., Bennett, C., Matamoros, A., and Rolfe, S. (2010). "Effects of Cross-Frame Placement and Skew on Distortion-Induced Fatigue in Steel Bridges." Transportation Research Record 2200, 62-68. Transportation Research Board, National Research Council, Washington, D.C.

Hassel, H. L. (2011). An Analytical Evaluation of Distortion-Induced Fatigue in Steel Bridges. (Master's thesis). University of Kansas, Lawrence, KS.

Illinois Department of Transportation (2009). Bridge Manual. Illinois Department of Transportation Bureau of Bridges and Structures, Springfield, IL.

Iowa Department of Transportation (2010). LRFD Bridge Design Manual. Iowa Department of Transportation Office of Bridges and Structures, Ames, IA.

Jajich, D. and Schultz, A. E. (2003). "Measurement and Analysis of Distortion-Induced Fatigue in Multigirder Steel Bridges." Journal of Bridge Engineering, 8(2), 84-91.

KDOT (2010). Design Manual: Volume III–Bridge Section. Kansas Department of Transportation, Topeka, KS.

Khalil, A., Wipf, T. J., Greimann, L., Wood, D. L., and Brakke, B. (1998). "Retrofit Solution for Out-of-Plane Distortion of X-Type Diaphragm Bridges." Transportation Conference Proceedings, Iowa Department of Transportation, 99-102.

Li, H. and Schultz, A. E. (2005). Analysis of Girder Differential Deflection and Web Gap Stress for Rapid Assessment of Distortional Fatigue in Multi-Girder Steel Bridges: Final Report. MN/RC-2005-38. Minnesota Department of Transportation, St. Paul, MN.

Roddis, W. M. K. and Zhao, Y. (2001). "Out-of-Plane Fatigue Cracking in Welded Steel Bridges: Why It Happened and How It Can Be Repaired." Welding Innovation, 18(2), 2-7.

SIMULIA. (2008). Abaqus FEA, Version 6.8.2. Providence, RI. http://www.simulia.com

Texas Department of Transportation (2009). Bridge Design Manual – LRFD. Texas Department of Transportation, Austin, TX.

Wang, L. and Helwig, T. A. (2008). "Stability Bracing Requirements for Steel Bridge Girders with Skewed Supports." Journal of Bridge Engineering, 13(2), 149-157.

Wisconsin Department of Transportation (2002). Bridge Manual. Wisconsin Department of Transportation, Madison, WI.

Yura, J. (2001). "Fundamentals of Beam Bracing." Engineering Journal, 38(1: 1st Qtr.), 11-26.

Yura, J., Phillips, B., Raju, S., and Web, S. (1992). Bracing of Steel Beams in Bridges. Research Report 1239-4F. Center for Transportation Research, University of Texas at Austin.

Zhao, Y. and Roddis, W. M. K. (2003) "Finite Element Study of Distortion-Induced Fatigue in Welded Steel Bridges." Transportation Research Record 1845, 57-65. Transportation Research Board, National Research Council, Washington, D.C.

D.2: Effects of Lateral Bracing Placement and Skew on Distortion-Induced Fatigue in Steel Bridges

Amanda S. Hartman[16],

Heidi L. Hassel[17],

Chris A. Adams[18],

Caroline Bennett[19], M. ASCE

Adolfo Matamoros[20], A.M. ASCE

Stan Rolfe[21], Hon. M. ASCE

D.2.1 Abstract

Due to the structural configuration of skewed steel bridges, girders at the same station are likely to experience different bending moments and deflections. Resulting differential deflections between adjacent girders leads to out-of-plane secondary stresses, which often results in a fatigue-critical connection between the cross frames and the girders. For this reason skewed steel bridges are particularly susceptible to distortion-induced fatigue.

This research explored the importance of lateral bracing placement in protecting bridges against distortion-induced fatigue. High-resolution three-dimensional finite element analyses of a bridge with multiple brace and skew configurations were performed to examine the relationships between skew angle, lateral bracing placement, and stresses at regions susceptible to distortion induced fatigue cracking. Bridges with skew angles of 0, 20, and 40 degrees and cross frames spaced at both 4.58 m (15 ft) and 9.15 m (30 ft) were investigated. Lateral bracing configurations examined included cross frames staggered perpendicular to the web of the girders as well as cross frames parallel to the support skew.

---

[16] Amanda S. Hartman, PhD, Structural Engineer, Burns and McDonnell, 9400 Ward Pkwy, Kansas City, MO 64114

[17] Heidi L. Hassel, MS, Structural Engineer, Burns and McDonnell, 9400 Ward Pkwy, Kansas City, MO 64114

[18] Chris A. Adams, Graduate Research Assistant, University of Kansas, 1530 W. 15th St., 2150 Learned Hall, Lawrence, KS 66045

[19] Caroline Bennett, ,PhD, PE, Associate Professor, University of Kansas, 1530 W. 15th St., Lawrence, KS 66045,

[20] Adolfo Matamoros, PhD, Professor, University of Kansas, 1530 W. 15th St., Lawrence, KS 66045

[21] Stan Rolfe, PhD, PE, A.P. Learned Distinguished Professor, University of Kansas, 1530 W. 15th St., Lawrence, KS 66045

The analysis conducted found maximum stresses in the web gap occurred in positive moment regions, but not necessarily in regions of highest differential deflection. The location of maximum stress demand was in the top web gap region in configurations with cross frames parallel to skew, but in the bottom web gap region when cross frames were staggered. Furthermore, skew angle and cross frame spacing slightly increased the maximum stress for parallel to skew cross frame arrangement.

D.2.2 Background

D.2.2.1 Distortion-Induced Fatigue

Distortion-induced fatigue is an undesired consequence initially born from an attempt to solve an existing fatigue problem in steel bridges. Prior to 1980, it was common to deliberately not attach connection stiffeners to girder flanges in an effort to avoid creating additional fatigue details. Several fatigue failures in tension flanges of European bridges in the 1930's reinforced the desire to avoid introducing imperfections and discontinuities in regions of high tensile stresses by not welding connection stiffeners to tension flanges (Fisher and Keating 1989). However well intentioned, high stress concentrations in the web gap region resulted from out-of-plane distortion in the absence of positive connection between the flange and transverse connection stiffener.

Most often, distortion-induced fatigue occurs at connections of transverse structural members (Khalil et al. 1998). Lateral braces between adjacent girders, connected to girder webs through transverse connection plates, are required to prevent instability during construction and aid in lateral load transfer between girders; however, web gaps between connection plates and girder flanges are the most common location for fatigue cracking. As load is applied, differential deflection occurs between adjacent steel girders. Because the top flange is restrained from lateral displacement by the concrete deck and the bottom flange is free to rotate, distortion occurs in the relatively flexible region of the unsupported web between the flange and connection stiffener (Figure D.12).
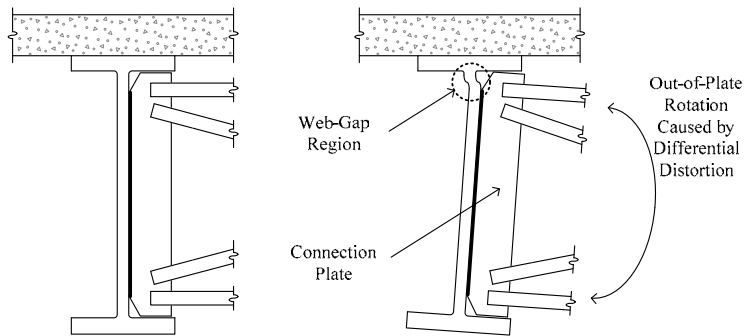
Figure D.12: Girder cross-section before and after differential displacement.

With web gap distortion accounting for the majority of fatigue cracks in bridges across the United States, there is a substantial body of literature (Roddis and Zhao 2001; Lindberg and Schultz 2007; Keating 1994; Connor and Fisher 2006; Fisher et al. 1990) including analytical and experimental studies investigating the expected performance of and repair methods for steel bridge girders subjected to distortion-induced fatigue. There has been much discussion about the location along a girder's length where fatigue cracks in the web gap region are most likely to form. A literature review conducted as part of this study did not show agreement between various studies due to the number of possible bridge geometric configurations (Berglund and Schultz 2006; Roddis and Zhao 2001; Khalil et al. 1998; Jajich and Schultz 2003; Barth and Bowman 2001; Fraser et al. 2000; Grondin et al. 2002; Roddis and Zhao 2003).

There is repeated disagreement concerning the region within continuous-span bridges most likely to experience distortion-induced fatigue cracking. Roddis and Zhao (2003) state that cracking in unskewed (i.e., right) bridges most frequently occurs in positive moment regions of bridge girders where differential girder deflections and out-of-plane bending moments are greatest. Conversely, Khalil et al. (1998) investigated a skewed bridge with X-type cross frames, and found that eight out of nine cracks due to differential deflections between adjacent girders occurred in the negative moment region. It should be noted that while there is evidence that distortion-induced fatigue may be problematic in negative bending regions of bridges (Khalil et al. 1998; Jajich and Schultz 2003), this limit state is more likely to occur if the bridge is skewed.

Several parameters have been found to have significant effects on bridge girder differential deflections. These parameters, examined using staggered diaphragms susceptible to web-gab distortion, include: girder spacing, angle of skew, span length, and deck thickness

349

(Berglund and Schultz 2006). Increasing skew angle tends to increase distortion-induced fatigue as quantified by increased differential deflection (Jajich and Schultz 2003), except in situations where the truck length approaches the span of the bridge (Berglund and Schultz 2006). Longer spans decrease differential deflections as the bridge is more flexible in the vertical direction and more uniform lateral load distribution between girders can occur. Berglund and Schultz (2006) found a linear relationship between differential deflection and girder spacing.

D.2.2.2 *Skewed Bridges*

Bridge supports are often skewed to accommodate complicated highway alignments, and the skew angle of the bridge influences distortion-induced fatigue demand placed on bridge girders. AASHTO Specifications (2013) allow bracing to be installed parallel to the skew angle if skew is less than 20 degrees [Figure D.13(a)]. However, when the skew angle is greater than 20 degrees, lateral connections and braces become too flexible due to longer brace lengths. Because of this, AASHTO (2013) specifies that bracing must be installed perpendicular to girders' webs for bridges skewed more than 20 degrees.

Bracing may either be non-staggered [Figure D.13(b)] or staggered [Figure D.13(c)], and it has been shown that stagger has an effect on the susceptibility of a bridge to fatigue cracks (Barth and Bowman 2001 and Fraser et al. 2000). However, conflicting conclusions have again been noted in the literature. Barth and Bowman (2001) reported that non-staggered diaphragms were more susceptible to fatigue cracking than comparable staggered diaphragm configurations. Conversely, Fraser, Grondin, and Kulak (2000) reported that when diaphragms were in a staggered configuration, fatigue cracks were found to be more pronounced than in bridges with unstaggered bracing.

(a) **(b)** **(c)**
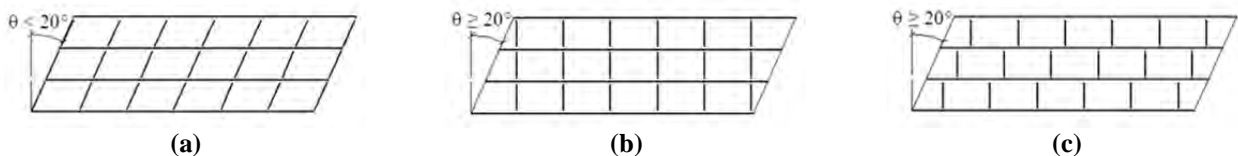
Figure D.13: Cross frame arrangements
(a) Skew < 20˚, cross frames placed parallel to skew; (b) Skew ≥ 20˚, non-staggered cross frames placed perpendicular to web; (c) skew ≥ 20˚, staggered cross frames placed perpendicular to web.

Estimates of remaining fatigue life for welded structures are commonly based on a nominal stress distribution away from the point of crack initiation. Because high stress gradients occur in the vicinity of welds and nominal stresses cannot be easily determined in regions of complex geometry (Roddis and Zhao 2003; Kim and Kang 2008), AASHTO (2013) S-N curves are not accurate predictors of fatigue life in these applications. To overcome this problem, analysis techniques have been developed to estimate the number of fatigue cycles to crack initiation using stress results from Finite Element (FE) analyses. One such method is Hot Spot Stress (HSS) analysis.

HSS analysis is defined as the sum of bending and membrane stresses at a structural discontinuity (Marquis and Kahonen 1996). Membrane stress is taken as the stress resulting from the effect of axial load only (axial load divided by an area). This analysis technique utilizes either a one-point procedure or a two-point extrapolation procedure to estimate the level of stress at the weld toe. The process of HSS analysis begins with calculating stress at a predetermined distance away from the weld toe. This distance is usually calculated based on plate thickness and/or weld length, and must be sufficiently far from the weld toe so that stresses are not influenced by the high stress gradients commonly observed at weld toes.

Although stresses are taken at points away from the weld toe, HSS analysis is dependent on mesh, element type, and extrapolation technique (Maddox 2002), which are important limitations. Despite limitations, HSS analysis is needed to examine distortion-induced stresses in steel bridge girders because nominal stress cannot be determined with confidence using closed form solutions, and was used in this study.

D.2.3 Modeling Methodology

D.2.3.1   Parameters for Study

Among the many parameters known to affect distortion-induced fatigue cracking in steel bridges, skew angle and cross frame placement are two widely varied parameters. To investigate the effects of skew and lateral brace placement on distortion-induced fatigue performance of steel bridges, three skew angles were chosen for study: 0, 20, and 40 degrees. Cross frame spacing was also varied, with spacings of 4.58 m (15.0 ft) and 9.15 m (30.0 ft). AASHTO (2013)

351

does not allow cross frames to be placed parallel to the skew angle in bridges with skew angles over 20 degrees, therefore, it was necessary to evaluate bridges with cross frames placed parallel to skew as well as placed perpendicular to the girder webs and staggered. There are several bridges in existence that have cross frames placed parallel to skew, with skew angles beyond 20 degrees. Additionally, it is worthwhile to investigate the effect of this parameter on bridge response to better understand the parameters that affect distortion-induced stresses in steel bridges. Therefore a 40 degree bridge was also analyzed. A total of ten finite element models (Table D.3) were created for analysis.

Table D.3: Finite Element Models Analyzed

Skew Angle	Parallel to Skew		Staggered	
	4.575 m (15 ft)	9.150 m (30 ft)	4.575 m (15 ft)	9.150 m (30 ft)
0	X	X		
20	X	X	X	X
40	X	X	X	X

D.2.3.2   Bridge Specifications

Bridge dimensions chosen for analysis were adapted from American Iron and Steel Institute (AISI) Example 2 (1997). The bridge consisted of two 27.5 m (90.0 ft) continuous spans with girder spacing of 3.05 m (10.0 ft). Positive and negative cross-section dimensions as well as an elevation of the bridge are shown in Figure D.14. This bridge was chosen for study because its complete design is widely available to interested readers, its typicality for two-span continuous bridge structures, and its use in other scientific articles to illustrate bridge engineering concepts (Barth et al. 2004).
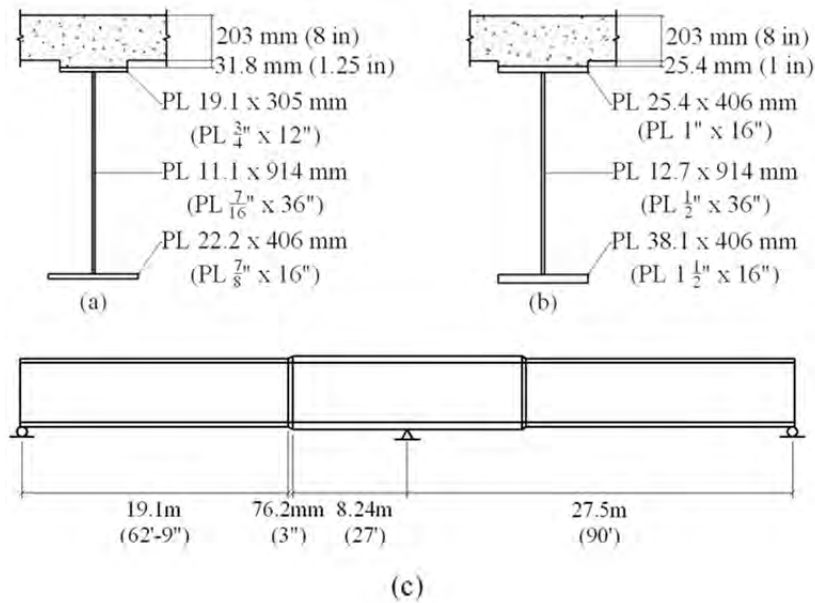
**Figure D.14: Cross-sections
(a) Positive girder cross-section. (b) Negative girder cross-section. (c) Location of positive and negative cross-sections.**

Four different cross frame placements were considered: parallel to the angle of skew and staggered perpendicular to the girder web for 4.58 m (15.0 ft) and 9.15 m (30.0 ft) spacing. Cross frame arrangements have been presented in Figure D.15, shown with 4.58 m (15.0 ft) spacing. The dashed lines in Figure D.15 represent the cross frames that were removed to form the 9.15 m (30.0 ft) spacing arrangement.
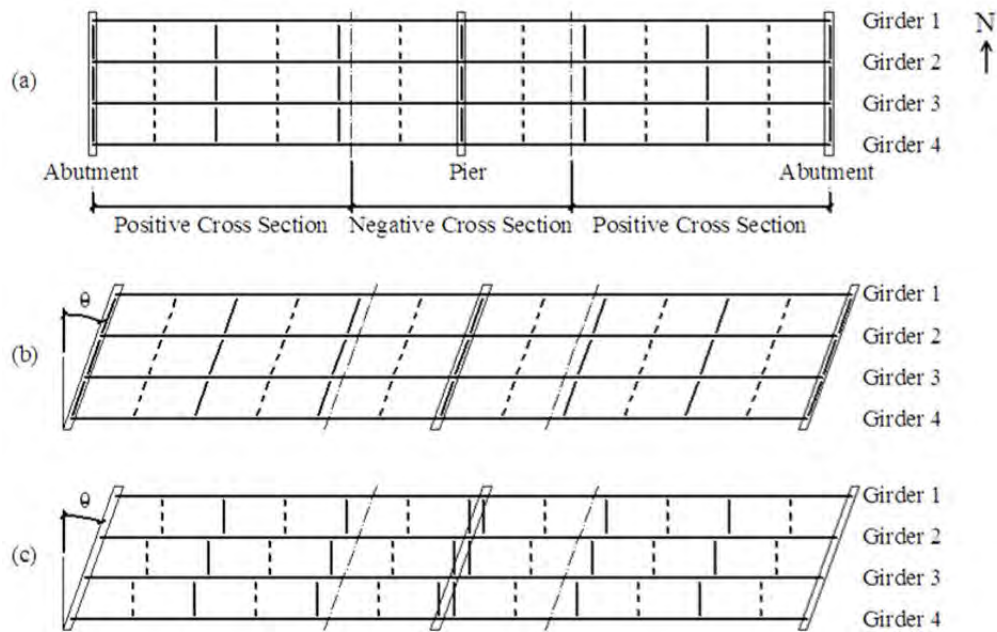
Figure D.15: Cross frame locations
(a) Right bridge cross frame locations; (b) Skewed bridge parallel to skew cross frame locations; (c) Skewed bridge staggered cross frame locations.

Cross frame members were designed based on slenderness in compression with a maximum effective slenderness ratio, KL/r, of 140 (NSBA). For the right bridge and the 20 degree skewed bridge with cross frames parallel to the skew, L102 X 102 X 15.9 mm (L4 X 4 X 5/8) brace elements were chosen with slenderness ratios 100 and 106 respectively. The 40 degree skewed bridge with cross frames placed parallel to the skew required WT 152 X 365 (WT 6 X 25) brace elements with a slenderness ratio of 97.9 to counteract the longer unbraced length due to the high degree of skew. All bridges with cross frames perpendicular to the web required utilized the same cross frames modeled in the right bridge.

To reflect construction constraints in a realistic manner, the connection plates for the skewed cross frames were modeled as bent rectangular plates. Bent connection plates allow for adequate welding around all sides perpendicular to the web, instead of attempting welds at acute angles. Connection plate dimensions are shown in Figure D.16.
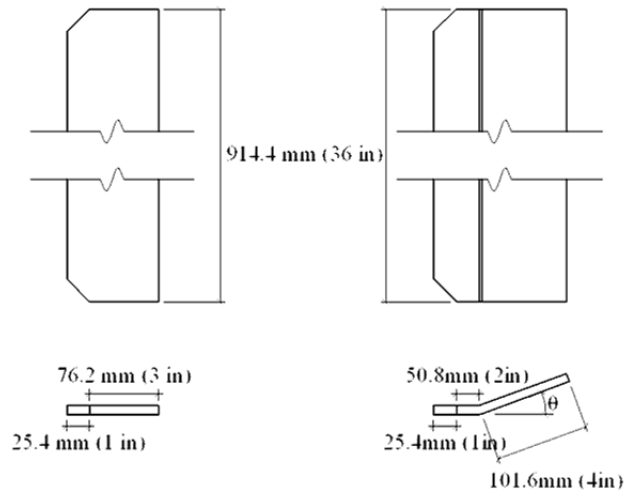
Figure D.16: Connection plate details

D.2.3.3　　Finite Element Modeling

A detailed analytical investigation was completed for each bridge using the commercially available FE modeling software Abaqus v.6.8-2. Each three-dimensional model was composed of five main parts: deck, girder top flanges and concrete haunch, girder webs, girder bottom flanges, and cross frames. These parts were needed to create densely meshed web gap regions, but simplified meshes and elements away from the areas under investigation. The adopted modeling strategy simplified the structure, while allowing for detailed analyses of areas of interest. Model parts were rigidly connected using surface-to-surface tie constraints. Element types, mesh sizes, constraints, and boundary conditions remained constant between models.

The deck was modeled using a linear-elastic material and four-node shell elements (S4R) with a mesh size of approximately 1.07 m (3.50 ft). Shell elements were chosen for the deck to improve computational efficiency. The reinforced concrete deck elements were eight inches thick and loaded on the top surface using a pressure load.

The load was applied over a 2.14 m (7.00 ft) width of deck centered over the third girder, and was continuous over the entire length of the bridge. The loaded section skewed along with the skew angle of the bridge, but the total area did not change. A 10.3 Pa (0.0015 ksi) pressure was used for a total load magnitude of 1220 kN (274 kips). The load chosen produced stress values large enough to make comparisons more meaningful and readily apparent to the reader. It should be noted that load placement was not studied as a varied parameter in this article,

although it is recognized that it would likely have an effect on distortion-induced stresses. Instead, load placement was held constant so that valid comparisons could be made between lateral brace placements and skew angles.
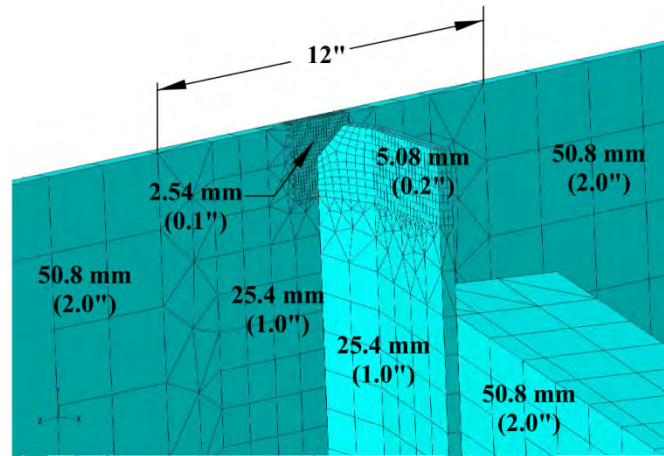
Figure D.17: Mesh seed sizes for finite element models

Eight-node, linear brick elements (C3D8R) were utilized in the girders, concrete haunch, and cross frames. The concrete haunch was modeled using brick elements instead of shell elements so that large shell elements with a constant depth could be used to define the primary surface of the deck. The top flange, concrete haunch, and bottom flange were meshed using a 50.8 mm (2.0 in.) mesh throughout. The web was meshed using small elements near the connection of the cross frames and then decreased in density away from the connection regions (Figure D.17). Regions of tetrahedral mesh were used between areas with different sizes of structured, hexagonal mesh to allow the elements to transition from one size to another. Cross frames were also meshed with a variety of element sizes to optimize efficiency of the models (Figure D.17).

Transition regions, 76.2 mm (3.0 in) wide, were used in the top flange, web, and bottom flange where the girder transitioned between positive and negative cross-sections. This region was meshed using a tetrahedral 50.8 mm (2.0 in) mesh. The transition was assumed to have negligible effects on overall bridge analysis because the region occurred at a point of minimal moment in the girder and was not located near a point of interest.

Each two-span bridge was modeled as continuous, pinned at the interior pier, and supported by rollers at the abutments. The boundary conditions of the FE models were approximated by applying restraints over a 152 mm (6.00 in) long section of the bottom flange centered over both abutments and the interior pier.

D.2.3.4   Stress Analysis – Hot Spot Stress Analysis

In determining stresses for comparison, it is critical to have a consistent 'measuring stick'. Fatigue is generally based on nominal stresses; however, this was not seen as practical for the complex geometry associated with web gap regions. Maximum tensile principal stress, a 3-D stress, was the chosen basis for comparison between bridge configurations. It was considered critical in determining distortion-induced fatigue vulnerability to account for stresses in all three directions, capturing both nominal and out-of-plane stresses.

Due to the complex geometry of the web gap region, HSS one-point procedure was used as a consistent method for determining stresses, rather than the absolute maximum stress. According to this procedure, a point was chosen away from the weld toe or connection to determine stresses that are comparable in nature. For this analysis, stresses were obtained at a distance of 0.20 in. (approximately half the web thickness) away from the edge of the connection plate on the web as seen in Figure D.18. Stresses for all nodes along the path were obtained, and the maximum along this path was chosen for each cross frame. This procedure provided a consistent comparison even as the stress distribution in the web gap changed between models.
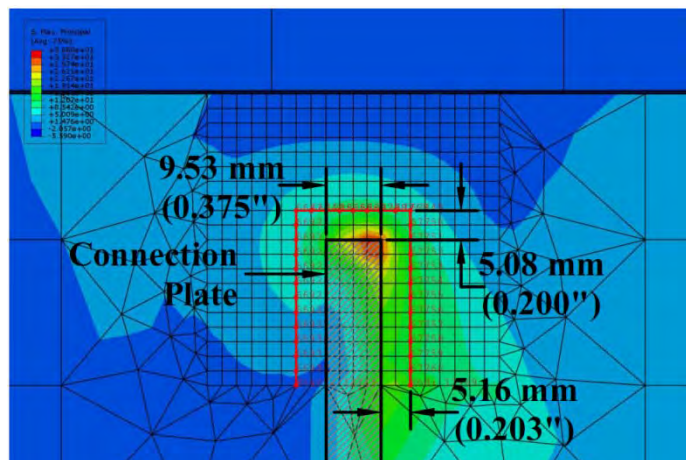
Figure D.18: Hot spot stress analysis path (Shown in red)

D.2.4 Results

D.2.4.1 Absolute and Differential Girder Deflection

Vulnerability to fatigue failure in areas surrounding the web gap has previously been considered to be directly related to the amount of differential deflection between adjacent girders. Therefore, the effect of skew angle, girder arrangement, and girder spacing on girder deflection and differential deflection between girders were evaluated in this study.

Vertical girder deflection at each cross frame location was determined using FE models. In all cases, the largest absolute and differential deflections were located in the positive moment regions, near the center of each span. Consistently, the loaded girder (Girder 3) experienced the most deflection. Figure D.19 shows the deflection profile for all four girders in the 40 degree skewed model, with cross frames positioned parallel to the skew angle every 4.58 m (15.0 ft). Deflection of Girder 2 was restrained by the north exterior girder (Girder 1), and therefore did not experience as much deflection as Girder 4. Differential deflection between girders ordered from highest to lowest in magnitude was as follows: Girder 1 to 2, Girder 2 to 3, Girder 3 to 4. These results were consistent regardless of skew angle or cross frame arrangement in all models evaluated.
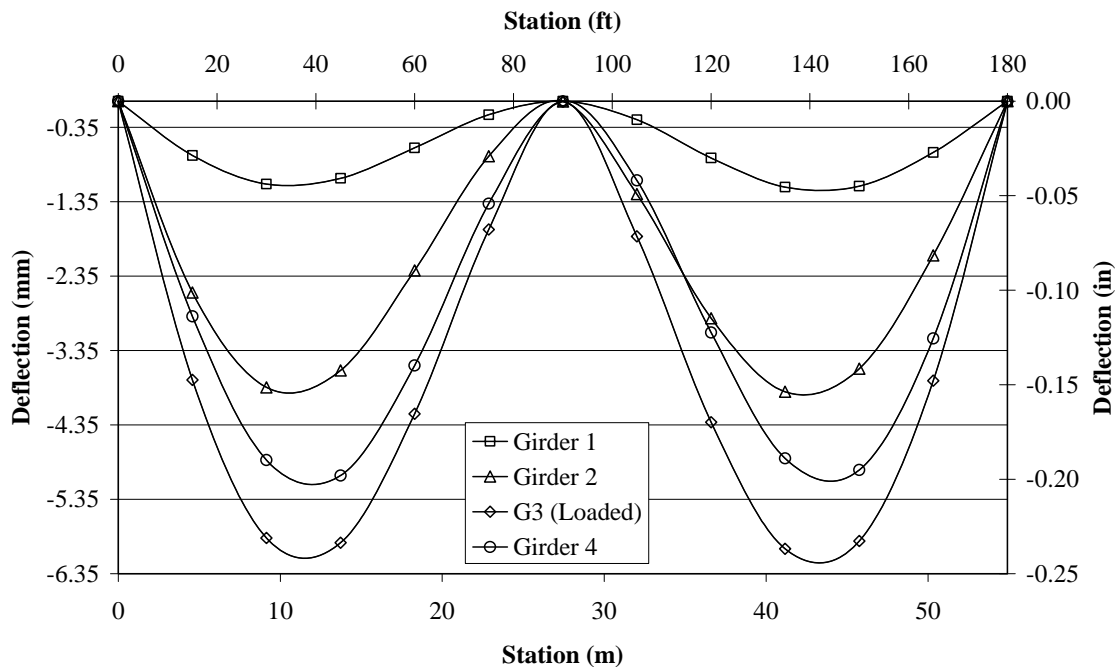
**Figure D.19: Deflected profile of girders from 40 degrees skewed model
Cross frames positioned parallel to skew, spaced at 4.58 m (15 ft)**

358

D.2.4.2   Relationship between Deflection and Stresses

One maximum principal stress value was extracted, using HSS analysis, for the top and bottom of each web-to-cross frame connection. Both stress and differential deflection quantities were highest in positive moment regions, but the differential deflections did not reliably correlate with the location of highest stress. Differential deflection was found to be greatest between Girders 1 and 2, but none of the highest stresses occurred in this region. The highest stresses for the parallel to skew bridges occurred at the connections for the cross frames between Girders 3 and 4, which was found to be the area of lowest differential deflection. In this study, differential deflection was not found to be a reliable predictor of the location of high web gap stress, although it has commonly been adopted as such in previous studies (Berglund and Schultz 2006).

Because maximum principal stresses were used for comparison, one would expect stresses in the web gap region to be affected by the amount of bending stress in the girders. In this analysis, the largest principal stresses were found in Girders 2, 3, and 4, and the location of maximum stress was in the positive bending moment region towards the center of the span, consistent with areas of high bending moment.

Although differential deflection between Girders 3 and 4 was found to be much smaller than that between Girders 2 and 3, the stresses were found to be consistently higher in Girder 4. This was likely due to tensile forces on the south side of Girder 2 (the side closest to the loaded girder) being balanced by tensile forces on the north side of Girder 2. Therefore, if two cross frames were attached to a girder across from each other, stresses tended to balance and drop in magnitude. This is consistent with what KDOT has observed in the field, as well as research performed by Fraser, Grondin, Kulak, and D'Andrea (Fraser et al. 2000; Grondin et al. 2002).

D.2.4.3   Bridges with Cross Frames Placed Parallel to Skew Angle

Results from bridge models with cross frames placed parallel to skew as well as the right bridge were compared to determine the effects of skew angle and cross frame spacing on stress demand. The top web gap region of the exterior girder adjacent to the loaded girder (Girder 4) was found to have the highest stress demand in all six models, with the stress magnitude in the interior girder adjacent to the loaded girder (Girder 2) slightly lower.

D.2.4.4 Skew Angle

Effect of skew angle on maximum stress magnitude was evaluated in bridges with cross frames placed parallel to the skew. Maximum stress at each cross frame along the length of the girder was determined from analytical models. Figure D.20 shows the value of maximum stress in Girder 4 (the girder with highest magnitude of stress demand) increased with skew angle, although only slightly. Research performed by Jajich and Schultz (2003) also found distortion-induced fatigue susceptibility increased with skew angle. A similar trend was noted for bridge models with the larger, 9.15 m (30.0 ft), cross frame spacing. The increase in stress demand between the right bridge and 20 degree skew models was found to be 13% for the 4.58 m (15.0 ft) spacing and 6% for the 9.15 m (30.0 ft) cross frame spacing. Increase in stress demand between the 20 and 40 degrees skew models was only found to be 4% for the 4.58 m (15.0 ft) spacing and 6% for the 9.15 m (30.0 ft) cross frame spacing.

Maximum stress in the interior girder adjacent to the loaded girder (Girder 2) behaved in an opposite manner. Stress on the south face (the face connected to the loaded girder) decreased with skew angle, although only slightly. Currently AASHTO Specifications (2013) prohibit construction of bridges with cross frames aligned parallel to the skew angle when the skew angle is greater than 20 degrees This research showed that for the bridge configurations analyzed, the increase in maximum principal stress was not significant between bridges with 20 and 40 degrees skew angles under the applied loading.
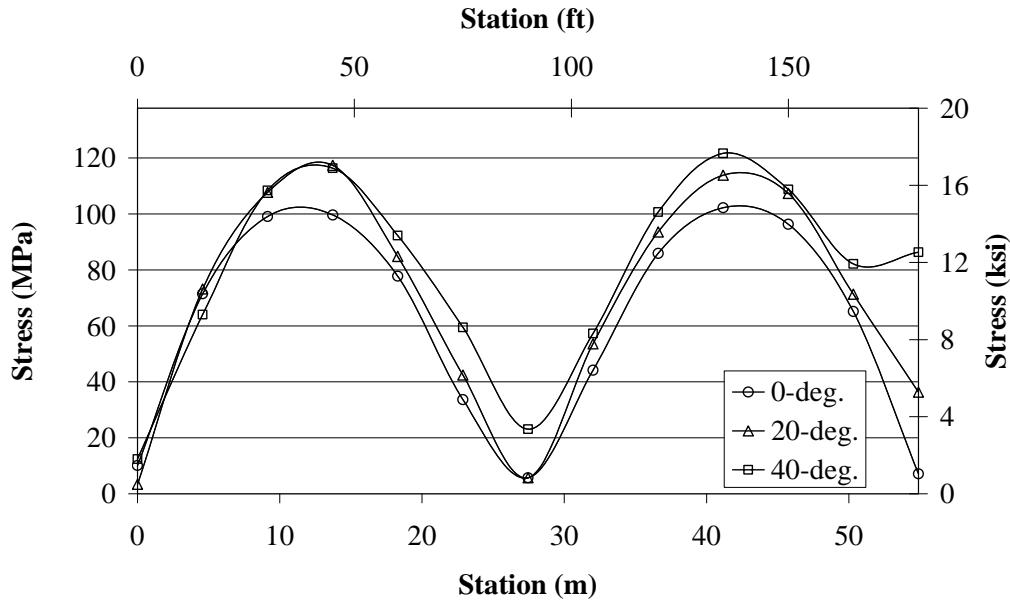
**Figure D.20: Maximum stress in top web gap region of girder 4-north
at each cross frame location in. parallel to skew models with 4.58 m (15 ft) spacing**

D.2.4.5   Effect of Cross Frame Spacing

Cross frame spacing was found to be proportional to maximum principal stress in bridges with cross frames placed parallel to the skew angle. Doubling cross frame spacing from 4.58 m to 9.15 m (15.0 ft to 30.0 ft) increased the maximum principal stress demand in each skewed bridge model by less than 10%. Therefore, cross frame spacing in a bridge with cross frames placed parallel to skew was found not to have a significant effect on stresses in the web gap region. It is important to remember that the bridge evaluated was only loaded in the vertical direction. Effects of cross frame spacing may be more significant if similar models with alternative load configurations were evaluated.

D.2.4.6   Effect of Staggered Cross Frames

Staggering the cross frames, in accordance with AASHTO Specifications (2013), tended to increase differential deflections because the cross frames were located at different stations on each girder. Comparing the results from the models with staggered cross frames to the models with cross frames placed parallel to skew, it was observed that although staggering the cross frames caused the location of maximum stress to change drastically, the magnitude of maximum stress changed by less than 1%.

361

Maximum stresses in the models with staggered cross frames occurred in the positive moment region of the loaded girder (Girder 3) in the bottom web gap region. In addition to increasing differential deflection, staggering the cross frames caused the bottom of the girder to displace transversely in reverse curvature along the length of the beam. At the top of the girder, the constraint imposed by the slab suppressed this mode of deformation. It is hypothesized that this change in girder response (as compared to models with cross-frames placed parallel to the skew) was the reason maximum stress demands were found in the bottom web gap region in configurations with staggered cross frames. Figure D.21 shows a cross frame between Girders 3 and 4 in the 40 degree skewed model with cross frames placed both parallel to the skew angle and staggered at the same station along the girder. The deflection scale and contouring levels are identical in both figures.

(a)   (b)
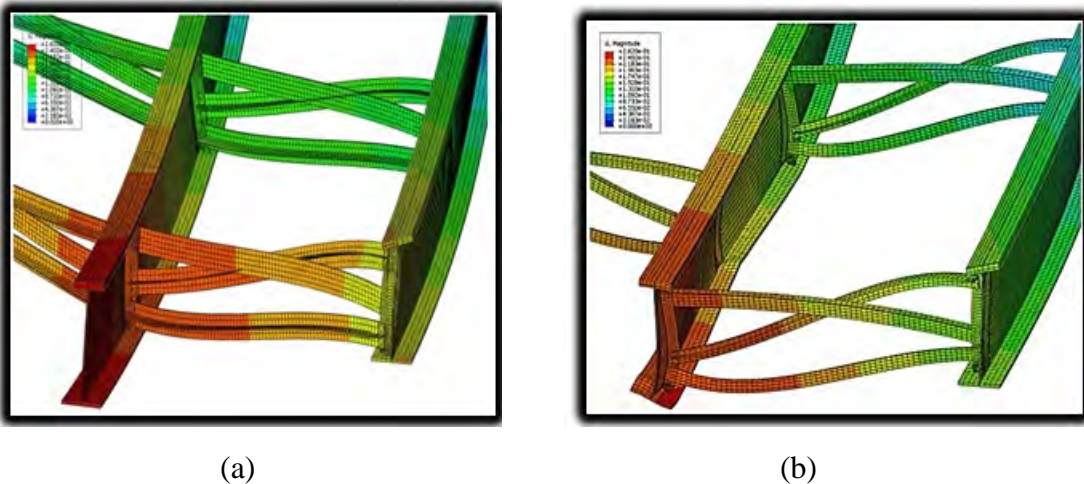
Figure D.21: Deflected shape of 40 degree skewed bridge
with 4.58 m (15.0 ft) cross frame spacing and: (a) cross frames placed parallel to skew;
(b) staggered cross frames. Deck removed from view for clarity

The spacing between cross frames on opposite sides of a girder, i.e., the amount of stagger, was directly influenced by angle of skew. Figure D.15(c) shows cross frame layout for the models with staggered cross frames. When two cross frames were in close proximity on opposite sides of the web, stresses acting on both sides tended to cancel each other out and reduced the tensile stress in this area. As skew angle approached 45 degrees, cross frames on opposite sides of the web became more evenly spaced and alternating transverse displacement

(reverse curvature effect) was increased. The maximum stress value was found in the 40 degree skew model with 4.57 m (15.0 ft) spacing. Stresses in all of the models dropped significantly (over 20%) when the cross frame spacing was changed from 4.58 to 9.15 m (15.0 to 30.0 ft). This behavior was due to decreased restraint resulting from fewer cross frames, leading to lower stress concentrations in the web gap region. In models with staggered cross frames, the maximum principal stress shifted from the girders adjacent to the loaded girder to the loaded girder itself. Maximum principal stress was no longer in the exterior girder because it did not have cross frames on both sides of the web causing reverse curvature. Staggered models showed more complicated behavior than models with cross frames placed parallel to the angle of skew. The magnitude of stress in the web gap region was significantly altered due to amount of stagger (directly related to the skew angle) and the number of cross frames.

D.2.5 Conclusions

The parametric study described in this paper investigated the effects of skew and lateral brace placement on stresses and differential deflections of a steel girder bridge. Specifically, skew angle, cross frame spacing, and cross frame arrangement were considered. Results of the study can be summarized as follows:

- Differential deflection and stress were found to be proportional, although differential deflection did not predict the row of cross frames corresponding with the highest stress demand.
- Maximum differential deflections and stresses occurred in positive moment regions for all of the bridges modeled.
- Maximum stresses consistently occurred in the top web gap region of the exterior girder adjacent to the loaded girder (Girder 4) in bridges with cross frames placed parallel to skew angle.
- Maximum stresses consistently occurred in the bottom web gap region of the loaded girder (Girder 3) in bridges with staggered cross frames. Therefore, it was found that bottom web gaps should not be neglected in analysis, and should be considered during fatigue life assessment of existing structures.

- Bridges with cross frames placed parallel to the skew angle and those with staggered cross frames behaved very differently, although the maximum stress was found to be similar for both brace placements considered.
- In bridges with cross frames placed parallel to the skew angle, increased cross frame spacing slightly increased the maximum stress in the bridge.
- Stagger and cross frame spacing had a large impact on the stresses in the web gap region of bridges with staggered cross frames, although the stress values did not increase proportionally to skew angle.
- In bridges with staggered cross frames, the restraint placed on the girder was found to be a significant parameter.

Since many bridges built prior to the mid-1980s are susceptible to distortion-induced fatigue, it is important to recognize bridges, and specific locations within bridges, prone to this type of failure in an effort to extend useful life through monitoring and repair of critical details. Although much research has been performed to identify regions of maximum differential deflections and to evaluate the influence of bridge geometry on differential deflection, little prior work has been done to quantify web gap stresses or relate differential deflections to stresses. This paper has attempted to provide a link to further guide bridge engineers in identifying details susceptible to distortion-induced fatigue cracking. It is hoped that improving current understanding of the effects of lateral brace placement and skew angle will guide judicious and deliberate implementation of lateral bracing schemes in future bridge designs.

D.2.6 References

AASHTO (2013). *2013 Interim Revisions to the AASHTO LRFD Bridge Design Specifications.* 6th ed. American Association of State Highway and Transportation Officials, Washington, D.C.

AISI Example 2: Two-Span Continuous Composite I Girder (1997). American Iron and Steel Institute, Washington, D.C.

Barth, A. S. and Bowman, M. D. (2001). "Fatigue Behavior of Welded Diaphragm-to-Beam Connections." *Journal of Structural Engineering*, 127(10), 1145-1152.

Barth, K. E., Hartnagel, B. A., White, D. W., and Barker, M. G. (2004). "Recommended Procedures for Simplified Inelastic Design of Steel I-Girder Bridges." *Journal of Bridge Engineering,* 9(3), 230-242.

Berglund, E. and Schultz, A. (2006). "Girder Differential Deflection and Distortion-Induced Fatigue in Skewed Steel Bridges." *Journal of Bridge Engineering*, 11(2), 169-177.

Connor, R. J. and Fisher, J. W. (2006). "Identifying Effective and Ineffective Retrofits for Distortion Fatigue Cracking in Steel Bridges Using Field Instrumentation." *Journal of Bridge Engineering,* 11(6), 745-752.

Cousins, T. E. and Stallings, J. M. (1998). "Laboratory Tests of Bolted Diaphragm-Girder Connections." *Journal of Bridge Engineering*, 3(2), 56-63.

Fisher, J. W., Jian, J., Wagner, D. C., and Yen, B. T. (1990). *Distortion-Induced Fatigue Cracking in Steel Bridges.* NCHRP Report 336. Transportation Research Board, National Research Council, Washington, D.C.

Fisher, J. W. and Keating, P. B. (1989). "Distortion-Induced Fatigue Cracking of Bridge Details with Web-gaps." *Journal of Constructional Steel Research,* 12(3-4), 215-228.

Fraser, R. E. K., Grondin, G. Y., and Kulak, G. L. (2000). *Behaviour of Distortion-Induced Fatigue Cracks in Bridge Girders*. Structural Engineering Report no. 235. University of Alberta, Edmonton, Canada.

Grondin, G. Y., Fraser, R., and D'Andrea, M. (2002). "Testing and Evaluation of Fatigue Damaged Girders." *4th Structural Specialty Conference.* Canadian Society for Civil Engineering, Montreal, Quebec.

Jajich, D. and Schultz, A. E. (2003). "Measurement and Analysis of Distortion-Induced Fatigue in Multigirder Steel Bridges." *Journal of Bridge Engineering*, 8(2), 84-91.

Keating, P. B. (1994). "Focusing on Fatigue." *Civil Engineering*, 64(11), 54-57.

Khalil, A., Wipf, T. J., Greimann, L., Wood, D. L., and Brakke, B. (1998). "Retrofit Solution for Out-of-Plane Distortion of X-Type Diaphragm Bridges." *Transportation Conference Proceedings, Iowa Department of Transportation*, 99-102.

Kim, M. H. and Kang, S. W. (2008). "Testing and Analysis of Fatigue Behaviour in Edge Details: a Comparative Study Using Hot Spot Structural Stresses." *Proceedings of the Institution of Mechanical Engineers, Part C: Journal of Mechanical Engineering Science*, 22(12), 2351-2363.

Lindberg, A. and Schultz, A. (2007). *Incorporation of Fatigue Detail Classification of Steel Bridges into the Minnesota Department of Transportation Database: Final Report*. Report MN/RC-2007-22. Minnesota Department of Transportation, St. Paul, MN.

Maddox, S. J. (2002). "Hot-Spot Stress Design Curves for Fatigue Assessment of Welded Structures." *International Journal of Offshore and Polar Engineering,* 12(2), 134-141.

Marquis, G. and Kahonen, A. (1995). *Fatigue Testing and Analysis using the Hot Spot Method*. VTT Publications no. 239. Technical Research Centre of Finland.

NSBA. *Steel Bridge Design Handbook: Example 2A: Two-Span Continuous Straight Composite I-Girder Bridge.* National Steel Bridge Alliance, American Institute of Steel Construction, Chicago, IL.

Roddis, W. M. K. and Zhao, Y. (2001). "Out-of-Plane Fatigue Cracking in Welded Steel Bridges: Why It Happened and How It Can Be Repaired." *Welding Innovation*, 18(2), 2-7.

Roddis, W. M. K. and Zhao, Y. (2003). "Finite-Element Analysis of Steel Bridge Distortion-Induced Fatigue." *Journal of Bridge Engineering*, 8(5), 259-266.

Wang, L. and Helwig, T. A. (2008). "Stability Bracing Requirements for Steel Bridge Girders with Skewed Supports." *Journal of Bridge Engineering*, 13(2), 149-157.

AD ASTRA PER ASPERA

Kansas
Department of Transportation